Konnektivität molekularer Domänen bei der kraftinduzierten Entfaltung einzelner Biomoleküle

Dissertation

an der Fakultät für Physik
der Ludwig-Maximilians-Universität
München

vorgelegt von

Stefan W. Stahl
aus Friedrichshafen

München, den 24. Mai 2012

Erstgutachter:	Prof. Dr. Hermann E. Gaub
Zweitgutachter:	Prof. Dr. Tim Liedl
Tag der mündlichen Prüfung:	2. August 2012

INHALT

1 ZUSAMMENFASSUNG

In den zellulären Stoffwechsel- und Signalnetzwerken existiert eine Vielzahl von logischen Abhängigkeiten, die auf Prozesse auf molekularer Ebene zurückzuführen sind. So lässt sich beispielsweise die Effizienz einer biochemischen Reaktion über Enzyme regulieren, deren Aktivitätsgrad von äußeren Parametern abhängt. Kraft stellt eine dieser Einflussgrößen dar. Diese Arbeit befasst sich damit, das Verhalten mehrerer, logisch verknüpfter, molekularer Domänen unter Krafteinwirkung zu studieren und sich deren Eigenschaften für nanotechnologische Verfahren zu Nutze zu machen.

Eine biomolekulare Domäne beschreibt einen Teil der Tertiärstruktur eines Biopolymers, der über atomare Wechselwirkungen wie Wasserstoffbrückenbindungen oder van-der-Waals-Kräfte eine solide globuläre Struktur bildet. Unter mechanischer Belastung bleibt diese für gewöhnlich für eine charakteristische Zeit stabil und entfaltet dann simultan als Ganzes. Die Kinetik der Entfaltung einer Domäne kann hierbei bedingt durch die Reihenfolge der strukturellen Elemente entlang der Polymersequenz vom Faltungszustand anderer Domänen abhängen.

Neben der Untersuchung von in der Natur vorkommenden Proteinen mit multiplen Domänen wurden artifizielle DNA- und proteinbasierte Systeme mit verschiedener Bindungsstärke konstruiert. Dies ermöglicht den gerichteten Transport einzelner, molekularer Bausteine mit der Präzision eines Rasterkraftmikroskopes im Nanometer-Bereich. Mithilfe dieser *Single-Molecule Cut-and-Paste* (SMCP) Technik können auf der Basis gerichteter, molekularer Erkennung räumliche Arrangements funktioneller Bausteine geschaffen werden. Diese lassen sich mittels Fluoreszenzmikroskopie als isoliertes System betrachten.

Die Zielsetzung bei der Untersuchung der natürlichen Systeme war es, deren Abhängigkeiten zu verstehen und herauszufinden, wie sich diese mit ihrer Funktion und den an das Protein gestellten Umgebungsbedingungen in Einklang bringen lassen. Die dabei gewonnene Erkenntnis liefert nicht nur wichtige Beiträge zur biologischen und medizinischen Grundlagenforschung, sondern kann, wie am Beispiel der SMCP-Technik ersichtlich, auch hilfreich bei der Entwicklung neuartiger Messmethoden der molekularen Bio- und Nanotechnologie sein.

Mittels Einzelmolekülkraftspektroskopie im „Konstante-Kraft“ (engl. *Force-Clamp*) Modus wurde die Kooperativität der fünf Proteindomänen des Enzyms Titinkinase untersucht. Dieses Muskelprotein wandelt in der Skelett- und Herzmuskulatur mechanische in biochemische Signale um und regelt dadurch den Umsatz weiterer Proteine und die

Expression von Genen. Es wird gezeigt, dass sich die einzelnen mechanisch induzierten Entfaltungsschritte gegenseitig bedingen und dass dies inhärent durch die molekulare Faltung des Proteins vorgegeben wird. Da Kraft zum natürlichen Parameterraum dieses Moleküls gehört, muss seine Struktur an kraftinduzierte konformationelle Änderungen angepasst sein. Durch die Abhängigkeit der Energiebarrieren während der Entfaltung wird gewährleistet, dass stabilisierende und enzymatisch wirksame Domänen nicht vor regulatorischen Domänen entfalten.

Myosin-Light-Chain Kinase (MLCK) ist ein weiteres Muskelenzym, bei dem es Hinweise auf eine mechanische Aktivierbarkeit gibt. Einzelmolekülexperimente dieser Dissertation zeigen, dass die Entfaltung der Kinase ebenfalls in mehreren Schritten vonstatten geht und dass einer der Zwischenzustände durch ATP-Bindung stabilisiert wird. Die absoluten Entfaltungskräfte liegen dabei unter denen der Titinkinase, was der Hypothese der mechanischen Aktivierbarkeit entgegenkommt.

Als weiteres System wurde das Cellulosom des thermophilen Bakteriums *Clostridium Thermocellum* auf seine mechanische Stabilität überprüft. Cellulosome sind an der Außenseite von Bakterien und Pilzen verankerte Proteinkomplexe, die in der Lage sind Lignozellulose zu zersetzen. Bei der Prozessierung der Cellulose können im Cellulosom hohe Scherkräfte auftreten, da dieses das gesamte Bakterium mit dem makromolekularen Substrat verknüpft. Mittels AFM-basierter Kraftspektroskopie wurde die Wirkung von Kraft auf einen Verbund verschiedener Konstituenten eines Cellulosoms untersucht. Es wird gezeigt, dass sich der Komplex im Vergleich zu anderen Biomolekülen durch eine extrem hohe mechanische Stabilität auszeichnet. Innerhalb der hohen Entfaltungskräfte besteht eine Hierarchie für die verschiedenen Komponenten. Bei vergleichsweise niedrigen Kräften entfalten die enzymatischen Domänen gefolgt von mittleren Kräften für das Entkoppeln der Enzyme mit dem Bindungspartner Cohesin. Sehr hohen Kräften halten die intramolekularen Wechselwirkungen der Cohesine und der Cellulose bindenden Domänen stand. Die Abstufung hoher Stabilitäten stellt eine sehr gute Anpassung an die natürlichen Anforderungen des Proteinkomplexes dar.

Für die durchgeführten Messungen wurde ein modulares Kraftmikroskop (AFM) entwickelt, das sich mit einem einzelmolekülsensitiven Fluoreszenzmikroskop kombinieren lässt. Die spezielle Konstruktion weist eine extrem hohe mechanische Stabilität auf. Mittels einer photothermischen Regelung kann das AFM darüber hinaus für sensitive Bildgebung weicher molekularer Oberflächen oder in einen extrem schnellen kraftspektroskopischen Messmodus mit konstanter Zugkraft verwendet werden. Die akkurate Arbeitsweise des Systems wurde in einem internationalen Vergleichsversuch bestätigt.

2 EINLEITUNG

Die Erdoberfläche wird nun schon seit mehreren Milliarden Jahren [1, 2] von Lebewesen bewohnt die verschiedener, vielfältiger und manchmal auch verwunderlicher kaum sein könnten. Betrachtet man diese Vielfalt und Komplexität, ist es erstaunlich, dass sie im Wesentlichen nur aus sehr wenigen der chemischen Elemente aufgebaut sind. Die Stoffzusammensetzung von lebender Materie unterscheidet sich deutlich von der Gesamtzusammensetzung der auf der Erde vorhandenen Materialien. Kohlenstoff (C), Wasserstoff (H), Sauerstoff (O) und Stickstoff (N) bilden die Grundlage eines jeden Organismus. Sie machen 96,5% des Gewichts eines Organismus aus [3]. Nimmt man noch Phosphor (P) und Schwefel (S) dazu kann man bereits sämtliche Aminosäuren sowie Lipide, Kohlenhydrate und Nukleotide bilden.

Diese scheinbar so einfachen Bausteine zu verstehen ist nicht immer eine einfache, aber häufig eine sehr faszinierende Aufgabe. So vielfältig die verschiedenen Organismen und ihre Lebensräume auch immer sein mögen, letzten Endes sind sie sich in vielen Aspekten auch sehr ähnlich. Sie entstehen aus einzelnen Zellen und ihr Bauplan ist in der Sequenz der DNA-Basen enthalten. Mit dieser Information ist eine Zelle in der Lage durch ein komplexes biochemisches Zusammenspiel zu einem einzigartigen Lebewesen zu differenzieren, das zu studieren sich die Biophysik zum Ziel gesetzt hat.

Ein lebender Organismus befindet sich ständig außerhalb des thermodynamischen Gleichgewichtes und muss dafür Energie aufbringen, die er aus seiner Umgebung bezieht. Nur so können viele der molekularen Reaktionen in einer Zelle in gerichteter Form ablaufen. Betrachtet man diese Prozesse im Detail, so stellt man fest, dass neben der Energie auch die Kraft eine wichtige Observable ist, da Kräfte für viele biologische Prozesse entweder einen bedeutenden Einflussfaktor darstellen oder aktiv durch sie aufgebracht werden. Die Muskelkontraktion ist ein naheliegendes Beispiel, das auch in der makroskopischen Welt offensichtlich ist. Auf molekularer Ebene findet sich deren Ursache im zyklischen, mit Konformationsänderungen verbundenen Binden und Dissoziieren von Myosinen und Aktinen unter Verbrauch des „molekularen Treibstoffs“ Adenosintriphosphat (ATP). Aber auch in weit weniger offensichtlichen Fällen sind Kräfte von Bedeutung. So finden beispielsweise Transportprozesse innerhalb von Zellen häufig durch Motorproteine in gerichteter Weise statt. Und auch bei der Aufnahme von Partikeln in Zellen oder dem aktiven Transport von Ionen durch Poren müssen Kräfte aufgebracht werden [4-8]. Darüber hinaus beeinflussen Kräfte, die von außen auf ein biologisches System wirken, dessen physiologische Prozesse. So hängen beispielsweise das Wachstum [9] und die Adhäsion [10] von Zellen oder auch der Wundheilungsprozess [11] von externen Kräften ab. Darüber hinaus werden

Sinnesorgane wie das Gehör [12] oder der Tastsinn [13] durch mechanische Stimulation gesteuert. Dazu werden extra- und intrazelluläre Kraftsensoren benötigt, deren Funktionsprinzip im Allgemeinen durch kraftinduzierte Konformationsänderungen auf molekularer Ebene beschrieben werden kann [14-16]. Dieses Funktionsprinzip besser zu verstehen ist von elementarem Interesse und Teil dieser Arbeit.

Die Funktion von Proteinen beruht auf ihrer Fähigkeit, mit anderen Molekülen wechselzuwirken. Diese wird durch die Faltung der Aminosäurekette in die Tertiärstruktur bestimmt und lässt sich dynamisch zum Beispiel über allosterische Regulation variieren. Somit gehen mit Funktionsuntersuchungen in der molekularen Biologie auch immer Strukturuntersuchungen einher. Vor exakt hundert Jahren gelang es Wissenschaftlern um Max von Laue in den Kellerräumen der Ludwig-Maximilians-Universität in München erstmals Kristallstrukturen durch Röntgenstreuung aufzulösen [17]. Die 14 Jahre später entdeckte Möglichkeit, dass auch Proteine kristallisiert werden können, führte zu einem Durchbruch in der Molekularbiologie [18]. Inzwischen ist die Kombination der beiden Techniken, die biologische Röntgenstrukturanalyse zu einem wichtigen Werkzeug geworden, wenn es darum geht, den Aufbau von Biomolekülen zu verstehen. Sie kann allerdings nur ein statisches Bild der intra- oder intermolekularen Zusammenhänge vermitteln.

Die native Umgebung von biomolekularen Kraftsensoren kennzeichnet jedoch eine hohe Dynamik und auf biomolekularen Maßstäben können bereits kleine Fluktuationen einzelner Moleküle weitreichende Konsequenzen haben [19-21]. Experimente mit einem Ensemble aus Molekülen wie die Oberflächenplasmonenresonanzspektroskopie [22] oder die Ramanspektroskopie [23] liefern bereits wichtige Informationen zur Dynamik von inter- und intramolekularen Prozessen. Allerdings setzt sich ihr Ergebnis immer aus einem gemittelten Beitrag der einzelnen Moleküle zusammen. Deshalb haben Wissenschaftler lange davon geträumt, derartige Experimente mit einzelnen Molekülen durchzuführen. Erwin Schrödinger behauptete 1952 noch, dass wir vermutlich niemals mit einzelnen Elektronen, Atomen oder Molekülen arbeiten können werden [24]. Die Vorteile eines Einzelmolekülansatzes liegen auf der Hand. Der Chemiker Urs Wild wird im diesem Kontext mit dem Satz zitiert, dass „einzelne Moleküle zu 100% rein[1] “ seien [25]. Darüber hinaus muss man bei Experimenten an einzelnen Molekülen seine Rückschlüsse nicht durch Beobachtung von Ensemblemittelwerten ziehen. Somit ermöglichen Einzelmolekülmessungen, die Beiträge verschiedener Populationen sich zu unterscheiden[2].

[1] Dabei ist allerdings zu beachten, dass der Begriff der Reinheit dem Konzept von Ensembles entspringt und somit für einzelne Moleküle streng genommen nicht anwendbar ist.

[2] Ein Beispiel hierzu aus dem täglichen Leben: Das durchschnittliche Monatsseinkommen beträgt in Deutschland derzeit ca. 3700 Euro brutto je Haushalt (Quelle: Statistisches Bundesamt; https://www.destatis.de). Anhand dieses Wertes lässt sich zwar, wenn man den Warenkorb zurate zieht, die Tendenz ablesen ob die Kaufkraft in Deutschland in den letzten Jahren gestiegen oder gesunken ist. Man kann mit dem Mittelwert aber beispielsweise nicht ermitteln, ob und wie sich die

Mit der Einzelmolekülkraftspektroskopie existiert seit ca. 20 Jahren eine Technik, die Einblicke in die Verhaltensweisen einzelner Moleküle unter Kraft bietet. Sie ist in der Lage, charakteristische, durch die Thermodynamik hervorgerufene Fluktuationen zu beobachten und kann deren Einflüsse auf die Stochastizität von Prozessen ermitteln. Das Rasterkraftmikroskop (engl. *Atomic Force Microscope* / AFM) ist ein ideales Werkzeug um das Verhalten einzelner Moleküle unter Kraft zu studieren. Mithilfe der AFM-basierten Kraftspektroskopie lassen sich einzelne Moleküle kontaktieren und in alle drei Raumrichtungen kontrolliert manipulieren. Dabei wird die Kraftantwort des Systems aufgezeichnet. Kraftspektroskopie eignet sich aber bei Weitem nicht nur, um Biomoleküle mit mechanischer Funktion zu analysieren. Sie kann ebenfalls weitreichende Einblicke in die Stabilität von interagierenden Systemen und in die Architektur von Proteinen erlauben.

Diese Arbeit befasst sich mit der Untersuchung der Konnektivität von molekularen Domänen, die Energiebarrieren bei der mechanisch induzierten Entfaltung von Biomolekülen hervorrufen. Eine molekulare Domäne ist ein Teil der Tertiärstruktur eines Biomoleküls, der sich unter Kraft als eine Einheit verhält und unter Belastung nach einer charakteristischen Zeit auf einmal entfaltet. Wie sich herausstellen wird, kann man die in einem Verbund von Biomolekülen auftretenden Domänen schematisch als Netzwerk darstellen. Unter Kraft können sich die von ihnen hervorgerufenen Energiebarrieren bedingen oder unabhängig voneinander entfalten. In diesem Kontext wird der Begriff Domänentopologie[3] für die Verteilung der zu einer Domäne gehörenden Primärstrukturelemente entlang der Sequenz sowie die daraus resultierende räumliche Anordnung der Tertiärstrukturelemente verwendet. Logische Abhängigkeiten im Entfaltungspfad mehrerer Domänen entstehen zum Beispiel, wenn Teile der Sequenz einer Domäne in der Primärstruktur von einer anderen Domäne unterbrochen werden.

In der Natur wird die Effizenz von molekularen Systemen häufig durch die geschickte Kombination mehrerer funktioneller Einheiten gesteigert. Das Cellulosom von Lignocellulose verarbeitenden Bakterien und Pilzen ist ein Paradebeispiel für ein Arrangement von

---

Armutsquote ausbreitet oder ob Frauen tendenziell mehr verdienen als Männer. Dies wird erst ermöglicht, wenn man die gewünschen Observablen für einzelne Personen oder Haushalte erhalten kann.

[3] Der Begriff „Topologie“ setzt sich aus den griechischen Wörtern τοπος (tópos) und λογος (lógos) für Ort und Lehre zusammen. Die Verwendung des Begriffes hängt in der Praxis vom verwendeten Kontext ab und so werden mit Topologie in verschiedenen wissenschaftlichen Disziplinen unterschiedliche Sachverhalte beschrieben. Im Duden findet sich als Begriffsbezeichnung „Lehre von der Lage und Anordnung geometrischer Gebilde im Raum“ [26]. Historisch betrachtet wurde der Begriff erstmals 1847 von Johann Benedikt Listing in seiner Schrift „Vorstudien zur Topologie“ [27] eingeführt und seine weitere Entwicklung angeregt. Seither wird er häufig in der Mathematik verwendet und bezeichnet dort ein „Teilgebiet, das aus der Analyse des Raumbegriffs Eigenschaften allgemeiner Räume herleitet“ [28]. In den Geowissenschaften beschreibt die Topologie räumliche und strukturelle Eigenschaften sowie Nachbarschaftsbeziehungen von Geoobjekten unabhängig von ihrer Ausdehnung und Form [29] und in den Sprachwissenschaften ist es die „Bezeichnung für Wort- und Satzgliedstellung“ [28], in der Informatik wird damit die Struktur der Verbindungen in einem Rechnernetz beschrieben [30] und in der Biologie und Medizin bezeichnet es die räumliche oder logische Anordnung der Teilstrukturen von Organen [31], Zellen [32] oder Molekülen [33, 34]. Darüber hinaus spricht man auch bei biologischen Netzwerken von deren Topologie wenn die Anordnung der Verknüpfungspunkte zueinander beschrieben wird.

Biomolekülen, bei dem das Zusammenarbeiten mehrerer Enzyme in einer definieren Anordnung effektiver als die Summe der einzelnen Teile ist. Es besteht aus verschiedenen molekularen Einheiten die einen strukturierten Komplex bilden und organisiert sich durch molekulare Erkennung.

Solche funktionalen Systeme aus mehreren Konstituenten künstlich in verschiedenen Komplexitätsstufen zu erschaffen ist von Interesse, wenn man deren Funktionsweise studieren möchte. Feynman drückte das mit den Worten „What I cannot create, I do not understand“ aus [35]. In dieser Arbeit wurde die *Single-Molecule Cut-and-Paste* Technik für den gerichteten Transport von Proteinen und funktionellen RNA-Bausteinen weiterentwickelt. Sie erlaubt mithilfe einer Kombination aus AFM und Fluoreszenzmikroskopie die kontrollierte Assemblierung funktioneller biomolekularer Einheiten zu komplexen Strukturen mit einer Präzision im Nanometerbereich. Die Grundlage bildet dabei der in der Biologie bekannte Prozess der Selbstorganisation durch molekulare Erkennung.

Mit der Synthetischen Biologie hat sich mittlerweile ein ganzer Industriezweig entwickelt, der sich Methoden der Bio- und Nanotechnologie zu Nutze macht und künstliche Systeme schafft, die nützliche Produkte liefern. Hier seien nur kurz die Beispiele der Biosynthese von Insulin, der Malariabekämpfung durch synthetisches Artemisinin oder die Potentiale von mit Enzymen gewonnenen Treibstoffen aus Biomasse erwähnt.

Bei dieser kumulativen Dissertation wird für eine detaillierte Beschreibung von Sachverhalten und Ergebnissen an entsprechenden Stellen auf die Publikationen im Anhang verwiesen.

3 BIOLOGISCHE GRUNDLAGEN

Biomoleküle können als sogenannte „weiche“ Materie beschrieben werden. Dies bedeutet, dass sie im Allgemeinen nicht in einer starren Konformation vorliegen, sondern dass diese dynamisch fluktuiert. Dies ist darauf zurückzuführen, dass auf molekularer Ebene die Reibungskräfte gegenüber Trägheit und Gravitation überwiegen während thermische Fluktuationen eine dominante Energiequelle darstellen. Anschaulich gesprochen kann man die Welt eines Biomoleküls auf makroskopischer Ebene in etwa mit dem Versuch vergleichen, inmitten eines Hurrikans in Honig zu schwimmen. Neben den Fluktuationen der Moleküle selbst spielen dynamische Wechselwirkungen zwischen Molekülen für biologische Prozesse eine wichtige Rolle. Im Folgenden sollen beispielhaft einige essentielle molekulare Wechselwirkungen kurz diskutiert werden.

3.1 Molekulare Wechselwirkungen

Die Regulation gerichteter biologischer Prozesse erfolgt häufig durch dynamische Interaktion einzelner Moleküle. Die Dynamik der Assoziation und Dissoziation eines Ensembles von wechselwirkenden Molekülen A und B kann hierbei in erster Näherung durch exponentielle Raten (k_{on}, k_{off}) beschrieben werden:

$$A + B \underset{k_{off}}{\overset{k_{on}}{\rightleftharpoons}} AB\,,$$

wobei die on-Rate abhängig von der Konzentration der beteiligten Moleküle ist. Langlebige Wechselwirkungen sind demnach durch niedrige off-Raten gekennzeichnet.

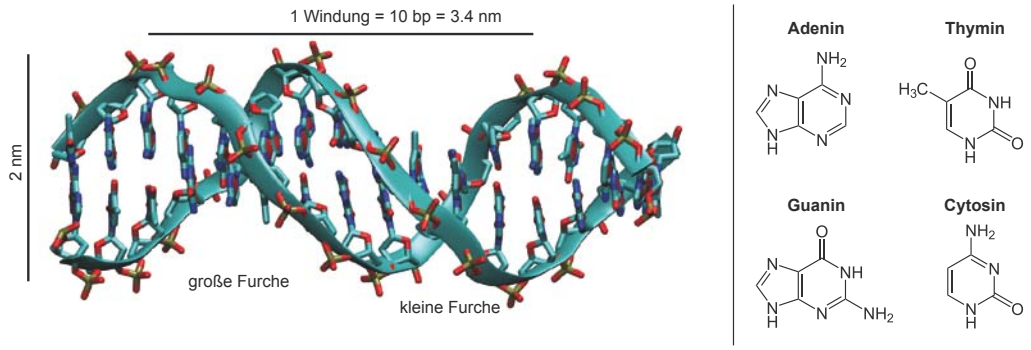

Abbildung 1 – Struktur von B-DNA (PDB: 3BSA)
Die doppelhelikale Struktur zweier komplementärer DNA-Stränge wird durch die Basenpaarungen und *base-stacking* stabilisiert. Das Basenpaar Adenin und Thymin bildet 2 Wasserstoffbrückenbindungen aus. Die Paarung von Guanosin und Cytosin hat durch ihre 3 Wasserstoffbrückenbindungen eine höhere Bindungsenergie.

Desoxiribonucleinsäure (DNA)

Ein Beispiel für eine langlebige Interaktion ist die Hybridisierung von DNA-Strängen, den Trägern der genetischen Information. Für das Überleben eines Organismus ist es wichtig, dass der in der Sequenz der Basen Adenosin (A), Cytosin (C), Guanosin (G) und Thymin (T) gespeicherte molekulare Bauplan unempfindlich gegenüber äußeren Einflüssen ist. Bereits die Mutationen einzelner Basen kann tödliche Konsequenzen haben. Die allgemein bekannte Konformation der Doppelhelix [36] stellt hierbei eine molekulare Wechselwirkung zwischen zwei komplementären Einzelsträngen dar, bei dem die Basen nach außen abgeschirmt sind. Darüber hinaus verringert die doppelt gespeicherte Information die Mutationsrate, da hierdurch Reparaturmechanismen ermöglicht werden. Die Ursache der attraktiven Wechselwirkung zwischen Adenosin und Thymin beziehungsweise Guanosin und Cytosin sind Wasserstoffbrückenbindungen. Das sogenannte *base stacking* [37] erhöht zusätzlich die Stabilität des Systems. In Abbildung 1 werden die Struktur von B-DNA sowie die Strukturformeln der Basen dargestellt. Im Falle zweier komplett komplementärer Stränge reichen bereits 20 - 30 Basenpaare für eine thermische Stabilität über viele Stunden aus. In eukaryotischen Zellen wird die DNA darüber hinaus im Zellkern vom Cytoplasma abgetrennt und durch Bindung zu Proteinen, den Histonen [38], organisiert. Acht DNA-bindende Histone bilden ein Nukleosom, die kleinste Verpackungseinheit der Chromosome.

Die hohe Spezifizität der DNA-Hybridisierung, welche über die Sequenz frei programmiert werden kann, ermöglicht vielseitige Anwendungen in der Bio-Nanotechnologie. Da heutzutage DNA-Oligomere mit über 100 Basenpaaren einfach synthetisiert werden können und innerhalb kurzer Zeit zu moderaten Preisen kommerziell erhältlich sind, ist es bereits möglich, komplexe DNA-Konstrukte zu erstellen, die wiederum aus hunderten von wechselwirkenden DNA-Einzelsträngen bestehen. Diese sogenannten DNA-Origami falten selbstorganisiert zu konstruierten zwei- [39] oder dreidimensionalen [40] Strukturen (Abbildung 2), die wiederum als Ankerpunkt für die präzise Anordnung von weiteren Molekülen [41] oder Nanopartikeln [42, 43] dienen können. Inzwischen lassen sich somit sogar nanoskalige Materialien mit konfektionierten optischen Eigenschaften erstellen [44].

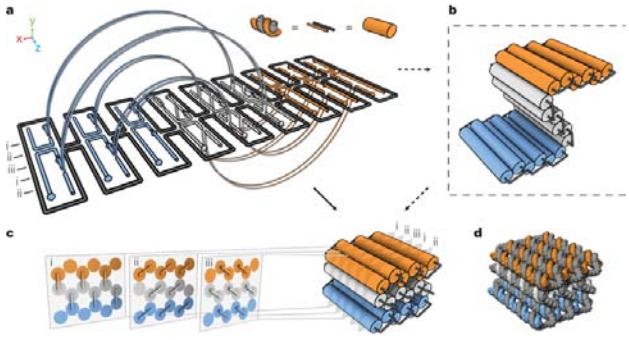

Abbildung 2 – DNA als molekularer Baustein
In sogenannten Origami-Strukturen werden dreidimensionale Objekte durch geschickte Hybridisierung vieler DNA-Oligomere (*staples*) mit einem langen einzelsträngigen DNA-Polymer erzeugt. *Nachdruck mit Genehmigung von Macmillan Publishers Ltd: Nature [40], Copyright 2009*

Antikörper – Antigen Wechselwirkungen

Ein weiteres sehr stabiles System, das aber häufig bereits einer höheren Dynamik unterlieget, bildet die Wechselwirkung von Antikörpern mit ihren Antigenen. Im Organismus werden diese in den Lymphozyten produziert und sind wichtig, um Schadstoffe für das Immunsystem zu markieren [45]. Sie erfreuen sich aber ebenfalls in der Biotechnologie aufgrund ihrer hohen Spezifizität und breiten Einsetzbarkeit einer hohen Beliebtheit, wenn es darum geht, ganze Moleküle oder auch nur atomare Änderungen an diesen zu detektieren. Im menschlichen Immunsystem bestehen Antikörper aus zwei leichten und zwei schweren Aminosäureketten, die jeweils zu mehreren sogenannten Ig-Domänen falten und im Verbund eine Y-förmige Struktur bilden. Diese ist in Abbildung 3 schematisch dargestellt.

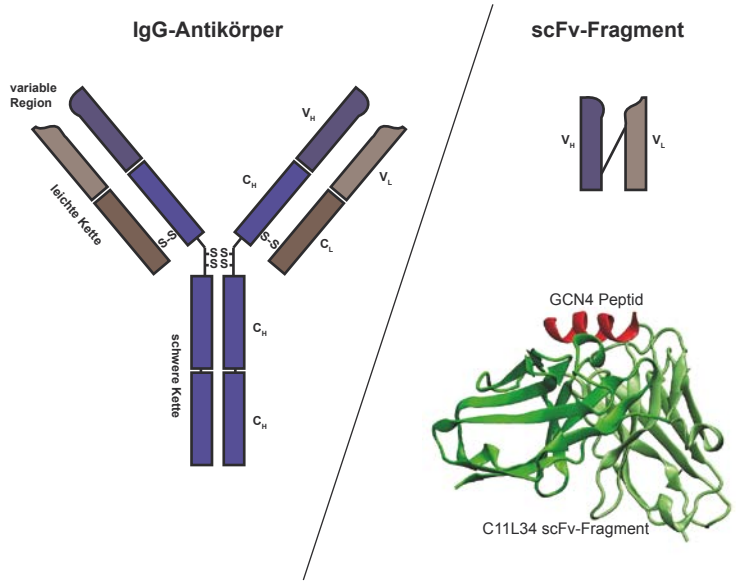

Abbildung 3 – Struktur von Antikörpern
Ein IgG-Antikörper besteht aus zwei leichten und zwei schweren Ketten. Diese enthalten jeweils ein variables Fv-Segment (V_H und V_L), mit dem die Epitope erkannt werden. Bei einem single-chain Fv-Fragment werden die zwei variblen Segmente einer leichten und einer schweren Kette co-exprimiert. Dargestellt ist die Kristallstrukur des scFv-Fragments C11L34 (PDB 1P4B). Mit ihm wurden Modifikationen an dem im Abschnitt 3.2 beschriebenen *Single-Molecule Cut-and-Paste* System durchgeführt.

Die schweren Ketten werden untereinander über zwei kovalente Disulfidbrücken stabilisiert, ebenso wechselwirken die leichten Ketten mit jeweils einer Disulfidbrücke mit den schweren. Somit stellt der Antikörper selbst auch ein Beispiel für eine stabile Protein-Protein Wechselwirkung dar. Die spezifische Bindung zum Antigen wird über die jeweils N-terminale Domäne einer schweren und einer leichten Kette, den sogenannten variablen Domänen ausgebildet. Sie bilden das Fv-Fragment, das für biotechnologische Zwecke auch ohne die übrigen Domänen in einer einzelnen Kette, dem scFv-Fragment (*single-chain variable fragment*) exprimiert werden kann. Wie im Abschnitt 6.3 beschrieben, wurde im Rahmen

dieser Arbeit die Wechselwirkung eines solchen Fragments mit seinem Antigen, einer kurzen Peptidsequenz, dazu verwendet einen gerichteten Transport von einzelnen Proteinen mit einer Präzision im Bereich weniger Nanometer durchzuführen.

Enzyme

Als abschließendes Beispiel für molekulare Wechselwirkungen mit hoher Dynamik soll nun die Wechselwirkung von Enzymen mit ihren Substraten dienen. Enzyme sind Proteine, die biochemische Reaktionen katalysieren, indem sie die energetische Aktivierungsbarriere durch Bindung zu ihren Substraten herabsetzen (Abbildung 4) Diese werden mit hoher Spezifizität am aktiven Zentrum des Enzyms gebunden und umgesetzt. Für eine hohe Umsatzrate müssen die Produkte eine niedrige Affinität zum Enzym und somit eine hohe off-Rate haben. Wenn Enzyme Teil eines biochemischen Signal- oder Stoffwechselnetzwerkes sind, ist wichtig, dass ihr Aktivitätsgrad abhängig von äußeren Parametern reguliert werden kann. Dies erfolgt häufig über allosterische Regulation, bei der das Binden von Aktivatoren oder Inhibitoren Konformationsänderungen hervorruft, die den Aktivitätsgrad des Enzyms beeinflussen.

Ein nicht unerheblicher Teil der Enzyme scheint aber auch über mechanische Kräfte reguliert werden zu können, die von der Umgebung direkt auf das Molekül ausgeübt werden. Beispiele für eine solche Mechanoenzymatik sind der für Blutgerinnung essentielle von-Willebrand-Faktor [16] oder das Muskelenzym Titinkinase [46], an deren Beispiel in dieser Arbeit die strukturellen Vorraussetzungen eines solchen, mechanisch aktivierten Enzyms diskutiert werden.

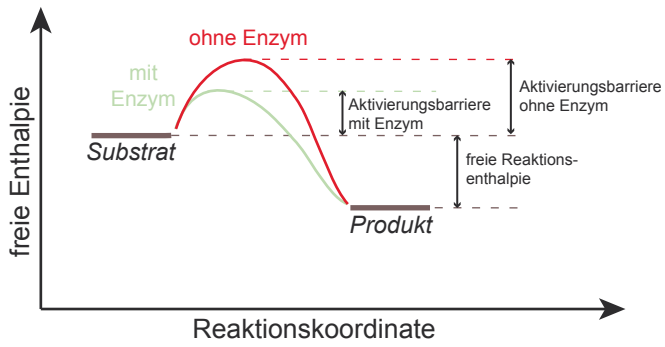

Abbildung 4 – Schematik zur Funktionsweise eines Enzyms
Die Reaktion von den Substraten zu den Produkten wird vom Enzym durch Herabsetzung der Aktivierungsenergie katalysiert.

3.2 Kräfte auf molekularer Ebene

Biologische Systeme werden häufig durch Kräfte beeinflusst, müssen auf diese reagieren oder gar selbst Kräfte erzeugen. Wie bereits in den vorigen Kapiteln erläutert wurde, können letztlich alle im Organismus ablaufenden Prozesse auf Wechselwirkungen auf molekularer

Ebene heruntergebrochen werden. Es stellt sich also zwangsläufig die Frage, wie die Detektion, Erzeugung und Relaxation von Kräften in biologischen Systemen auf molekularer Ebene stattfindet. Im Folgenden soll wiederum beispielhaft dargestellt werden, wie diese Prozesse strukturiert sind.

Krafterzeugung auf molekularer Ebene

Das naheliegendste Beispiel eines krafterzeugenden Systems in der Biologie ist der menschliche Muskel. Man unterscheidet zwischen der *glatten Muskulatur*, die in Blutgefäßwänden und Hohlorganen auftritt und deren Durchmesser reguliert und der im Bewegungsapparat und Herzen auftretenden *quergestreiften Muskulatur* / *Skelett-muskulatur.* Zellen der quergestreiften Muskulatur bestehen aus parallelen Anordnungen von sogenannten Riesenzellen, die mehrere Zentimeter lang werden können. Sie entstehen durch Differenzierung und Fusionierung vieler Vorläuferzellen, den Myoblasten, und enthalten deshalb auch mehrere Zellkerne. Das kontraktive Organell der Muskelfasern sind die Myofibrillen, die wiederum aus mehreren Sarkomeren bestehen. In einem Sarkomer sind viele Filamente wie Aktin, Myosin und Titin parallel angeordnet, und verschieben sich bei der Muskelkontraktion gegeneinander (Gleitfilamenttheorie, vergleiche Abbildung 5). Glatte Muskeln hingegen bestehen aus einzelnen Zellen, deren Länge in der Regel mehrere dutzend Mikrometer nicht überschreitet. Unter dem Lichtmikroskop betrachtet erscheint ihr Cytoplasma homogen, da ihnen im Gegensatz zur quergestreiften Muskulatur die Organisation der Aktin- und Mysosin-Filamente zu Sarkomeren fehlt. Aus physiologischen Gründen müssen glatte Muskelzellen keine hohen Kontraktionsgeschwindigkeiten aufbringen, dafür aber größere Kräfte über lange Zeit erzeugen können.

Obwohl sich die Histologie der beiden beschriebenen Muskeltypen stark unterscheidet, ist der molekulare Wirkmechanismus der Krafterzeugung nahezu identisch. Die erwähnten Myosinfilamente entstehen durch Polymerisation von jeweils hundert bis zweihundert Myosinen, deren Kopfgruppen in einer helikalen Anordnung nach außen gerichtet sind und mit den Aktinfilamenten wechselwirken. Unter Verbrauch von ATP ändern diese zyklisch ihre Konformatin sowie ihren Kontakt zu den Aktinfilamenten. Dadurch wird eine gerichtete Bewegung der Filamente zueinander erreicht.

Neben den Myosinen gibt es noch weitere Motorproteine, die sich entlang von Filamenten fortbewegen. Dies sind beispielsweise die an Mikrotubuli bindenden Kinesine und Dyneine. Darüber hinaus gibt es auch molekulare Motoren, die Kraft durch Drehbewegungen erzeugen, wie die ATP-Synthase [6] oder die Flagellenmotoren von Bakterien [47].

Aber auch viele Enzyme müssen für ihren Wirkmechanismus Kräfte auf molekularer Ebene aufbringen. Als Beispiel seien hier die DNA-Helicasen erwähnt, die in der Replikationsgabel die doppelsträngige DNA öffnen [48].

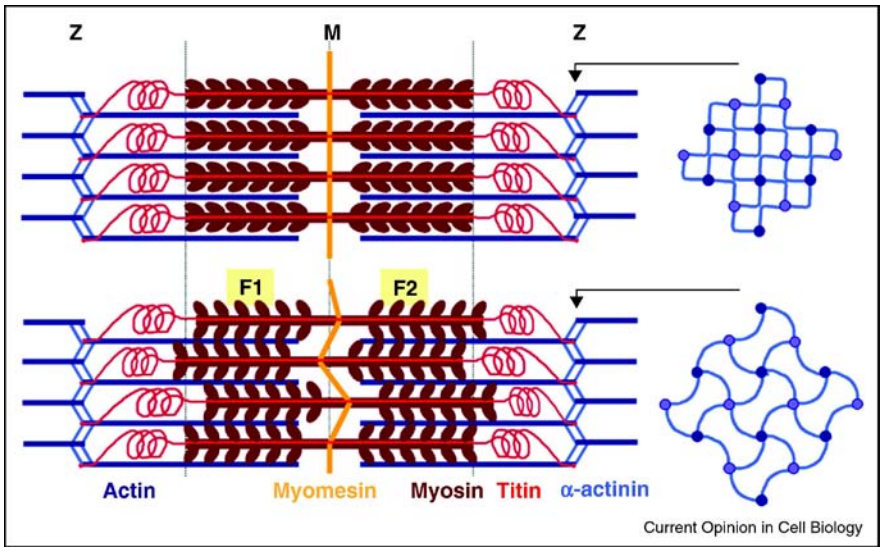

Abbildung 5 – Struktur des Sarkomers von Zellen der Skelettmuskulatur
Schematische Representation des Sarkomers in Ruhe (oben) und unter isometrischer Kontraktion (unten). Die wesentlichen strukturellen Änderungen der Z-Scheiben und M-Banden werden dargestellt. Die Z-Scheibe ändert sich von einer quadratischen Gitterstruktur (oben) zu der geflochtenen Stuktur (unten) und Scherkräfte zwischen benachbarten Myosin-Filamenten führen aufgrund stochastischer Kraftungleichheiten zwischen den zwei antiparallelen Myosin-Filament-Hälften F1 und F2 zu einer Verzerrung der M-Bande. Aktive Zugkräfte belasten dadurch ebenfalls die entropischen Titin-Federn (rot).
Nachdruck von „Current Opinion in Cell Biology“ [49], Copyright (2011) mit Erlaubnis von Elsevier.

Passive, stabilitätserhaltende Systeme

Neben der aktiven Krafterzeugung ist die Transmission und Relaxation von Kräften auf zellulärer und molekularer Ebene entscheidend. Für die passive Elastizität der eben erwähnten quergestreiften Muskelzellen ist Titin, das mit bis zu 34.350 Aminosäuren größte bekannte Protein, maßgeblich verantwortlich [50]. Es verbindet im Sarkomer die Z- mit den M-Banden und positioniert die Myosinfilamente relativ zu den Aktinen. Bei Dehnung des Muskels werden zunächst die nach der Aminosäurenzusammensetzung benannten und strukturlose Knäuel bildenden PEVK-Regionen gestreckt. Die Rückstellkraft beim Dehnen ist hierbei entropischer Natur [51-53]. Darüber hinaus existieren im Titin mehrere hundert strukturierte, unabhängig gefaltete Proteindomänen, die in zwei Klassen eingeteilt werden können: die Fibronektin-III-artigen (Fn) Domänen [54] und die Immunoglobulin-artigen (Ig) Domänen [55]. Beide bestehen aus antiparallelen β-Faltblättern (vergleiche Abbildung 3 und Abbildung 20). Wenn bei einer sehr starken Belastung die aktive Kontraktionskraft der Fasern überschritten wird, übernimmt Titin gewissermaßen die Rolle eines molekularen Sicherheitsgurtes, indem diese Domänen schlagartig entfalten. Die Stabilität der Ig- und Fn-Domänen wurde bereits in vielen kraftspektroskopischen Messungen untersucht [56-60]. Es hat sich herausgestellt, dass die bei der sukzessiven Domänenentfaltung dissipierten Energien diejenigen zum Aufbrechen von kovalenten Bindungen übersteigen, was die eben erwähnte Schutzfunktion ausmacht. Man benutzt bekannte Entfaltungsmuster von Ig- und

Fn-Domänen häufig auch in der Kraftspektroskopie als sogenannte Marker-Domänen für die Selektion verwertbarer Proteinentfaltungskurven [61-64]. Hierbei wird das zu untersuchende Protein mit flankierenden Markerdomänen co-exprimiert.

In Zellverbänden wie Gewebe und Organen müssen interzelluläre Wechselwirkungen ebenfalls eine hohe mechanische Stabilität und Integrität aufweisen. Darüber hinaus müssen diese für verschiedene Gewebearten spezifisch sein. Für die Zell-Zell Adhäsion sind beispielsweise Cadherine [65] und N-CAMs (nerve cell adhesion molecules) verantwortlich, die bei der Entstehung einzelner Krebs-Arten maßgeblich sind [66]. Für das Binden zur extrazellulären Matrix (ECM) hingegen sind Moleküle wie die Klasse der Integrine [67] essentiell, die zusammen mit anderen Proteinen in sogenannten fokalen Adhäsionen das Aktin-Zytoskelett der Zelle an die ECM binden und wichtige Aufgaben bei der Zellkommunikation übernehmen [68].

Mechanotransduktion / Kraftsensoren

Wenn Kräfte als Stimulus für das Übertragen von Signalen in biologischen Netzwerken dienen, spricht man von biomechanischer Signaltransduktion bzw. Mechanotransduktion. Im Falle des menschlichen Tastsinnes ist dieser Mechanismus naheliegend, aber auch beim Gehör und Gleichgewichtsorgan, Schmerzempfinden, der eben erwähnten Muskelkontraktion oder der Regulation von Blutgefäßen finden derartige Prozesse statt [69]. Essentiell ist hierfür ein Kraftsensor, der den mechanischen Input in ein biochemisches Signal umwandelt.

Der molekulare Wirkmechanismus solcher Kraftsensoren war noch bis vor Kurzem unerschlossen und stellt auch heute noch ein wachsendes Forschungsgebiet dar [9, 14]. Insbesondere scheint es eine Klasse der Proteinkinasen zu geben, die mechanisch aktiviert werden können. Proteinkinasen sind Enyzme, die den funktionellen Zustand ihrer Substrate durch Phosphorylierung, d.h. dem Übertrag einer Phosphatgruppe, verändern. Im Falle eines Signalmoleküls kann die Phosphorylierung die Affinität zu Rezeptormolekülen verändern. Aber auch die Rezeptoren oder Enzyme selbst können ihre Aktivität durch Auto- oder Transphosphorylierung beeinflussen. Im menschlichen Organismus sind über 500 Gene bekannt, die Proteinkinasen kodieren. Ihre Gesamtheit beizeichnet man als Kinom [70]. Im Rahmen dieser Dissertation wurde die molekulare Architektur des im Sarkomer der quergestreiften Muskulatur vorkommenden Kraftsensors Titinkinase (TK) sowie die Möglichkeit einer mechanischen Aktivierung der die Aktivität von glatten Muskeln regelnden Myosin-Light-Chain Kinase (MLCK) untersucht.

Beide Enzyme sind Serin/Threonin spezifische Kinasen, die ohne äußere Einflüsse autoinhibiert sind. Dies bedeutet, dass ein Teil der gefalteten Proteinstruktur das aktive Zentrum verdeckt und somit Substratbindung verhindert. Im Falle der MLCK kann die Aktivierung mittels allosterischer Regulation durch Binden des Calcium/Calmodulin-Komplexes erfolgen [71]. Die komplette und unphosphorylierte Form der Titinkinase

hingegen wird trotz hoher Sequenzanalogien nicht über diesen sonst üblichen Signalweg aktiviert [72]. Molekulardynamiksimulationen [73] und kraftspektroskopische Messungen [46, 74] legen nahe, dass die Autoinhibierung direkt durch mechanisches Aufklappen der die Bindungstasche verdeckenden Strukturelemente sowie die Phosphorylierung des ebenfalls inhibierenden Tyrosin-170 aufgehoben wird. Die partiell geöffnete Kinase ist dann in der Lage, ihre Substrate zu phosphorylieren (vergleiche Abbildung 6). Dadurch wird der Proteinumsatz im Muskel sowie die Expression von Muskelproteinen im Zellkern reguliert [75].

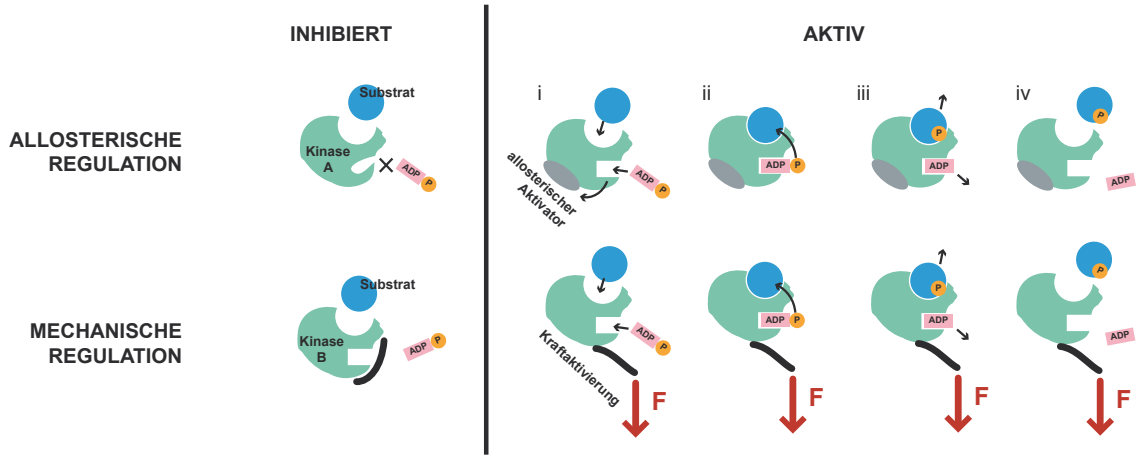

Abbildung 6 – Regulation von Enzymen am Beispiel zweier Kinasen
In der inaktiven Form ist die Bindung des Substrates und/oder des Kosubstrates ATP inhibiert. Diese Inhibierung kann entweder durch Binden eines allosterischen Regulators (z.B. Calmodulin) oder durch mechanisch induzierte Konformationsänderungen aufgehoben werden. Danach kann die Kinase sowohl Substrat als auch ATP binden (i) und den Triphosphatrest des ATP auf das Substrat übertragen (ii). Danach dissoziieren das Substrat und das ADP (iii-iv).

Wie wichtig und zugleich empfindlich solche Kraftsensoren sind, ist eindrucksvoll an einer erblichen Myopathie ersichtlich, bei der die Mutation einer einzelnen Aminosäure in der regulatorischen Helix αR1 der Titinkinase zu einer Muskelschwäche führt, die im schlimmsten Fall über das Versagen der Atemmuskulatur zum Tod führen kann [76, 77]. Untersuchungen haben gezeigt, dass die starke Strukturierung der Sarkomere verloren geht und die Z- und M-Banden sich nicht mehr klar hervorheben. Sogenannte Knock-Out-Mäuse, bei denen die Titinkinase des Herzmuskels gentechnisch deletiert wurde, sind ebenfalls nur bedingt lebensfähig, da deren Herzmuskel übernatürlich früh versagt [78].

3.3 Single-Molecule Cut-and-Paste auf Grundlage eines hierarchischen Kraftsystems

In den vorangegangen Kapiteln wurde erörtert, bei welchen biologischen Prozessen Krafteinflüsse auf molekularer Ebene relevant sind und wie sich deren Wirkmechanismus strukturiert. Neben der Untersuchung von Systemen, bei denen Kräfte zum natürlichen Parameterraum gehören, kann man sich in der Bio-Nanotechnologie aber auch Systeme

verschiedener Bindungskräfte bei der Konstruktion artifizieller Systeme oder Untersuchung von biomolekularen Wechselwirkungen im Allgemeinen zu Nutze machen. Eine hierzu verwendete Technik wird *Single-Molecule Cut-and-Paste* (SMCP) genannt und wurde von Kufer et al. 2008 zum ersten Mal auf Basis von DNA-DNA Interaktionen mit verschiedener mechanischer Stabilität vorgestellt [79]. Sie kombiniert die hochspezifische molekulare Erkennung mit der räumlichen Präzision des AFMs und ermöglicht dadurch den gerichteten Transport einzelner Moleküle mit einer Präzision im Bereich weniger Nanometer.

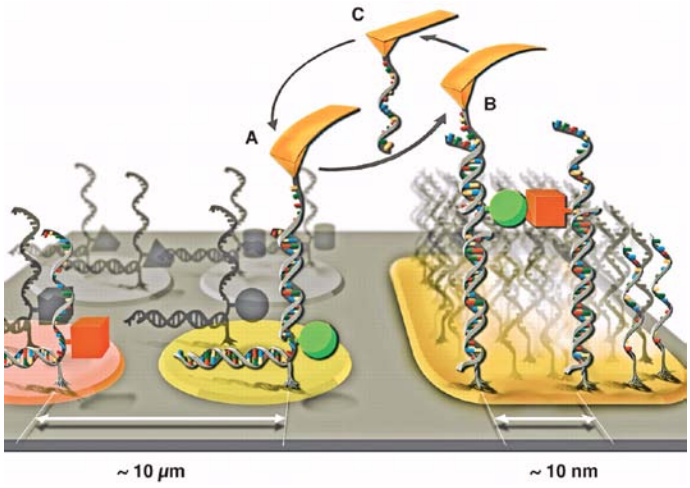

Abbildung 7 – Illustration zur Funktionsweise der *Single-Molecule Cut-and-Paste* Technik
In der Depot-Region werden mit DNA verknüpfte funktionelle Einheiten durch spezifische Hybridisierung verankert. (A) Ein einzelsträngiger Überlapp kann am Cantilever befestigte DNA binden und ist mechanisch stabiler als die in Zipper-Konfiguration an die Oberfläche gebundene DNA. (B) Nach dem Übertrag auf den Cantilever wird die DNA in die Zielregion verfahren und dort abgesetzt. Dort ist beim Zurückziehen des Cantilevers die Bindung zur Oberfläche stabiler und der Cantilever kann für einen neuen Transportprozess verwendet werden (C).
Aus „Science" [79]. Nachdruck mit Genehmigung von AAAS.

Erforderlich ist hierzu ein System aus drei molekularen Wechselwirkungen, die sich in ihrer mechanischen Stabilität unterscheiden. Die zu transportierenden Objekte werden in den Depot-Regionen mittels einer thermisch stabilen Wechselwirkung mit möglichst niedrigen Dissoziationskräften verankert. Sie verfügen darüber hinaus über eine Erkennungssequenz mittlerer Bindungsstärke, die mit ihrem am AFM-Cantilever befestigten Konterpart wechselwirkt, wenn dieser im Depot in Kontakt mit der Oberfläche gebracht wird. Werden nun beim Zurückziehen des Cantilevers beide Bindungen gleichzeitig beansprucht, reißt die Verbindung zur Oberfläche mit höherer Wahrscheinlichkeit und das Molekül wird auf den Cantilever übertragen. Nun wird es mithilfe des AFMs in die Ziel-Region verfahren und dort mittels einer noch stärkeren Wechselwirkung analog zum Aufnahmeprozess platziert. Für eine langfristige Befestigung muss diese Bindung wiederum eine hohe thermische Stabilität aufweisen. Nach dem Transport ist die Erkennungssequenz am Cantilever wieder frei für den nächsten Zyklus und so kann sukzessive ein Arrangement verschiedener molekularer Bausteine auf der Oberfläche realisiert werden. Detektiert werden diese beispielsweise über

Fluoreszenzmikroskopie. Wie jedoch kann man die für die Depot-Funktionalisierung benötigte Wechselwirkung realisieren, die mechanisch leicht, aber thermisch vernachlässigbar dissoziiert?

Auf die Details zur Theorie kraftinduzierter Bindungsbrüche wird im folgenden Kapitel eingegangen. Hier soll nur kurz erwähnt werden, dass für die thermische Stabilität die Bindungsenergie ΔG zwischen den Konstituenten maßgeblich ist. Sie muss zusammen mit einer eventuell vorhandenen Aktivierungsbarriere ΔG_{on} durch thermische Fluktuationen überwunden werden und gemäß dem Van't Hoff-Arrhenius Gesetz hängt die natürliche Dissoziationsrate exponentiell von der Bindungsenergie ab:

$$k_{off} = \nu_{off} \cdot e^{\frac{-(\Delta G + \Delta G_{on})}{k_B T}}$$

Beschleunigt man den thermischen Bindungsbruch durch Anlegen einer externen Kraft *F,* erhält man einen zusätzlichen Energiebeitrag $-F \cdot \Delta x$, der proportional zur zurückgelegten Distanz ist. Wenn die Kraft also über eine lange Strecke wirkt, können auch bei niedrigen Kräften relevante Energien aufgebracht werden, die zum Bindungsbruch führen.

Beim DNA-basierten *Single-Molecule Cut-and-Paste* macht man sich die Tatsache zu Nutze, dass DNA-Doppelstränge immer antiparallel ausgerichtet sind. Sie besitzen ein 3'- und ein 5'-Ende, das nach dem für die Polymerisation verwendeten Kohlenstoffatom am Zuckerrückgrat benannt ist. Bei der Synthese kann die Polymerase neue Nukleotide jeweils nur an die OH-Gruppe am 3'-Ende anfügen. Lagern sich nun zwei DNA-Stränge aneinander an, hat die Doppelhelix an jedem Ende jeweils ein 3'- und ein 5'-Ende die unabhängig voneinander bei der Synthese zu Ankern modifiziert werden können. So kann man abhängig von den Ankerpositionen drei verschiedene Zuggeometrien erreichen.

Wenn je ein 3'- und ein 5'-Ende als Anker dienen, spricht man von der sogenannten *Zipper-Geometrie*. Die Fälle, in denen entweder an beiden 3'- oder an beiden 5'-Enden befestigt wird, fasst man zur *Scher-Geometrie* zusammen. Beide Geometrien unterscheiden sich grundlegend, wenn die Bindung unter Kraft steht. Im Falle der *Zipper-Geometrie* liegt die Kraft im Wesentlichen nur am letzten Basenpaar an. Die DNA öffnet sich ähnlich wie bei einem Reißverschluss Basenpaar für Basenpaar bei relativ niedrigen Kräften im Bereich von 15-25 pN, die vom AT/GC-Verhältnis abhängen und über eine lange Distanz [80-82]. Belastet man hingegen eine *Scher-Geometrie*, verteilt sich die Kraft gleichmäßig über alle Basenpaare und der Bindungsbruch erfolgt über eine kurze Distanz bei höheren Kräften, die von der komplementären Sequenzlänge abhängen. Dabei gibt es aufgrund der Helizität der DNA wiederum Unterschiede abhängig davon, ob man die 3'- oder den 5'-Enden der DNA als Ankerpunkte verwendet hat [83].

Das komplette hierarchische Kraftsystem für *Single-Molecule Cut-and-Paste* ist in Abbildung 8 dargestellt. Im Depot verwendet man einen 30-35 Basenpaar (bp) langen DNA-Strang in

Zipper-Geometrie als Anker. An einen 20 Basen langen einzelsträngigen Überhang kann die Cantilever-DNA-Sequenz in *Scher-Geometrie* binden. Obwohl deren Bindungsenergie niedriger ist, ist sie aus den eben genannten Gründen mechanisch stabiler und die DNA wird auf den Cantilever übertragen. In der Ziel-Region dient dieselbe Sequenz wie im Depot als Bindungspartner. Da die DNA dort aber am anderen Ende fixiert ist, werden beim Zurückziehen des Cantilevers beide Bindungen in *Scher-Geometrie* belastet und die Verbindung zur Oberfläche hat aufgrund ihrer größeren Länge die höhere mechanische Stabilität.

Im Rahmen dieser Dissertation wurden sowohl die Genauigkeit der *Single-Molecule Cut-and-Paste* Technik untersucht, als auch verschiedene Anwendungsgebiete demonstriert. Darüber hinaus wurde das Kraftsystem soweit verändert, dass auch der Transport von Proteinen statt DNA ermöglicht wird. Dies ist beispielsweise hilfreich, wenn man einzelne oder wenige Enzyme in einer definierten Anordnung zueinander isoliert betrachten möchte.

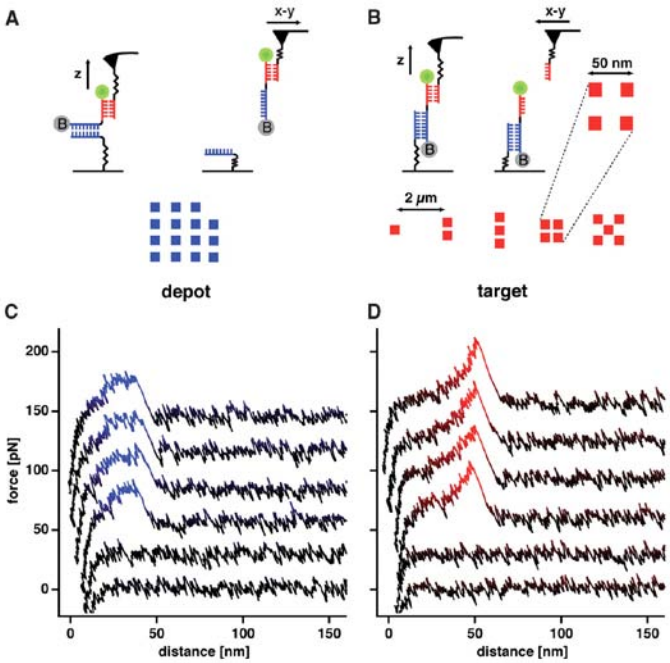

Abbildung 8 – Schematik zum *Single-Molecule Cut-and-Paste* Prozess
(A) Verankerungsgeometrie in der Depotregion. Die DNA ist in Zipper-Konfiguration an die Oberfläche gebunden. Ein kurzer Überhang bindet die Cantilever-DNA in der Scher-Konfiguration. Obwohl ihre Bindungsenergie niedriger ist, ist die Scher-Geometrie mechanisch stabiler als die Verbindung zur Oberfläche und ein Übertrag der Transport-DNA auf den Cantilever ist möglich. (B) Geometrie in der Zielregion. Beide Interaktionen erfolgen in der Scher-Konfiguration. Aufgrund der niedrigeren Bindungsenergie der Cantileversequenz verbleibt die DNA an der Oberfläche und kann dort mit der Präzision des AFMs positioniert werden. (C) Repräsentative Kraftkurven in der Depotregion. Sie weisen das für *Unzipping* typische Plateau auf. (D) Repräsentative Kraftkurven in der Zielregion. Die Abrisskräfte sind höher als im Depot.
Aus „Science" [79]. Nachdruck mit Genehmigung von AAAS.

4 METHODEN

Um mikrobiologische Systeme zu untersuchen, reichen herkömmliche Mikroskopietechniken schon seit längerem nicht mehr aus, da ihr Auflösungsvermögen nicht in den Bereich einzelner Moleküle hinabreicht und keine Manipulationen mit ihnen möglich sind. Hochauflösende Techniken wie die Rasterelektronenmikroskopie oder die Röntgenstrukturanalyse können bereits umfassenderen Einblick in die Strukturierung der biologischen Materie liefern, ermöglichen aber keine Aussagen über dynamische Prozesse. Für diese werden bevorzugt zeitaufgelöste Spektroskopietechniken verwendet. In diesem Kapitel sollen die für diese Arbeit relevanten Methoden kurz zusammengefasst werden.

4.1 Einzelmolekül-Kraftspektroskopie

Das Prinzip der Kraftspektroskopie besteht in der Untersuchung des Verhaltens einzelner Moleküle oder Zellen unter Kraft. Diese ruft bei den zu untersuchenden Objekten Konformationsänderungen hervor, die über die Änderung ihres End-zu-End Abstandes *x(t)* bestimmt werden. Die Kraft *F* selbst wird durch Messung der Auslenkung einer im Vorhinein kalibrierten Feder detektiert. Dabei unterscheidet die Art der Feder und das Prinzip der Kraft- und Abstandsdetektion die verschiedenen kraftspektroskopischen Techniken. Eine Übersicht über die verwendeten Verfahren findet sich in Tabelle 1, ein detaillierter Vergleich beispielsweise in Referenz [84].

Unter den derzeit gebräuchlichen Kraftspektroskopie-Messmethoden besitzen die *magnetischen Fallen* [85-87] die höchste Kraftauflösung, jedoch sind Zeitauflösung und Maximalkraft limitiert. Die Messsonden bestehen aus wenige Mikrometer großen, paramagnetischen Kügelchen, die in einem inhomogenen Magnetfeld magnetisiert werden. Die Oberfläche der Sonden ist chemisch so modifiziert, dass sich Biomoleküle daran koppeln lassen. Das zu untersuchende System wird zwischen die Oberfläche und das Kügelchen gespannt. Die Stärke des Magnetfeldgradienten bestimmt die auf die Sonde wirkende Kraft

$$\vec{F}_{mag} = -\nabla(\vec{m} \cdot \vec{B})$$

Sie muss vom untersuchten Biomolekül kompensiert werden. Der Abstand des Kügelchens zur Oberfläche wird mithilfe von Reflexions-Interferenz-Kontrast Mikroskopie (RICM) bestimmt. Ein großer Vorteil dieser Technik besteht darin viele Proben parallel im Beobachtungssegmet untersuchen zu können und dass durch Rotation des Magneten auch Torsionskräfte auf die Moleküle ausgeübt werden können.

Technik	*Prinzip schematisch*	*Kraftbereich*	*Vor-/Nachteile*
Magnetische Falle	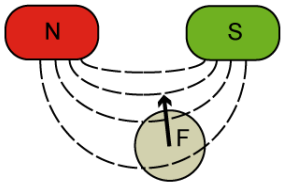	10 fN - 10 pN	+ Torsionskräfte + Parallelität - nur Kontrolle über Kraft
Optische Falle	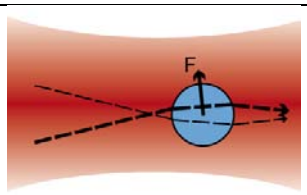	0.1 - 150 pN	+ hohe Kraftauflösung + Kontrolle über Kraft und Abstand - niedrige dynamische Sensorbandbreite (aufgrund kleiner Federkonstante)
Biomembran-Kraftspektroskopie	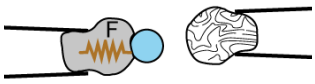	0.5 pN - 1 nN	+ Federsteifigkeit variabel - große Wechselwirkungsflächen
Zentrifugal-Kraftspektroskopie		1 fN – 1 µN	+ großer zugänglicher Kraftbereich + Parallelität - nur Kontrolle über Kraft - niedrige Aktuatordynamik (aufgrund Trägheit des Systems)
AFM	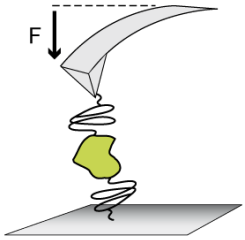	> 1 pN	+ hohe Sensor- und Aktuatordynamik + Kontrolle über Kraft und Abstand + kleine Wechselwirkungsflächen + leichte Automatisierbarkeit + kann gleichzeitig zur Bildgebung verwendet werden - Kraftauflösung für manche Anwendungen beschränkt

Tabelle 1 – Übersicht über die verschiedenen Untersuchungsmethoden der Kraftspektroskopie

Optische Fallen arbeiten ebenfalls mit mikrometergroßen Kügelchen (Beads). Ein Unterschied zum Brechungsindex des Mediums bewirkt, dass auf sie eine Kraft in Richtung des Fokus eines Laserstrahls wirkt [88-90]. Ursache ist, dass durch die Brechung, Reflexion und Streuung des Lichts ein Impulsübertrag auf das Teilchen stattfindet. Im Fokus des Laserstrahls kompensieren sich die Kräfte und durch Verschieben des Strahlzentrums kann

der Bead bewegt werden. Die Kraft wird bei bekanntem Potential über den Abstand des Beads zum Strahlzentrum bestimmt. Realisiert man eine optische Falle mit zwei Fokussen, die auf denselben optischen Komponenten beruhen, ist es möglich sehr driftstabile Systeme mit einer guten Kraftauflösung zu erhalten.

Die *Biomembran-Kraftspektroskopie* verwendet als Kraftsensor rote Blutkörperchen (Erythrozyten), die mit einer Glaskapillare angesaugt werden und deren Steifigkeit sich durch die Höhe des Unterdrucks einstellen lässt [91, 92]. An den Erythrozyten wird wiederum ein Glaskügelchen befestigt, das mit den zu untersuchenden Molekülen funktionalisiert ist. Die anliegende Kraft wird über die Deformation der Blutzellen bestimmt.

Eine vergleichsweise neue Kraftspektroskopietechnik, die eindrücklich zeigt wie bereits mit einfachen Mitteln brauchbare Einzelmolekül-Kraftspektroskopieergebnisse erzielt werden können, ist die *Zentrifugal-Kraftspektroskopie*. Hier werden analog zur magnetischen Falle Biomoleküle zwischen eine Oberfläche und Beads eingespannt. Anschließend wird das gesamte System bestehend aus Kamera, Objektiv und Probenkammer um eine gemeinsame Achse gedreht [93]. Abhängig von Beadgröße und Umdrehungszahl ist ein sehr großer Kraftbereich experimentell zugänglich. Der Nachteil besteht wiederum darin, dass keine direkte Kontrolle über den Abstand erreicht werden kann und das System nur für Messungen bei konstanter Kraft mit niedriger Dynamik geeignet ist.

Das Rasterkraftmikroskop / AFM

Ursprünglich wurde das Rasterkraftmikroskop entwickelt, um die Topographie von nichtleitenden Festkörperoberflächen mit atomarer Auflösung bestimmen und die wirkenden Kräfte messen zu können. Gerd Binnig, Calvin Quate und Christoph Gerber erweiterten dazu 1986 ein Rastertunnelmikroskop, indem sie nicht mehr direkt mit der Spitze des Tunnelmikroskops die Oberfläche abrasterten, sondern als Messsonde eine Blattfeder mit einer scharfen Spitze verwendeten. Beim Abrastern der Oberfläche mit Piezostellelementen folgt diese der Topographie der Probe. Die Auslenkung der Feder wurde über einen Tunnelstrom detektiert [94]. Inzwischen wird als Auslenkungssignal gewöhnlich die Position eines an der Blattfeder (Cantilever) reflektierten Laserstrahls mithilfe einer geteilten Photodiode bestimmt. Darüber hinaus kommen auch interferometrische Messprinzipien in Frage [95]. Die Möglichkeit mithilfe des AFMs Bilder von biologischen Proben in wässriger Umgebung mit einer Auflösung im Nanometerbereich zu erhalten, wurde schnell erkannt und erfolgreich umgesetzt [96-99].

Durch Weiterentwicklung erschloss sich schließlich auch die Kraftspektroskopie als Anwendungsbereich. So konnten durch Einspannen von Biomolekülen zwischen Spitze und Oberfläche beispielsweise die mechanische Stärke von Rezeptor-Ligand-Paaren [100] bestimmt, oder das Verhalten von DNA und Proteinen unter Kraft untersucht werden [56, 57, 82]. Ein entscheidender Vorteil der AFM-basierten Kraftspektroskopie ist, dass aufgrund der kleinen Wechselwirkungsfläche und den exakten piezoelektrischen Stellelementen auch in

lateraler Richtung eine präzise Kontrolle über einzelne Biomoleküle ermöglicht wird und sich die Technik verhältnismäßig leicht automatisieren lässt.

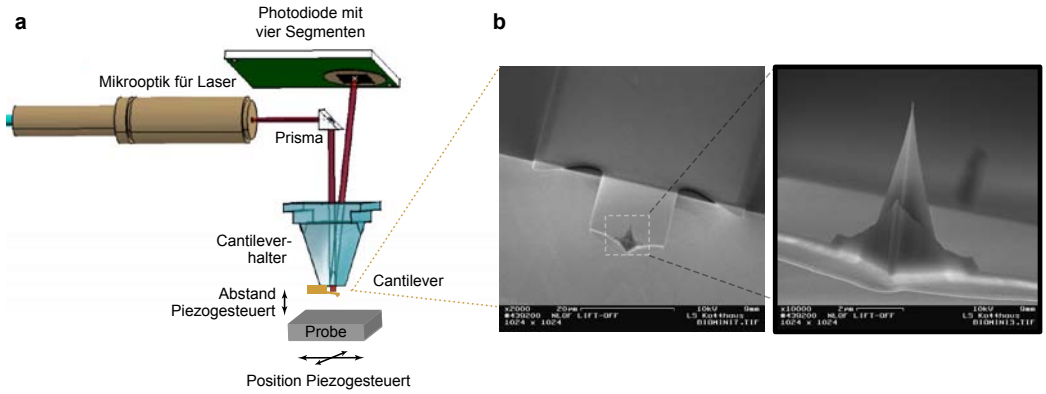

Abbildung 9 – Grundelemente eines AFM
(a) Schematischer Aufbau. Ein Laserstrahl wird auf die Spitze des Cantilevers fokussiert und dort reflektiert. Die Position des Rückreflexes wird mit einer Vierquadrantenphotodiode ausgelesen. Der Abstand zur Oberfläche und die Position der Probe wird mit Piezostellelementen geregelt. (b) Elektronenmikroskopieaufnahme eines Olympus-AC40TS-Cantilevers. Während der Messung ist der Lever um 180° gedreht und die in der Ausschnittsvergrößerung zu sehende Siliziumspitze zeigt nach unten. Die Aufnahmen wurden freundlicherweise von Stephan Heucke zur Verfügung gestellt.

Um nun die Kräfte auf einzelne Biomoleküle quantitativ bestimmen zu können, muss man durch Kalibrierung des Cantilevers der ermittelten Auslenkung eine Kraft zuordnen können. Für kleine Auslenkungen verhält sich der Cantilever wie eine hookesche Feder und die Kraft ist proportional zur Auslenkung: $F = k \cdot \Delta x$. Die Proportionalitätskonstante k wird Federkonstante genannt und wird beispielsweise über die thermisch induzierten Schwingungen des Cantilevers ermittelt. Dazu wird die frequenzabhängige Oszillationsamplitude *A(f)* des Cantilevers mit dem Modell eines gedämpften harmonischen Oszillators beschrieben [101]. Der thermisch angeregte Energiebeitrag pro Freiheitsgrad, der quadratisch in den Hamilton-Operator eingeht, beträgt gemäß dem Equipartitionstheorem $k_bT/2$. Es gilt

$$A(f) = A_0 \sqrt{\frac{f_R^4}{(f^2 - f_R^2)^2 + \left(\frac{f \cdot f_R}{Q}\right)^2}}$$

mit der Amplitude A_0 bei Frequenz 0 Hz, der Resonanzfrequenz f_R und dem Qualitätsfaktor *Q*. Für den Cantilever muss hierbei beachtet werden, dass im Rauschspektrum mehrere Schwingungsmoden mit jeweils diesem Faktor angeregt werden. Für eine korrekte Eichung mithilfe des Rauschspektrums müssen mehrere Korrekturfaktoren berücksichtigt werden. Insbesondere sei zum Beispiel auf den sogenannten *kappa-Faktor* hingewiesen, der das unterschiedliche Biegeprofil für einen frei schwingenden und einen oberflächengebundenen

Cantilever beschreibt und der von der Art der verwendeten Cantilevergeometrie abhängt [102]. Eine praktische Erklärung der relevanten Faktoren findet sich beispielsweise in Referenz [103].

Für eine gute Auflösung von Kräften benötigt man kleine Sonden mit einer niedrigen Federkonstante. Dies folgt aus der Identität $k<\Delta x^2>=k_bT$. Mithilfe von $\Delta F=k\Delta x$ ergibt sich direkt, dass das mittlere quadratische Abstandsrauschen $<\Delta x^2>$ eines Cantilevers antiproportional und das mittlere quadratische Kraftrauschen $<\Delta F^2>$ proportional zu seiner Federkonstante k ist. Relevant ist in der Praxis allerdings auch, dass man für Messdaten innerhalb einer gewissen Frequenzbandbreite B aufnimmt. Für die innerhalb dieser Bandbreite minimal detektierbare Kraft gilt gemäß Referenz [104]

$$F_{\min} = \sqrt{4k_B T \gamma B}.$$

Bei gegebener Temperatur lässt sich diese Kraft also nur durch Verkleinerung des Dämpfungskoeffizienten γ minimieren, was zum Beispiel durch Reduktion der Cantilevergröße erreicht wird.

Systematische Fehler sind eine häufige Fehlerquelle für misskalibrierte Cantilever. Neben allgemeinen systematischen Fehlern wie der Problematik, dass die üblicherweise verwendeten Fitfunktionen für Cantilever mit hohen Dämpfungsfaktoren nicht mehr optimal geeignet sind [105], spielen häufig auch gerätespezifische Fehlerquellen eine entscheidende Rolle. Ein nicht korrekt kalibrierter Z-Positionssensor führt bei Verwendung der thermischen Kalibrierung zwangsläufig bei der Bestimmung der Rauschamplitude des Cantilevers zu Fehlern. Darüber hinaus kann zum Beispiel eine eingeschränkte Dynamik der Photodiode frequenzabhängige Verzerrungen des Rauschspektrums hervorrufen oder aber eine fehlerhafte Softwareimplementierung zu systematischen Abweichungen führen. Deshalb ist es wichtig, ein neu konstruiertes Gerät auf systematische Fehler zu untersuchen.

Um eine Vergleichbarkeit der für diese Dissertation relevanten Messdaten mit denen anderer Gruppen zu gewährleisten, wurde mit dem im Abschnitt 4.4 beschriebenen AFM an einem internationalem Ringversuch teilgenommen, bei dem dieselben Cantilever von verschiedenen Gruppen kalibriert wurden um gerätespezifische Abweichungen festzustellen. Es stellte sich heraus, dass das von unserer Gruppe verwendete Gerät bei sämtlichen Kalibrierverfahren im direkten Vergleich sehr geringe Abweichungen von den mittleren Werten aufweist (vgl. Abbildung 10). Details können Publikation P6 entnommen werden.

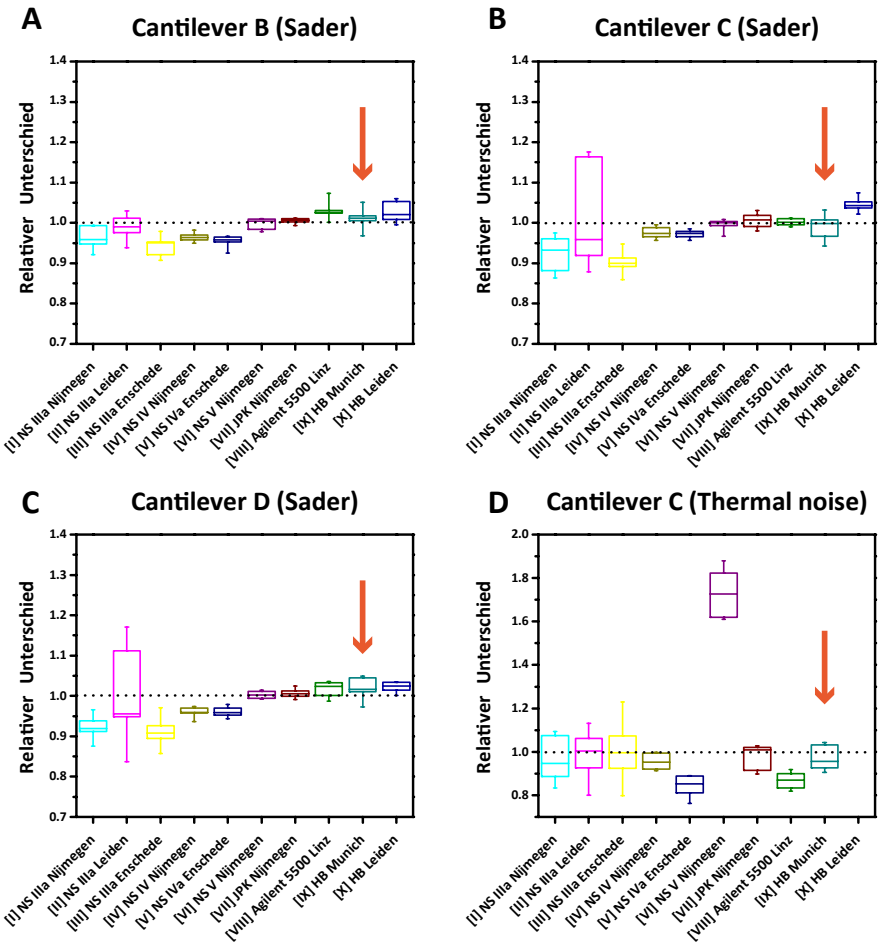

Abbildung 10 – Ergebnisse des Ringversuchs zur Cantileverkalibrierung
Als Referenz dient jeweis der Mittelwert der für einen Cantilever ermittelten Federkonstanten. Ergebnisse des in dieser Arbeit verwendeten AFMs sind in rot gekennzeichnet. Nach [106].

Elastizität von Polymeren

Die Untersuchung von Biomolekülen mittels Kraftspektroskopie beinhaltet grundsätzlich die Beobachtung der Elastizität und Kraftantwort von Polymeren. In einem zyklischen Prozess werden die Moleküle entweder über spezifische oder unspezifische Wechselwirkungen mit dem Cantilever kontaktiert, gedehnt und die vom System aufgebrachte Kraft in Abhängigkeit von Ort und/oder Zeit bestimmt. Betrachtet man die Kraftantwort eines Polymers ohne Sekundärstruktur in Abhängigkeit der Ausdehnung, stellt man fest, dass die Kraft nichtlinear vom Ort abhängt und stetig steigt. Die Rückstellkraft ist entropischer Natur und darauf zurückzuführen, dass mit zunehmendem End-zu-End Abstand der zugängliche Konformationsraum des Polymers eingeschränkt wird. Das gängigste Modell, das dieses Verhalten beschreibt ist das *Worm-Like-Chain (WLC) Modell*. Es betrachtet das Polymer als einen flexiblen Stab, der thermisch fluktuiert und sich dadurch ständig verbiegt. Als Maß für die Flexibiliät dient die Korrelation der Tangentenvektoren $\vec{t}$ in einem Abstand Δx. Beim WLC-Modell wird diese Abhängigkeit als exponentiell angenommen:

$$\left\langle \vec{t}(x) \cdot \vec{t}(x+\Delta x) \right\rangle = e^{-\Delta x / p}$$

Somit beschreibt die Persistenzlänge *p* die charakteristische Distanz, ab der thermische Fluktuationen zu einer nennenswerten Verbiegung des Stabes führen. Je weicher das Polymer, um so kleiner ist die Persistenzlänge. Eine analytische Näherungsformel für die Kraftantwort, die das Verhalten von Polymeren unter Kraft gut beschreibt [107, 108] , lautet

$$F_{WLC}(x) = \frac{k_B T}{p}\left(\frac{1}{4}(1-\frac{x}{L})^{-2} - \frac{x}{L} - \frac{1}{4}\right)$$

Die Konturlänge *L* entspricht dem Weg entlang des Polymerrückgrats und ist ein charakteristisches Maß in der Kraftspektroskopie, da mit ihr beispielsweise die Größen molekularer Domänen und Positionen von Energiebarrieren bestimmt werden können. Das WLC-Modell kann die Kraftantwort von Proteinen jedoch nicht vollständig wiedergeben. So sinkt beispielsweise die optimale Persistenzlänge mit steigender Kraft [57]. Das QM-WLC-Modell [109] enthält eine Erweiterung, die neben den rein entropischen Kräften auch eine enthalpische Streckung des Rückgrats beschreibt. Weitere in der Literatur anzutreffende Polymermodelle sind das *Freely-Jointed-Chain Modell* [85, 110, 111] sowie das *Freely-Rotating-Chain Modell* [112] und deren Erweiterungen [113]. Eine sehr nützliche Analysemethode, bei der eine Transformation der Kraftkurven vom Kraft-Abstandsraum *F(x)* in den Kraft-Konturlängenraum *F(L)* direkte Aussagen über Positionen und Längeninkremente erlaubt, findet sich in Referenz [114] und ist in Abbildung 11 schematisch dargestellt.

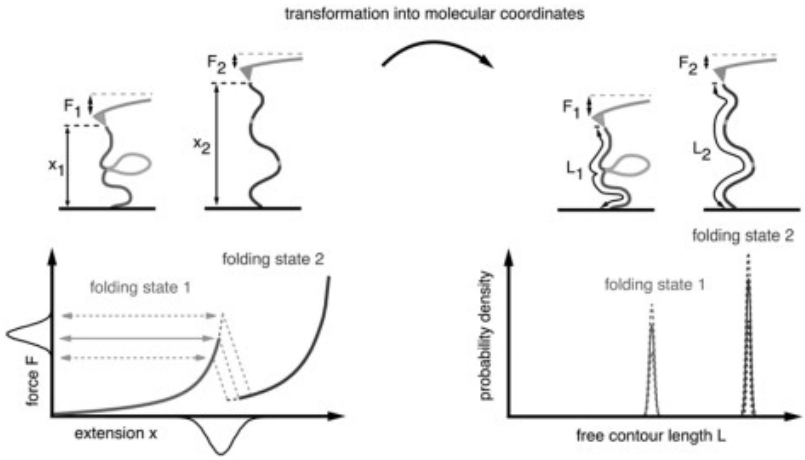

Abbildung 11 – Konturlängentransformation
Da die gängigen Polymermodelle bijektive Abbildungen sind kann man Kraft-Abstands Daten F(x) unter Zuhilfenahme eines dieser Modelle eindeutig in Kraft-Konturlängendaten F(L) transformieren. Dies ermöglicht eine einfache Auswertung von absoluten und relativen Positionen von Energiebarrieren während der Entfaltung. Aus den bestimmten Konturlängeninkrementen lässt sich beispielsweise die Anzahl der in der entsprechenden Faltung vorhandenen Aminosäuren bestimmen (vergleiche Kapitel 5).
Nachdruck von „Biophysical Journal" [114], Copyright (2008), mit Erlaubnis von Elsevier.

Der „Konstante-Kraft“ – Modus

Möchte man die mechanische Stabilität molekularer Domänen oder Bindungen kraftspektroskopisch charakterisieren, stellt man fest, dass die beobachteten Entfaltungskräfte stark streuen und mit zunehmender Zuggeschwindigkeit steigen. Dies ist darauf zurückzuführen, dass die Dissoziation der Moleküle ein thermisch angeregter Prozess ist, der unter Kraft im Nichtgleichgewicht stattfindet. Um zu Dissoziieren müssen die Moleküle eine Energiebarriere ΔG_{off} überwinden, für die ihnen die thermische Energie $k_B T$ zur Verfügung steht. Unter Vernachlässigung von Rückreaktionen hängt die Entfaltungsrate k_{off} nach dem Van’t Hoff-Arrhenius Gesetz exponentiell von der Energiebarriere ab und ist proportional zu einer Anklopffrequenz ν_{off}. Durch Anlegen einer Kraft „verkippt“ man die Energielandschaft der Moleküle entlang der Abstandskoordinate x. Dies wird in Abbildung 12 illustriert. Man erhält einen zusätzlichen Energieterm $F\Delta x$, der die Energiebarriere absenkt:

$$k_{off}(F) \approx \nu_{off} \cdot e^{-\frac{\Delta G_{off} - F\Delta x}{k_B T}} = k_{off,0} \cdot e^{\frac{F\Delta x}{k_B T}} \quad \Big|_{x_{A,F} - x_A << x_B - x_A}$$

Unter Experimentierbedingungen mit konstanter Zuggeschwindigkeit hängt die am Molekül anliegende Kraft aufgrund der eben erwähnten nichtlinearen Kraftantwort der Biopolymere vom End-zu-End Abstand des Moleküls und damit auch implizit von der Zeit ab. Dies macht den oben beschriebenen Zusammenhang $k_{off}(F)$ nichttrivial. Streckt man das Molekül aber möglichst schnell bis zu dem Punkt, an dem eine gewünschte Kraft erreicht wird und hält diese im Anschluss über ein aktives Feedback zeitlich konstant, erhält man einen sehr direkten Zugang zu den Parametern der oben skizzierten Energielandschaft. Diese Art von Kraftspektroskopie nennt man den „Konstante-Kraft“ (engl. *Force-Clamp*) Modus. Um die Potentialweite Δx zum Maximum der Energiebarriere und die natürliche off-Rate $k_{off,0}$ der Bindung zu erhalten, muss man die Entfaltungsraten bei verschiedenen Zugkräften ermitteln und dann deren exponentiellen Zusammenhang bestimmen.

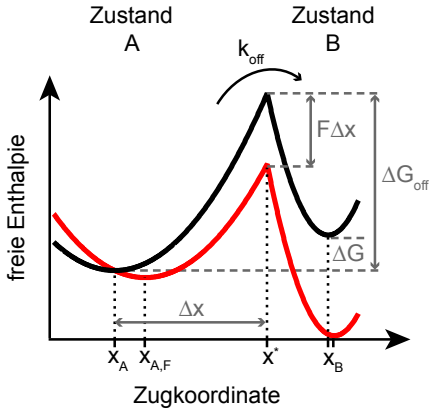

Abbildung 12 – Einfluss einer konstanten Kraft auf die Energielandschaft
Der zusätzliche Energieterm Fx verursacht eine Verkippung der Energielandschaft. Die Energiebarriere zum Übergang in den Zustand B wird dadurch abgesenkt. Zu Beachten ist auch, dass sich die Positionen der Potentialminima unter Kraft verschieben können.

Das Bell-Evans Modell

Für den Fall konstanter Zuggeschwindigkeiten wurden ebenfalls Modelle konstruiert, die Zugang zu den Parametern der Energielandschaft erlauben. Das am weitesten verbreitete Modell ist hierbei das sogenannte Bell-Evans Modell [91, 115, 116]. Unter der Annahme einer konstanten Ladungsrate $\dot{F} = dF/dt$ und kraftunabhängigen Potentialweite Δx erhält man für die wahrscheinlichste Abrisskraft *F** die Abhängigkeit

$$F^*(\dot{F}) = \frac{k_B T}{\Delta x} \cdot \left(\ln\left(\frac{\Delta x}{k_{off} \cdot k_B T} \right) + \ln\left(\dot{F} \right) \right)$$

Man sieht, dass die wahrscheinlichste Abrisskraft logarithmisch von der Ladungsrate abhängt. Inzwischen gibt es auch Erweiterungen dieser Modelle, die weniger restriktiv sind. Ein von Dudko und Szabo vorgeschlagenes Modell [117-119] setzt beispielsweise nicht mehr voraus, dass die Potentialweite Δx unabhängig von der Zugkraft ist. Abbildung 12 illustriert, dass dies in der Tat keine allgemeingültige Annahme ist.

4.2 Fluoreszenzmikroskopie

Die Fluoreszenzmikroskopie ist heute ein viel genutztes Mittel um biologische Systeme zu betrachten. Der entscheidende Vorteil gegenüber anderen optischen Mikroskopietechniken ist, dass man den beobachteten Kontrast selber bestimmt, indem man seine Proben an spezifischen Stellen mit Fluorophoren markiert. Diese werden anschließend mit Licht geeigneter Wellenlänge angeregt und emittieren dieses wieder mit einer spektralen Verschiebung zu längeren Wellenlängen. Das Verhältnis der emittierten zu den absorbierten Photonen wird hierbei Quanteneffizienz oder auch Quantenausbeute genannt.

Möchte man nun mittels Fluoreszenzspektroskopie Einzelmolekülsensitivität erreichen, ist dies technisch nur durch ausreichend hohe Signale der einzelnen Fluorophore bei einem optimierten Signal-Hintergrund-Verhältnis möglich. Ein möglichst hohes Signal erzielt man durch hinreichend starke Anregungsintensitäten und die Wahl von Farbstoffen mit hohem Absorptionsquerschnitt und hoher Quanteneffizienz. Außerdem gilt es Fluorophore zu wählen, die in den erforderlichen Pufferbedingen langlebig und stabil emittieren.
Geeignete Optimierungsmöglichkeiten des Signal-Hintergrund-Verhältnisses hängen davon ab, ob der Fluoreszenzhintergrund von denselben oder andersartigen Molekülen als den zur Markierung verwendeten Fluorophoren hervorgerufen wird. Wenn dieselben Moleküle den Hintergrund verursachen, steigt dieser proportional zum Signal. Durch Einschränkung des Anregungs- und Detektionsvolumens kann jedoch die Anzahl der zum Hintergrund beitragenden Moleküle verringert werden, was in einem besseren Signal-Hintergrund-Verhältnis resultiert. Gängige hierzu verwendete Methoden sind die konfokale Mikroskopie [120] oder TIRF-Mikroskopie [121] und deren Erweiterungen wie die Mehrphotonenmikroskopie [122]. Nullmoden-Wellenleiter (engl. *zero-mode waveguides*,

ZMWG) [123] stellen hierbei eine noch recht junge aber sehr vielversprechende Technik dar, bei der die Anregungsvolumen bis in den Zeptoliter-Bereich reduziert werden kann. Allerdings ist die für den zu beobachteten Prozess zur Verfügung stehende Fläche ebenfalls durch den Waveguide begrenzt. Weiterhin sind fluorogene Proben [124, 125] hilfreich, um den Fluoreszenzhintergrund zu reduzieren, da sie ihren Absorptionsquerschnitt oder ihre Fluoreszenzquantenausbeute erhöhen, wenn sie an das zu beobachtende Molekül gebunden haben. Die im Rahmen dieser Arbeit verwendeten Techniken werden im Folgenden kurz vorgestellt.

TIRF-Mikroskopie

TIRFM ist die englische Abkürzung für *total internal reflectition fluorescence microscopy*. Um das angeregte Volumen möglichst klein zu halten, wird ein auf mehrere Quradratmikrometer aufgeweiteter Laserstrahl unter einem flachen Winkel an einer Glasgrenzfläche reflektiert. Der für Totalreflexion benötigte kritische Winkel beträgt $\theta_c = \arcsin(n_{Medium}/n_{Glas})$. Wird der Zustand von Totalreflexion erreicht, erhält man auf der gegenüberliegenden Seite der Grenzfläche ein evaneszentes Feld mit exponentiellem Intensitätsverlauf *I(z)*. Die Eindringtiefe *d* ist hierbei durch die Wellenlänge λ_0, den Einfallswinkel θ, sowie die Brechungsindizes *n* gegeben.

$$I(z) = I_0 e^{-z/d} \; ; d = \frac{\lambda_0}{4\pi\sqrt{n_{Medium}^2 \sin^2(\theta) - n_{Glas}^2}}$$

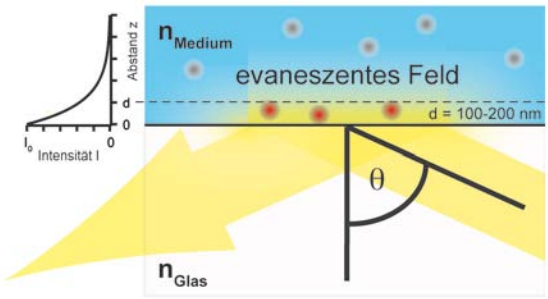

Abbildung 13 – *Total Internal Reflection Fluorescence Microscopy* (TIRFM)
Durch flachen Einfall des Anregungslasers ($\theta > \theta_c$) wird auf der gegenüberliegenden Seite der Grenzfläche ein evaneszentes Feld mit exponentiellem Intensitätsverlauf angeregt. Dies führt dazu, dass nur oberflächennahe Farbstoffe angeregt und beobachtet werden.

Objektivbasierte TIRF-Mikroskopie [126] hat gegenüber auf Prismen basierenden TIRF-Mikroskopen den Vorteil, dass bei ihr ein Halbraum für weitere Anwendungen wie das AFM frei bleibt. Das verwendete Objektiv muss hierbei mindestens eine numerische Apertur von der Größe des Brechungindex des Mediums besitzen, um Totalreflexion zu erreichen:

$$NA \geq n_{Glas} \sin(\theta_c) = n_{Glas} \frac{n_{Medium}}{n_{Glas}}$$

Hochauflösende Mikroskopietechniken

Aufgrund der Beugung von Licht können zwei benachbarte Punktlichtquellen mit einem konventionellen Mikroskop nur aufgelöst werden, wenn ihr Abstand zueinander größer als $x = 0{,}61 \cdot \lambda / NA$ ist. Dieses nach dem Physiker Lord Rayleigh benannte Kriterium ergibt sich aus dem Abstand des ersten Minimums vom Zentrum der durch Besselfunktionen beschreibbaren Beugungsscheibchen.

Möchte man auch Objekte, deren Abstand kleiner als diese Auflösungsgrenze ist, voneinander unterscheiden, kann man sich damit behelfen, dass man die Position einzelner Lichtquellen durch die Bestimmung des Zentrums ihres Intensitätsprofils bei ausreichend hoher Photonenzahl nanometer-genau lokalisieren kann [127, 128]. Entscheidend für eine Lokalisation mehrerer Fluorophore in einem beugungsbegrenzten Bereich ist, dass man die Fluoreszenz der einzelnen Farbstoffe zeitlich separiert. Ist man in der Lage Bedingungen zu schaffen, bei denen im zeitlichen Mittel jeweils nur ein Molekül im beugungsbegrenzten Bereich aktiv fluoresziert, kann man die Positionen sämtlicher Moleküle rekonstruieren und ein hochaufgelöstes Bild erhalten. Ein kontrolliertes Blinkverhalten der Moleküle kann über Photoaktivierung oder chemische Reaktionen erreicht werden. Häufig verwendete Techniken sind PALM [129], FPALM [130], STORM [131] und BLINKM [132].

Eine alternative Methode zum Verbessern der Auflösung ist die sogenannte STED-Mikroskopie [133]. Es handelt sich um ein konfokales Mikroskop, bei dem ein weiterer Laser mit donut-förmigem Strahlprofil rund um das zu beobachtende Areal fluoreszente Anregungen der Farbstoffe durch stimulierte Emission verhindert. Nichtlinearitäten in der stimulierten Emission ermöglichen es, den fluoreszenten Bereich auf Werte unterhalb der beugungslimitierten Auflösungsgrenze zu reduzieren.

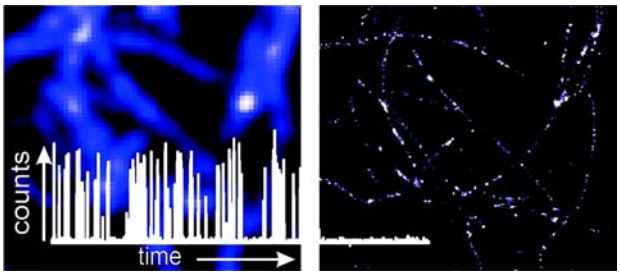

Abbildung 14 – Bildrekonstruktion durch Lokalisation einzelner Fluorophore
Bei der BLINKM-Technik wird durch Zugabe geeigneter Oxidations- und Reduktionsmittel die Blinkcharakteristik der Farbstoffe gezielt beeinflusst. Leuchtet im Mittel weniger als ein Molekül pro beugungslimitiertem Bereich gleichzeitig, lässt sich durch Lokalisation ein hochaufgelöstes Bild rekonstruieren.
Nachdruck mit Genehmigung von „Journal of the American Chemical Society" [132], Copyright (2008) American Chemical Society.

4.3 Der photothermische Effekt

Die folgende Beschreibung des photothermischen Effekts beinhaltet die Grundlagen der in Kapitel 4.4 beschriebenen neuartigen Aktuationsmethode für schnelle Kraftspektroskopie.

In der AFM-basierten Kraftspektroskopie und Bildgebung werden üblicherweise Cantilever verwendet, die aus Siliziumnitrid bestehen und auf ihrer Oberseite eine metallische Beschichtung besitzen. Diese erhöht den Reflexionskoeffizienten und führt somit zu einem besseren Messsignal. Darüber hinaus existieren auch Cantilever mit Beschichtungen auf der Unterseite, die eine nicht auf Silizium basierende chemische Funktionalisierung ermöglicht. Wird nun der Detektionslaser auf dem Cantilever fokussiert, erhitzt sich der Lever lokal durch Absorption eines Teils der Laserstrahlung. Für einen mehrschichtigen Cantilever mit verschiedenen thermischen Ausdehnungskoeffizienten α führen die Temperaturänderungen analog zu den gebräuchlichen Bimetallschaltern zu einer Verbiegung des Cantilevers. Im Folgenden soll die zeitabhängige Biegung eines balkenförmigen Cantilevers durch Änderung der Leistung eines auf den Cantilever fokussierten Lasers mit gegebener Modulationsfrequenz ω etwas detaillierter beschrieben werden. Eine ausführlichere Beschreibung des verwendeten Modells findet sich in Ramos et al. [134].

Die Ausbreitung der Temperaturgradienten im Cantilever kann mithilfe der thermischen Diffusion beschrieben werden. Für den Fall, dass der Durchmesser des modulierten Laserspots größer als die Breite des Balkens ist, kann man in guter Näherung eine konstante Temperatur quer zur Leverachse annehmen. Selbige Annahme trifft auch für das Temperaturprofil in z-Richtung zu, da die thermische Diffusionslänge größer als die Dicke der verwendeten Cantilever ist. Zur Berechnung der Temperaturverteilung eignet sich deshalb die eindimensionale Wärmediffusionsgleichung

$$\frac{\partial T}{\partial t} = K\frac{\partial^2 T}{\partial x^2} - \beta T$$

Dabei setzen sich die Parameter *K* und β folgendermaßen aus der thermischen Leitfähigkeit κ, der Dichte ρ, der spezifischen Wärmekapazität c_p, der Balkendicke *d* und dem Wärmeübergangskoeffizient *h* zusammen:

$$K = \frac{\kappa_1 d_1 + \kappa_2 d_2}{c_{p,1}\rho_1 d_1 + c_{p,2}\rho_2 d_2}, \beta = \frac{h_1 + h_2}{c_{p,1}\rho_1 d_1 + c_{p,2}\rho_2 d_2}$$

Die Indizes 1 und 2 bezeichnen jeweils Beschichtung und Trägermaterial. Eine Auflistung der relevanten Materialkonstanten für Siliziumnitrid, Gold und Aluminium findet sich in Tabelle 2. Setzt man analog zu Ramos et al. voraus, dass die Temperatur mit der gleichen

Frequenz ω wie der modulierte Laser oszilliert, ergeben sich Temperaturprofile der Form $T(x,t) = T_0 + \Delta T(x)exp(i\omega t)$. Die frequenzabhängige Erhöhung der Temperatur am Einstrahlort ist in Abbildung 15c anhand des Beispiels eines handelsüblichen Cantilevers dargestellt.

Die effektiv auf den Balken wirkende Kraft F_n berechnet sich über die Integration der Temperaturerhöhung über die Krümmung der Eigenmode $\psi_n^0(x)$.

$$F_n = c_{th} \int_0^L \Delta T(x) \frac{d^2 \psi_n^0(x)}{dx^2} dx$$

mit einer Konstante c_{th}, die von den verwendeten Materialien und der Balkengeometrie abhängt. Mit Hilfe der Euler-Bernoulli-Theorie lässt sich nun die Amplitude der betrachteten Eigenmode bestimmen [135]. Dabei ist zu bemerken, dass eine Schwingungsmode am besten in einem Bereich mit hoher Krümmung anzuregen ist. Für die Grundmode eines Balkenlevers befindet sich der optimale Arbeitspunkt bei circa 15% der Gesamtlänge L [136]. Aufgrund der Unterschiede der Absorptionskoeffizienten gilt für einen einseitig beschichteten Cantilever weiterhin, dass eine photothermische Anregung von der nichtmetallischen Seite circa dreifach so effektiv ist.

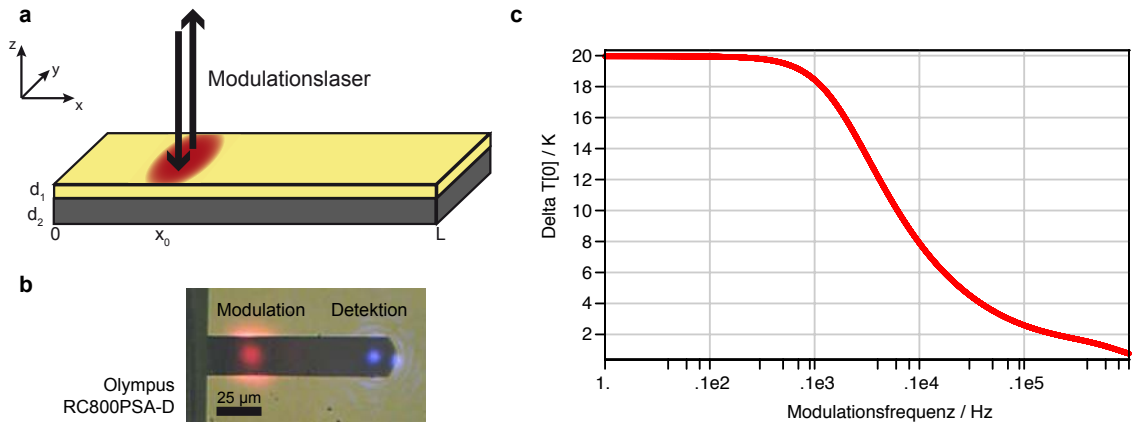

Abbildung 15 – Photothermische Cantileveranregung
(a) Schematik des Modells zur Berechnung des Photothermischen Effektes. (b) Kameraaufnahme eines Olympus RC800PSA Cantilevers mit fokussiertem Modulations- und Detektionslaser. (c) Frequenzabhängigkeit der theoretischen Temperaturerhöhung am Einstrahlort für einen Veeco MLCT-B Cantilever und 0,5 mW absorbierte Laserleistung.

Material	*Wärme-kapazität* c_p	Dichte ρ	*Therm. Leitf.* κ	*Ausdehungs-koeffizient* α	*Elastizitäts-modul* E
SiN	750 J/kgK	3400 kg/m^3	32 W/mK	3,2x10^{-6}K^{-1}	250 GPa
Au	135 J/kgK	19300 kg/m^3	346 W/mK	14,2x10^{-6}K^{-1}	80 GPa
Al	900 J/kgK	2700 kg/m^3	220 W/mK	23,8x10^{-6}K^{-1}	70 GPa

Tabelle 2 – Materialkonstanten von Siliziumnitrid, Gold und Aluminium

4.4 TIRF-AFM Kombination mit photothermischer Cantilever-Regelung

Im Rahmen dieser Arbeit wurde ein modulares AFM entwickelt, das über die Möglichkeit verfügt, mittels eines zweiten Lasers den Cantilever über photothermische Anregung gezielt auszulenken. Darüber hinaus ist es in der Lage, sowohl automatisiert und eigenständig Kraftspektroskopiedaten über einen Zeitraum mehrerer Tage aufzunehmen, als auch mit einem TIRF-Fluoreszenzmikroskop kombiniert zu werden.

Das Designkriterium für den AFM-Kopf ist dabei, so klein und kompakt wie möglich zu bleiben, was die absolute Drift von Komponenten verringert und aufgrund einer geringeren Masse eine möglichst hohe Dynamik ermöglicht. Weiterhin muss der für die Abstandsregelung verwendete Z-Piezo im AFM-Kopf enthalten sein, damit eine Relativbewegung zwischen Cantilever und Oberfläche keine Defokussierung des Fluoreszenzmikroskops zur Folge hat. Das TIRF-Mikroskop wiederum muss eine möglichst hohe mechanische Stabilität aufweisen, um die AFM-Messungen nicht zu beeinflussen. Aufgrund der für objektivbasiertes TIRF erforderlichen hohen numerischen Aperturen (NA > 1.33), die kurze Arbeitsabstände zur Folge haben, müssen kombinierte Messungen auf dünnen Glasproben stattfinden. Die verwendeten Deckgläser sind darüber hinaus über das Immersionsöl mechanisch mit dem Objektiv gekoppelt. Herkömmliche Mikroskope mit Objektivrevolver neigen hier zu einer unnötig hohen Rauschamplitude der Oberfläche. Bei dem im Rahmen dieser Arbeit verwendeten Mikroskopdesign mit feststehendem Objektiv ist diese Rauschamplitude deutlich reduziert. Details dazu finden sich in Publikation P2.

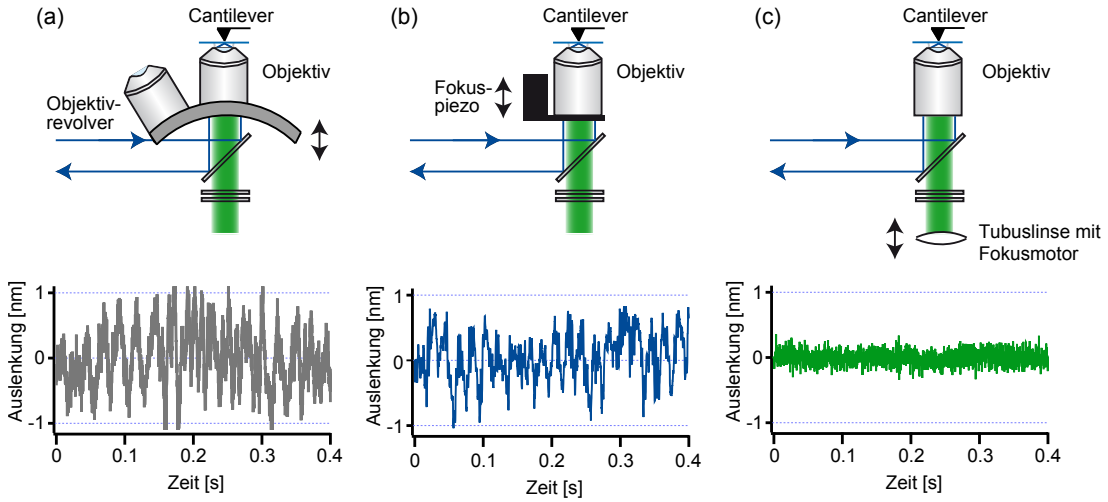

Abbildung 16 – Eigenschwingungsamplituden verschiedener Mikroskoptypen mit Ölimersionsobjektiven
(a) Konventionelles Design mit Objektivrevolver. (b) Mikroskop mit aktiver Positionsregelung durch einen komerziellen Objektivpiezo. (c) Design mit feststehender Objektivlinse. Zur Fokussierung wird die Tubusline bewegt. Diese kann mechanisch von der Probe entkoppelt werden. Adaptiert von [P3].

Wie eingangs erwähnt, kann am AFM-Kopf optional ein zweiter Laser zur gezielten Aktuation des Cantilevers angebracht werden. Abbildung 17 zeigt, dass die statische Auslenkung der Blattfeder mit Abweichungen <1% proportional zur angelegten Laserleistung ist. Mit zunehmender Frequenz sinkt jedoch die Effektivität der Anregung und es können aufgrund der verzögerten Abkühlung [137] und beschränkten Eigendynamik der Cantilever Hystereseeffekte auftreten. Je nach verwendeter Levergeometrie liegen die Grenzfrequenzen im niedrigen bis mittleren kHz-Bereich. Unter Verwendung hoher Laserleistungen und geeigneter Regelungselektronik, die die Frequenzantwort des Cantilevers glättet, können über den photothermischen Effekt aber auch Dynamiken bis in den MHz-Bereich erzielt werden [138].

Bislang erstreckte sich der Anwendungsbereich photothermischer Cantilever-Aktuation auf den bildgebenden Bereich [138-141] (Abbildung 38) und um optisch getriebene Mikro-Resonatoren mit hohen Q-Faktoren zu erhalten [142-144]. Mit diesen lassen sich beispielsweise Biosensoren realisieren [145]. In der Kraftspektroskopie besteht aber ebenfalls ein Bedarf an schnellen mikroskaligen Aktuatoren. Mit dem oben beschriebenen AFM wurde im Rahmen dieser Arbeit ein Akutatorsystem entwickelt, das 10-mal schnellere Reaktionszeiten im „Konstante-Kraft“ Modus aufweist, als bis dato realisierte Systeme. Mit schnelleren Regelkreisen lassen sich die Totzeiten nach dem Entfalten biomolekularer Domänen verringern und somit die kraftabhängigen Entfaltungsraten genauer und über einen größeren zeitlichen Umfang bestimmen. Dies eröffnet die Möglichkeit, auch kurzfristige Ereignisse zu charakterisieren, die mit langsamen Systemen entweder gar nicht oder nur unzureichend bestimmt werden können.

Das entwickelte Regelungssystem basiert auf einem kombinierten Aktuatorsystem aus einem herkömmlichen Piezoelement für große Distanzen und einem photothermisch geregelten Cantilever für schnelle Reaktionszeiten. Eine Schematik findet sich in Abbildung 18. Details können der Publikation P3 entnommen werden.

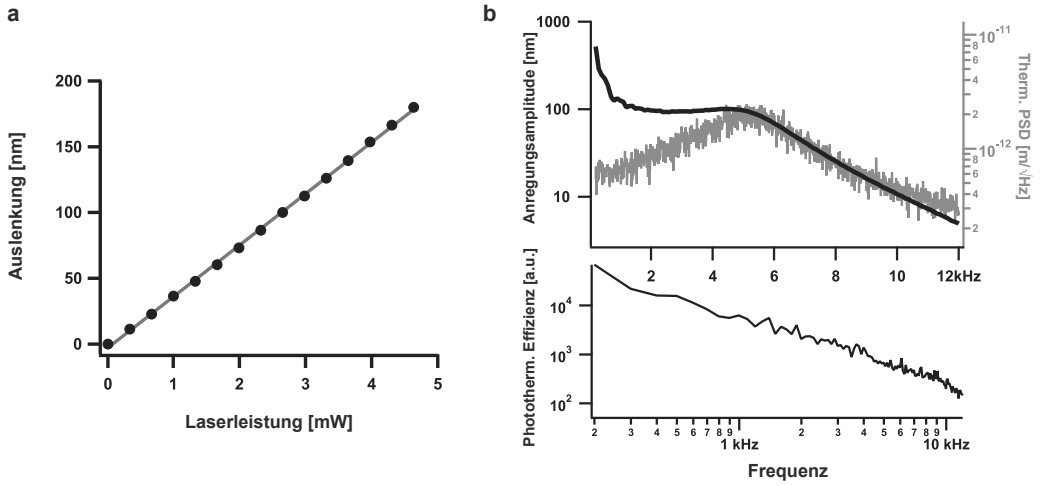

Abbildung 17 – Charakteristik der photothermischen Anregung eines Cantilevers (Olympus RC800PSA-D)
(a) Bei statischer Anregung ist die Auslenkung des Cantilevers proportional zur angelegten Laserleistung. (b) Bei dynamischer Anregung sinkt die Anregungseffizienz deutlich mit zunehmender Frequenz. Sie setzt sich aus der mechanischen Anregbarkeit des Cantilevers (grau) und der photothermischen Effizienz zusammen. Adaptiert von [P3].

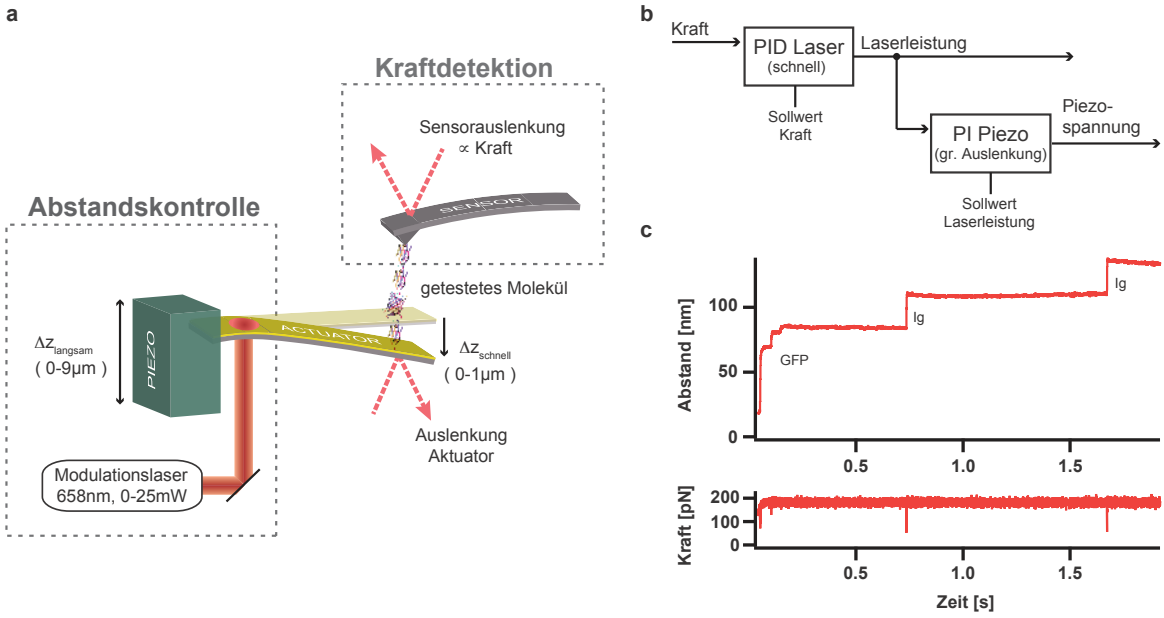

Abbildung 18 – Photothermische Distanzregelung für einen schnellen „Konstante-Kraft“ Regelkreis (nach [146]).
(a) Schematik des verwendeten Aufbaus. Das zu untersuchende Molekül wird zwischen zwei Cantilever gespannt. Der eine dient wie in herkömmlichen AFM-Anwendungen als Kraftsensor, der andere wird über den photothermischen Effekt ausgelenkt und dient zusammen mit einem Piezoelement als sehr schneller Aktuator. (b) Aufbau des Aktuatorregelkreises. Die Auslenkung des Sensors regelt die Position des Aktuatorcantilevers. Dessen Abweichungen vom Sollwert werden langfristig durch das Piezoelement kompensiert. (c) Beispielkurve der mit dem Regelkreis erzwungenen Entfaltung eines Ig-GFP Fusionsproteins. Adaptiert von [P3].

5 RÄUMLICHE UND LOGISCHE ANORDNUNG MULTIPLER MOLEKULARER DOMÄNEN

In Kapitel 3.1 wurden Beispiele für intermolekulare Wechselwirkungen gegeben und darauf eingegangen, wie Kräfte auf molekularer Ebene aufgebaut und detektiert werden können. Dieses Kapitel beinhaltet eine Erweiterung auch auf intramolekulare Interaktionen. Infrage kommende Topologien sowie deren Auswirkung auf die Konnektivität zweier verknüpfter molekularer Domänen werden diskutiert. Mithilfe der beschriebenen Grundelemente und deren Abhängigkeiten lassen sich beliebig große Netzwerke erstellen oder beschreiben. Darüber hinaus wird diskutiert werden, wie sich Topologien auf kraftspektroskopische Messungen auswirken beziehungsweise mit welchen Methoden man verschiedene Konnektivitäten voneinander unterscheiden kann.

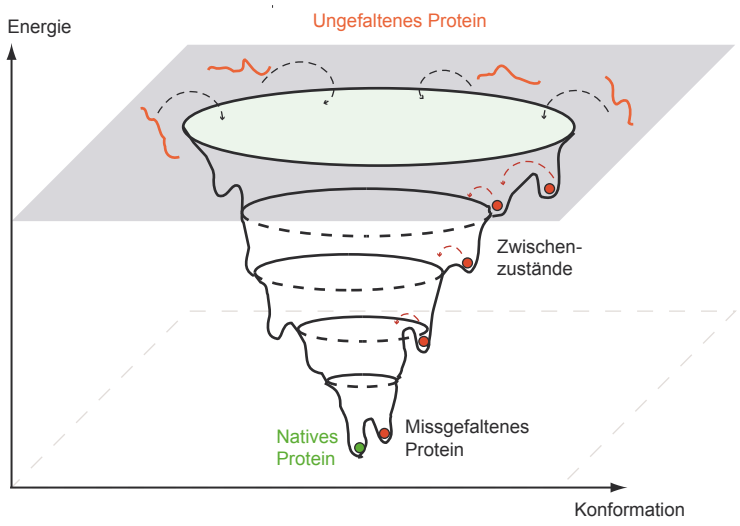

Abbildung 19 – Proteinfaltung
Die an den Ribosomen synthetisierten Proteine müssen in ihre native Form falten, um ihre Funktion zu erhalten. Dabei wird die Gesamtenergie des Systems durch Änderungen der Konformation minimiert. Durch thermische Anregung können Zwischenzustände überwunden werden, die lokale Energieminima darstellen. Sind die Energiebarrieren zu hoch, können irreversible Missfaltungen auftreten.

Darstellung einer kraftspektroskopischen Energiebarriere

Große Biomoleküle sind Polymere, deren Struktur durch die Sequenz ihrer Monomere definiert wird. Deren physikalische und chemische Eigenschaften bestimmen eine Potentiallandschaft im Konformationsraum, die wiederum das Falten des Polymers zu seiner funktionellen Struktur und dessen Dynamik bestimmt (vergleiche Abbildung 19). Die Abfolge der Monomere bezeichnet man deshalb als *Primärstruktur*. Charakteristische

Strukturelemente wie α-Helices und β-Faltblätter für Proteine oder Haarnadelstrukturen für DNA und RNA bezeichnet man als *Sekundärstruktur*. Die *Tertiärstruktur* ist durch die Interaktion dieser Elemente definiert und beschreibt die gesamte Struktur eines einzelnen Biomoleküls. Zur Vereinfachung beschränken sich die Beschreibungen im Folgenden auf Proteine bei denen die Kraft zwischen N- und C-Terminus angelegt wird. Die beschriebenen Zusammenhänge gelten jedoch ebenfalls für andere Polymermoleküle wie DNA oder RNA.

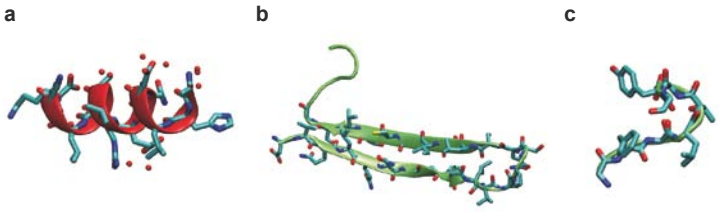

Abbildung 20 – Sekundärstrukturelemente von gefalteten Proteinen
Abhängig von der Abfolge der Aminosäuren und deren Eigenschaften können sich bei der Proteinfaltung charakteristische Anordnungen der Seitenketten einstellen: (a) α-Helix, (b) β-Faltblatt und (c) flexible, unstrukturierte Schlaufen werden auch „*random coil*“ genannt.

Die Tertiärstruktur von Proteinen ist häufig durch eine modulare Architektur gekennzeichnet, die aus mehreren diskreten strukturierten Regionen besteht, die im folgenden Domänen genannt werden. Formen mehrere Biomoleküle einen stabilen molekularen Komplex, bezeichnet man dessen Aufbau konsequenterweise als *Quartärstruktur*. Unter Kraft entfalten für gewöhnlich die einer Domäne zugehörigen Aminosäuren gleichzeitig oder es dissoziieren Teile der Quartärstruktur. Dabei ist für den Entfaltungspfad und die Dynamik relevant, welche Teile der Sequenz sich in der Gesamtstruktur zu einer molekularen Domäne zusammenlagern und ob diese über das Rückgrat des Polymers miteinander verbunden sind oder zu verschiedenen Molekülen gehören. Darüber hinaus spielt diese Domänentopologie auch bei katalytischen und regulatorischen Prozessen und der Proteinfaltung eine wichtige Rolle [34]. Schematisch kann man eine intramolekulare Domäne für die Kraftspektroskopie zu einer Bindung *B* und einer entropischen Feder mit definierter Konturlänge ΔL zusammenfassen. Unter Last bleibt die Bindung für eine gewisse Zeit stabil, da sie eine Energiebarriere darstellt. Wird diese durch Zuführen von Energie überwunden, entfaltet die Domäne und die Feder wird gestreckt (Abbildung 21). Das zu erwartende Konturlängeninkrement lässt sich dabei aus der Anzahl der an der Faltung beteiligten Aminosäuren *N* und dem Domänendurchmesser Δx folgendermaßen bestimmen [61]:

$$\Delta L = N \cdot 0{,}365 nm - \Delta x$$

Intermolekulare Wechselwirkungen lassen sich ebenfalls mit einer Energiebarriere symbolisieren. In diesem Fall entfällt die entropische Feder, da nach dem Bindungsbruch keine Verbindung mehr zwischen den Bindungspartnern besteht.

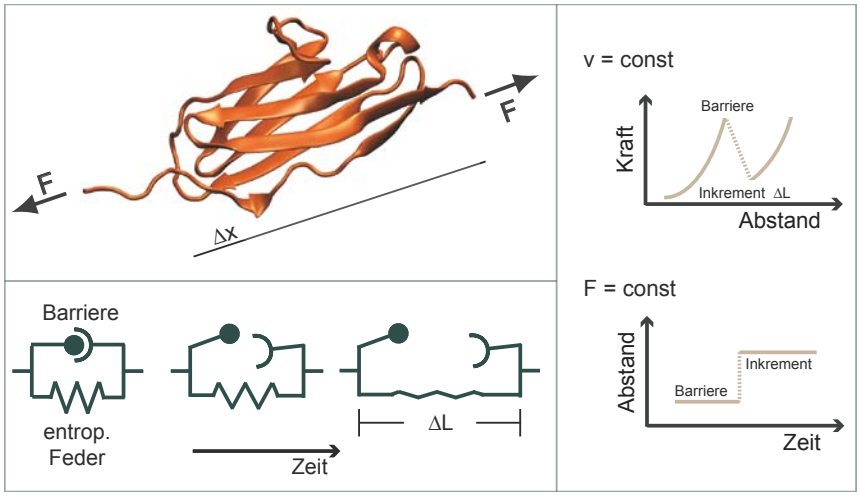

Abbildung 21 – Schematische Darstellung einer molekularen Domäne
Eine globuläre Domäne (hier am Beispiel der Ig27-Domäne von humanem kardialem Titin – PDB: 1WAA) lässt sich schematisch durch die Kombination einer Energiebarriere und einer entropischen Feder darstellen. Unter Last bleibt die Domäne eine Zeit stabil, bis es zu einem mechanisch induzierten Bindungsbruch kommt. In der Kraftkurve ist daraufhin das Konturlängeninkrement ΔL zu beobachten. Der Zusammenhang zu der Anzahl der in der Domäne vorhanden Aminosäuren N und dem Domänendurchmesser Δx lässt sich wie folgt ermitteln [61]: $\Delta L = N*0{,}365\ nm - \Delta x$.

Mögliche Konnektivitäten zweier molekularer Domänen

Molekulare Domänen entfalten unter Last unabhängig voneinander, wenn die Aminosäuren der betrachteten Domänen jeweils eine zusammenhängende Sequenz bilden und keine für die Tertiärstruktur relevanten Wechselwirkungen zwischen den Domänen auftreten. Abhängig von ihrer relativen Positionierung entlang des Kraftvektors kann man bei den unabhängigen Domänen zwischen seriellen und parallelen Orientierungen unterscheiden. Serielle Orientierungen treten beispielsweise auf, wenn man repetitive Proteine mittels Kraftspektroskopie vermisst. Dabei werden identische Domänen mehrfach hintereinander im selben Aminosäurestrang exprimiert. In den Entfaltungskurven tritt dann dasselbe Muster mehrfach auf dient als molekularer Fingerabdruck. Parallele Orientierungen treten beispielsweise auf, wenn mehrere Moleküle zwischen Cantilever und Oberfläche simultan belastet werden. Dies erschwert die Auswertbarkeit der gewonnen Daten und wird deshalb durch Anpassen der Oberflächenanbindungsdichten vermieden.

Wenn jedoch die Aminosäuresequenz einer Domäne von einer anderen Domäne unterbrochen wird, ergeben sich logische Abhängigkeiten im Entfaltungspfad. Die innen liegende Domäne kann zwar über atomare Wechselwirkungen Kräfte transmittieren, jedoch nicht vor der außen liegenden Domäne entfalten. Dies lässt sich beispielsweise am Protein T4-Lysozym illustrieren (Abbildung 22).

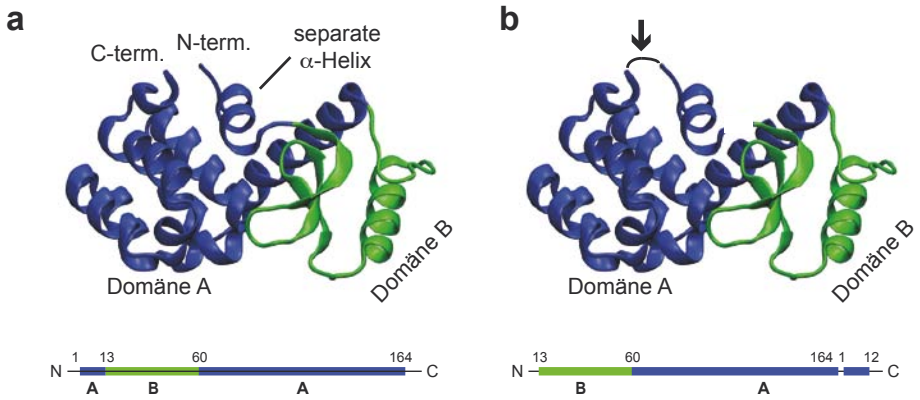

Abbildung 22 – Domänentopologie des Enzyms T4-Lysozym (PDB 1L63)
(a) Das Protein besteht aus zwei globulären Domänen, die bei mechanischer Entfaltung voneinander abhängig sind. Die Domäne A besteht aus zwei Sequenzabschnitten, die die Domäne B umrahmen. Bei Belastung zwischen N- und C-Terminus wird zunächst die N-terminale α-Helix entfaltet, was eine Destabilisierung der gesamten Domäne zur Folge hat. Daraufhin folgt eine Belastung der Domäne B. (b) Durch zyklische Permutation kann die Abhängigkeit der Domänen aufgehoben werden.

Kraftspektroskopische Messungen an diesem Enzym zeigten, dass die Struktur aus zwei globulären Domänen besteht die abhängig voneinander falten [34] und entfalten [147]. Dabei wird die Domäne A von der Domäne B unterbrochen. Erstere besteht aus einem etwa 100 Aminosäuren langen α-helikalen Teil am C-Terminus und einer weiteren 12 Aminosäuren langen α-Helix am N-Terminus. Dazwischen befindet sich in der Sequenz die etwa 50 Aminosäuren lange Domäne B. Man bezeichnet die Domänentopologie von Domäne A als *diskontinuierliche Subdomäne* wohingegen Domäne B eine *kontinuierliche Subdomäne* darstellt [148]. Li et al. beobachteten, dass bei Belastung zwischen dem N- und dem C-Terminus entweder beide Domänen simultan entfalten oder ein in der Distanz relativ breit streuender Zwischenschritt in der Entfaltung auftritt [147]. Dies ist darauf zurückzuführen, dass zunächst die N-terminale Helix von Domäne A entfaltet, was aber ebenfalls eine signifikante Destabilisierung der restlichen Domäne A mit sich führt. Im Falle eines auftretenden Zwischenschritts kann dieser sowohl die Domäne A als auch die Domäne B betreffen. Durch zyklische Permutation kann auch aus Domäne A eine kontinuierliche Subdomäne gemacht werden. Hierzu wird die 12 Aminosäuren lange α-Helix mit einem kurzen Linker einfach C-terminal exprimiert. Das Protein faltet dann immer noch stabil und besitzt eine ähnliche Bindungsenergie wie der Wildtyp [149]. Bustamante et al. konnten mit optischen Fallen sowohl das Falten, als auch das Entfalten der Domänen untersuchen. Die Entfaltung erfolgt nun wie erwartet unabhängig. Ferner stellten sie fest, dass die Domäne A auch ohne Domäne B stabil faltet. Zustände, in denen Domäne B ohne Domäne A stabil ist, wurden jedoch nicht beobachtet. Insgesamt ging durch Entkopplung der Domänen die mechanische Stabilität in den gewählten Zuggeometrien stark zurück [34].

Somit zeigt das Beispiel des T4-Lysozyms eindrücklich, dass die Konnektivität molekularer Domänen durch die Sequenztopologie der Domänen determiniert werden kann. Eine

kontinuierliche Subdomäne, die sich innerhalb einer diskontinuierlichen Subdomäne befindet, kann bei Belastung zwischen den Termini nicht vor der diskontinuierlichen Domäne entfalten. Allerdings kann im Umkehrschluss im Falle zweier aneinandergrenzender kontinuierlicher Subdomänen, die in direkter Wechselwirkung zueinander stehen, nicht ausgeschlossen werden, dass es Abhängigkeiten in ihrem Faltungs- oder Entfaltungspfad gibt. Wie bereits erwähnt, scheint es im Falle des zyklisch permutierten T4-Lysozyms immer noch eine Kooperativität in der Faltung der Domänen zu geben.

Man geht zunehmend davon aus, dass abhängige Domänen nicht nur bei gerichteter Proteinfaltung sondern auch bei enzymatischen und regulatorischen Prozessen relevant sind. Im Rahmen dieser Doktorarbeit wurde die Konnektivität der Energiebarrieren des Muskelenzyms Titinkinase untersucht und es konnte gezeigt werden, dass Titinkinase eine sich bedingende Barrierenstruktur aufweist, die maßgeblichen Einfluss auf die Funktionsweise des Enzyms hat. Diese Zusammenhänge werden im Kapitel 6.1 dargelegt.

Eine Übersicht über mögliche Domänenkonnektivitäten findet sich in Abbildung 23.

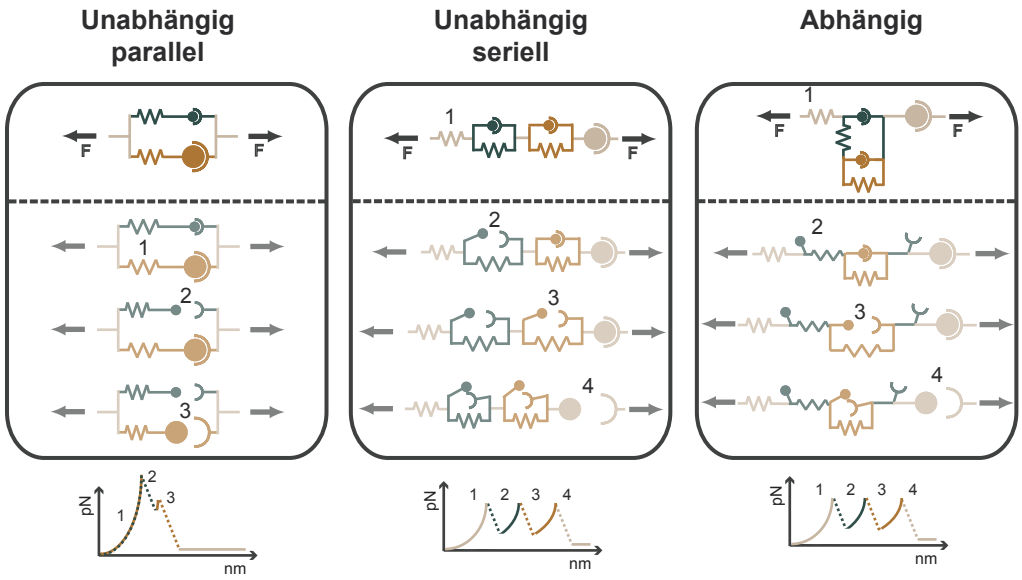

Abbildung 23 – Mögliche Konnektivitäten zweier molekularer Domänen
In Kraftspektroskopieexperimenten mit konstanter Zuggeschwindigkeit lassen sich Abhängigkeiten im Allgemeinen nicht erkennen.

Unterscheidbarkeit von Domänenkonnektivitäten mittels Kraftspektroskopie

Abhängigkeiten im Entfaltungspfad können sich in Kraftspektroskopieexperimenten in verschiedener Weise manifestieren. Besitzen abhängige Domänen eine niedrigere mechanische Stabilität als die vorgeschalteten Domänen, beobachtet man bei Experimenten

mit konstanter Zuggeschwindigkeit Entfaltungskräfte[4] mit absteigender Größe. Dies kann aber auch bei unabhängigen parallelen Konnektivitäten der Fall sein (vergleiche Abbildung 23 – links). Kann man jedoch Mehrfachereignisse ausschließen[5], sind aufeinanderfolgende Ereignisse mit absteigenden Kräften ein eindeutiges Merkmal bedingter Entfaltungen. Beobachtet man jedoch Entfaltungsereignisse mit ähnlichen Kräften oder aufsteigender Krafthierarchie, kann durch Kraftspektroskopie mit konstanter Zuggeschwindigkeit keine eindeutige Aussage über die Konnektivität molekularer Domänen gemacht werden.

Abhilfe schafft hier der „Konstante Kraft" Modus. Betrachtet man hier die Zeitabhängigkeit der Entfaltungswahrscheinlichkeit, erhält man für eine Domäne *i*, die sich als Markov'sches Zweizustandssystem beschreiben lässt, wie in Kapitel 4.1 beschrieben, eine exponentiell abfallende Wahrscheinlichkeitsdichte mit der Entfaltungsrate k_i. Dies ist für Proteindomänen im Allgemeinen in guter Näherung gegeben [150, 151]. Abweichungen können beispielsweise auftreten, wenn sich die individuellen Domänen einer Art nicht exakt gleich verhalten. Man bezeichnet dies als statische [152] oder dynamische [153] Unordnung, je nachdem ob die Unterschiede permanent sind oder durch zeitliche Fluktuationen hervorgerufen werden. Die resultierenden Entfaltungswahrscheinlichkeiten sind aber immer noch monoton fallend und weichen für gewöhnlich nicht stark von Exponentialfunktionen ab.

Die Entfaltungswahrscheinlichkeitsdichte $p_i(t)$ für eine abhängige Domäne unterscheidet sich deutlich von diesem exponentiellen Verhalten, da zunächst der Zustand mit exponentiell abnehmender Wahrscheinlichkeitsdichte durch Entfalten der abschirmenden Domäne bevölkert werden muss. Für den Fall, dass der Zustand i nur durch den Zustand i-1 bevölkert wird und mit einer Rate zerfällt, ergeben sich folglich abhängige Differentialgleichungen der Art

$$\frac{d}{dt} p_i(t) = k_{i-1} p_{i-1}(t) - k_i p_i(t).$$

Besteht eine Verknüpfung zu weiteren Zuständen, müssen auch deren Raten berücksichtigt werden. Die Lösungen für den Fall unterschiedlicher Raten setzen sich aus zwei Exponentialfunktionen zusammen. Mit der Anfangsbedingung $p_{i-1}(0)=k_{i-1}$ und $p_i(0)=0$ erhält man

$$p_i(t) = \frac{k_{i-1} k_i}{(k_{i-1} - k_i)} \left(e^{-k_{i-1} t} - e^{-k_i t} \right).$$

Für den Fall identischer Raten k_i reduziert sich dieser Ausdruck zu

[4] Es müssen die wahrscheinlichsten Kräfte betrachtet werden, da wie eingangs erwähnt die Entfaltungs- und Dissoziationsereignisse in der Kraftspektroskopie immer thermisch getriebene Prozesse mit hoher Streuung sind.

[5] Dies ist zum Beispiel durch Betrachtung der optimal fittenden Persistenzlänge möglich.

$$p_i(t) = k_i^{\,2}\, t\, e^{-k_i t}.$$

Die Wahrscheinlichkeitsdichte ist folglich nicht mehr monoton fallend sondern steigt zunächst an, erreicht nach einer charakteristischen Zeit eine maximale Entfaltungswahrscheinlichkeit und fällt im Anschluss wieder monoton ab. Abbildung 24 verdeutlicht dies anhand mehrerer Beispiele. Unter anderem wurde der Fall einer Serie abhängiger Ereignisse mit gleicher Entfaltungsrate beschrieben. Die Wahrscheinlichkeitsdichten höheren Abhängigkeitsgrades nähern sich dabei immer mehr einer Gauß'schen Verteilung an.

Somit ist Kraftspektroskopie im „Konstante Kraft" Modus in der Lage, abhängige Entfaltungsereignisse zu detektieren.

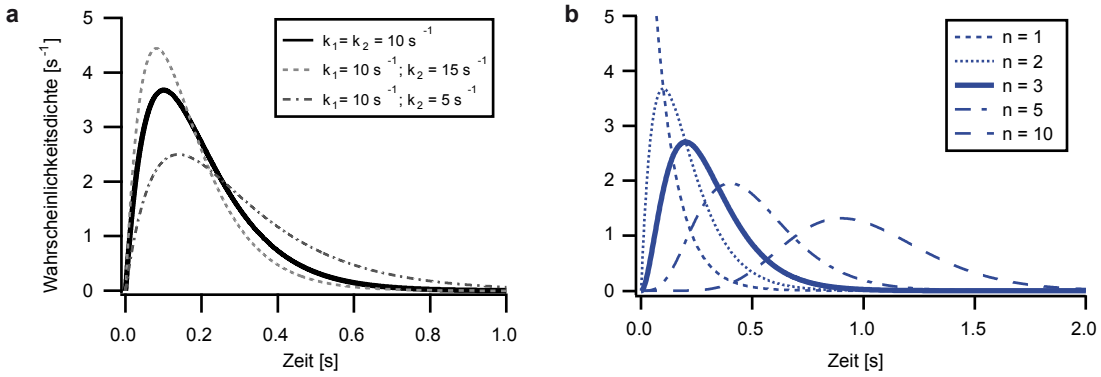

Abbildung 24 – Wahrscheinlichkeitsdichten abhängiger molekularer Entfaltungsereignisse

(a) Entfaltungswahrscheinlichkeit einer exponentiell zerfallenden Domäne, die von einer weiteren exponentiell zerfallenden Domäne abhängig ist. (b) Entfaltungswahrscheinlichkeit der n-ten Domäne in einer Serie hintereinandergeschalteter Ereignisse mit $k = 10\ s^{-1}$.

6 ERGEBNISSE

Nach der Diskussion der biologischen und physikalischen Grundlagen sowie der relevanten Methoden sollen im Folgenden die Ergebnisse dieser Arbeit zusammengefasst werden. Ausführliche Beschreibungen finden sich in den in Kapitel 8 gelisteten Publikationen und Manuskripten.

6.1 Kraftspektroskopische Untersuchung muskulärer Proteinkinasen

Im Laufe der letzten Jahre hat sich zunehmend herausgestellt, dass Kraft eine wichtige Rolle bei regulatorischen Mechanismen auf zellulärer Ebene spielt. Die biologische Reaktion auf mechanische Belastung beruht oft auf den konformationellen Änderungen einzelner Moleküle. Sie dienen den Zellen als Kraftsensoren und müssen in den regulatorischen Netzwerken Kräfte in ein biochemisches Signal umwandeln. Ein Kerngebiet dieser Arbeit befasst sich mit Untersuchungen der mechanischen Stabilität von in Muskelgewebe vorkommenden Proteinkinasen sowie deren Interaktionen mit ihren Substraten. Grundlegende Informationen zum Aufbau und der Funktionsweise von Muskelgewebe finden sich im Kapitel 3.2. Bei den Proteinkinasen handelt es sich um eine Klasse von Enzymen, die Phosphatgruppen auf ihre Substrate übertragen und dadurch deren funktionellen Zustand verändern. Anhand immer neuer Beispiele wird ersichtlich, dass diese einen wichtigen Beitrag bei der Steuerung molekularer Netzwerke über biomechanische Signaltransduktion liefern. Neben den im Rahmen dieser Dissertation untersuchten Enzymen *Titinkinase* (TK) und *Myosin-Light-Chain-Kinase* (MLCK) die zur Klasse der Serin-Threonin spezifischen Kinasen gehören, finden sich ebenfalls Hinweise auf eine über Mechanotransduktion geregelte Funktionsweise zum Beispiel bei der *Focal-Adhesion Kinase* (FAK) [154-158], der *Tyrosinkinase Fyn* [159, 160] oder den *Src-Familiy-Kinasen (SFKs)* [161-163]. Sämtliche der zuletzt genannten Enzyme sind Vertreter der Klasse der Tyrosinkinasen. Dies bedeutet, dass sie ihre Substrate spezifisch an der Hydroxygruppe der Aminosäure Tyrosin phosphorylieren. Die Beteiligung mehrerer Kinaseklassen an mechanosensorischen Prozessen deutet darauf hin, dass es sich bei den beobachteten Funktionsprinzipien um ein allgemeingültiges Konzept der molekularen Biologie handelt. Um dieses zu ergründen, ist es essentiell die molekulare Architektur solcher enzymatischer Kraftsensoren zu verstehen. Sie bildet die Basis dafür, wie konformationelle Änderungen, mechanische Stabilität und Funktion zusammenhängen.

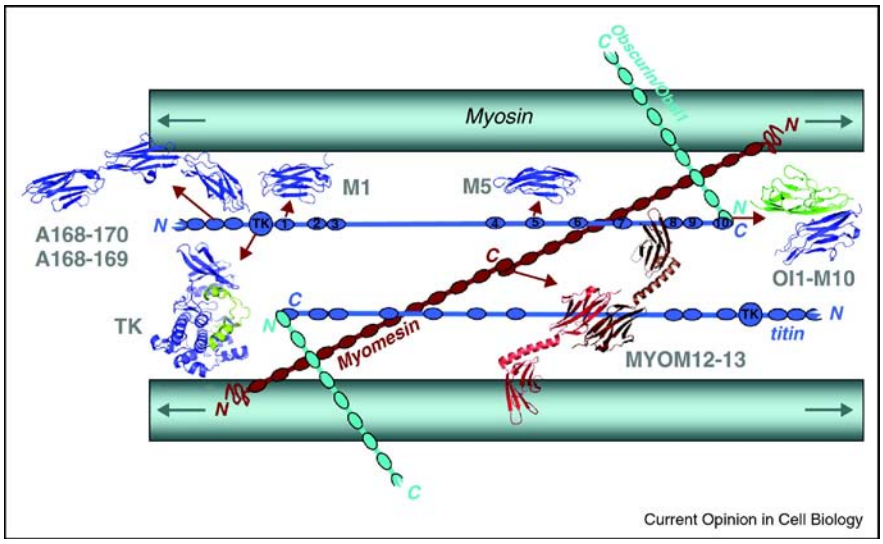

Abbildung 25 – Schematische Repräsentation der M-Bande
Myosinfilamente werden von antiparallelen Myomesindimeren (MYOM12-13) quervernetzt. Letztere bilden einen Komplex mit Obscurin/Obsl1, das wiederum Titin C-terminal bindet (OL1-M10). Die katalytische Kinasedomäne von Titin (TK) befindet sich in der Umgebung der M-Bande. Obwohl dieses Modell sich mit bekannten Wechselwirkungen und Proteinlokalisationen deckt, sind weitere Verbindungen für Tititn denkbar und die Konformation der als Linien dargestellten Linkerregionen ist noch unbekannt.
Nachdruck von „Current Opinion in Cell Biology" [49], Copyright (2011) mit Erlaubnis von Elsevier.

Barrierenstruktur des Muskelenzyms Titinkinase

Titinkinase bildet die einzige katalytisch aktive Domäne im Makromolekül Titin, das im Sarkomer die Z- mit den M-Banden verbindet und den Muskelzellen passive Elastizität gibt (vgl. Kapitel 3.2). In der Aminosäuresequenz von Titin befindet sich die Titinkinase (TK) in der Nähe des C-terminalen Endes des Proteins. Somit lokalisiert sie im Sarkomer entlang der M-Banden, die die Myosinfilamente miteinander quervernetzen und dem gesamten Sarkomer als Querstabilisierung dienen. Während aktiver Muskelkontraktion können Scherkräfte zwischen benachbarten Myosinfilamenten zu einer Verzerrung der M-Bande im Bereich von mindestens 10 nm führen (Abbildung 5) [49, 164]. Dies tritt vor allem zu Tage, wenn durch strukturelle Beschädigung einzelne Myosinfilamente geschwächt werden. Durch Verzerrungen der M-Bande können Zugkräfte zwischen dem N- und dem C-terminalen Ende der Kinasedomäne in Titin auftreten und deren Struktur beeinflussen. Ferner ist bekannt, dass künstlich aktivierte TK-Domänen den Proteinumsatz im Muskel sowie die Expression von Muskelproteinen im Zellkern regulieren [75]. Das grundlegende Verhalten des nativen Kinasemoleküls und der es umgebenden Ig- und Fn-Domänen unter Kraft wurde bereits in dieser Arbeit vorangegangenen Experimenten mit einer Kombination aus Einzelmolekülkraftspektroskopie, Molekulardynamiksimulationen und enzymatischer Analyse untersucht [46, 73, 74]. Das dabei ermittelte Funktionsprinzip lässt sich folgendermaßen zusammenfassen: In ihrer unbelasteten Konformation ist TK durch zwei unabhängige Mechanismen autoinhibiert. Zum einen verdecken C-terminale regulatorische

Sekundärstrukturelemente die ATP-Bindungsstelle und zum anderen inhibiert die Aminosäure Tyrosin-170 die katalytische Base Aspartat-127.

Im Gegensatz zu anderen Kinasen ist kein physiologisch relevanter Ligand bekannt, der die intramolekulare Inhibierung aufheben kann. Eine zugängliche ATP-Bindungstasche kann aber durch Anlegen von Kraft geschaffen werden. Dabei löst sich nach dem ermittelten Modell unter Last zunächst das β-Faltblatt R1-C10 und anschließend die α-Helix R2 aus der Struktur, was eine geöffnete und funktionelle ATP-Bindungstasche zur Folge hat (vergleiche Abbildung 26). Die weitere Überführung in einen aktiven Zustand der Kinase erfolgt über Autophosphorylierung des inhibierenden Tyrosin-170. Experimente von der Gruppe um Mathias Gautel am King's College London zeigen, dass dies eine Aufhebung der Blockierung der katalytischen Base zur Folge hat und TK nun Substrate wie Nbr1 phosphorylieren kann [46, 75].

In dieser Arbeit vorangegangenen Einzelmolekül-Kraftspektroskopieexperimenten mit konstanter Zuggeschwindigkeit wurde beobachtet, dass Titinkinase kraftinduziert in mehreren Schritten mit einer regelmäßigen Reihenfolge entfaltet. Die auftretenden Energiebarrieren werden deshalb fortlaufend von 1 bis 5 nummeriert. Das Auftreten einer zusätzlichen Barriere mit der Bezeichnung 2* ist zuggeschwindigkeitsabhängig und wurde mit dem Binden von ATP in Verbindung gebracht [46]. Mutationen der Bindungstasche grenzen die Lokalisierung dieser Barriere weiter ein, da diese sich in den beobachten Häufigkeiten der Barriere 2* vom Wildtyp unterscheiden. Das typische Entfaltungsmuster findet sich in Abbildung 27b.

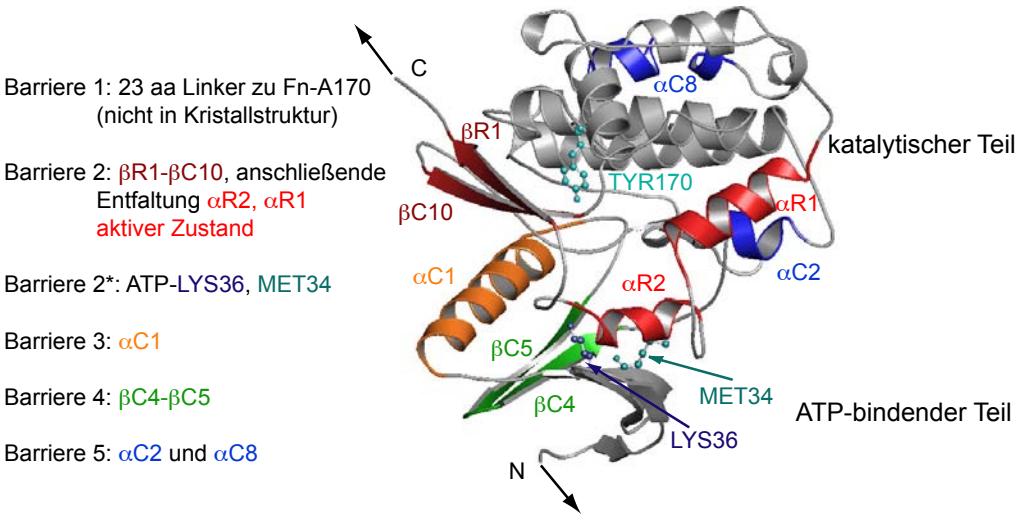

Abbildung 26 – Kristallstruktur des molekularen Kraftsensors Titinkinase (PDB 1TKI)
Farblich hervorgehoben sind die in [46] ermittelten Strukturelemente, von denen vermutet wird, dass sie Barrieren im Entfaltungspfad hervorrufen. Darüber hinaus sind für die Funktionalität relevante Aminosäuren im Gittermodell dargestellt. Die Grafik wurde freundlicherweise von Elias Puchner zur Verfügung gestellt.

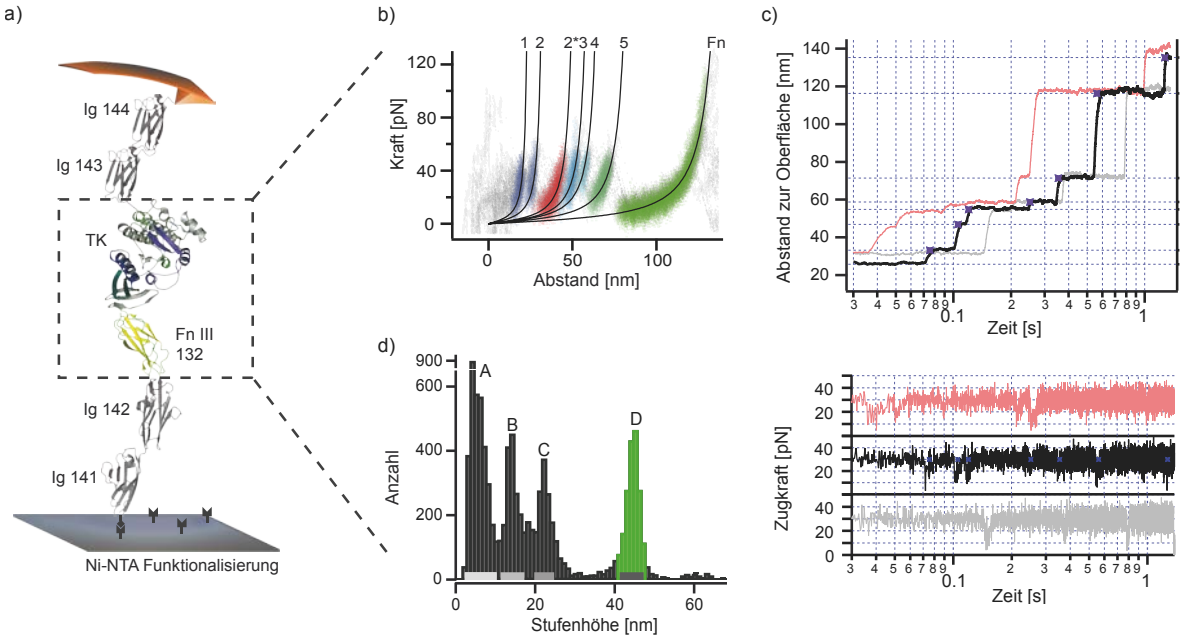

Abbildung 27 – Einzelmolekül-Kraftspektroskopie an Titinkinase (nach [165])
(a) Das vermessene Proteinkonstrukt besteht aus der Kinasedomäne (TK) sowie den es umgebenden Fibronectin- und Ig-Domänen. Die Kontaktierung erfolgt an der Oberfläche spezifisch über den His-Tag des Proteins und am Cantilever unspezifisch an einer im Vorhinein unbekannten Stelle. (b) Charakteristisches Entfaltungsmuster bei konstanter Zuggeschwindigkeit. Die Entfaltung der Kinase-Domäne erfolgt über maximal 6 Schritte. Dabei hängt die Wahrscheinlichkeit, die gesondert bezeichnete Barriere 2* zu beobachten, von der Zuggeschwindigkeit ab. Die Ig-Domänen entfalten bei höheren Kräften und längern Distanzen. (c) Charakteristisches Entfaltungsmuster im „Konstante-Kraft“ Modus. Entfaltungsereignisse erzeugen einen kurzen Einbruch in der Zugkraft und ein treppenförmiges Profil im Abstandsgraph. Die Barrieren lassen sich dabei über die Höhe der Inkremente bestimmen. (d) Automatische Analyse der auftretenden Inkremente von ca. 10.000 Entfaltungsereignissen. Es lassen sich vier klare Populationen ausmachen, von denen die Population D eindeutig mit dem Entfaltungsschritt 5 identifiziert werden kann. Die Populationen A-C setzen sich aus verschiedenen Entfaltungsereignissen zusammen. Adaptiert von [P5].

Für das Auftreten eines regelmäßigen Entfaltungsmusters mit definierter Reihenfolge können mehrere Ursachen verantwortlich sein. Es ist beispielsweise möglich, dass sich die Subdomänen in ihrer mechanischen Stabilität unterscheiden und zunächst die labileren Teile entfalten. In diesem Fall würde man von einer *Mechanischen Hierarchie* sprechen. Ein weiteres vorstellbares Szenario ergibt sich, wenn wie im Kapitel 5 beschrieben, durch die Domänentopologie definierte Abhängigkeiten im Entfaltungspfad bestehen. Diesen Fall kann man als *Topologische Konnektivität* bezeichnen.

Eine kraftspektroskopische Unterscheidung der beiden Szenarien ist wie eingangs beschrieben bei konstanter Zuggeschwindigkeit nicht trivial. Im „Konstante-Kraft“ Modus jedoch sollte sich die Konnektivität von Domänen über ihre zeitabhängige Entfaltungswahrscheinlichkeit erkennen lassen. Im Falle unabhängiger Domänen ist diese für ein Zweizustandsmodell mit thermisch induzierter Überwindung einer Energiebarriere exponentialverteilt. Im Falle Topologischer Konnektivität erwartet man jedoch Gamma-

ähnliche Verteilungen mit einer maximalen Entfaltungswahrscheinlichkeit nach einer charakteristischen Zeit τ (vergleiche Kapitel 5). Deshalb wurden für diese Arbeit Kraftspektroskopiemessungen an Titinkinase im „Konstante-Kraft“ Modus durchgeführt.

Abbildung 27 zeigt eine Übersicht über die verwendeten experimentellen Gegebenheiten sowie typische Entfaltungskurven, die in diesem Zusammenhang ermittelt wurden. Sie weisen das charakteristische treppenförmige Profil des „Konstante-Kraft“-Modus auf. Durch Analyse der auftretenden Stufenhöhen und Entfaltungszeiten ist bereits eine erste Charakterisierung der Entfaltungsschritte möglich. Da Barriere 5 unter konstanter Zuggeschwindigkeit immer zuletzt entfaltet, sollten für die dazugehörige Proteindomäne die Unterschiede zwischen den beschriebenen Szenarien am deutlichsten zum Vorschein treten. Darüber hinaus lässt sich diese Domäne zweifelsfrei allein anhand ihrer Stufenhöhe identifizieren. Ermittelt man aus den Entfaltungszeitpunkten die zeitabhängige Entfaltungswahrscheinlichkeitsdichte, weist diese eine offensichtlich nicht exponentialverteilte Charakteristik auf, die sehr gut mit einer Gamma-Verteilung genähert werden kann. Die Zeitverteilung zum der Barriere 5 vorausgehenden Ereignis hingegen ist klar exponentialverteilt (Abbildung 28). Dies zeigt, dass man eine einzelne Domäne gut mit einem Zweizustands-Markov-Prozess beschreiben kann und dass die Subdomäne zu Barriere 5 klar vom Faltungszustand der vorangehenden Domänen abhängt.

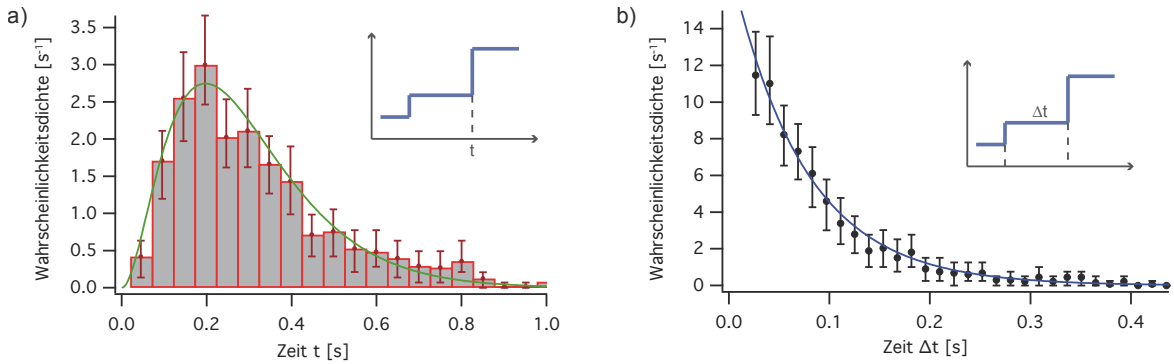

Abbildung 28 – Zeitabhängige Entfaltungswahrscheinlichkeiten für Barriere 5 von TK
(a) Die Wahrscheinlichkeitsdichte für den absoluten Entfaltungszeitpunkt nach Anlegen der Kraft lässt sich gut durch eine Gamma-Funktion nähern. (b) Die relative Wahrscheinlichkeitsdichte zum vorangehenden Ereignis ist exponentialverteilt. Adaptiert von [P5].

Eine eindeutige Identifizierung der verbleibenden Barrieren allein anhand ihrer Stufenhöhen ist aufgrund der experimentellen Streuung nicht möglich. Betrachtet man aber sowohl die Stufenhöhe als auch die Position relativ zur Barriere 5, so stellt man fest, dass ca. 90 % der beobachteten Stufen der gleichen determinierten Entfaltungsreihenfolge von Barriere 1-5 der TK entsprechen. Die verbleibenden Ereignisse lassen sich durch partielles oder vollständiges Entfalten der unabhängigen Ig- und Fn-Domänen und Kontaktierungen des

Proteinkonstrukts mit dem Cantilever innerhalb der Kinasedomäne erklären. Dies hat entweder eine Verschiebung der Lokalisierung der Barrieren oder aber ein unkontrolliertes Entfalten der Kinasedomäne zur Folge.

Mithilfe der relativen Positionierung zu Barriere 5 können auch für die verbleibenden Subdomänen der TK charakteristische Entfaltungsraten bestimmt werden. Es stellte sich heraus, dass auch diese exponentialverteilt mit den Entfaltungsraten k_i sind. Durch Lösen des Differentialgleichungssystems

$$\frac{d}{dt}\begin{pmatrix} p_1 \\ p_2 \\ p_{2^*} \\ p_3 \\ p_4 \\ p_5 \end{pmatrix} = \begin{pmatrix} -k_1 & & & & & \\ k_1 & -k_2 & & & & \\ & pk_2 & -k_{2^*} & & & \\ & (1-p)k_2 & k_{2^*} & -k_3 & & \\ & & & k_3 & -k_4 & \\ & & & & k_4 & -k_5 \end{pmatrix} \begin{pmatrix} p_1 \\ p_2 \\ p_{2^*} \\ p_3 \\ p_4 \\ p_5 \end{pmatrix}$$

lassen sich die Wahrscheinlichkeitsverteilungen p_i für den in Abbildung 29a dargestellten verzweigten Entfaltungspfad ermitteln. *p* beschreibt hierbei die Wahrscheinlichkeit, dass die zusätzliche Energiebarriere 2* beobachtet wird. Es zeigte sich, dass diese in guter Näherung mit den experimentell gemessenen Daten übereinstimmen (Abbildung 29). Darüber hinaus konnte das unabhängige Entfalten der benachbarten Fibronectin-Domäne durch ihre exponentielle Wahrscheinlichkeitsdichte nachgewiesen werden.

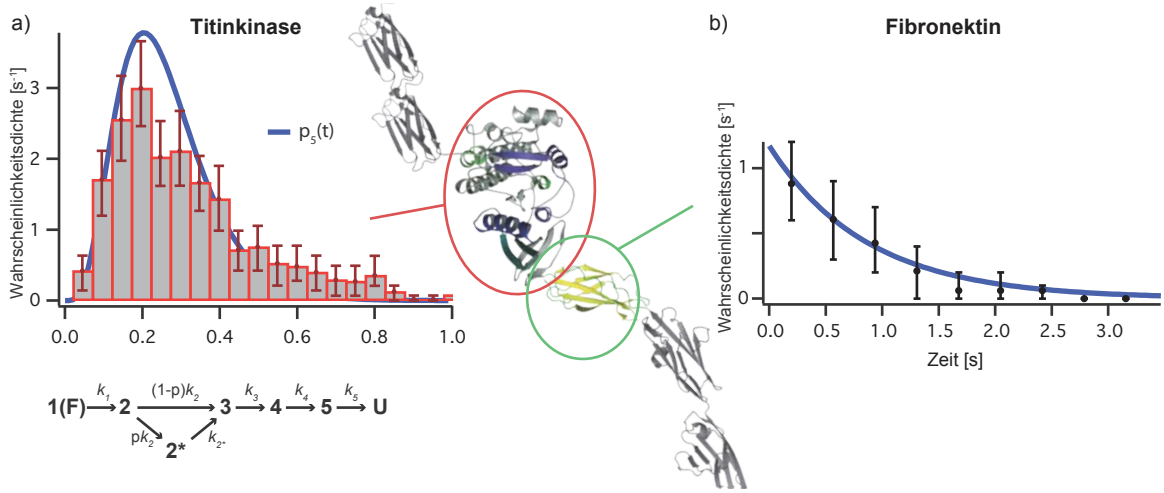

Abbildung 29 – Entfaltungswahrscheinlichkeiten für Titinkinase und Fibronektin
(a) Die Verteilung der Zeitpunkte, bis die komplette Kinasedomäne entfaltet ist lassen sich gut mit dem schematisch skizziertem sequentiellen Modell $p_5(t)$ beschreiben, bei dem sich sämtliche Barrieren bedingen und mit der Wahrscheinlichkeit p die zusätzliche Energiebarriere 2* auftritt. (b) Die exponentiell abfallende Entfaltungswahrscheinlichkeit für die Fibronektin-Domäne lässt deutlich erkennen, dass es sich hierbei um ein unabhängiges Ereignis handelt. Adaptiert von [P5].

Zusammengefasst lässt sich sagen, dass mithilfe der beschriebenen Experimente die molekulare Architektur des Enzyms Titinkinase als Modellsystem eines molekularen Kraftsensors entschlüsselt werden konnte. Die zur Faltung beitragenden Subdomänen des Enzyms sind so miteinander verknüpft, dass regulatorische vor stabilsierenden und enzymatisch wirksamen Domänen entfalten müssen. Dies gewährleistet, dass das Enzym über konformationelle Änderungen reguliert werden kann ohne dass es seine Funktionalität und strukturelle Integrität verliert. Die gewonnenen Ergebnisse legen nahe, dass eine abhängige Konnektivität für alle ermittelten Energiebarrieren vorliegt. Für die anfangs entfaltenden regulatorischen Domänen untereinander lässt sich allerdings eine in der Entfaltung unabhängige mechanische Hierarchie experimentell nicht vollständig ausschließen.

Mechanische Stabilität und ATP-Affinität der Myosin-Light-Chain Kinase

Neben dem mechanisch induzierten Entfalten von Titinkinase wurde im Rahmen dieser Arbeit die mechanische Stabilität der *Smooth Muscle Myosin-Light-Chain Kinase* (smMLCK) als weiterer Vertreter einer im Muskelgewebe vorkommenden Serin/Threonin spezifischen Kinase untersucht. Diese reguliert die Kontraktion im glatten Muskelgewebe durch Phosphorylierung eines Serins der leichten Kette der Myosinköpfe. Im unphosphorylierten Zustand können die Myosine nicht an die Aktinfilamente binden und somit auch keine den Muskel kontrahierende Kraft aufbringen. Durch Einfluss von Calcium aus dem extrazellulärem Raum oder dem sarkoplasmatischen Retikulum in das Cytosol der Muskelzelle wird eine Kontraktion der glatten Muskulatur hervorgerufen, indem das Calcium von Calmodulin rekrutiert wird. Durch Binden des Ca-/Calmodulin-Komplex an die MLCK wird deren Autoinhibierung aufgehoben und MLCK aktiviert wiederum die Myosinköpfe durch Phosphorylierung. Dies führt zu einer permanenten Kontraktion der Muskelfilamente, die erst durch Dephosphorylierung der Myosine durch *Myosin-Light-Chain-Phosphatase* (MLCP), den Antagonisten der MLCK, aufgehoben wird [166].

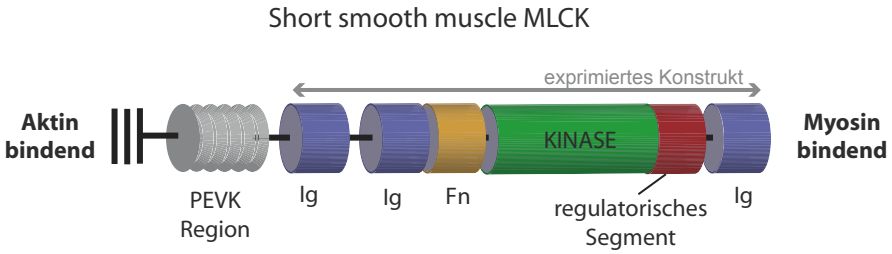

Abbildung 30 – Schema der Domänenabfolge der kurzen MLCK in glatter Muskulatur

Im Gegensatz zur Titinkinase ist die MLCK nicht Teil eines in der Muskelzelle fest verankerten Komplexes sondern besteht neben der Kinasedomäne lediglich aus drei Ig-artigen Domänen, einer Fibronektindomäne sowie einer elastischen PEVK-Region (vergleiche Abbildung 30). Eine Kristallstruktur der Kinasedomäne existiert zum gegenwärtigen Zeitpunkt noch nicht. Jüngste Ergebnisse der Forschung an glatter Muskulatur erweisen sich als Indizien dafür, dass alternativ zur Aktivierung der Kinase über allosterische Regulation durch Calmodulin ebenfalls eine direkte mechanische Aktivierung von MLCK existieren könnte:

Das MLCK-Konstrukt ist im Prinzip im Cytoplasma der Muskelzelle frei beweglich. Allerdings wurden am N-terminalen Ende eine Affinität zu Aktin [167-171] und am C-terminalen Ende eine Affinität zu Myosin [172] nachgewiesen. Dabei scheint eine der Aktinbindungsstellen calmodulin-abhängig zu sein [173]. Es ist folglich also denkbar, dass die MLCK im glatten Muskelgewebe Aktine und Myosine miteinander quervernetzt und zwischen dem N- und dem C-Terminus belastet wird, wenn die Myosinköpfe nicht an Aktin gebunden haben oder sich aktiv vorwärtsbewegen. MLCK scheint dabei einen aktivierenden Effekt auf die Aktin-Myosin-

Bindung auszuüben, wenn die Myosine nicht phosphoryliert sind und im Falle phosphorylierter Myosine eher inhibitorisch zu wirken [174]. Mehrere Publikationen konnten ferner mechanisch stimulierte Prozesse in glatter und skelettaler Muskulatur mit MLCK in Verbindung bringen [175-178].

Dies diente als Anhaltspunkt, die mechanische Stabilität von MLCK mithilfe AFM-basierter Kraftspektroskopie zu untersuchen. Abbildung 31 zeigt eine Überlagerung typischer Entfaltungskurven. Die Entfaltungen der Fibronektin- und Ig-Domänen sind klar ersichtlich. Im Bereich davor sind mehrere Barrieren zu erkennen, die bei vergleichsweise niedrigen Entfaltungskräften < 40 pN überwunden werden. Ihr kombiniertes Längeninkrement entspricht den Erwartungen einer Entfaltung der Kinasedomäne. Die im Vergleich zur Titinkinase niedrigen Entfaltungskräfte sind bereits eine erste interessante Beobachtung. Im Falle einer mechanischen Regulation kommen voraussichtlich nicht Ungleichheiten ganzer Myosinbündel sondern eher die Kräfte einzelner Myosinköpfe als Auslöser in Frage. Ferner konnte beobachtet werden, dass die Stabilität der zweiten Barriere eine starke ATP-Abhängigkeit aufweist. In Anwesenheit von ATP gibt es eine Population höherer Entfaltungskräfte, deren Häufigkeit mit steigender ATP-Konzentration wächst (Abbildung 32). Somit kann auch für die MLCK eine Ligandenbindung mittels Einzelmolekül-kraftspektroskopie nachgewiesen werden.

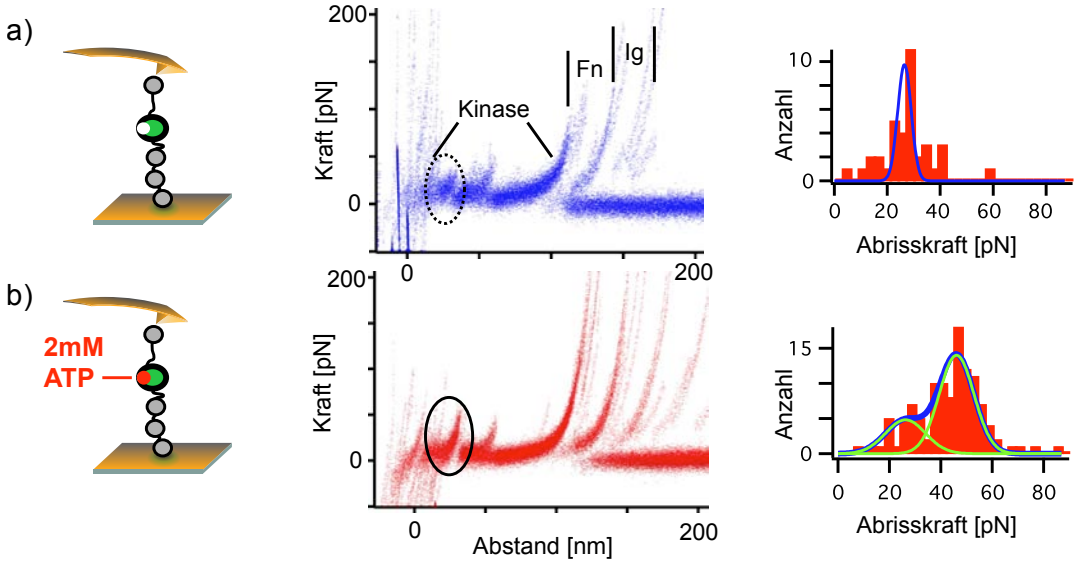

Abbildung 31 – Kraftspektroskopie an MLCK aus glatter Muskulatur
(a) Experimente ohne ATP zeigen, dass die Kinasedomäne bei vergleichsweise niedrigen Kräften < 40 pN entfaltet. (b) Zugabe von 2 mM ATP führt zu einer deutlichen Stabilisierung einer der Energiebarrieren in der Entfaltung der Kinase. Im entsprechenden Krafthistogramm ist eine Population bei höheren Kräften zu erkennen.

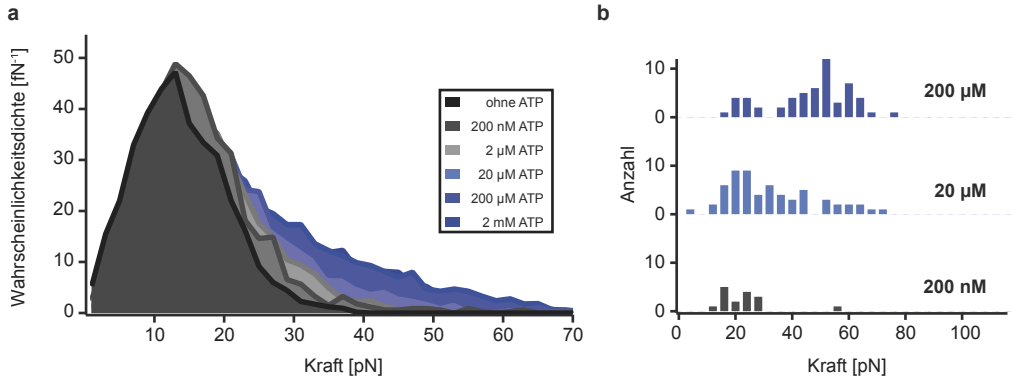

Abbildung 32 – ATP Abhängigkeit der Entfaltungskräfte der stabilisierten Barriere von MLCK
(a) Verteilung der detektierten Kräfte für die entsprechende Konturlänge. Mit zunehmender ATP-Konzentration steigen die erreichten Kräfte. Bei ca. 200 µM ATP tritt eine Sättigung auf. (b) In den Abrisskrafthistogrammen für verschiedene ATP-Konzentrationen lassen sich zwei Populationen ausmachen.

Es wäre interessant festzustellen, ob die beobachtete ATP-Bindung kraftinduziert ist, oder ob das Co-Substrat bereits ohne Konformationsänderungen der Kinase Zugang zur Bindungstasche hat. In der Literatur gibt es dazu widersprüchliche Aussagen. Ikebe et. al. beschreiben einen kompetitiven Effekt zwischen der ATP-Bindung und dem C-terminalen autoinhibierenden Peptid der Kinase [179]. In einer weiteren Publikation derselben Gruppe wurde jedoch beobachtet, dass ein ATP-Analog das aktive Zentrum auch ohne Aktivierung durch Calmodulin markieren kann [180], was sich mit ähnlichen Daten einer anderen Gruppe deckt [181]. Um ein mechanisch induziertes Binden zu überprüfen, kommen von Seite der Einzelmolekülkraftspektroskopie beispielsweise detaillierte Analysen der Zug-geschwindigkeitsabhängigkeiten oder sogenannte *„Pump and Probe“*-Experimente [74] in Frage. Niedrige Ausbeuten verwertbarer Kurven mit dem verwendeten Proteinkonstrukt, die darauf zurückzuführen sind, dass für eine unspezifische Kontaktierung des Cantilevers nur die einzelne C-terminale Ig-Domäne zur Verfügung steht, haben dies bislang verhindert. Messungen mit einem modifizierten Konstrukt, bei dem die Position der Anker getauscht und eine zusätzliche C-terminale Ig-Domäne mit der Kinase co-exprimiert wurde, erhöhte die Kraftkurvenausbeute drastisch. Allerdings wurde bei diesem Konstrukt die Autoinhibierung der Kinase aus bislang noch nicht im Detail geklärten Gründen aufgehoben. Deshalb eignet es sich nicht um Rückschlüsse auf das native Kinasekonstrukt zu ziehen.

6.2 Mechanische Stabilität des Cellulosoms

Cellulose ist das am häufigsten vorkommende organische Makromolekül auf der Erde [3]. Es findet sich als Bestandteil in den Pflanzenzellwänden und gibt diesen mechanische Stabilität. Chemisch gesehen handelt es sich um ein Polysaccharid aus Glucose, das zu Mirkrofibrillen vernetzt und aufgrund dieser speziellen Quervernetzung nicht vom menschlichen Organismus abgebaut werden kann. Die Zugfestigkeit der Cellulose-Mikrofibrillen ist vergleichbar mit Stahl und kann den durch die Pflanzenzellen aufgebauten osmotischen Druck kompensieren. An den Oberflächen der Mikrofibrillen befinden sich *quervernetzende Glykane*, die aus verschiedenen Zuckerarten bestehen (z.B. Glucose, Xylose, Mannose). Deren Struktur kennzeichnet ein langes Grundgerüst, von dem kurze Seitenketten anderer Zucker abzweigen. Sie stabilisieren die Fasern über nichtkovalente Bindungen. Darüber hinaus bilden stark hydratisierte *Pektine* einen weiteren quervernetzenden Bestandteil von Pflanzenzellwänden.

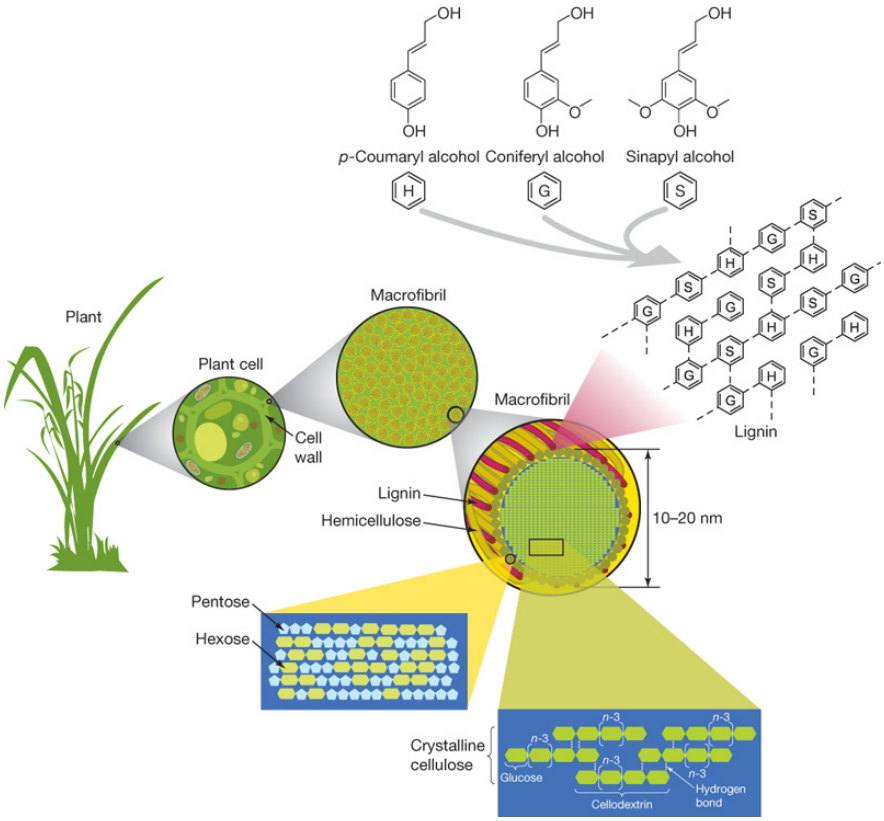

Abbildung 33 – Aufbau lignocellulosehaltiger Biomasse
Der Hauptbestandteil von Lignocellulose ist Cellulose, eine β(1-4)-verknüpfte Kette von Glucosemolekülen. In den Hemicellulosefasern wird die Cellulose durch verschiedenen 5- und 6-Ring-Zucker wie Arabinose, Galactose, Glucose, Mannose und Xylose umgeben. Lignin besteht aus phenolischen Hauptbestandteilen (p-Coumaryl Alkohol (H), Coniferyl Alkohol (G) und Sinapyl Alkohol (S) und entsteht durch Polymerisation dieser Komponenten. Deren Verhältnis zueinander variiert zwischen verschiedenen Pflanzenarten. Cellulose, Hemicellulose und Lignin formen Strukturen, die Mikrofibrillen genannt werden und die sich wiederum zu Makrofibrillen zusammenlagern. Diese geben den Pflanzenzellwänden mechanische Stabilität.
Nachdruck mit Genehmigung von Macmillan Publishers Ltd: Nature [182], Copyright (2008)

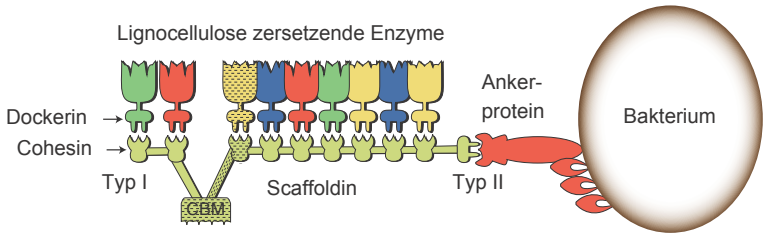

Abbildung 34 – Cellulosom des Bakteriums *Clostridium Thermocellum*
Das Cellulosom dieses thermophilen Bakteriums besteht aus einem Scaffoldin mit 9 Cohesinen und einer Cellulose bindenden Einheit (CBM). Darauf können die enzymatischen Einheiten über die hochspezifische Cohesin-Dockerin Typ I Wechselwirkung binden. Das Scaffoldin wiederum ist über eine Cohesin-Dockerin Typ II Wechselwirkung mit auf der Zelloberseite exponierten Ankerproteinen verbunden.

In verholzten Pflanzen gibt im Laufe der Zeit eingelagertes *Lignin* den Zellwände eine hohe Druckstabilität, indem es sonst vorhandene Hohlräume ausfüllt. Wegen seines hohen Energiegehalts und der Unverdaubarkeit für den menschlichen Organismus wird Biomasse aus Lignocellulose als aussichtsreicher Kandidat für die Produktion von sogenannten Biotreibstoffen der zweiten Generation gehandelt [183-185]. Im Gegensatz zum heute zumeist verwendeten Mais und Zucker kompetitieren diese nicht direkt mit der Nahrungsmittelproduktion. Der Aufbau von Lignocellulose ist in Abbildung 33 dargestellt.

Lignineinlagerungen und die daraus resultierende dichte Struktur mit einem hohen Verknüpfungsgrad sorgen ebenfalls dafür, die Pflanze vor Schädlingen wie Pilzen oder Bakterien zu schützen, weil sie die Zugänglichkeit des Materials für degradierende Enzyme stark einschränken. Dies hat zur Folge, dass Biomasse aus Lignocellulose nur langsam abgebaut werden kann. Um dies zu gewährleisten haben auf der kompetitiven Seite der Evolutionsschiene einige Bakterien und Pilze komplexe Enzymverbände entwickelt, die sich auf der Außenseite der Zelle befinden und durch ihr molekulares Zusammenspiel in der Lage sind, auch Lignocellulose zu zersetzen. Diese Einheiten werden *Cellulosom* genannt. Die Struktur eines Cellulosoms kann in verschiedene Untergruppen zerlegt werden, deren molekulare Zusammensetzung sich von Spezies zu Spezies unterscheidet.

Das *Scaffoldin* bildet das Grundgerüst eines jeden Cellulosoms. Es organisiert als molekulares Steckbrett die verschiedenen cellulolytischen Untereinheiten durch molekulare Erkennungsprozesse und besteht aus globulären *Cohesin-Domänen* und Cellulose bindenden Einheiten (*Cellulose Binding Module – CBM*). *Dockerine* bilden in einem molekularen Erkennungsprozess das Gegenstück zu den Cohesinen. Sie sind mit den Enzymen verbundenen und ordnen diese entlang des Scaffoldins an. Der *Cohesin-Dockerin Komplex* weist eine extrem hohe Affinität auf, dessen off-Raten mit konventionellen

Techniken fast nicht bestimmbar sind. Neben diesem Typ I Cohesin-Dockerin Komplex existiert die Typ II Verbindung von Cohesin und Dockerin als weiterer molekularer Anker. Mit ihm wird das Scaffoldin mit auf den Zellwänden der cellulolytischen Organismen vorhandenen Proteinen verbunden. Das Schema eines Cellulosoms findet sich Abbildung 34. In vielen Organismen besteht das Scaffoldin aus mehreren querverzweigenden Monomeren.

Die mechanische Stabilität des Cellulosoms ist relevant, weil es die makromolekulare Cellulose mit dem Bakterium verbindet. Zwischen diesen für mikroskopische Verhältnisse extrem großen Objekten können in laminaren Flüssen hohe Scherkräfte auftreten, die das Cellulosom belasten. Es gibt weiterhin vielversprechende Ansätze, künstliche Cellulosome zu schaffen. Für eine erfolgreiche Anwendung der im folgenden Kapitel beschriebenen *Single-Molecule Cut-and-Paste* Technik zum gerichteten Transport von Enzymen des Cellulosoms ist es unabkömmlich, deren mechanische Stabilität und Bindungsstärke zu kennen.

Deshalb wurde als Teilprojekt dieser Dissertation ein molekularer Komplex aus vier Konstituenten des Cellulosoms kraftspektroskopisch vermessen. Die Proteine wurden dabei von der am Weizmann Institut in Tel Aviv ansässigen Gruppe um Ed Bayer zur Verfügung gestellt. Es handelt sich dabei um ein Konstrukt aus der Cellulose bindenden Einheit (CBM) des thermophilen Bakteriums *Claustridium thermocellum* und der benachbarten Cohesin-Domäne A2C. Der molekulare Wechselwirkungspartner ist das Dockerin-Modul Cel48S von Claustridium thermocellum, das mit einer C-terminalen Xylanase des Bakteriums *Geobacillus stearothermophilus* co-exprimiert wurde. Beide Konstrukte verfügen über Cystein-Mutationen zur spezifischen Oberflächenanbindung.

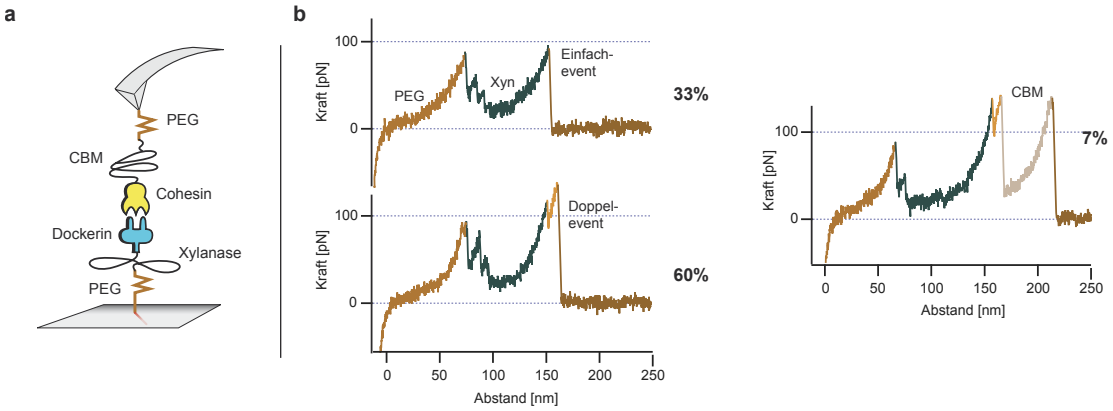

Abbildung 35 – Typische Entfaltungsmuster der kraftspektroskopisch vermessenen Cellulosomdomänen
(a) Schematik des Proteinkonstruktes. Bei den durchgeführten Experimenten wurde wahlweise das Cohesin oder das Dockerin an der Oberfläche und das entsprechende Gegenstück am Cantilever durch kovalente Immobilisierung von Cystein-Residuen befestigt. (b) Typische Entfaltungskurven in der in (a) dargestellten Konfiguration weisen ein charakteristisches Xylanase-Entfaltungsmuster mit absteigenden Kräften und dann wahlweise ein einzelnes oder doppeltes Entfaltungsereignis auf. In seltenen Fällen kann auch die stabile Entfaltung der CBM-Domäne beobachtet werden.

Die Kraftspektroskopiemessungen weisen ein hochgradig spezifisches und typisches Entfaltungsmuster auf, das in Abbildung 35 dargestellt ist. Charakteristisch ist eine sequentielle Entfaltung über maximal zwei Zwischenschritte mit absteigender Entfaltungskraft, der ein Doppelereignis mit 8 nm Konturlängeninkrement bei hoher Kraft (> 100 pN) folgt. Dabei entsprechen die ersten Längeninkremente den Erwartungen einer Entfaltung der Xylanase-Domäne. Die absteigende Krafthierarchie beweist darüber hinaus, dass es sich um abhängige Ereignisse handeln muss. Bei etwa einem Drittel der Entfaltungsereignisse ist nach der Entfaltung der Xylanase nur ein einzelnes abschließendes Dissoziationsereignis zu beobachten. Die Dissoziationskräfte sind hierbei geringfügig niedriger als bei dem doppelten Ereignis. Weitere 7 % der Kurven weisen ein zusätzliches Ereignis bei hohen Kräften auf, das dem Entfalten der CBM-Domäne entspricht.

Man kann also eine Krafthierachie in der Entfaltung feststellen. Die enzymatischen Domänen entfalten als erstes. Enzyme weisen häufig eine hohe Flexibilität auf, um sich optimal an ihre Substrate anpassen zu können. Für verschiedene Xylanasen wurden aktivitätsabhängige Konformationsänderungen berichtet [186-191]. Es erscheint also logisch, dass sie die niedrigste mechanische Stabilität aufweisen. Für eine vollständige Betrachtung der Zusammenhänge muss allerdings beachtet werden, dass die in diesen Kraftspektroskopieexperimenten durchgeführte Belastung der Xylanase vermutlich keinen physiologischen Bedingungen entspricht, da sich der Kraftangriffspunkt an einer gut zugänglichen Loop-Region befindet, deren Affinität zum Substrat nicht bekannt ist. Darüber hinaus ist zu bemerken, dass die Grundstabilität der Xylanase im Vergleich zu den im vorangehenden Kapitel diskutierten kraftaktivierten Proteinkinasen relativ hoch ist.

Die Schnittstelle zwischen Cohesin und Dockerin weist ebenfalls eine außergewöhnlich hohe Stabilität für Rezeptor-Ligand-Systeme dieser Größenordnung auf, was sich mit ihrer extrem hohen Affinität deckt. Die Entfaltungskräfte >100 pN liegen deutlich über den bislang in dieser Gruppe vermessenen Wechselwirkungskräften von Proteinen [192-196]. Lediglich die Biotin-Streptavidin-Bindung weist ähnliche Stabilitäten auf [91, 100, 197].

Den stabilsten Teil des Cellulosoms bilden die intramolekularen Faltungen der Proteindomänen des Scaffoldin. Da im Rahmen dieser Experimente CBM-Entfaltungen nur selten beobachtet werden konnten, stellt die Wechselwirkungsstärke der Typ I Cohesin-Dockerin-Bindung ein unteres Limit für ihre Entfaltung dar. Ferner haben Valbuena et al. in Kraftspektroskopieexperimenten mit vergleichbaren Ladungsraten wahrscheinlichste Entfaltungskräfte für Cohesin-Domänen zwischen 200 und 500 pN gemessen [63].

Als weiterer interessanter Effekt konnte in den Kraftspektroskopieexperimenten zur Cohesin-Dockerin-Wechselwirkung ein kraftinduziertes Dissoziieren der im Dockerin gebundenen Calciumionen nachgewiesen werden. Dies wird in Abbildung 36a verdeutlicht. Dissoziiert man in einem Puffer, der statt Calcium 2 mM des Kationenfängers EDTA enthält, wiederholt Cohesin-Dockerin-Bindungen mit demselben Dockerin, kann man im Gegensatz zur

Situation unter Bedingungen mit Calcium binnen kürzester Zeit keine Wechselwirkung mehr feststellen. Untersucht man mit demselben Cohesin verschiedene Dockerine, sind auch ohne Calcium im Puffer identische Wechselwirkungskräfte mit einer nur geringfügig reduzierten Statistik messbar. Dies beweist, dass der Verlust der Calcium-Ionen nicht durch die EDTA-Moleküle selbst, sondern durch Kraft induziert wird.

Abbildung 36b zeigt die Ladungsratenabhängigkeit der Wechselwirkungskräfte der mit der Cohesin-Dockerin-Bindung verbundenen Entfaltungsereignisse. Die Abrisskräfte lassen sich durch zwei destabilisierende Cohesin-Punktmutationen deutlich reduzieren.

Die Natur der doppelten Ereignisse konnte mit den vorhandenen Proteinen noch nicht abschließend geklärt werden. Eine Lokalisation des Ereignisses in der Dockerin-Domäne ist sehr wahrscheinlich, da Entfaltungen der übrigen Proteindomänen unabhängig von diesem Ereignis gemessen wurden. Dockerine haben die untypische Eigenschaft, dass sie das Cohesin in zwei verschiedenen um 180° zueinander gedrehten Konfigurationen binden können [198]. Dies gibt der Cellulosomzusammensetzung einen größeren Konfigurationsraum und man vermutet, dass dadurch die Lignocellulosezersetzung effizienter vonstatten gehen kann [199]. Es ist wahrscheinlich, dass das Auftreten des doppelten Ereignisses und dessen Wahrscheinlichkeit auf die verschiedenen Bindungskonfigurationen zurückzuführen ist. Dieselbe Potentialweite in den Ladungsratenabhängigkeiten ist ein Indiz dafür, dass es sich bei den letzten Abrissereignissen in beiden Fällen um ein vergleichbares Ereignis handelt. Eine ausführlichere Diskussion findet sich in Manuskript M1.

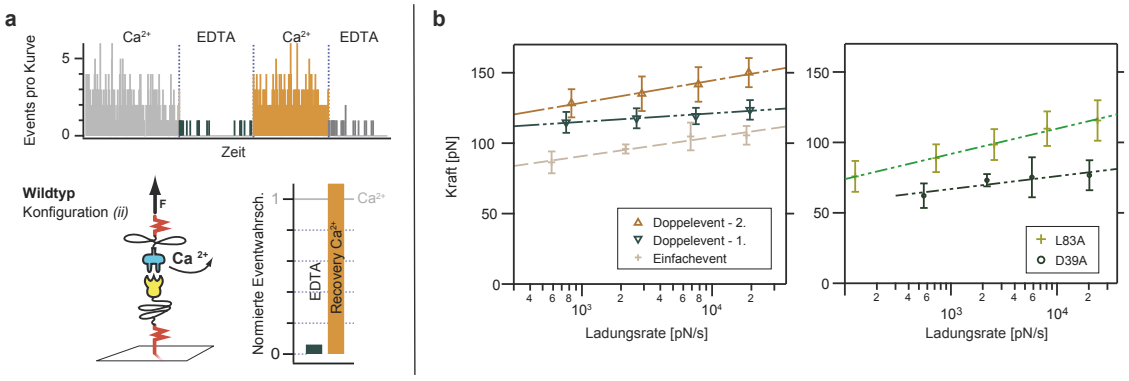

Abbildung 36 – Mechanische Stabilität der Cohesin-Dockerin Bindung
(a) Die im Dockerin gebundenen Calciumionen dissoziieren reversibel beim forcierten Entbinden des Cohesin-Dockerin Komplexes. Wenn Calcium im Puffer vorhanden ist, werden dauerhaft Interaktionen gemessen. Ersetzt man dieses durch den Ionenfänger EDTA, sinkt die Anzahl der Wechselwirkungen rapide. (b) Ladungsratenabhäniggkeit der einzelnen Entfaltungsevents. Durch destabilisierende Cohesinmutationen (L83A und D39A) können die Entfaltungskräfte deutlich herabgesetzt werden.

6.3 Nanoassemblierung von DNA und Proteinen

„Ich möchte nun zum Thema meines Vortrags übergehen und über einige Versuche berichten, die das Ziel haben, einfachste organisierte Systeme von Molekülen zu bauen, das heißt Anordnungen einzelner Moleküle, welche Eigenschaften haben, die durch die Besonderheit dieser Anordnung bedingt sind. Während die Moleküle schon in den einfachsten biologischen Strukturen in hoch organisierter Weise assoziiert sind, fehlt es dem Chemiker an Methoden, um Moleküle in vorausgeplanter Weise aneinanderzufügen. Er kann sehr komplizierte Moleküle synthetisieren, aber er kann nicht wie die Natur Aggregate von verschiedenen Molekülen in geplanter Ordnung bauen. Er sollte eine Pinzette haben, mit der er einzelne Moleküle herauszieht und sie in der geplanten Ordnung ABCD aneinanderfügt.“ [200] Mit diesen Worten begann der Chemiker Hans Kuhn 1965 seinen Vortrag bei den Verhandlungen der Schweizerischen Naturkundlichen Gesellschaft. Ferner schreibt er : „Man kann das ferne Ziel der Herstellung größerer organisierter Assoziate von Molekülen in zwei Aspekten sehen: Einerseits wird man bestrebt sein, einfache biologische Strukturen nachzuahmen; andererseits wird man sich bemühen, ganz unabhängig vom Vorbild der Natur irgendwelche der Phantasie entspringende Anordnungen von Molekülen herzustellen, die nützliche, von der genauen Anordnung der Moleküle im Aggregat abhängige Eigenschaften haben und die somit Werkzeuge mit molekulardimensionierten Bauelementen darstellen.“

Treffender kann man die Zielsetzung und Vorgehensweise der *Single-Molecule Cut-and-Paste* Technik [79] kaum formulieren. Die von ihm noch rein hypothetisch als wünschenswert bezeichnete Möglichkeit, einzelne Moleküle zu transportieren, um ein System mit grundlegend neuen Eigenschaften zu schaffen, wurde erstmals Anfang der neunziger Jahre mithilfe von Rastersondentechniken im Ultrahochvakuum erreicht [201-204]. Das von Don Eigler und Erhard Schweizer aus 35 Xenonatomen konstruierte IBM Logo wird als Geburtsstunde der molekularen Mechanosynthese betrachtet [205]. Mit den sogenannten „Quantum Corrals“ konnten sie darüber hinaus Strukturen erschaffen, deren Elektronen eine Wellenfunktion mit neuartigen, auf der Relativpositionierung beruhenden Eigenschaften haben [206]. Die Umsetzung einer derartigen Technik unter biokompatiblen Bedingungen stellte eine Hürde dar, die auf Einzelmolekülebene durch die im Kapitel 3.2 beschriebene *Single-Molecule Cut-and-Paste Technik* überwunden wurde. Im Rahmen dieser Arbeit wurden diverse Anwendungsgebiete der SMCP-Technik erschlossen sowie deren Präzision charakterisiert.

Einzelne Moleküle isoliert von Ihrer Umgebung zu beobachten hat den entscheidenden Vorteil, dass der Einfluss weiterer Moleküle zum Messsignal reduziert wird und ein minimalistisches System immer bessere Möglichkeiten bietet, den relevanten Parametersatz

zu verstehen. Neben der abstandsabhängigen Untersuchung der Interaktion verschiedener Moleküle und der Möglichkeit der funktionalen Assemblierung hat die SMCP-Technik einen weiteren großen Vorteil: Mit ihr kann eine Brücke zwischen den um Größenordnungen verschiedenen Oberflächenanbindungsdichten geschaffen werden, die für kombinierte Fluoreszenz- und Kraftspektroskopiemessungen benötigt werden. Konventionelle fluoreszenzspektroskopische Einzelmolekülmessungen benötigen Oberflächenanbindungsdichten der Größenordnung <1/µm^2. Mit einem AFM kann man unter diesen Bedingungen keine effiziente Kontaktierung der Moleküle bewerkstelligen, da die Wechselwirkungsfläche der AFM-Spitze in der Größenordung von 100 nm^2 ist. Man würde im Mittel nur alle 10.000 Kraftkurven eine Interaktion erwarten. Die SMCP-Technik umgeht diese Problematik elegant, weil sie in der Depot-Region hohe Funktionalisierungsdichten erlaubt. In der Zielregion hingegen sind fluoreszenzmikroskopische Einzelmolekülmessungen möglich. Somit gewährleistet SMCP kombinierte Kraftspektroskopie- und Fluoreszenzmessungen mit hoher Effizienz.

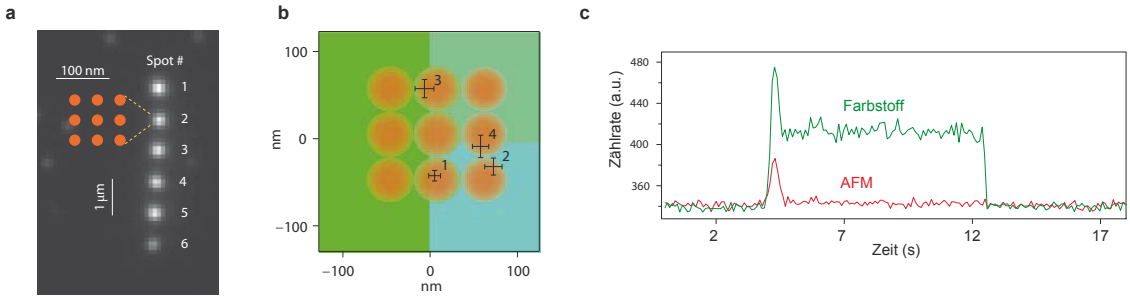

Abbildung 37 – Untersuchungen zur Genauigkeit des SMCP-Prozesses
(a) Mithilfe der SMCP-Technik wurde ein Muster bestehend aus mehreren, 3x3 Punkte enthaltenden Mustern mit 50 nm Punktabstand geschrieben. (b) Die Positonen der Farbstoffe eines jeden Musters wurden durch schrittweises Photobleichen ermittelt. Daraus ergibt sich die Präzision der Single-Molecule Cut-and-Paste Technik in der gegebenen Konfiguration zu ±11 nm. (c) Detektion eines einzelnen Absetzprozesses. Auf dem roten Detektionskanal sieht man inelastisch an der Cantileverspitze gestreutes Licht, wenn diese ins evaneszente Feld eindringt. Der grüne Detektionskanal zeigt sowohl Streuung an der Spitze als auch das Signal des abgesetzen Fluorophors. Da nur ein Bleichschritt vorhanden ist, weiß man, dass man ein einzelnes Molekül abgesetzt hat. Adaptiert von [P1].

Genauigkeit des Transportprozesses

Um das Potential von SMCP als Technik für die gerichtete Assemblierung nanoskaliger Objekte ergründen zu können, muss neben der in der grundlegenden Publikation [79] unter Beweis gestellten Robustheit bei hohen Wiederholraten auch die Präzision der Transportprozesse untersucht werden. Da die laterale Präzision des Rasterkraftmikrokops weit über der durch die Auflösungsgrenze limitierten und zur Detektion verwendeten Fluoreszenzmikroskopie liegt, muss man unter Bedingungen arbeiten, die hochauflösende Mikroskopie erlauben (vergleiche Kapitel 4.2). Zunächst ist es wichtig, festzustellen, dass man tatsächlich einzelne Moleküle transportiert. Dies kann durch Betrachten der Bleichkurven fluoreszenzmarkierter Transport-DNA beim Absetzprozess verifiziert werden.

Weisen diese nach Entfernen des Cantilevers von der Oberfläche ein Signal auf, das in einem einzelnen Bleichschritt verschwindet, kann man sicher sein, ein einzelnes Molekül transportiert zu haben. Über schrittweises Photobleichen kann darüber hinaus auch die Position mehrerer Moleküle in einem beugungslimitiertem Bereich der Oberfläche bestimmt werden. Obwohl sich diese zunächst überlagern, können sie zeitlich durch ihre einzelnen Bleichschritte getrennt werden. Durch Anfitten der Fluoreszenzsignale mit Gaußfunktionen und Subtraktion noch nicht gebleichter Komponenten konnte der Positionierungsfehler beim Schreiben von 3x3-Punkte-Mustern mit 50 nm Punktabstand ermittelt werden. Die Positionierungsgenauigkeit beträgt ±11 nm, was sich mit einem einfachen Modell der Längenfluktuationen der DNA und der zur Kopplung und Passivierung verwendeten Polyethylenglycolmoleküle (PEG) deckt. Durch Reduzieren der Länge der PEG-Moleküle sollte sich die Genauigkeit weiter verbessern lassen. Details zu den durchgeführten Experimenten finden sich in Publikation P1.

Positionierung von Nichtnukleotiden

Die ursprüngliche Realisierung der SMCP-Technik verwendet zum Aufbau des hierarchischen Kraftsystems verschiedene Zuggeometrien und Bindungsstärken von DNA. Die Technik ist aber nicht auf die Positionierung von Nukleotiden beschränkt, sondern ermöglicht es auch, weitere nanoskalige Objekte damit zu positionieren.

Dazu bieten sich zwei grundlegende Möglichkeiten an. Zum einen kann man zunächst mithilfe von SMCP ein Grundgerüst aus DNA-Molekülen schreiben, das spezifische Bindungsstellen für die Kopplung weiterer Bausteine aufweist. Zum anderen kann man das hierarchische Kraftsystem auch ganz oder teilweise durch nicht auf DNA-Hybridisierung basierende Wechselwirkungen aufbauen. Beide Ansätze wurden im Rahmen dieser Arbeit erfolgreich für die relative Positionierung von molekularen Bausteinen verfolgt.

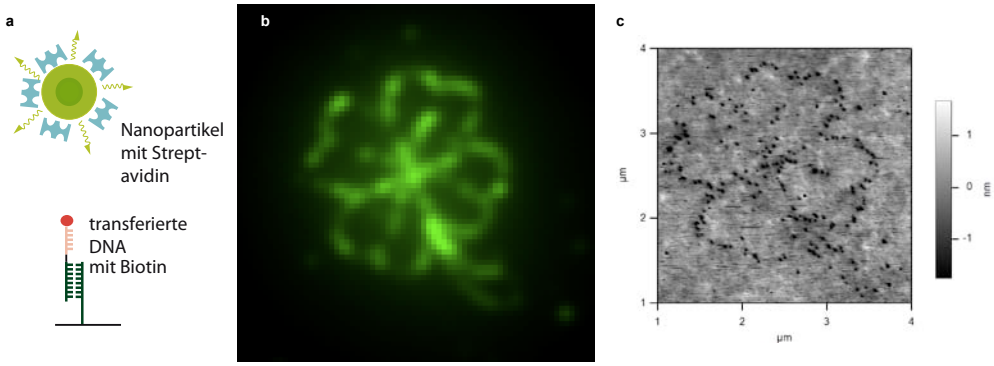

Abbildung 38 – Assemblierung durch spezifische Kopplung
(a) Unter Verwendung der SMCP-Technik wurden biotinylierte Transferstränge an definierten Stellen in der Zielregion deponiert. In einem „*Pull-down*"-Ansatz können so mit Streptavidin funktionalisierte Halbleiter-Nanopartikel durch spezifische Bindung zu den Biotinen positioniert werden. (b) Fluoreszenzmikroskopieaufnahme nach erfolgter Kopplung der Nanopartikel. (c) Topographisches AFM-Bild. Mit photothermischer Anregung (vgl. Kapitel 4.4) lassen sich auch auf dem weichen PEG-Film Nanopartikel erkennen. Durch laterale Kräfte während des Scans wurden manche Nanopartikel verschoben.

Möchte man den Transferstrang mit einer weiteren Bindungsstelle für die nachträgliche Kopplung molekularer Bausteine verwenden, so sollte diese eine hohe Spezifizität aufweisen. Darüber hinaus sollte der mit der DNA verknüpfte Ligand nicht zu groß sein, um kein sterisches Hindernis beim Transport darzustellen. Biotin erfüllt beide Eigenschaften und wurde für einen gerichteten Selbstassemblierungsprozess mit den Transfer-DNA-Strängen verbunden. Als Modellsystem wurden mit Streptavidin gekoppelte Halbleiter-Nanokristalle nach dem Erstellen eines SMCP-Musters in geringer Konzentration zur Pufferlösung gegeben. Es konnte beobachtet werden, wie sich diese mit hoher Spezifizität an die zur Verfügung gestellten Bindungsstellen anlagern. Details finden sich in Abbildung 38 und Publikation P1.

Die Möglichkeiten des eben vorgestellten Ansatzes, molekulare Bausteine im Nachhinein zu koppeln sind vielfältig, aber dennoch nicht komplett universell. Wenn man beispielsweise verschiedene Konstituenten mittels SMCP relativ zueinander positionieren möchte, braucht man verschiedene zueinander orthogonale Bindungsstellen. Diese müssen wie eben erwähnt hoch spezifisch und klein sein. Darüber hinaus lagert sich auch immer ein Teil der Bausteine an willkürlichen Positionen unspezifisch an der Oberfläche an.

Deshalb ist es häufig sinnvoll, die Moleküle direkt zu transportieren. Neben DNA machen Proteine einen Großteil der mit Einzelmolekülmikroskopietechniken untersuchten Biomoleküle aus. Es ist folglich also wünschenswert, das SMCP-System für den gerichteten Proteintransport zu modifizieren.

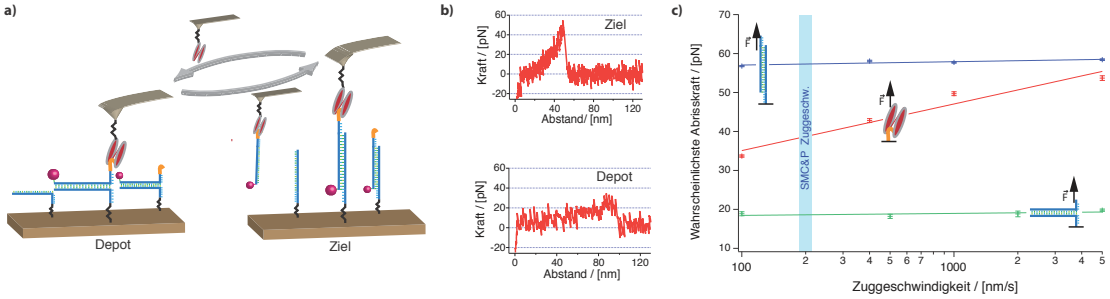

Abbildung 39 – SMCP mit Hilfe eines Peptid-Ankers
(a) Schematik des Transportsystems. Am Cantilever ist ein scFv-Antikörperfragment gekoppelt dessen Epitop ein mit der Transport-DNA verknüpftes Peptidstück ist. Sind die Dissoziationskräfte korrekt eingestellt, erlaubt das System den Transport von Molekülen. (b) Repräsentative Kraftkurven in der Depot- und Zielregion. (c) Zuggeschwindigkeitsabhängigkeit der wahrscheinlichsten Abrisskräfte der Bindungen im System. Durch Wahl einer geeigneten Geschwindigkeit lässt sich das System optimieren. Adaptiert von [P7].

In einem ersten Ansatz wurde dabei die Wechselwirkung mit dem Cantilever durch eine spezifische Antikörper-Peptid Wechselwirkung ersetzt (siehe Abbildung 39). Die Peptidsequenz kann dann mit dem zu transportierenden Protein co-exprimiert werden und dient als molekularer Anker. Am Cantilever wird lediglich die DNA-Sequenz durch ein spezifisch gekoppeltes Antikörperfragment (scFv-Fragment, vergleiche Kapitel 3.1) mit

geeigneter Bindungsstärke ersetzt. Das System wurde erfolgreich durch den Transport von fluoreszenzmarkierten DNA-Peptid Chimären getestet. Experimentelle Zusammenhänge finden sich in Publikation P7.

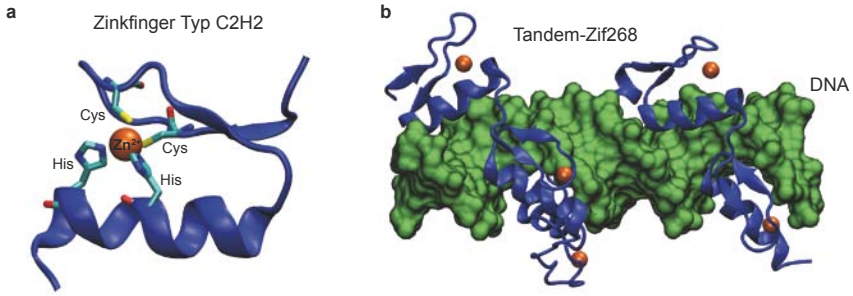

Abbildung 40 – Zinkfinger-DNA Wechselwirkung
(a) Bei Zinkfingern vom Typ C2H2 wird das Zinkion über zwei Cystein- und zwei Histidin-seitenketten koordinativ gebunden. (b) Die Wechselwirkung mit der großen Furche der DNA ist sequenzspezifisch und erfolgt primär über die α-Helix der Zinkfingermotive. Dargestellt ist ein Tandem-Zinkfinger, der aus insgesamt 6 Zinkfingermotiven besteht (PDB 1P47).

Für den Transport von Proteinen müssen weiterhin geeignete Depot- und Zielwechselwirkungen vorhanden sein. Sie dürfen nur sehr niedrige off-Raten aufweisen, da sonst keine dauerhafte Assemblierung möglich ist beziehungsweise Hintergrund durch sich in der Depot-Region ablösende Moleküle entsteht, die wiederum in der Lage sind spezifisch an willkürlichen Positionen in der Ziel-Region zu binden. Da sich die DNA-Wechselwirkung im Zipper- und Schermodus gut bewährt hat, liegt es nahe, auf dieser aufzubauen. Zinkfinger sind Proteine, die sequenzspezifisch mit hoher Affinität an doppelsträngige DNA binden (Abbildung 40). Exprimiert man also das zu transportierende Protein sowohl mit dem Peptid-Anker als auch mit einer oder mehrerer Zinkfinger-Domänen, kann man ein Transportsystem für funktionellen Proteintransport auf SMCP-Basis schaffen. Eine Schematik findet sich in Abbildung 41. Die erfolgreiche Umsetzung wird in Manuskript M1 beschrieben.

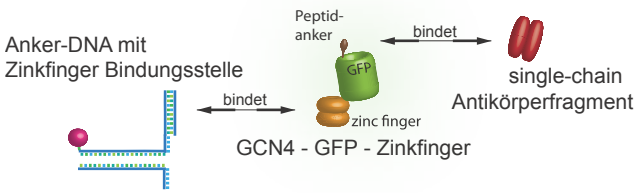

Abbildung 41 – SMCP für den gerichteten Proteintransport
Das zu transportierende Protein (hier GFP als Modellsystem) wird mit der GCN4-Peptidsequenz und Zinkfingermotiven co-exprimiert. Diese binden an ein doppelsträngiges DNA-Stück, das an einem einzelsträngigen Überhang sowohl in der Depot- als auch in der Zielregion binden kann. Von Cantileverseite wird das Konstrukt mit dem in Publikation P7 beschriebenen scFv-Fragment kontaktiert.

Funktionelle Assemblierung

Neben dem Transport einzelner, funktionaler Einheiten besteht eine weitere Zielsetzung der Single-Molecule Cut-and-Paste Technik darin, durch den Transport Systeme mit Eigenschaften zu erzeugen, die die der einzelnen Bausteine übersteigen. Also darin, erst durch den molekularen Zusammenbau und die Ausrichtung von Objekten Funktionalität zu erschaffen. Beispiele, in denen sich die Natur derartiger Methoden bedient, sind das in Kapitel 6.2 beschreibene Cellulosom, der Pyruvatdehydrogenase-Komplex [207] oder aber das Photosytem von Pflanzenzellen [208]. Der experimentelle Nachweis funktioneller Assemblierung mittels SMCP findet sich in Publikation 0. Als Modellsystem wurde eine RNA-Aptamerstruktur gewählt, die den fluorogenen Farbstoff Malachitgrün bindet [209]. Seine Struktur besteht aus drei Phenylringen, die in Lösung frei rotieren können [210]. Die Rotation ermöglicht die Relaxation angeregter Zustände über nichtfluoreszente Prozesse und verhindert so eine effiziente Fluoreszenz durch eine niedrige Quantenausbeute. Lagert sich der Farbstoff allerdings an einer Bindungsstelle an, wird die Rotation unterbunden und das Molekül beginnt zu fluoreszieren. Mittels SMCP wurde nun die RNA-Aptamerstruktur aus zwei Hälften zusammengesetzt. Da Malachitgrün nicht an die einzelnen Aptamerhälften bindet, wird an der Oberfläche spezifisch dort Fluoreszenz erzeugt, wo ein Aptamer positioniert wurde[6].

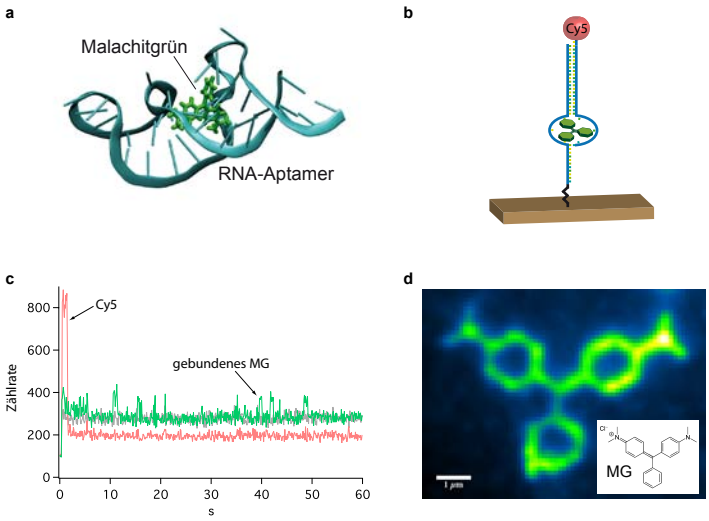

Abbildung 42 – Funktionelle Assemblierung von Aptamer-Bindungstaschen für Malachitgrün (MG)
(a) MG-Aptamer (PDB 1Q8N). (b) Mit SMCP wird das Aptamer in der Zielregion aus zwei Teilen zusammengesetzt. (c) Über das Bleichen des am Transportstrang vorhandenen Fluorophors kann ein erfolgreicher Transport verifiziert werden. Die danach auftauchenden Blinkereignisse sind auf Binden von Malachitgrünmolekülen zurückzuführen. (b) SMCP-Muster der Malachitgrün-Strukturformel. Beobachtet wird die Fluoreszenzverstärkung der im Aptamer gebundenen MG-Moleküle. Adaptiert von [0].

[6] Malachitgrün lagert sich auch gerne an Stellen mit nicht vollständiger Passivierung an, was einen unerwünschten Hintergrund in den Fluoreszenzmessungen bedeuten kann. Möglichkeiten diesen effizient zu umgehen finden sich in der Doktorarbeit meines Kollegen Mathias Strackharn.

SMCP als Validierungsstandard in der hochauflösenden Mikroskopie

Ein auf den ersten Blick vielleicht nicht offensichtliches Anwendungsgebiet der SMCP-Technik findet sich in der Verwendung als Validierungsstandard für hochauflösende Mikroskopietechniken. Mittels SMCP kann man Muster von Fluorophoren mit definierten Abständen erzeugen. Dies ist extrem hilfreich, wenn man die Parameter hochauflösender Mikroskopiemethoden optimieren oder ganz allgemein die Auflösungsgrenze der verwendeten Technik studieren möchte. In einem Kollaborationsprojekt mit der Arbeitsgruppe um Prof. Philip Tinnefeld wurden SMCP-Muster erzeugt, die die Abhängigkeit des Auflösungsvermögen von deren BLINK-Mikroskopietechnik [132] von den gewählten Umgebungsparametern charakterisieren konnten. Details zur Durchführung und Technik finden sich in Publikation P4.

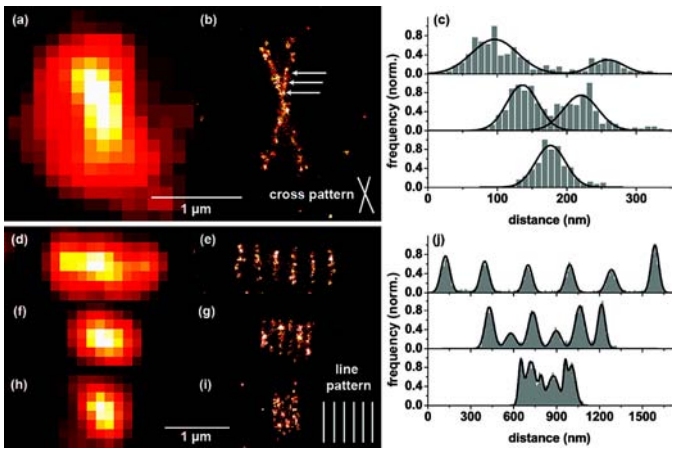

Abbildung 43 – SMCP Muster zur Kalibrierung hochauflösender Mikroskopietechniken Linke Spalte - Die Aufnahmen mit TIRF-Mikroskopie können die SMCP-Muster nicht auflösen. Mitte - Unter Verwendung der BLINKM-Technik sind Positionsbestimmungen der einzelnen Fluorophore möglich. Rechts – Histogramme der x-Positionen.
Nachdruck mit Genehmigung von NanoLetters [P4]. Copyright (2009) American Chemical Society.

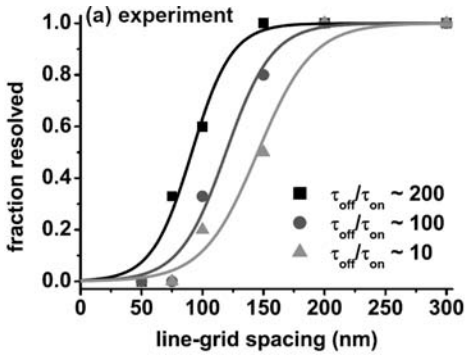

Abbildung 44 – Optimierung der Auflösbarkeit durch Variation der chemischen Umgebung Durch Einstellung der Konzentration an Oxidations- und Reduktionsmitteln in der Lösung können die Blinkcharakteristiken der Fluorophore variiert werden. Mithilfe reproduzierbarer SMCP-Muster als Validierungsstandart sind Optimierungen möglich.
Nachdruck mit Genehmigung von NanoLetters [P4]. Copyright (2009) American Chemical Society.

7 AUSBLICK

Die in dieser Arbeit untersuchten Zusammenhänge zur mechanischen Stabilität und Konnektivität molekularer Domänen bieten diverse Anknüpfungspunkte für zukünftige Experimente. So bietet es sich beispielsweise an, die gewonnen Erkenntnisse zur molekularen Architektur des Kraftsensors Titinkinase auch auf weitere Enzyme anzuwenden und zu überprüfen, ob diese ähnlichen Funktionsprinzipien unterliegen.

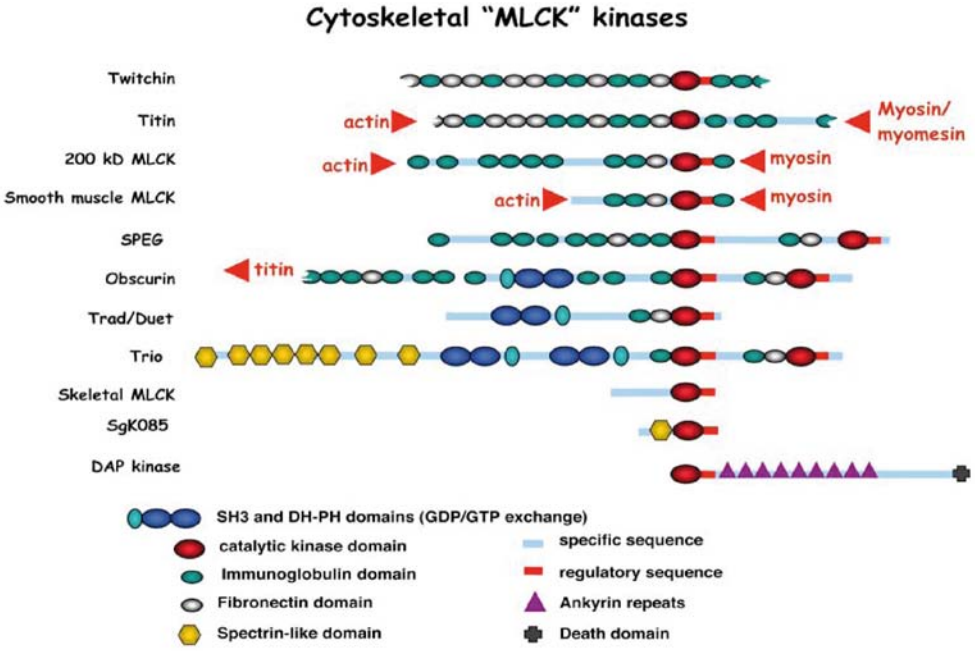

Abbildung 45 – MLCK-ähnliche Kinasen des Zytoskellets
Neben Titinkinase und MLCK existieren artverwandte Kinasen in weiteren strukturellen Proteinen des Zytoskellets, die in ihrer natürlichen Umgebung Kräften ausgesetzt sind. Die Grafik wurde freundlicherweise von Mathias Gautel zur Verfügung gestellt.

Abbildung 45 zeigt eine Reihe von MLCK-ähnlichen Kinasen, von denen erwartet wird, dass sie in ihrer biomolekularen Umgebung ebenfalls Kräften ausgesetzt sind. Es liegt also nahe, diese ebenfalls auf Konnektivitäten in ihrer molekularen Architektur zu untersuchen und darüber hinaus festzustellen, ob die Bindung von Liganden oder die Phosphorylierung von Substraten auch bei ihnen durch Kraft induziert wird. Dies ist zum einen von grundlegendem wissenschaftlichem Interesse, kann aber auch von Bedeutung für die Medizin sein. Sowohl am Beispiel der Titinkinase [77] als auch der Myosin-Light-Chain-Kinase [211] wird deutlich, dass Mutationen in den Enzymen durch Unterbrechungen in den Signalwegen zu schwerwiegenden und teilweise tödlich verlaufenden Krankheiten führen. Untersuchungen zum veränderten Stabilitätsverhalten können hierbei wichtige Einblicke zur Ursache der Fehlfunktionen im molekularem Detail liefern.

Dabei ist es wünschenswert, Liganden nicht nur indirekt durch Änderungen in der kraftspektroskopischen Signatur zu detektieren. Fluoreszenzmarkierte Substrate und FRET-Messungen bieten hierfür vielversprechende Ansätze. Da die hierfür benötigten Substratkonzentrationen im Allgemeinen zu hoch für konventionelle Fluoreszenzmikroskopietechniken wie TIRF sind, müssen für simultane Einzelmolekülmessungen neuartige Ansätze mit verringertem Anregungsvolumen verwendet werden. Die im Kapitel 4.2 erwähnten *Zero-Mode-Waveguides* erfüllen diese Anforderung. Erste Versuche in unserer Gruppe, diese Fluoreszenzmikroskopietechnik mit AFM-basierter Kraftspektroskopie zu verbinden, zeigen, dass wir nach dem erfolgreichen Überwinden experimenteller Hürden inzwischen in der Lage sind, Daten in ausreichend hoher Statistik zu liefern. Der Ansatz, in den Waveguides auftretende Randeffekte durch zentrale Platzierung von Molekülen mit der Single-Molecule Cut-and-Paste Technik zu vermeiden, ist ebenfalls vielversprechend.

Weitere Anwendungsgebiete der SMCP-Technik finden sich in der gezielten Erzeugung definierter Enzymnetzwerke. Durch Kontrolle der Abstände von Enzymen sowie der Diffusionseigenschaften ihrer Substrate, die in einem Netzwerk interagieren, lässt sich mit SMCP ein Ansatz synthetischer Einzelmolekülbiologie verfolgen. Mit diesem lassen sich natürlich auftretende Interaktionen nachstellen und kontrolliert untersuchen oder aber auch neuartige artifizielle Systeme erstellen. Die in dieser Arbeit demonstrierte erfolgreiche Umsetzung des Transports von Proteinen unter Aufrechterhaltung ihrer funktionellen Konformation legt den Grundstein für diese neue Untersuchungs- und Manipulationsmethode.

Kraftspektroskopische Untersuchungen des Cellulosoms sowie SMCP-basierte Experimente mit deren enzymatischen Einheiten bieten ebenfalls ein weitreichendes Potential. Zunächst ist es interessant, neben der im Rahmen dieser Arbeit untersuchten Typ I Cohesin-Dockerin-Wechselwirkung von Clostridium Thermocellum auch die mechanische Stabilität der Typ II Interaktion zu verstehen. Sie verknüpft das Scaffoldin mit dem Organismus und ist durch Quervernetzung von Bakterium und Cellulose hohen Kräften ausgesetzt. Darüber hinaus kann eine detaillierte Untersuchung des beobachteten doppelten Entfaltungsereignisses essentielle Information zur Natur des doppelten Bindungsmodus der Cohesin-Dockerin Interaktion liefern. Von diesem wird vermutet, dass er dem Enyzmkomplex durch Vergrößerung des Konfigurationsraums eine erhöhte Effizienz verleiht [199]. Wenn beide Ereignisse miteinander zusammenhängen, sollte dies durch Dockerin-Mutationen nachweisbar sein, die eine der beiden Bindungskonfigurationen ganz oder teilweise ausschließen [212]. In diesem Kontext ist ferner interessant festzustellen, ob eines der Ereignisse mit dem beobachteten kraftinduziertem Dissoziieren von Calcium-Ionen aus der Dockerin-Domäne in Verbindung gebracht werden kann.

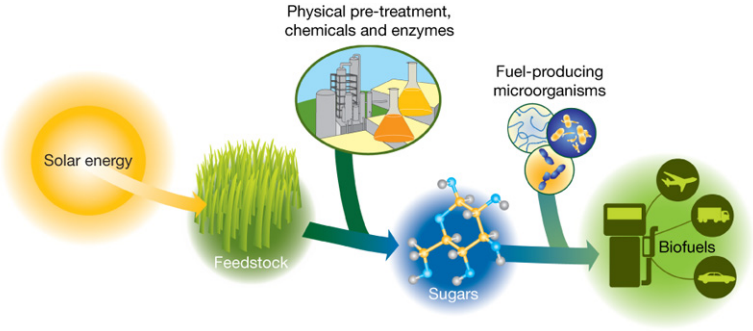

Abbildung 46 – Synthese von Biotreibstoffen
Solarenergie wird durch Photosynthese in Form von Lignocellulose gespeichert. Diese wird durch physikalische und chemische Vorprozesse sowie enzymatische Reaktionen in einfache 5- und 6-Ring-Zucker gespalten. Die Einfachzucker können anschließend von Mikroorganismen zu Treibstoffen verarbeitet werden.
Nachdruck mit Genehmigung von Macmillan Publishers Ltd: Nature [182], Copyright (2008)

Wie bereits eingangs erwähnt wurde, sucht die Industrie derzeit mit großem Nachdruck nach Möglichkeiten, lignocellulosehaltige Biomasse effizient zu Biotreibstoffen der zweiten Generation zu verarbeiten. Das Nadelöhr ist hierbei noch der Aufschluss der Lignocellulose, der derzeit nur unter hohem Kosten- und Energieaufwand vonstatten gehen kann [184]. Cellulosome sind in der Natur vorkommende Systeme, die diese Arbeit verrichten. Eine Kultivierung von cellulosomhaltigen Bakterien oder Pilzen für industrielle Zwecke ist bislang noch nicht effizient genug. In großen Mengen synthetisch exprimierte Cellulosom-Enzyme werden als aussichtsreicher Kandidat gehandelt um das Problem langsam wachsender und relativ langsam arbeitender natürlicher Organismen zu umgehen. Man versucht mit sogenannten Designer-Cellulosomen [213-215] Enzyme verschiedener Spezies effizient miteinander zu kombinieren. Da die Ordnung der einzelnen Enzyme relevant ist, muss derzeit für jede Kombination mit gentechnischen Methoden der Molekularbiologie ein neues Grundgerüst erzeugt werden. Dies ist ein relativ langwieriges und kompliziertes Verfahren. Die SMCP-Technik hingegen ist in der Lage verschiedenste Konstellationen einzelner Proteine in kurzer Zeit zu erzeugen. Deshalb wird ein weiterer Anwendungsfokus darin liegen, enzymatisch aktive Cellulosom-Komplexe auf Oberflächen zu erzeugen (Abbildung 47). Ist so eine effizient arbeitende Kombination gefunden, kann man versuchen, diese großindustriell zu erzeugen, um Lignocellulose zu verarbeiten.

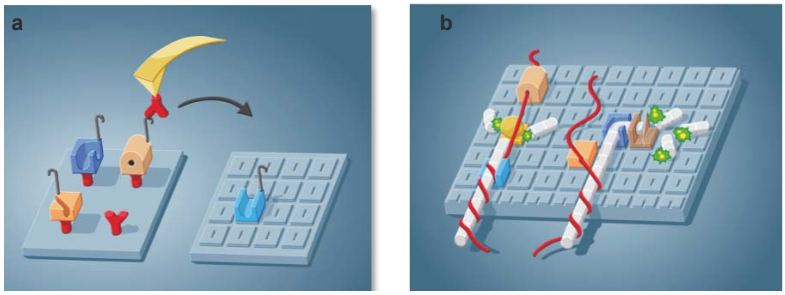

Abbildung 47 – Projekt: Funktionales Single-Molecule Cut-and-Paste mit Enzymen des Cellulosoms
(a) Auf der Oberfläche exprimierte Cellulosomenzyme werden mit der SMCP-Technik relativ zueinander angeordnet. (b) Mithilfe eines geeigneten Fluoreszenztests wird die Aktiviät der verschiedenen Geometrien untersucht.

Im Rahmen dieser Arbeit wurde mit dem photothermischen Effekt ein um eine Größenordnung schnelleres Force-Clamp-Feedback realisiert, als dies bislang möglich war. Ein experimenteller Nachteil der vorgestellten Methode liegt darin, dass in der derzeitigen Realisierung zwei Cantilever aufeinander justiert werden müssen. Dadurch steht zum einen nur eine begrenzte Fläche für die Funktionalisierung zur Verfügung und zum anderen muss darauf geachtet werden, dass kein Übersprechen des Anregungssignals auf den Detektionskanal auftritt. Eine technische Erweiterung, die dies umgeht, besteht darin, denselben Cantilever als Aktuator und Sensor zu verwenden. Dies setzt allerdings eine detaillierte Charakterisierung der Dynamik des photothermischen Effekts für den jeweils verwendeten Cantilever voraus. Da diese zum Beispiel stark vom Einstrahlort des Anregungslasers und dessen Fokussierung abhängt, muss dies anhand eines definierten Protokolls vor jedem Experiment überprüft werden. Variiert man diese aber nicht, kann man prinzipiell nach der Charakterisierung Kraftbeiträge vom Protein von solchen, die durch den photothermischen Effekt hervorgerufen werden, trennen und somit schnelle Regelkreise auch mit konventionellen AFMs umsetzen, die nur einen Cantilever besitzen. Ein Ansatz, der in diese Richtung zielt, wurde von Crampton et al. verfolgt [216]. Sie verwendeten die für eine konstante Cantileverauslenkung benötigte photothermische Leistung als Maß für die von den Proteinen aufgebrachte Kraft und konnten so die sonst vorhandenen „Totzeiten“ nach einem Abrissereignis vermeiden.

8 ANHANG

8.1 Publikationen

P1 NANOPARTICLE SELF-ASSEMBLY ON A DNA-SCAFFOLD WRITTEN BY SINGLE-MOLECULE CUT-AND-PASTE

Puchner EM, Kufer SK, Strackharn M, Stahl SW and Gaub HE.

NANO LETTERS 2008 Nov; 8(11):3692-5

NANO LETTERS

Subscriber access provided by UNIV MUNICH

Letter

Nanoparticle Self-Assembly on a DNA-Scaffold Written by Single-Molecule Cut-and-Paste

Elias M. Puchner, Stefan K. Kufer, Mathias Strackharn, Stefan W. Stahl, and Hermann E. Gaub

Nano Lett., **2008**, 8 (11), 3692-3695• DOI: 10.1021/nl8018627 • Publication Date (Web): 01 October 2008

Downloaded from http://pubs.acs.org on April 2, 2009

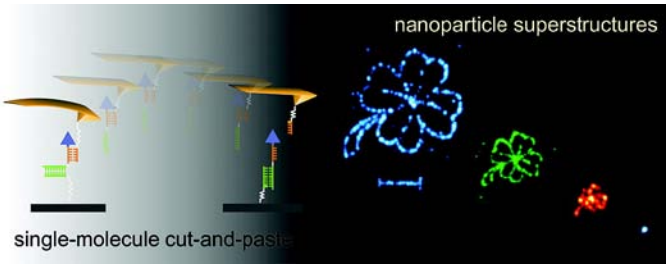

More About This Article

Additional resources and features associated with this article are available within the HTML version:

- Supporting Information
- Access to high resolution figures
- Links to articles and content related to this article
- Copyright permission to reproduce figures and/or text from this article

View the Full Text HTML

ACS Publications
High quality. High impact.

Nano Letters is published by the American Chemical Society. 1155 Sixteenth Street N.W., Washington, DC 20036

NANO LETTERS

2008
Vol. 8, No. 11
3692-3695

Nanoparticle Self-Assembly on a DNA-Scaffold Written by Single-Molecule Cut-and-Paste

Elias M. Puchner,[†,‡] Stefan K. Kufer,[†] Mathias Strackharn,[†] Stefan W. Stahl,[†] and Hermann E. Gaub*[,†]

Chair for Applied Physics, Center for Nanoscience and Center for Integrated Protein Science Munich, Ludwig-Maximilians-Universität Munich, Amalienstrasse 54, 80799 Munich

Received June 27, 2008; Revised Manuscript Received September 16, 2008

ABSTRACT

Self-assembly guided by molecular recognition has in the past been employed to assemble nanoparticle superstructures like hypercrystals or nanoparticle molecules. An alternative approach, the direct molecule-by-molecule assembly of nanoscale superstructures, was demonstrated recently. Here we present a hybrid approach where we first assemble a pattern of binding sites one-by-one at a surface and then allow different nanoparticles to attach by self-assembly. For this approach, biotin bearing DNA oligomers were picked up from a depot using a cDNA strand bound to an AFM tip. These units were deposited in the target area by hybridization, forming a recognition pattern on this surface. Fluorescent semiconductor nanoparticles conjugated with streptavidin were allowed to assemble on this scaffold and to form the final nanoparticle superstructures.

Two fundamentally different strategies, commonly referred to as top-down or bottom-up, are feasible for the assembly of functional nanosystems. The bottom-up approach has two extremes. In the first, the building blocks are allowed to self-assemble, for example, guided by molecular recognition, much in the way mother nature does in embryogenesis.[1−7] Alternatively, the building blocks are assembled one-by-one, for example, using the tip of a scanning probe microscope, as we have demonstrated recently.[8,9] With the single-molecule cut-and-paste (SMCP) approach, we combine the precision of an AFM[10−12] with the selectivity of the DNA interaction. The units to be assembled, here biotin, are picked up with an AFM tip from a depot, where both the interaction of the unit with the depot surface as well as with the tip are mediated by specific DNA oligomers. Also the target area is covered with DNA oligomers. The interaction forces are chosen by binding geometry and by sequence such that the unit is first transferred from the depot to the tip and then from the tip to the target, allowing for a cyclic operation and thus the assembly of complex patterns of units. In this study, we have merged these two very successful strategies of self- and one-by-one assembly. We combined molecule-by-molecule assembly of patterns of binding sites with the self-assembly of nanoparticles[13] guided by specific molecular interactions to the scaffold.

* To whom the correspondence should be addressed. Email: gaub@lmu.de.
† Chair for Applied Physics, Munich.
‡ Center for Integrated Protein Science, Munich.

10.1021/nl8018627 CCC: $40.75 © 2008 American Chemical Society
Published on Web 10/01/2008

The surface assembly process of the binding scaffold is schematically depicted in Figure 1. Both depot and target areas were functionalized with DNA anchor oligomers capable of hybridizing with the so-called transfer DNA via a 30 basepair (bp) DNA sequence. In the depot area, the anchor oligomers are covalently attached with the 5′ end and in the target area with the 3′ end. The depot area was then loaded with the transfer DNA, which is used as a carrier for the binding site for the nanoparticles, in this case biotin. The transfer DNA is designed such that it hybridizes at its 5′ end with the anchor sequence and has a 20 bp overhang at the 3′ end. An AFM cantilever was covalently functionalized with a 20 bp DNA oligomer complementary to the overhang sequence. This cantilever was carefully lowered toward the depot surface allowing the tip oligomer to hybridize with the transfer DNA. This approach had been either stopped upon surface contact or alternatively, proximity had been detected by increased viscous damping of the tip vibrations. Typical force extension traces of this contact and noncontact pick up are shown in the Supporting Information (Figure S4).

Upon withdrawing the tip from the surface, the force that is built up in the molecular complex propagates through the two oligomers with the different geometries. Whereas the anchor duplex is loaded in unzip geometry, the tip duplex is loaded in shear geometry. As has been shown, the unbinding forces for these two configurations under load differ signifi-

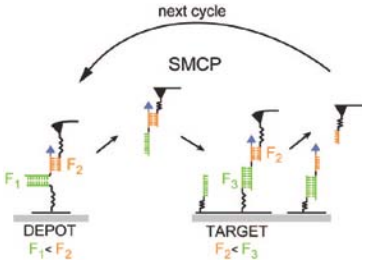

Figure 1. Schematics of the SMCP process. The transfer DNA oligomers carry biotin as the functional binding site (blue). They are stored in the depot area through specific DNA hybridization (30 bp, green) to the covalently immobilized depot anchor oligomer in the zipper geometry. The overhanging sequence of the transfer DNA is complementary to a 20 bp sequence, which is covalently attached to a tip of an AFM cantilever. When the cantilever is brought into contact with the surface, a 20 bp duplex (yellow) in shear geometry is formed. Although the binding energy of the transfer DNA to the depot is higher, the unbinding force F_1 is lower than the unbinding force F_2 between the tip and the transfer DNA due to the different unbinding geometries (zipper vs shear). Therefore, the transfer DNA remains on the tip sequence upon retraction of the cantilever. The tip is then moved to the target area with nm-precision and again brought into contact with the surface. Here the free part of the transfer DNA hybridizes to the 30 bp target sequence in shear mode. Since its rupture force F_3 is the highest, the transfer DNA including its functional unit biotin remains on the target site when removing the cantilever. Having transferred one functional unit in this way, the tip sequence is free again for the next cut-and-paste cycle.

cantly.[14,15] The rationale behind this effect is that the mechanical work to overcome the binding energy is performed over paths of different length, resulting in different forces. Despite the higher thermodynamic stability of the 30 bp anchor duplex compared to the 20 bp tip duplex, the rupture probability for the anchor is higher by an order of magnitude than that of the tip duplex. For a quantitative analysis see ref 16. As a result, the transfer DNA with the functional unit biotin is now bound to the tip and may be transferred to the target area.

At the target site the tip is lowered again, allowing the transfer DNA to hybridize at the chosen position with an anchor oligomer. Now, due to the different attachment, both duplexes are loaded in shear geometry when the tip is withdrawn. The longer anchor oligomer keeps the transfer DNA bound, and the tip is free again and ready to pick up the next object. The efficiency of the cut-and-paste process depends both on the density of DNA oligomers and the tip size. It can be adjusted so that rarely more than one oligomer per cycle is picked up.[8] As a consequence of this low functionalization density no pick up occurs in the majority of the attempts. In this study, we have chosen a tip radius of about 20 nm (MLCT lever C, Veeco Instruments GmbH, Mannheim, Germany) and a high functionalization density so that in each cycle at least one molecule, and in most cases more than one molecule, was picked up and delivered. For a detailed description of this ordered system of unbinding forces and the experimental setup see the Supporting Information (Figure S2).

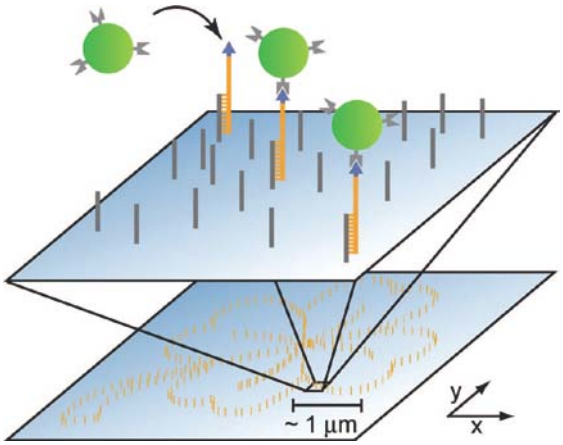

Figure 2. Sketch of the self-assembly of nanoparticles to a defined pattern guided by molecular recognition. SMCP allows the creation of DNA scaffolds of arbitrary shape and size. Here, a 5 μm sized pattern with the shape of a cloverleaf was created by transferring the biotin-modified transfer DNAs one-by-one to the target area. The spacing of binding sites was chosen to be 100 nm. In a second step this DNA scaffold allows for the self-assembly of streptavidin conjugated nanoparticles to form a superstructure.

All transfer steps are monitored online by force extension traces, which have clearly distinguishable fingerprints for each of the unzip or shear processes (see Supporting Information). If needed, each of the individual steps may be corrected or repeated. It should be pointed out here that this hierarchy of binding forces, which is the basis of this single-molecule cut-and-paste surface assembly (SMCP), may be established by a variety of interactions of physical, chemical, or biological nature. We chose DNA here since its properties are conveniently programmed by their sequence and binding geometry. It should also be mentioned that although the AFM potentially has sub-Angström positioning precision, the use of the polymeric spacers that we employ for the attachment of the DNA oligomers to the tip and the surface reduces this precision to the 10 nm range, which for our purposes is easily tolerable.

Following this protocol we now assembled a pattern of attachment points at the target site. We placed biotins 100 nm apart from each other along the outline of a cloverleaf. This is schematically shown in Figure 2. We then incubated the sample with a 500 pM solution of fluorescent nanoparticles (Qdots, streptavidin conjugate starter kit, Invitrogen, California) carrying an average of seven streptavidins, which recognize and selectively bind to biotin.[17] Although some spots of the written pattern may consist of more than one biotin because of the chosen high cut-and-paste efficiency, binding of more than one nanoparticle is unlikely because of their large size (about 20 nm) and their low concentration. We followed the binding process online by fluorescence microscopy in TIRF excitation. As can be seen in the picture series in Figure 3, the nanoparticles gradually assembled on the scaffold and finally decorated the outline of the cloverleaf. We encourage the reader to watch the movie of this nanoparticle attachment to the DNA scaffold published in

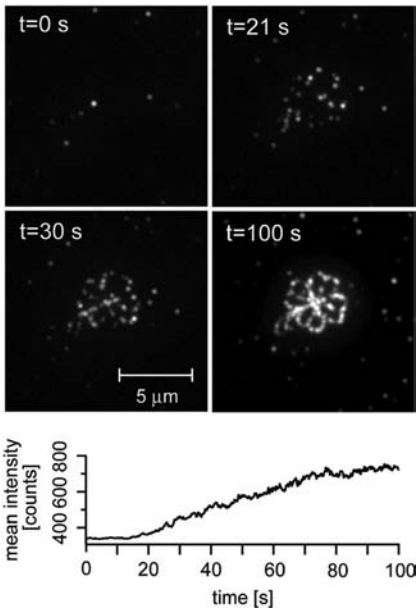

Figure 3. Time evolution of the nanoparticle superstructure formation. At time $t = 0$, streptavidin conjugated nanoparticles were incubated on the sample at a concentration of 500 pM. After approximately 20 s, the particles are close to the surface and start to specifically bind to the biotin-DNA scaffold until saturation is reached. The binding kinetics was followed by plotting the mean intensity of the observed area against the time (bottom). After 100 s the formation was completed.

the Supporting Information, as it demonstrates this process in a much clearer way.

This self-assembly process on the predefined scaffold is completed within minutes. Because of the specific binding between biotin and streptavidin and the low concentration of only 500 pM of the nanoparticles, nonspecific adhesion was negligible as can be seen in Figure 3. It is interesting to note that not all of the positions light up, although our transfer protocols corroborate that a biotin was deposited at these optical voids. A comparison of AFM images (not shown here) with the fluorescence images demonstrated that nanoparticles had bound at these positions. Obviously those nanoparticles had been optically inactive, a phenomenon that has been frequently described in the literature.[18,19]

For demonstration purposes, we rewrote the pattern in different sizes and allowed different nanoparticles to assemble on them (see Figure 4). Again a sizable fraction of the nanoparticles was optically inactive. In the assembly of the red pattern, thermal drift caused a slight distortion of the pattern, but even the scale bar could be trustfully assembled. Since for this study we always used the biotin−streptavidin interaction as the coupler, only single component structures were assembled. However, since a multitude of couplers with orthogonal affinities is available, the assembly of multicomponent structures would be straightforward.[20−23]

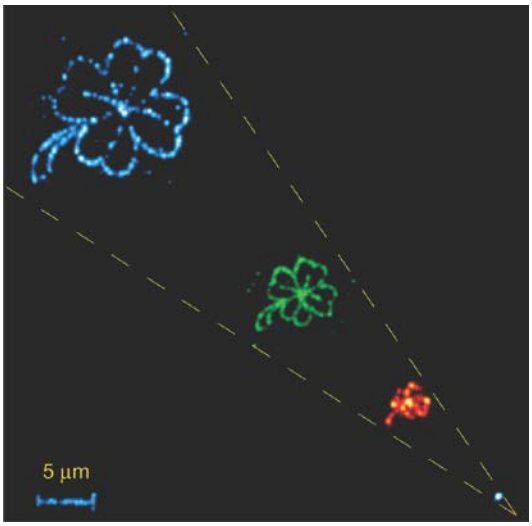

Figure 4. Nanoparticle superstructures of different sizes and compounds. To show the possibility to create freely programmable architectures from different compounds, the superstructure was scaled down and built with nanoparticles of different size. For the first cloverleaf (10 μm, blue), we used nanoparticles emitting at a wavelength of 525 nm, for the second one (5 μm, green) particles emitting at 565 nm, and for the third one (2.5 μm, red), already close to the limit of optical resolution, particles emitting at a wavelength of 705 nm. Please note that the 5 μm scalebar also represents a nanoparticle superstructure. The images are standard deviation maps of the recorded movies.

Nanoparticle self-assembly guided by specific molecular interactions has in the past been very successfully used to design complex structures with novel functions promising a rich field of new applications.[24−29] Here we have expanded this concept by a written scaffold and demonstrated that molecule-by-molecule assembly of a binding pattern combined with the self-assembly of semiconductor nanoparticles guided by molecular interactions is a straightforward and very general means to create nanoparticle superstructures.[30] Whereas the assembly of planar nanoparticle structures of arbitrary design can easily be assembled this way, an expansion into the third dimension appears challenging but achievable. Covalent cross-linking of the DNA oligomers after hybridization can be employed to stabilize the scaffold, and multifunctionality of the nanoparticles attachment sites may be used to build subsequent layers of structures. This could lead to a new dimension of complexity and novel effects.

Acknowledgment. We thank A. Fornof, H. Gumpp, H. Clausen-Schaumann, W. Parak, and P. Tinnefeld for helpful discussions. This work was supported by the German Science Foundation, FUNS, and the Nanosystems Initiative Munich (NIM).

Note Added after ASAP Publication: This paper was published ASAP on October 1, 2008. Author affiliations and Acknowledgment were updated. The revised paper was reposted on October 8, 2008.

Supporting Information Available: This material is available free of charge via the Internet at http://pubs.acs.org.

References

(1) Park, S. Y.; Lytton-Jean, A. K. R.; Lee, B.; Weigand, S.; Schatz, G. C.; Mirkin, C. A. *Nature* **2008**, *451* (7178), 553–556.
(2) Shevchenko, E. V.; Ringler, M.; Schwemer, A.; Talapin, D. V.; Klar, T. A.; Rogach, A. L.; Feldmann, J.; Alivisatos, A. P. *J. Am. Chem. Soc.* **2008**, *130* (11), 3274.
(3) Nykypanchuk, D.; Maye, M. M.; van der Lelie, D.; Gang, O. *Nature* **2008**, *451* (7178), 549–552.
(4) Mirkin, C. A.; Letsinger, R. L.; Mucic, R. C.; Storhoff, J. J. *Nature* **1996**, *382* (6592), 607–609.
(5) Alivisatos, A. P.; Johnsson, K. P.; Peng, X. G.; Wilson, T. E.; Loweth, C. J.; Bruchez, M. P.; Schultz, P. G. *Nature* **1996**, *382* (6592), 609–611.
(6) Maye, M. M.; Nykypanchuk, D.; van der Lelie, D.; Gang, O. *Small* **2007**, *3* (10), 1678–1682.
(7) Mirkin, C. A. *Inorg. Chem.* **2000**, *39* (11), 2258–2272.
(8) Kufer, S. K.; Puchner, E. M.; Gumpp, H.; Liedl, T.; Gaub, H. E. *Science* **2008**, *319* (5863), 594–596.
(9) Duwez, A. S.; Cuenot, S.; Jerome, C.; Gabriel, S.; Jerome, R.; Rapino, S.; Zerbetto, F. *Nat. Nanotechnol.* **2006**, *1* (2), 122–125.
(10) Binnig, G.; Quate, C. F.; Gerber, C. *Phys. Rev. Lett.* **1986**, *56* (9), 930–933.
(11) Radmacher, M.; Fritz, M.; Hansma, H. G.; Hansma, P. K. *Science* **1994**, *265* (5178), 1577–1579.
(12) Radmacher, M.; Tillmann, R. W.; Fritz, M.; Gaub, H. E. *Science* **1992**, *257* (5078), 1900–1905.
(13) Steigerwald, M. L.; Alivisatos, A. P.; Gibson, J. M.; Harris, T. D.; Kortan, R.; Muller, A. J.; Thayer, A. M.; Duncan, T. M.; Douglass, D. C.; Brus, L. E. *J. Am. Chem. Soc.* **1988**, *110* (10), 3046–3050.
(14) Rief, M.; Clausen-Schaumann, H.; Gaub, H. E. *Nat. Struct. Biol.* **1999**, *6* (4), 346–349.
(15) Strunz, T.; Oroszlan, K.; Schafer, R.; Guntherodt, H. J. *Proc. Natl. Acad. Sci. U.S.A.* **1999**, *96* (20), 11277–11282.
(16) Morfill, J.; Kuhner, F.; Blank, K.; Lugmaier, R. A.; Sedlmair, J.; Gaub, H. E. *Biophys. J.* **2007**, *93* (7), 2400–2409.
(17) Mann, S.; Shenton, W.; Li, M.; Connolly, S.; Fitzmaurice, D. *Adv. Mater.* **2000**, *12* (2), 147–150.
(18) Kuno, M.; Fromm, D. P.; Hamann, H. F.; Gallagher, A.; Nesbitt, D. J. *J. Chem. Phys.* **2000**, *112* (7), 3117–3120.
(19) Kuno, M.; Fromm, D. P.; Johnson, S. T.; Gallagher, A.; Nesbitt, D. J. *Phys. Rev. B* **2003**, *67* (12).
(20) Lacoste, T. D.; Michalet, X.; Pinaud, F.; Chemla, D. S.; Alivisatos, A. P.; Weiss, S. *Proc. Natl. Acad. Sci. U.S.A.* **2000**, *97* (17), 9461–9466.
(21) Gerion, D.; Parak, W. J.; Williams, S. C.; Zanchet, D.; Micheel, C. M.; Alivisatos, A. P. *J. Am. Chem. Soc.* **2002**, *124* (24), 7070–7074.
(22) Sperling, R. A.; Pellegrino, T.; Li, J. K.; Chang, W. H.; Parak, W. J. *Adv. Funct. Mater.* **2006**, *16* (7), 943–948.
(23) Levy, R.; Wang, Z. X.; Duchesne, L.; Doty, R. C.; Cooper, A. I.; Brust, M.; Fernig, D. G. *ChemBioChem* **2006**, *7* (4), 592–594.
(24) Bek, A.; Jansen, R.; Ringler, M.; Mayilo, S.; Klar, T. A.; Feldmann, J. *Nano Lett.* **2008**, *8* (2), 485–490.
(25) Clapp, A. R.; Medintz, I. L.; Uyeda, H. T.; Fisher, B. R.; Goldman, E. R.; Bawendi, M. G.; Mattoussi, H. *J. Am. Chem. Soc.* **2005**, *127* (51), 18212–18221.
(26) Huang, Y.; Duan, X. F.; Cui, Y.; Lauhon, L. J.; Kim, K. H.; Lieber, C. M. *Science* **2001**, *294* (5545), 1313–1317.
(27) Parak, W. J.; Gerion, D.; Pellegrino, T.; Zanchet, D.; Micheel, C.; Williams, S. C.; Boudreau, R.; Le Gros, M. A.; Larabell, C. A.; Alivisatos, A. P. *Nanotechnology* **2003**, *14* (7), R15–R27.
(28) Brennan, J. L.; Hatzakis, N. S.; Tshikhudo, T. R.; Dirvianskyte, N.; Razumas, V.; Patkar, S.; Vind, J.; Svendsen, A.; Nolte, R. J. M.; Rowan, A. E.; Brust, M. *Bioconjugate Chem.* **2006**, *17* (6), 1373–1375.
(29) Zhou, D.; Piper, J. D.; Abell, C.; Klenerman, D.; Kang, D. J.; Ying, L. *Chem. Commun. (Cambridge, U.K.)* **2005**, (38), 4807–9.
(30) Pellegrino, T.; Kudera, S.; Liedl, T.; Munoz Javier, A.; Manna, L.; Parak, W. J. *Small* **2005**, *1* (1), 48–63.

NL8018627

Supplementary Information

Nanoparticle Self-Assembly on a DNA-Scaffold written by Single-Molecule Cut-and-Paste

E.M. Puchner, S.K. Kufer, M. Strackharn, S. Stahl and H.E. Gaub*

Chair for Applied Physics, Center for Nanoscience and Center for Integrated Protein Science Munich,

Ludwig-Maximilians-Universität Munich,

Amalienstr. 54, 80799 Munich

*To whom correspondence should be addressed.
Email: gaub@lmu.de

Sample Preparation
Depot and target areas were prepared on a cover slip as described in [1]. Briefly, cover slips were amino functionalized and covalently modified with NHS-PEG-maleimide (M = 5000 g/mol, Nektar, Huntsville, Alabama, USA). After rinsing with H_2O, a PDMS flow chamber with two channels was mounted on one cover slip. Both channels were connected to a peristaltic pump. The anchor oligomers for the depot and target area were reduced using TCEP solution (Pierce, Rockford, Illinois, USA) in order to generate free mercaptans. The left channel (depot area) was rinsed for 1 h with a 10 µM solution of depot anchor oligomers and the right one (target area) with a 10 µM solution of target anchor oligomers. Afterwards both channels were rinsed with H_2O to remove all non-covalently bound oligomers. The left channel (depot area) was rinsed with a 1 µM solution of transfer DNA dissolved in saline sodium citrate (SSC) buffer (150 mM NaCl, 15 mM sodium citrate, pH 7) for 1 h. All oligomers used in this study were synthesized from IBA (IBA GmbH, Göttingen, Germany) and of HPLC-grade. After rinsing the depot channel for 5 min with SSC buffer to remove all non-hybridized transfer DNA, the PDMS flow chamber was removed and the cover slip was dried in a nitrogen stream. Finally the cover slip was mounted to the AFM-TIRF sample holder and immersed in SSC buffer.

AFM Measurements
All SCMP experiments were performed with a custom build AFM [2] at room temperature in SSC buffer (Fig. S1). Silicon nitride cantilevers (MLCT-AUHW, Veeco Probes, Camarillo, California, USA) were amino functionalized and covalently modified with NHS-PEG-maleimide (M = 5000 g/mol, Nektar, Huntsville, Alabama, USA) as described in [1]. The spring constant of the DNA modified cantilever was calibrated in solution using the equipartition theorem [3,4]. This method yielded a spring constant of about 15 pN/nm and a resonance frequency of 1.24 kHz for the cantilevers used in this study. The tip was withdrawn from the surface at a speed of 1500 nm/s until it was 2 µm above the surface. The protocol for the SMCP as well as the data recording was programmed using Igor Pro 5.03 (Wave Metrics, Lake Oswego, Oregon, USA). An Asylum Research controller, which provides ADC and DAC channels as well as a DSP board, was used for setting up feedback loops. Cantilever positioning for pickup and delivery was controlled in closed-loop operation. The precision was set to ±4 nm.

Total Internal Reflection Fluorescence (TIRF) Microscope
Single-molecule fluorescence microscopy was carried out in TIRF excitation (Fig. S1). Fluorescence excitation of nanoparticles was performed by a 532 nm, 75 mW DPSS laser (Crystalaser, Nevada, USA) and by a 473nm, 100 mW DPSS laser (Laser Quantum, UK) through a 100x/1.49 oil immersion objective lens (Nikon CFI Apochromat TIRF, Japan), where the collimated laser beam is focused in the back focal plane of the objective lens such that the beam is totally reflected at the cover slip. Fluorescence light is either split by color with a commercial Dual View (Optical Insights, Arizona, USA) with Brightline HC 582/75 (Semrock, New York, USA) and ET 700/75 (Chroma, Vermont, USA) as emission filters for the green and red channel respectively and a dichroic mirror with a cut-off wavelength of 630 nm (630DCLP) when using 532 nm excitation or filtered by a emission filter HQ 525/50 (Chroma, Vermont, USA) when using 473 nm excitation wavelength. The emitted light is detected by a 512 x 512 pixel back-illuminated EMCCD camera (DU-897, Andor, Belfast, Ireland). Time series where recorded in frame-transfer mode with an integration time of 100 ms per frame. The EMCCD chip was typically operated at a temperature of -75°C and an electron multiplication gain of 300x was used. The magnification was 96, i.e. 125 nm are

imaged to one pixel.

The SMCP force system

The probe of an atomic force microscope (AFM) was used to assemble individual single stranded DNA (ssDNA) oligomers one by one in aqueous solutions at room temperature. The oligomers were stored on well-defined depot areas, picked up with the tip of an AFM cantilever and reassembled with nanometer precision on a spatial distinct target area. The storage, the pick up and the deposition of the DNA oligomers were realized by using an ordered system of unbinding forces based on DNA interactions.

The dissociation rates of DNA duplexes under load are highly dependent on loading geometries and DNA sequences [5,6]. The geometry, in which the DNA duplex is stretched at opposite 5' and 3' ends, is called "shear mode" [5] (Fig. S2e), whereas the arrangement when double strands are loaded by pulling on the 5' and 3' extremities of one end of the duplex is called "unzip mode" [7] (Fig. S2a). These two geometries are well distinguishable concerning their dissociation properties under load.

The rupture forces of DNA duplexes loaded in unzip mode are independent both of the length of the DNA sequence and the loading rate, but vary for G-C and A-T interactions. G-C pairing results in a dissociation force of 20 pN whereas A-T gives 10 pN [6]. The dissociation forces for DNA duplexes loaded in shear geometry depend both on the length and sequence of the DNA and the loading rate [5].

To store the transfer DNA in the depot, a 30 base pair (bp) long anchor sequence with mixed G-C and A-T is used (Fig. S2a). The transfer DNA has in addition to this 30 bp anchor sequence a 20 bp handle sequence for pick up. The AFM-tip is covalently modified with a DNA oligomer, which is complementary to the handle sequence and forms a duplex if tip approaches the depot area (Fig. S2b). If the tip is retracted from the depot, the anchor sequence is loaded in unzip mode whereas the handle sequence is loaded in shear mode. Although the 30 bp anchor sequence is longer than the 20 bp handle sequence, its unbinding probability under load is much higher than for the handle sequence so that the transfer DNA is picked up (Fig. S2c, Fig. 4).

After translocation of the transfer DNA to its target site the cantilever is moved down. Since the target area is covalently modified with DNA oligomers that are complementary to the anchor sequence a 30 bp duplex in shear geometry is formed (Fig S2d). As the dissociation force of duplexes in shear geometry depends on the length of the DNA sequence the shorter handle sequence ruptures first and the transfer DNA is attached to the target site (Fig. S2e, Fig. 4). The DNA sequences of the oligomers used in this study are shown in Fig. S3.

Hybridization of fluorescent nanoparticles to the DNA scaffold

For the hybridization to the DNA-biotin scaffold, the following fluorescent semiconductor nanoparticles were used:
Invitrogen, Germany, streptavidin conjugate, 1 μM solution, Qdot 525 (colored blue), Qdot 565 (colored green), and Qdot 705 (colored red). The nanoparticles were incubated on the written DNA-biotin pattern at a final concentration of 500 pM in 0.1x SSC buffer. After about one minute, the self assembly process of nanoparticles to the pattern was complete.

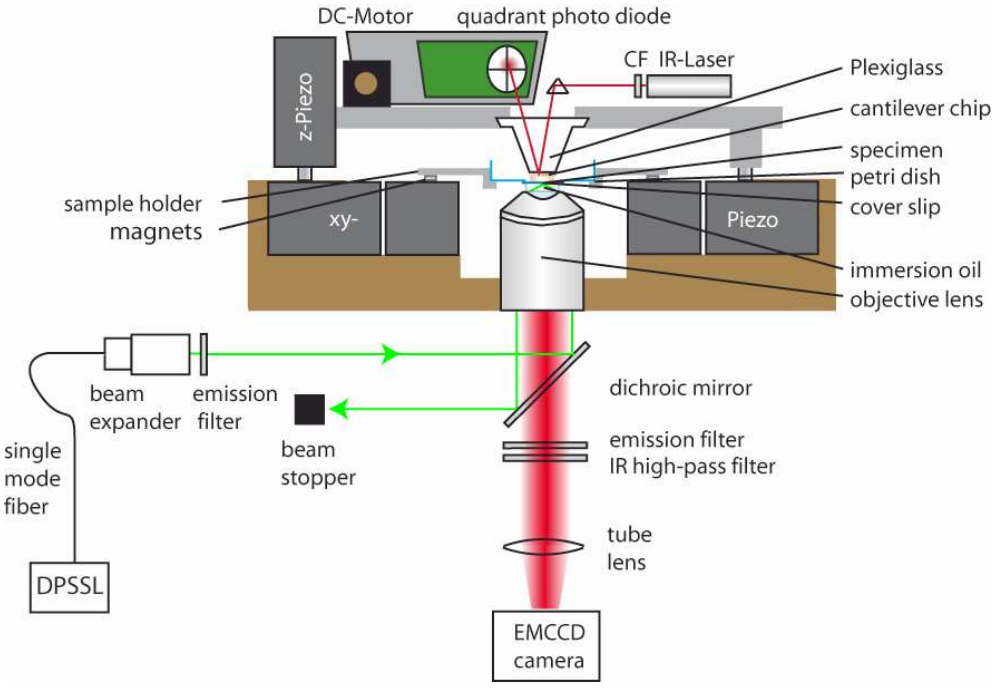

Fig. S1. Experimental setup. A custom built AFM, which is moveable in z direction via a piezo, is combined with an inverted microscope for objective-type TIRF excitation. The cover slip with the depot- and target areas on top is glued into a drilled petri dish. The petri dish is placed in a sample holder, which is fixed through magnets on x-y piezo scanner.

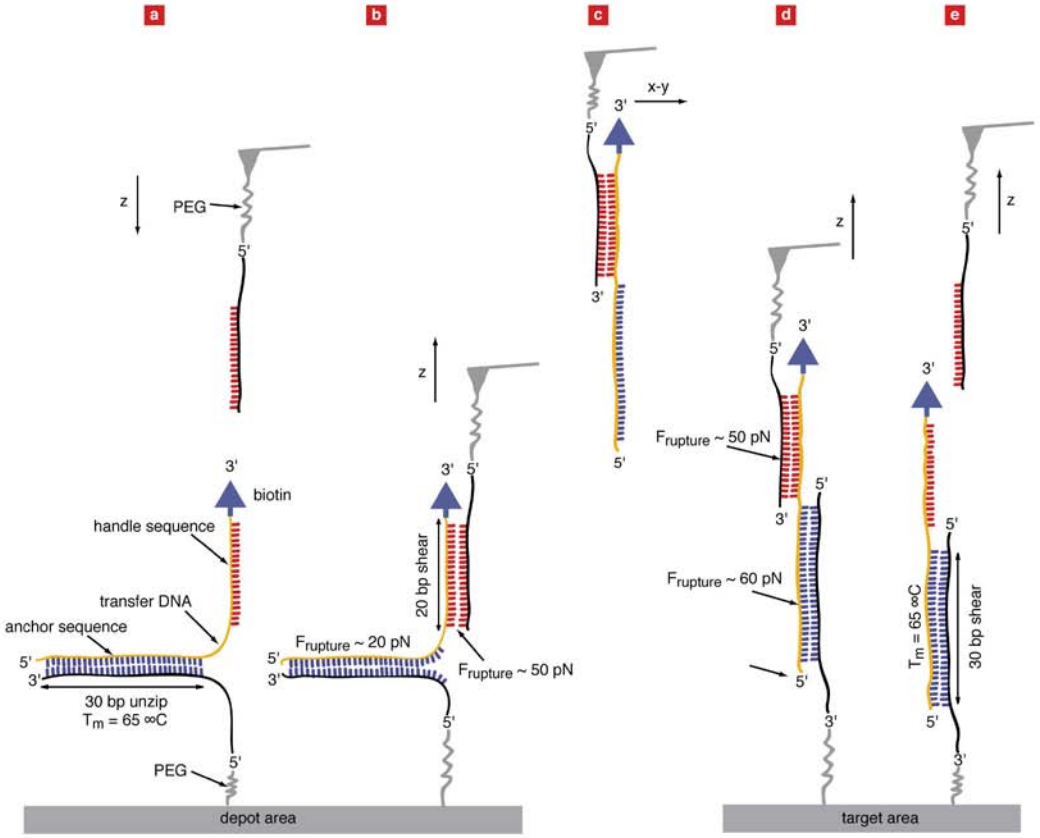

Fig. S2. Schematic illustration of the hierarchical force system. (a) To prevent unspecific adsorption, polyethylenglycol (PEG) molecules are covalently attached to the depot area. DNA oligomers, complementary to the anchor sequence of the transfer DNA, are covalently bound with their 5' end to these PEG molecules. Transfer DNA oligomers, which were modified with biotin labels at the 3' end, are hybridized to this anchor sequences. The tip of an AFM cantilever is also covalently modified with PEG molecules and a single DNA oligomer, which is complementary to the handle sequence of the transfer DNA. (b) When the tip is in contact with the surface a duplex between the transfer DNA and the cantilever DNA is formed. When the tip is retracted, the anchor sequence is loaded in unzip mode and the handle sequence in shear mode. As the unbinding probability for the anchor sequence is higher, the transfer DNA is picked up. (c and d) The target site is also covalently modified with PEG molecules. DNA oligomers, complementary to the anchor sequence of the transfer DNA, are bound with their 3' end to the PEG molecules. After translocation, the tip is moved down and a duplex is formed. When the tip is retracted, the handle and the anchor sequences are loaded in shear mode, but this time the shorter handle sequence ruptures first and the transfer DNA is attached to its target site. The tip is now in its initial state and the cycle can be repeated over and over again.

Fig. S3. Oligomers used in this study. The transfer DNA is 80 bp long and has a biotin label at its 3' end. The 30 bp long sequence on the 5' end is used to anchor the transfer DNA both to the depot and to the target site. The 20 bp long sequence on the 3' end is used as a handle for pick up. All oligomers were synthesized and purified (HPLC-grade) form IBA (IBA GmbH, Göttingen, Germany).

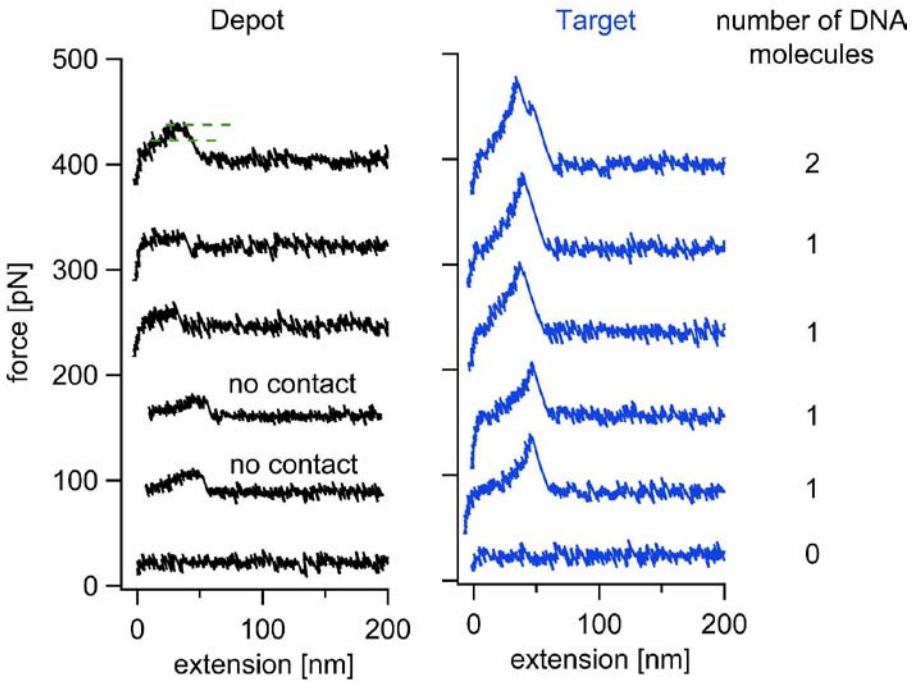

Fig. S4. Typical force extension traces of the depot and target region. In the depot region, the transfer DNA oligomer is separated from the depot oligomer in the zipper geometry. This separation process results in a force plateau of about 18 pN. As indicated, the transfer oligomers can also be picked up without contacting the surface. In the target region the transfer oligomer is separated from the tip oligomer in the shear geometry. Here, the force extension traces follows the elasticity of the PEG-spacer and the DNA until they are separated at forces of about 50 pN. For each cut-and-paste cycle, the number DNA oligomers which were picked up and delivered, can be counted. As an example we show traces where two, one and no DNA molecule was detected.

movie S5. Hybridization of nanoparticles to the DNA scaffold. (separate download)

References:

1. Kufer, S.K., Puchner, E.M., Gumpp, H., Liedl, T. & Gaub, H.E. Single-Molecule Cut-and-Paste Surface Assembly. Science 319, 594-596 (2008).

2. Kühner, F., Lugmaier, R., Mihatsch, S. & Gaub, H.E. Print your atomic force microscope. Rev. Sci. Instrum. 78 (2007).

3. Florin, E.L. et al. Sensing specific molecular interactions with the atomic force microscope. Biosensors and Bioelectronics 10, 895-901 (1995).

4. Butt, H.-J. & Jaschke, M. Calculation of thermal noise in atomic force microscopy. Nanotechnology 6, 1-7 (1995).

5. Strunz, T., Oroszlan, K., Schafer, R. & Guntherodt, H.J. Dynamic force spectroscopy of single DNA molecules. Proceedings of the National Academy of Sciences of the United States of America 96, 11277-11282 (1999).

6. Rief, M., Clausen-Schaumann, H. & Gaub, H.E. Sequence-dependent mechanics of single DNA molecules. Nat Struct Biol 6, 346-349 (1999).

7. Levinthal, C. & Crane, H.R. On the Unwinding of DNA. PNAS 42, 436-438 (1956).

4. Rubinstein, R.H.C. Polymer Physics. Oxford University Press (2005).

5. Oesterhelt, F., Rief, M. & Gaub, H.E. Single molecule force spectroscopy by AFM indicates helical structure of poly(ethylene-glycol) in water. New Journal of Physics 1 (1999).

6. Smith, S.B., Cui, Y.J. & Bustamante, C. Overstretching B-DNA: The elastic response of individual double-stranded and single-stranded DNA molecules. Science 271, 795-799 (1996).

P2 OPTICALLY MONITORING THE MECHANICAL ASSEMBLY OF SINGLE MOLECULES

Kufer SK, Strackharn M, Stahl SW, Gumpp H, Puchner EM and Gaub HE.

NATURE NANOTECHNOLOGY 2009 Jan;4(1):45-9.

nature nanotechnology

LETTERS

CORRECTED ONLINE: 8 DECEMBER 2008
PUBLISHED ONLINE: 23 NOVEMBER 2008 | DOI: 10.1038/NNANO.2008.333

Optically monitoring the mechanical assembly of single molecules

Stefan K. Kufer[1], Mathias Strackharn[1], Stefan W. Stahl[1], Hermann Gumpp[1], Elias M. Puchner[1,2] and Hermann E. Gaub[1]*

Bottom-up assembly at the level of individual molecules requires a combination of utmost spatial precision and efficient monitoring. We have previously shown how to 'cut-and-paste' single molecules[1], and other groups have demonstrated that it is possible to beat the diffraction limit in optical microscopy[2–4]. Here we show that a combination of single-molecule cut-and-paste surface assembly[1], total internal reflection fluorescence microscopy and atomic force microscopy[5–8] can be used to deposit individual fluorophores in well-defined nanoscale patterns and also to monitor the process in real time with nanometre precision. Although the size of the pattern is well below the optical resolution of the microscope, the individual dyes are identified by localizing the centroids and detecting the photobleaching of the fluorophores. With this combination of methods, individual dyes or labelled biomolecules can be arranged at will for specific functions, such as coupled fluorophore systems or tailored enzyme cascades, and monitored with nanoscale precision.

Objects smaller than the diffraction limit of an imaging system are projected as blurry spots with the size of a Rayleigh disc. However, the centre position of individual fluorophors can be determined with nanometre precision, and the precision is only limited by the number of photons collected from the object[9–12]. Multiple emitters within a diffraction-limited spot may also be localized if their individual contributions to the overall signal can be discriminated either spectrally or by other means. In recent years various techniques, subsumed under the expression super-resolution imaging (SRI), have been developed, which use different methods to extract one high-resolution image from a series of low-resolution images[13–19].

Impressive proof-of-principle experiments for SRI have been reported in the literature, where samples were designed with different fluorophores on defined positions[13,15,16,19]. Predominantly DNA duplexes with modified bases were used as molecular rulers for this purpose. We recently introduced a new means to assemble individual nanoscale functional units, which we term single-molecule cut-and-paste (SMCP). It combines the precision of atomic force microscopy (AFM) with the selectivity of DNA hybridization. Here, we have used this technique to assemble a two-dimensional pattern of individual fluorophores, which we then localized by SRI.

The SMCP system used here makes use of a transfer DNA with an anchor and a handle oligomer carrying a single Cy3 dye molecule. The anchor oligo provides a thermodynamically stable attachment of the transfer DNA in both the depot and the target area. The handle oligo allows pick up of the transfer DNA with the AFM tip and repositioning of the transfer DNA from the depot to the target. The binding geometry and overlap length of the oligomers were chosen such that this cut-and-paste process could be operated in cycles. (See Supplementary Information for details of the underlying hierarchical system of the unbinding forces.)

Figure 1 shows the step-by-step deposition of a single fluorophore that had previously been picked up from the depot area. When the tip is lowered towards the target site (Fig. 1a, black curve), the anchor oligomer hybridizes with a complementary strand. When the tip is withdrawn from the surface, both duplexes are loaded in shear mode, but the shorter handle duplex ruptures first, and the transfer system remains at the target site (Fig. 1b). As force–distance curves of both pick-up and deposition process are recorded, the process can be validated with these characteristic AFM fingerprints (Fig. 1a).

With microfluorescence only a very low background signal is detected when the tip is far away from the surface (Fig. 1c). When the tip penetrates the evanescence excitation field, a strong fluorescence signal from the dye molecule is detected in the green channel of the camera, while the tip is visible in both the red and the green detection channels[20]. When the tip is withdrawn, the signal from the tip vanishes, but the dye emits constantly until it bleaches in a single step. See Supplementary Information, Movie M1, for a detailed demonstration of this deposition event, and Movie M2 for an animation of the SMCP process. The intensity–time trace in Fig. 1d clearly shows the deposition of a single molecule. This bleaching step size in fluorescence intensity remains the same throughout a large number of experiments. Together with the clear signature in the single-molecule force scans during deposition it shows unambiguously that SMCP provides exquisite control of the deposition of individual fluorophores.

The position of this single molecule can now be located by fitting Gaussians to the intensity distribution. To evaluate the mechanical stability of our combined instrument, the fluorophore position of each frame was plotted in Fig. 2a. As can be seen from Fig. 2b,c no systematic drift of the molecule is observed and the standard deviation for the 100 ms localization was determined to be $\pm$13 nm. By summing all images, the signal-to-noise ratio could be improved drastically. This molecule, which remained active for more than 8 s, could thus be located with a precision better than $\pm$1.4 nm. This value is a benchmark for the accuracy with which we can determine the position of a single fluorophore.

Next, the spatial precision of the SMCP process was examined. As was pointed out by Smalley in his dispute with Drexler[21], 'complete' mechanical control over an assembly process at the single-molecule level is hardly possible because of two intrinsic fundamental limitations commonly referred to as the fat and sticky finger problem. SMCP makes use of this seeming limitation in that it uses the selective 'stickiness' between the DNA oligomers used for transfer and assembly. However, the spatial precision of the paste process is then limited by the size of the DNA oligomer, by the

[1]Centre for Nanoscience and Physics Department, University of Munich, Amalienstrasse 54, 80799 Munich, Germany, [2]Centre for Integrated Protein Science Munich, Butenandtstrasse 5 - 13, 81377 Munich, Germany; *e-mail: Gaub@LMU.de

© 2009 Macmillan Publishers Limited. All rights reserved.

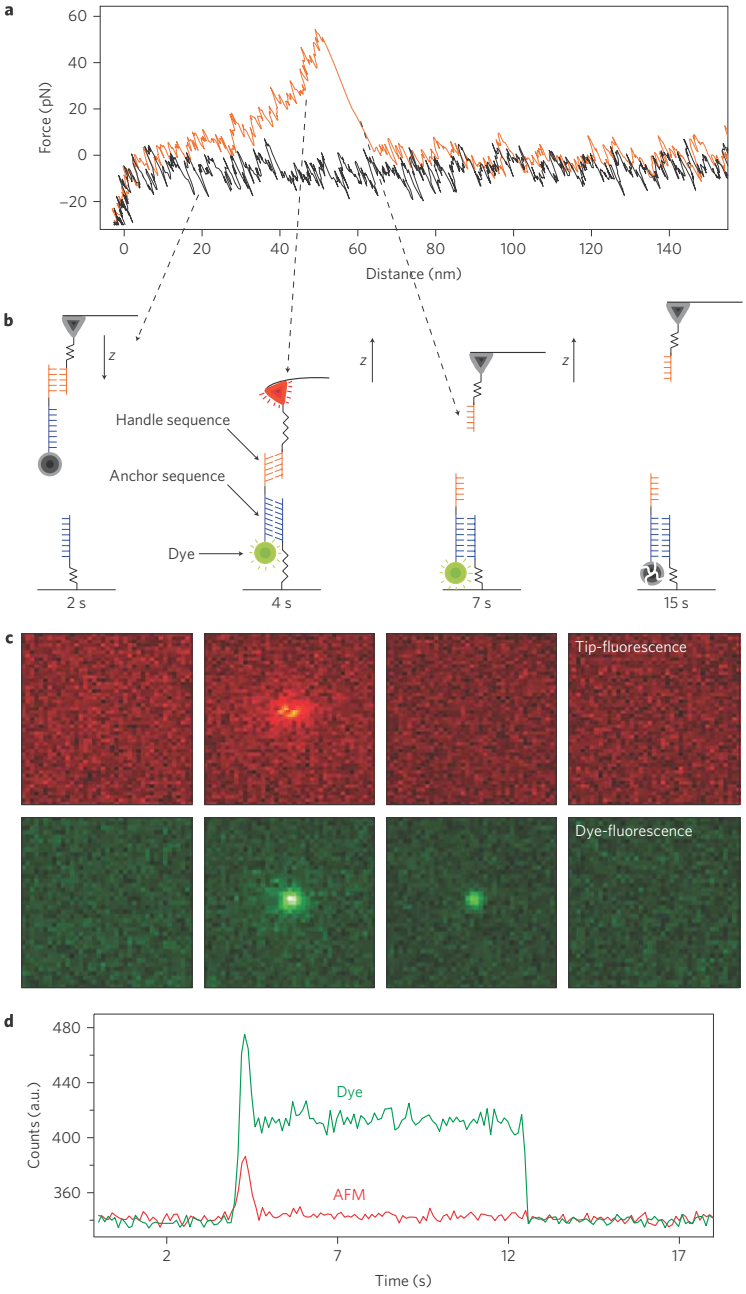

Figure 1 | Monitoring the deposition of a single molecule by AFM and TIRF microscopy. a, A typical force–distance curve of the deposition process. The tip is lowered until it contacts the surface (black curve) and a DNA duplex forms. As the tip retracts, the force increases gradually until the short handle sequence ruptures (red curve). **b**,**c**, As long as the tip is far away from the surface (**b**, 2 s), no fluorescence is detectable (**c**). When the tip penetrates the evanescent excitation field (**b**, 4 s), a strong signal is detected in both the red and green channels (**c**). When the cantilever retracts (**b**, 7 s), the fluorescence from the tip (red) vanishes but the transfer DNA (green) remains anchored and emits photons until it photobleaches (**c**). **d**, Intensity–time traces at the deposition site.

functionalization density of the target area, and by the rotational mobility of the polyethylene glycol (PEG)-spacers used for the covalent attachment of the oligomers to the surfaces. A sketch of this situation is provided in Fig. 3a.

Experimentally, the SMCP precision and the long-term stability of the setup were determined by successively depositing molecules at different positions on the target area. However, because in our setup only the sample is moved, the position of the deposited

© 2009 Macmillan Publishers Limited. All rights reserved.

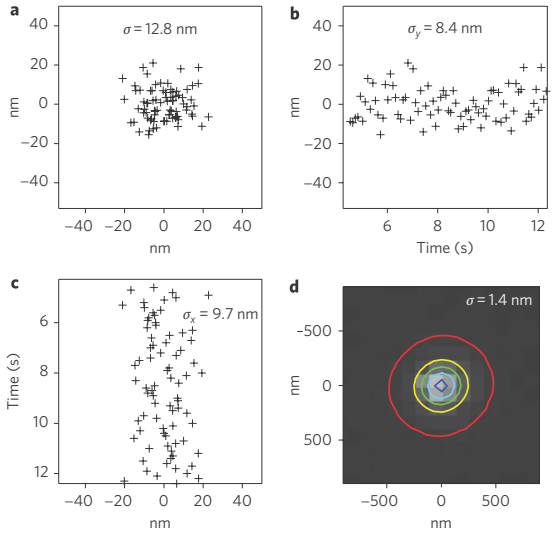

Figure 2 | Localizing single molecules with nanometre precision. **a**, During the lifetime of a single fluorophore deposited in Fig. 1, each frame was fitted with two-dimensional Gaussians. **b**,**c**, Temporal development of the centroid coordinates. **d**, Because the position of the dye is drift-free (**b**,**c**), an average intensity image of this period was summed and fitted with a single Gaussian. The accuracy of the position obtained from the optical part of the instrument was determined to be ±1.4 nm.

molecules relative to the optical axis of the instrument remained constant. For each deposition process a movie was recorded, and the positions of the pasted molecules were determined as described above. The positions of nine single fluorophores deposited in this way in intervals of five minutes are shown in Fig. 3c. The spatial uncertainty of the experiment presented in Fig. 3c arises first from the SMCP process itself, but also from the spatial drift of the setup (Fig. 3d,e). The systematic thermal drift shown in this particular example was chosen to highlight the advantage of our procedure to isolate potential artifacts. An estimate of the SMCP process itself can be given by subtracting the drift (see lines in Fig. 3d,e), resulting in a precision of the y-position of ±11 nm. Under the given conditions of spacer length and anchor density this value can be seen as a benchmark for the precision of deposition. This value agrees well with the predictions of the simple model depicted in Fig. 3a,c, which is the result of the calculation given in the Supplementary Information.

To demonstrate the possibility of assembling and resolving a pattern comprising several single fluorophores we pasted six spots at a distance of 1 μm from one another (Fig. 4a). Each spot was assembled in nine SMCP cycles, as outlined in Fig. 4a. However, on average, a fluorophore was deposited only at every second attempt. Our goal was to identify the location of the pasted molecules by optical means. The intensity-time trace of the 16-pixel diffraction-limited spot no. 4 is shown in Fig. 4b. The stepwise decay with an exponential envelope is a clear indication for uncorrelated subsequent single fluorophore photobleaching. This stepwise decay of the overall intensity is also seen in the sequence of images in Fig. 4c. We used the sequential photobleaching of the fluorophores to discriminate between them in the following way. The last plateau arises from the last single fluorophore. Therefore, the

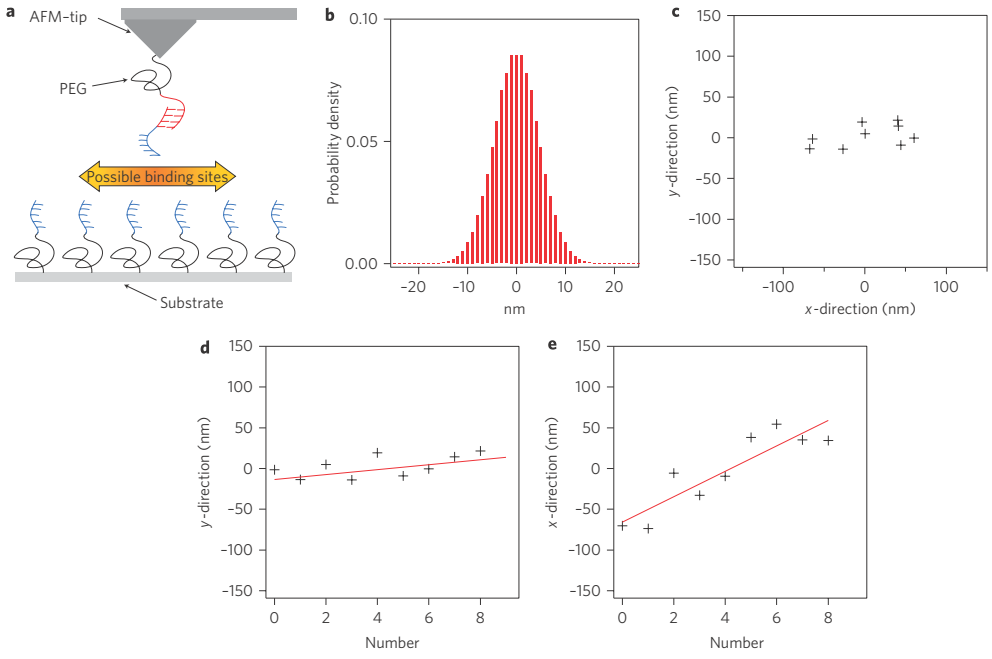

Figure 3 | Positional accuracy of the SMCP process. **a**,**b**, Positional uncertainty occurs when the PEG- and DNA-modified AFM tip probes for potential binding sites. **c**, Uncertainty was measured by successively depositing several single transfer-DNA molecules. The uncertainty of the coordinates of the centroid is determined by both the SMCP process and the spatial drift of the setup. **d**,**e**, To estimate long-term stability, intervals of 5 min between subsequent depositions were chosen and the complete experiment lasted ~45 min. During this time, the instrument drifted laterally and the uncertainty was determined by subtracting this instrumental drift.

© 2009 Macmillan Publishers Limited. All rights reserved.

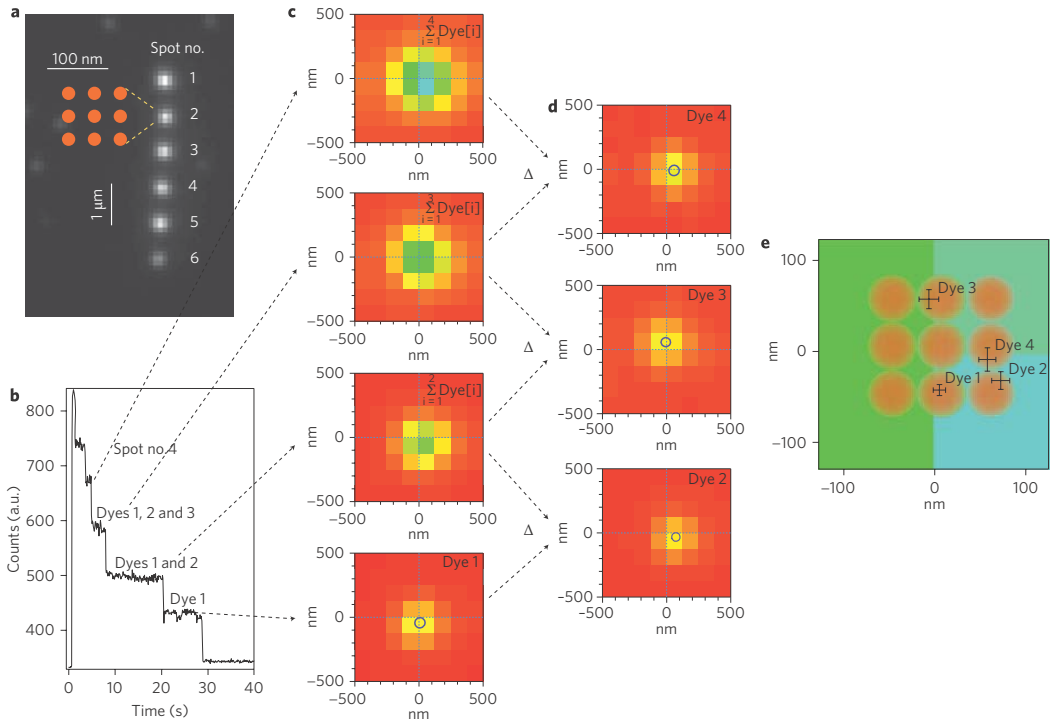

Figure 4 | Determining the position of deposited dyes by photobleaching. a, Fluorescence micrograph of a pattern consisting of six spots at a distance of 1 µm from one another. Each spot was assembled over nine SMCP cycles and deposited as sketched in the inset. **b**, Intensity–time trace of the diffraction-limited spot no. 4. During excitation, the Cy3 labels photobleach and show the typical stepwise decay of single fluorophores. After 20 s only one dye is left. **c**, Average intensity images were calculated for periods of constant signal. **d**, Subsequent images were subtracted to determine the intensity of the photobleached fluorophores, and two-dimensional Gaussians were fitted to each image. **e**, The positions of the four dyes.

centroid of the corresponding image gives its position. The second-to-last plateau arises from the two last fluorophores. We subtracted the image of the last plateau from the image corresponding to the second plateau. The remaining fluorescence distribution must therefore stem from the second-to-last fluorophore, and its centroid was so determined. With this iterative analysis we determined the position of the remaining fluorophores (Fig. 4d). As can be seen in Fig. 4e, the measured positions agree well with the expected positions in the assembly pattern. As can also be seen, the size of the error bars increases with decreasing lifetime of the fluorophore. We therefore restricted our quantitative analysis to the last four molecules. Nevertheless, the precision of the localization of the pasted molecules within the diffraction-limited ensemble by means of SRI turned out to be as good as $\pm$12 nm.

In summary, we have demonstrated that SMCP surface assembly combined with SRI allows the deposition process of single fluorophors to be monitored in real time and also the localization of the deposited molecules with nanometre precision. The precision of the SMCP process was determined to be $\pm$11 nm. This value may be improved considerably by using shorter spacers and with an optimized system of unbinding forces, for example, by using covalent anchor chemistry in the target area. In doing so, patterns of arbitrary shape and with arbitrary numbers of single molecules may be created. Such patterns could be used as test systems for novel SRI techniques, but could also help to investigate dye–dye interactions in a very controlled manner. In this study we have not made use of the potential to assemble different fluorophores in well-defined pattern and to analyse their resulting spectral properties, but such investigations are feasible and are expected to shed new light on the interaction among fluorophores and also between dye molecules and photonic nanostructures or optically active nanoparticles[22,27].

Methods

Sample preparation. Depot and target areas were prepared on a cover slip as described in ref. 1. Briefly, cover slips were amino functionalized and covalently modified with N-hydroxy-succinimide-ester (NHS)–PEG–maleimide (M = 5,000 g mol^{-1}; Nektar). After rinsing with H_2O, a PDMS flow chamber with two channels was mounted on one cover slip. Both channels were connected to a peristaltic pump. The anchor oligomers for the depot and target area were reduced using tris(2-carboxyethyl) phosphine (TCEP) solution (Pierce) in order to generate free mercaptans. The left channel (depot area) was rinsed for 1 h with a 10 µM solution of depot anchor oligomers and the right one (target area) with a 10 µM solution of target anchor oligomers. Afterwards, both channels were rinsed with H_2O to remove all non-covalently bound oligomers. The left channel (depot area) was rinsed with a 1 µM solution of transfer DNA dissolved in saline sodium citrate (SSC) buffer (150 mM NaCl, 15 mM sodium citrate, pH 7) for 1 h. All oligomers used in this study were synthesized by IBA (IBA GmbH) and were of HPLC grade. After rinsing the depot channel for 5 min with SSC buffer to remove all non-hybridized transfer DNA, the PDMS flow chamber was removed and the cover slip was dried in a nitrogen stream. Finally the cover slip was mounted to the AFM–total internal reflection fluorescence (TIRF) sample holder and immersed in SSC buffer.

Total internal reflection fluorescence microscope. Single-molecule fluorescence microscopy was carried out under TIRF excitation. Fluorescence excitation of the Cy3 dyes was performed using a 532 nm, 75 mW DPSS laser (Crystalaser) through a ×100/1.49 oil immersion objective lens (Nikon CFI Apochromat TIRF), with the collimated laser beam focused at the back focal plane of the objective lens such that the beam was totally reflected at the cover slip. Fluorescence light was split by colour with a commercial Dual View (Optical Insights) with Brightline HC 582/75

© 2009 Macmillan Publishers Limited. All rights reserved.

(Semrock) and ET 700/75 (Chroma) as emission filters for the green and red channels, respectively, and a dichroic mirror with a cutoff wavelength of 630 nm (630DCLP). The emitted light was detected using a 512×512 pixel back-illuminated electron multiplying charge-coupled device (EMCCD) camera (DU-897, Andor). Time series were recorded in frame-transfer mode with an integration time of 100 ms per frame. The EMCCD chip was typically operated at a temperature of −75 °C and an electron multiplication gain of ×300 was used. The magnification was 96; that means one pixel is equivalent to a distance of 125 nm.

AFM measurements. All SCMP experiments were performed with a custom-built AFM[23] at room temperature in SSC buffer. Silicon nitride cantilevers (MLCT-AUHW, Veeco Probes) were amino functionalized and covalently modified with NHS–PEG–maleimide ($M = 5{,}000$ g mol^{-1}; Nektar) as described in ref. 24. The spring constant of the DNA-modified cantilever was calibrated in solution using the equipartition theorem[25,26]. This method yielded a spring constant of 12.9 pN nm^{-1} and a resonance frequency of 1.24 kHz for the cantilever used in this study. The tip was withdrawn from the surface at a speed of 1,500 nm s^{-1} until it was 2 μm above the surface. The protocol for the SMCP as well as the data recording was programmed using Igor Pro 5.03 (Wave Metrics). An Asylum Research controller, which provides analog-to-digital converter (ADC) and digital-to-analog converter (DAC) channels as well as a DSP board, was used for setting up feedback loops. Cantilever positioning for pickup and delivery was controlled in closed-loop operation. The precision was set to ±4 nm.

Data analysis. Fluorescence images were analysed with Igor Pro 6.01 (Wave Metrics). Intensity–time traces were produced by calculating the average intensity over 4×4 pixels in every frame. Centroid localization of a single molecule was performed by fitting a two-dimensional Gaussian distribution to an 11×11-pixel diffraction-limited image. For localizing the positions of each fluorophore within a cluster, the individual contributions to the intensity images were extracted by calculating an average intensity image for every period of constant signal, then subtracting subsequent images from each other. The differences indicate the average intensities of the contributing fluorophores. The positions of the fluorophores were again determined by fitting two-dimensional Gaussians.

Received 13 June 2008; accepted 22 October 2008; published online 23 November 2008

References

1. Kufer, S. K., Puchner, E. M., Gumpp, H., Liedl, T. & Gaub, H. E. Single-molecule cut-and-paste surface assembly. *Science* **319,** 594–596 (2008).
2. Hell, S. W. & Wichmann, J. Breaking the diffraction resolution limit by stimulated emission: stimulated-emission-depletion fluorescence microscopy. *Opt. Lett.* **19,** 780–782 (1994).
3. Xie, X. S. & Dunn, R. C. Probing single molecule dynamics. *Science* **265,** 361–364 (1994).
4. Dyba, M. & Hell, S. W. Focal spots of size lambda λ/23 open up far-field fluorescence microscopy at 33 nm axial resolution. *Phys. Rev. Lett.* **88,** 163901 (2002).
5. Binnig, G., Quate, C. F. & Gerber, C. Atomic force microscope. *Phys. Rev Lett.* **56,** 930–933 (1986).
6. Hansma, P. K., Elings, V. B., Marti, O. & Bracker, C. E. Scanning tunneling microscopy and atomic force microscopy: application to biology and technology. *Science* **242,** 209–216 (1988).
7. Radmacher, M., Tillmann, R. W., Fritz, M. & Gaub, H. E. From molecules to cells: imaging soft samples with the atomic force microscope. *Science* **257,** 1900–1905 (1992).
8. Duwez, A. S. *et al.* Mechanochemistry: targeted delivery of single molecules. *Nature Nanotech.* **1,** 122–125 (2006).
9. Bobroff, N. Position measurement with a resolution and noise-limited instrument. *Rev. Sci. Instrum.* **57,** 1152–1157 (1986).
10. Thompson, R. E., Larson, D. R. & Webb, W. W. Precise nanometer localization analysis for individual fluorescent probes. *Biophys. J.* **82,** 2775–2783 (2002).
11. Ober, R. J., Ram, S. & Ward, E. S. Localization accuracy in single-molecule microscopy. *Biophys. J.* **86,** 1185–1200 (2004).
12. Yildiz, A. *et al.* Myosin V walks hand-over-hand: single fluorophore imaging with 1.5 nm localization. *Science* **300,** 2061–2065 (2003).
13. Qu, X., Wu, D., Mets, L. & Scherer, N. F. Nanometer-localized multiple single-molecule fluorescence microscopy. *Proc. Natl Acad. Sci. USA* **101,** 11298–11303 (2004).
14. Betzig, E. *et al.* Imaging intracellular fluorescent proteins at nanometer resolution. *Science* **313,** 1642–1645 (2006).
15. Rust, M. J., Bates, M. & Zhuang, X. Sub-diffraction-limit imaging by stochastic optical reconstruction microscopy (STORM). *Nature Methods* **3,** 793–796 (2006).
16. Gordon, M. P., Ha, T. & Selvin, P. R. Single-molecule high-resolution imaging with photobleaching. *Proc. Natl Acad. Sci. USA* **101,** 6462–6465 (2004).
17. Tinnefeld, P. & Sauer, M. Branching out of single-molecule fluorescence spectroscopy: challenges for chemistry and influence on biology. *Angew. Chem. Int. Ed.* **44,** 2642–2671 (2005).
18. Lacoste, T. D. *et al.* Ultrahigh-resolution multicolor colocalization of single fluorescent probes. *Proc. Natl Acad. Sci. USA* **97,** 9461–9466 (2000).
19. Churchman, L. S., Okten, Z., Rock, R. S., Dawson, J. F. & Spudich, J. A. Single molecule high-resolution colocalization of Cy3 and Cy5 attached to macromolecules measures intramolecular distances through time. *Proc. Natl Acad. Sci. USA* **102,** 1419–1423 (2005).
20. Gaiduk, A., Kühnemuth, R., Antonik, M. & Seidel, C. A. M. Optical characteristics of atomic force microscopy tips for single-molecule fluorescence applications. *Chem. Phys. Chem.* **6,** 976–983 (2005).
21. Baum, R. Nanotechnology: Drexler and Smalley make the case for and against 'molecular assemblers'. *Chem. Eng. News* **81,** 37–42 (2003).
22. Bek, A. *et al.* Fluorescence enhancement in hot spots of AFM-designed gold nanoparticle sandwiches. *Nano Lett.* **8,** 485–490 (2008).
23. Kühner, F., Lugmaier, R., Mihatsch, S. & Gaub, H. E. Print your atomic force microscope. *Rev. Sci. Instrum.* **78,** 075105 (2007).
24. Morfill, J. *et al.* B–S transition in short oligonucleotides. *Biophys. J.* **93,** 2400–2409 (2007).
25. Florin, E. L. *et al.* Sensing specific molecular interactions with the atomic force microscope. *Biosen. Bioelectr.* **10,** 895–901 (1995).
26. Butt, H.-J. & Jaschke, M. Calculation of thermal noise in atomic force microscopy. *Nanotechnology* **6,** 1–7 (1995).
27. Puchner, E. M., Kufer, S. K., Strackharn, M., Stahl, S. W. & Gaub, H. E. Nanoparticle self-assembly on a DNA-scaffold written by single-molecule cut-and-paste. *Nano Lett.* **8,** 3692–3695 (2008).

Acknowledgements

We thank P. Tinnefeld and A. Fornof for helpful discussions. This work was supported by the German Science Foundation, the Nanosystems Initiative Munich (NIM) and Functional Nanosystems (FuNS).

Author contributions

S.K.K. and H.E.G. conceived and designed the experiments and co-wrote the paper. S.K.K., M.S. and S.W.S. performed the experiments. S.K.K. and E.M.P. analysed the data. M.S., S.W.S., H.G. and E.M.P. built the AFM–TIRF setup. M.S., S.K.K. and H.E.G. developed the theoretical model of the SMCP spatial uncertainty.

Additional information

Supplementary Information accompanies this paper at www.nature.com/naturenanotechnology. Reprints and permission information is available online at http://npg.nature.com/reprintsandpermissions/. Correspondence and requests for materials should be addressed to H.E.G.

© 2009 Macmillan Publishers Limited. All rights reserved.

Supplementary information

Optically monitoring the mechanical assembly of single molecules

Stefan K. Kufer[1], Mathias Strackharn[1], Stefan W. Stahl[1], Hermann Gumpp[1], Elias M. Puchner[1,2] and Hermann E. Gaub[1*]

Hierarchical force system for SMCP:
The probe of an atomic force microscope (AFM) was used to assemble individual single stranded DNA (ssDNA) oligomers carrying dye molecules one by one in aqueous solutions at room temperature. The oligomers were stored on well-defined depot areas, picked up with the tip of an AFM cantilever and reassembled with nanometer precision on a spatial distinct target area. The storage, the pick up and the deposition of the DNA oligomers were realized by using an ordered system of unbinding forces based on DNA interactions.

The dissociation rates of DNA duplexes under load are highly dependent of loading geometries and DNA sequences respectively[1, 2]. When the duplex is stretched along its molecular axis, this means that the DNA duplex is loaded at opposite 5' ends or 3' ends, respectively, one speaks of "shear mode"[1] (Fig. S1e). The topological arrangement when double strands are loaded by pulling on the 5' and 3' extremities of one end of the duplex is called "unzip mode"[3] (Fig. S1a). These two geometries are well distinguishable concerning their dissociation properties under load.

The rupture forces for DNA duplexes loaded in unzip mode are independent both of the length of the DNA oligomer and the loading rate, but vary for G-C and A-T interactions. G-C pairing results in a dissociation force of roughly 20 pN whereas A-T gives rise to roughly 10 pN[2]. The dissociation forces for DNA duplexes loaded in shear geometry depend both on the length and the loading rate[1].

To connect the transfer DNA to the depot a 30 base pair (bp) long anchor sequence with mixed G-C and A-T is used (Fig. S1a). The transfer DNA has in addition to this 30 bp anchor sequence a 20 bp handle sequence for pick up. The AFM-tip is covalently modified with a ssDNA strand. Since this strand is complementary to the handle sequence a duplex is formed as the tip approaches the depot area (Fig. S1b). Then the tip is retraced from the depot the anchor sequence is loaded in unzip mode whereas the handle sequence in shear mode. Although the 30 bp anchor sequence is longer than the 20 bp handle sequence, its unbinding probability under load is much higher than for the handle sequence and the transfer DNA is picked up (Fig. S1c).

[1]Center for Nanoscience & Physics Department, University Munich, Amalienstr. 54, 80799 Munich
[2]Center for Integrated Protein Science Munich
[*] E-mail: Gaub@LMU.de

© 2008 **Macmillan Publishers Limited. All rights reserved.**

After translocation of the transfer DNA to its target site the cantilever is lowered towards the surface. Since the target area is covalently modified with ssDNA oligomers that are complementary to the anchor sequence a 30 bp duplex in shear geometry is formed (Fig S1d). As the dissociation force of duplexes in shear geometry depends on the length of the DNA sequence the shorter handle sequence ruptures first and the transfer DNA is attached to the target site (Fig. S1e). It was shown[4] that a length difference of 10 base pairs (bp) is sufficient to make the rupture of the shorter handle duplex more likely by one order of magnitude than the rupture of the longer anchor duplex. The DNA sequences of the oligomers used in this study are shown in Fig. S2. The experimental setup for the SMCP process is shown in Fig. S3.

Calculation of the SCMP lateral uncertainty:
For an estimation of lateral uncertainty the total construct consisting of the transfer DNA attached to the cantilever DNA that again is bound to the tip by a PEG spacer was treated in the model of the freely jointed chain (FJC) as one polymer with the effective Kuhn length b_{eff}, where b_{eff} was obtained by calculating the weighted average Kuhn length of the three sequences. The weighting coefficients are for each sequence respectively the ratio of sequence contour length to the contour length of the total construct:

$$b_{eff} = \frac{l_{PEG}}{l_{tot}} b_{PEG} + \frac{l_{dsDNA}}{l_{tot}} b_{dsDNA} + \frac{l_{ssDNA}}{l_{tot}} b_{ssDNA},$$

with l_i the contour lengths and b_i the Kuhn lengths. The effective number of Kuhn monomers is then given by $N_{eff} = \frac{l_{tot}}{b_{eff}}$.

The FJC model[5] predicts the distribution of end-to-end distances along each axis as

$$P(x_i) = \sqrt{\frac{3}{2\pi N_{eff} {b_{eff}}^2}} \exp\left(-\frac{3{x_i}^2}{2N_{eff} {b_{eff}}^2} \right).$$

As for the estimation of the binding probability $P_{binding}$, we assume that the approach of the tip to the surface is faster then the polymer fluctuations. In this case every conformation in the lower half-space contributes to the binding probability, such that the binding probability along the x-axis when the molecule approaches the surface in z-direction corresponds to

$$P_{binding}(x) = \frac{1}{A_{norm}} P(x) \int_{-\infty}^{0} P(z)dz = P(x),$$

where the normalization constant A_{norm} equals the definite integral because of the normalized function $P(x)$. So the binding probability is described by the Gaussian function $P(x)$.

It is worth stressing the fact that if the approach of the tip is slow compared to the polymer fluctuations the binding probability shrinks to a point like distribution. This is because of the fact that if the tip is approached to a distance that is in the range of the contour length of the polymer, it will bind preferred in the projection point of the tip. That means that the calculated distribution above is the worst case that could happen.

We testet that simple model by simulating the polymer as freely jointed chain with the parameters b_{PEG}=1.1 nm[5], N_{PEG}=27[6], b_{ssDNA}=1.5 nm[7] and N_{DNA}=8[7], and N_{dsDNA}=1 and

© 2008 **Macmillan Publishers Limited. All rights reserved.**

b_{dsDNA}=6.8 nm[7]. Fig. S4 shows that the simulation and the FJC model do match in a satisfactory manner.

References:

1. Strunz, T., Oroszlan, K., Schafer, R. & Guntherodt, H.J. Dynamic force spectroscopy of single DNA molecules. *Proceedings of the National Academy of Sciences of the United States of America* **96**, 11277-11282 (1999).
2. Rief, M., Clausen-Schaumann, H. & Gaub, H.E. Sequence-dependent mechanics of single DNA molecules. *Nat Struct Biol* **6**, 346-349 (1999).
3. Levinthal, C. & Crane, H.R. On the Unwinding of DNA. *PNAS* **42**, 436-438 (1956).
4. Albrecht, C. et al. DNA: A Programmable Force Sensor. Science 301, 367-370 (2003).
5. Rubinstein, R.H.C. Polymer Physics. *Oxford University Press* (2005).
6. Oesterhelt, F., Rief, M. & Gaub, H.E. Single molecule force spectroscopy by AFM indicates helical structure of poly(ethylene-glycol) in water. *New Journal of Physics* **1** (1999).
7. Smith, S.B., Cui, Y.J. & Bustamante, C. Overstretching B-DNA: The elastic response of individual double-stranded and single-stranded DNA molecules. *Science* **271**, 795-799 (1996).

© 2008 **Macmillan Publishers Limited. All rights reserved.**

Figures:

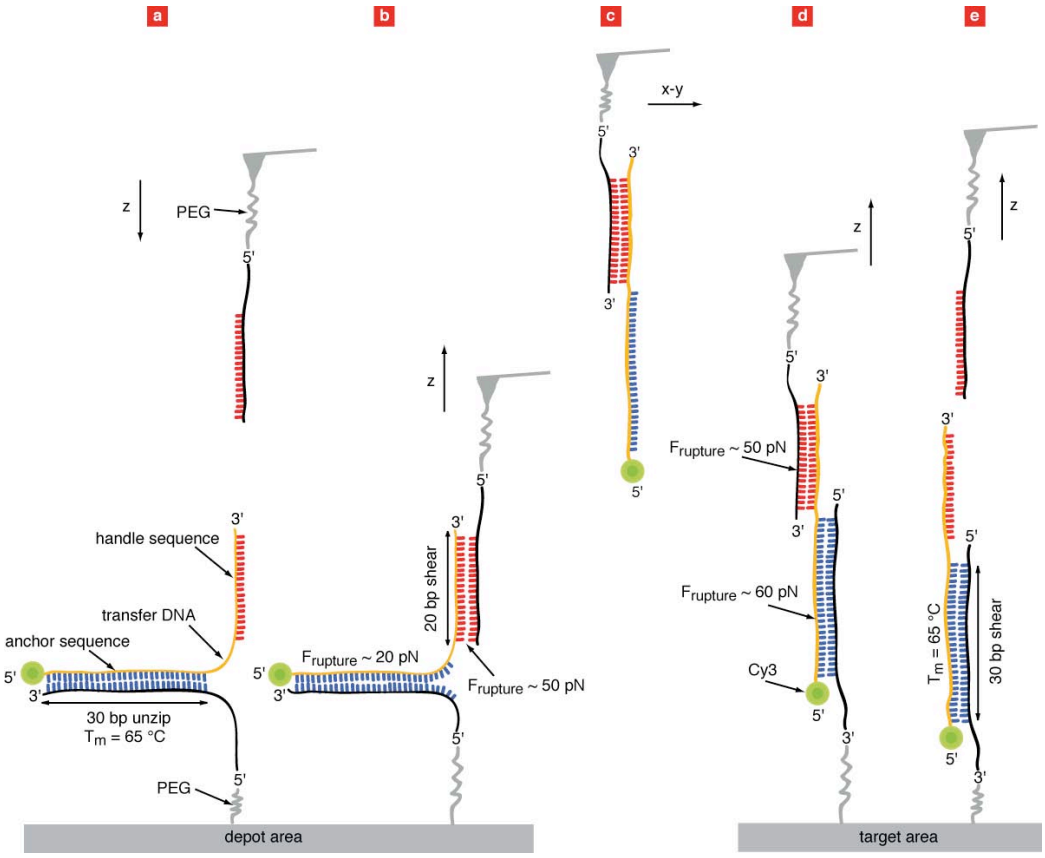

Fig. S1. Schematic illustration of the hierarchical force system. (a) To prevent unspecific adsorption, polyethylenglycol (PEG) molecules are covalently attached to the target area. DNA oligomers, complementary to the anchor sequence of the transfer DNA, are covalently bonded with their 5' end to these PEG molecules. Transfer DNA oligomers, which were modified with Cy3 labels on the 5' end, are hybridized to this anchor sequences. The tip of an AFM cantilever is also covalently modified with PEG molecules and a single DNA oligomer, which is complementary to the handle sequence of the transfer DNA, is bonded covalently with its 5' end to a PEG molecule. (b) When the tip is brought into contact with the surface a duplex between the transfer DNA and the cantilever DNA is formed. When the tip is retracted the anchor sequence is loaded in unzip mode and the handle sequence in shear mode. As the unbinding probability for the anchor sequence is higher, the transfer DNA is picked up. (c and d) The target site is also covalently modified with PEG molecules. DNA oligomers, complementary to the anchor sequence of the transfer DNA, are bonded with their 3' end to the PEG molecules. After translocation the tip is moved down and a duplex is formed. When the tip is retracted the handle and the anchor sequences are loaded in shear mode, but this time the shorter handle sequence ruptures first and the transfer DNA is attached to its target site. The tip is now in its initial state and the cycle could be repeated over and over again.

© 2008 **Macmillan Publishers Limited. All rights reserved.**

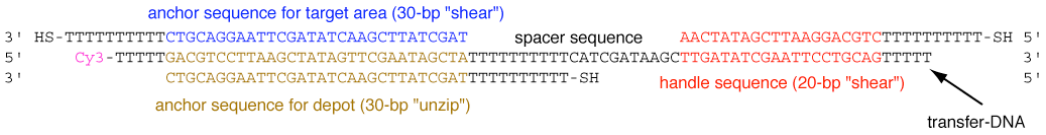

Fig. S2. Oligomers used in this study. The transfer DNA is 80 bp long and has a Cy3 label on the 5' end. The 30 bp long sequence on the 5' end is used to anchor the transfer DNA both to the depot and to the target site. The 20 bp long sequence on the 3' end is used as a handle for pick up. All oligomers were synthesized and purified (HPLC-grade) form IBA (IBA GmbH, Göttingen, Germany).

© 2008 **Macmillan Publishers Limited. All rights reserved.**

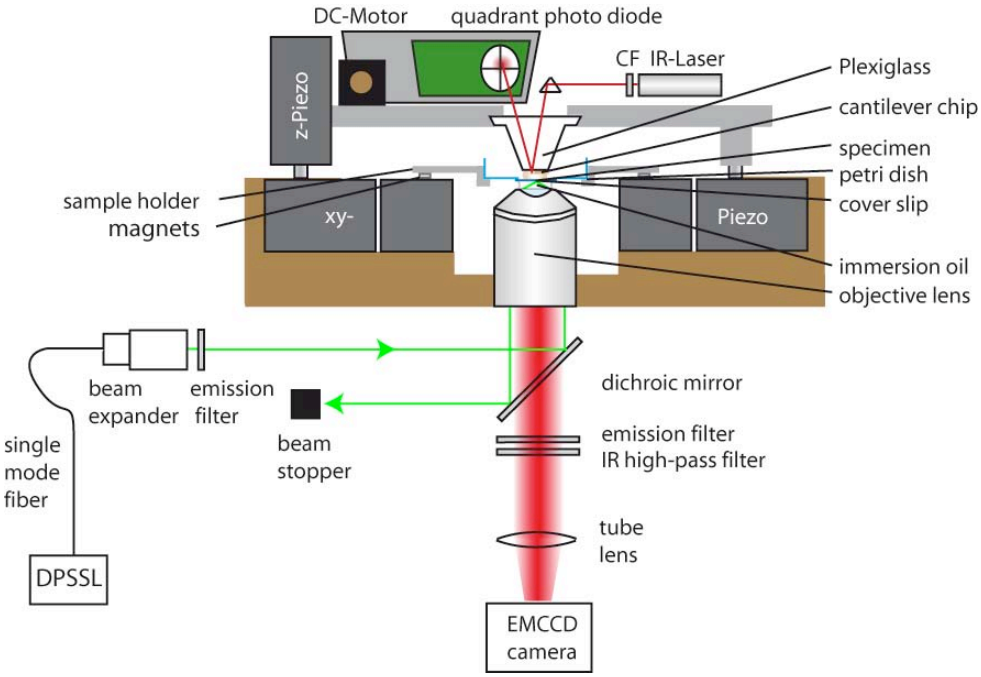

Fig. S3. Experimental setup. A custom built AFM head, which is actuated in z direction via a piezo, is combined with an inverted microscope for objective-type wide-field TIRF excitation. The cover slip with the depot- and target areas on top is glued into a bored petri dish. The petri dish is placed in a sample holder, which is fixed through magnets on x-y piezo scanner.

© 2008 **Macmillan Publishers Limited. All rights reserved.**

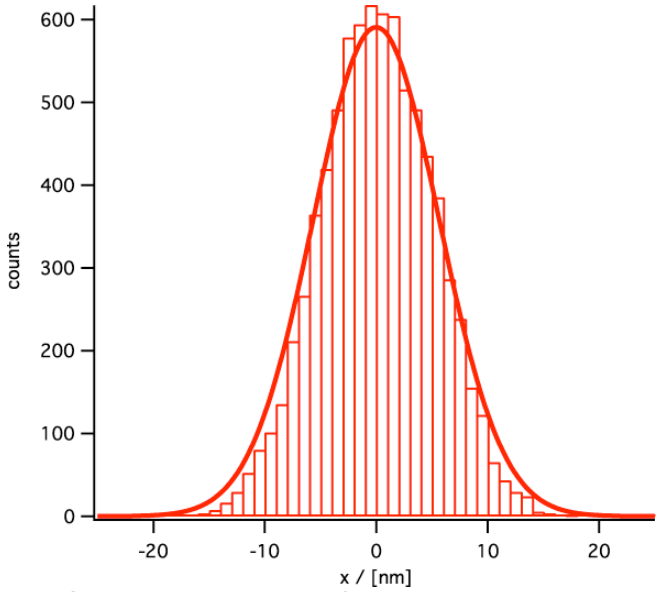

Fig. S4. The end position of the end-to-end vector obtained by simulation of the conjugated polymer in FJC model is shown as histogram, the thick line describes shows the distribution according to the FJC model using an effective Kuhn length an effective monomer number.

© 2008 **Macmillan Publishers Limited. All rights reserved.**

Supplementary: (Supplementary.pdf, 340 KB)

The supplementary describes the SMCP force system in detail and provides a simple theoretical model to estimate the precision of the SMCP process.

Movie_M1: (Movie_M1.mov, 1,6 MB)

The movie M1 shows the deposition of a single molecule monitored with single molecule fluorescence microscopy. As long as the tip is far away from the surface (2 s), no fluorescence is detectable. When the tip penetrates the evanescent excitation field (4 s), a strong signal is detected in both the red and green channels. When the cantilever retracts (7 s), the fluorescence from the tip (red) vanishes but the transfer DNA (green) remains anchored and emits photons until it photobleaches.

Movie_M2: (Movie_M2.mov, 2,9 MB)

The movie M2 shows an animation of the SMCP process.

© 2008 **Macmillan Publishers Limited. All rights reserved.**

P3 ULTRASTABLE COMBINED ATOMIC FORCE AND TOTAL INTERNAL REFLECTION FLUORESCENCE MICROSCOPE

Gumpp H, Stahl SW, Strackharn M, Puchner EM and Gaub HE.

REVIEW OF SCIENTIFIC INSTRUMENTS 2009 Jun;80(6):063704

REVIEW OF SCIENTIFIC INSTRUMENTS **80**, 063704 (2009)

Ultrastable combined atomic force and total internal fluorescence microscope

H. Gumpp, S. W. Stahl, M. Strackharn, E. M. Puchner,[a] and H. E. Gaub
Chair for Applied Physics and Center for NanoScience, Ludwig-Maximilians-University Munich, Amalienstr. 54, D-80799 Munich, Germany

(Received 7 March 2009; accepted 4 May 2009; published online 22 June 2009)

Combining atomic force microscope (AFM) with other microscopy techniques has expanded the range of potential applications for single molecule investigations dramatically. Particularly hybrid instruments with total internal reflection fluorescence (TIRF) excitation have opened new routes in life sciences. Here we present a novel design for such a hybrid microscope, which overcomes the limitations of conventional combinations caused by their limited mechanical stability. A thorough analysis of the noise spectra and a comparison of the different designs and the different operation modes are given. With this instrument we demonstrate single molecule manipulation by AFM and simultaneous TIRF imaging. © *2009 American Institute of Physics.* [DOI: 10.1063/1.3148224]

I. INTRODUCTION

The atomic force microscope (AFM) has revolutionized nanoscience in many ways. It is now widely used in biophysics as a tool to image nanoscale structures, as well as to measure and apply forces in a well-defined manner.[1–3] While AFM techniques are very precise in terms of spatial and force resolution, even the fastest AFMs currently are orders of magnitude slower in terms of imaging compared to optical methods.[4] On the other hand traditional optical microscopy provides fast readout but is limited by diffraction. Therefore it is obvious that AFM and single molecule fluorescence microscopy are complementing each other in a favorable manner.[5–7] As the AFM is a tool to operate on surfaces, the choice of total internal reflection fluorescence (TIRF) as illumination source for single molecule microscopy is convenient. However positional noise of the sample on the nanometer length scale that could have been neglected in sole single molecule TIRF microscope setups become an issue. Such fluctuations hamper high-precision AFM measurements.

In previous studies we have investigated in great detail the effect of mechanical vibrations of the AFM on the measured unbinding forces of molecular complexes.[8] It is obvious that a fluctuating cantilever, but in the same way a fluctuating sample position, causes force fluctuations in the molecular complex under investigation, which add to the externally applied force. Since bond rupture is a nonequilibrium process, these fluctuations do not average out to zero but reduce the force, which has to be applied externally to break the bond. Particularly when stiff and short handles are used as linkers, fluctuation in the relative distance between tip and sample surface may lead to drastic artifacts.

In optical microscopy, such fluctuations, e.g., caused by vibrations of the microscope, stay often unnoticed since they are below the optical resolution limit. It is particularly the direct coupling of mechanical noise via the oil immersion, which is essential for TIRF, which causes severe problems. Also in high-resolution fluorescence techniques such as 4π-stimulated emission depletion (STED), photo-activated localization microscopy (PALM), or stochastic optical reconstruction microscopy (STORM) such fluctuations remain unnoticed, since their characteristic time typically lies above the integration time of the detectors and thus are averaged out. Not so in mechanical experiments, where such position fluctuations result in force fluctuations which may result in bond ruptures. To cope with this issue we analyzed potential sources of such fluctuations and as a consequence of our analysis developed a very compact microscope setup featuring a solid connection between an immersion objective lens, the AFM, and the sample. By mechanically decoupling the focusing mechanism from the sample and the AFM head, vibrations limiting the force resolution could be eliminated virtually completely.

II. SAMPLE POSITION FLUCTUATIONS IN TIRF MICROSCOPY

Several different methods are commonly used for fluorescence excitation in the evanescent field (TIRF).[9,10] Whereas prism-based systems allow for use of variety of glass substrates and incident angles, and are not limited by the numerical aperture (NA) of the objective lens, combining them with an AFM is difficult. An objective-type TIRF setup installed on an inverted microscope as it was introduced by Tokunaga *et al.*[11] offers the advantage of using an objective lens with high numerical aperture for excitation as well as for collection of emission, therefore leaving the upper half space above the sample free. A scanning probe microscope (SPM) such as the AFM may then be placed above the sample for simultaneous imaging, force measurements, and manipulation of the sample. Several implementations of this concept are already reported in the literature.[5–7,12–15]

Since high NA-objective lenses have very short working distances, objective-type TIRF can only be performed on

[a]Center for Integrated Protein Science Munich.

 © 2009 American Institute of Physics

Downloaded 24 Jun 2009 to 129.187.254.47. Redistribution subject to AIP license or copyright; see http://rsi.aip.org/rsi/copyright.jsp

thin cover slips, with a thickness of up to 0.15 mm. These thin glass substrates are prone to deformation and vibrations, coupling through the system acoustically an even more important mechanically, and through the air, which hampers high-resolution AFM measurements. While sound coupling into the system can be damped effectively by placing the whole setup in a soundproof box, mechanical vibrations are still hard to handle. Oscillations below 100 Hz, as arising from the building, can be effectively damped by active tables, but higher frequencies and especially noise sources inside the microscope itself still have to be eliminated.

A high NA-objective lens needs immersion oil to be operated to match the refractive index of the glass substrate. When using the objective lens for adjusting the focus, as it is done with virtually all commercially available objective-type TIRF setups so far, additional vibrations from, e.g., a focusing piezo are coupled into the glass cover slip. Moreover, moving the objective lens for controlling the focus during the experiment introduces drift mediated by the immersion oil's viscosity. However, for TIRF illumination the focus needs to be adjusted very precisely, because the evanescent field is only a few hundred nanometers in depth. During long measurements temperature changes as well as buffer evaporation may cause the surface to drift out of focus. Hence when operating commercially available focus piezo stages of the objective lens in a closed loop in order to correct for this focus drift, strong vibrations couple into the sample through the immersion oil, thereby making high-resolution AFM experiments virtually impossible.

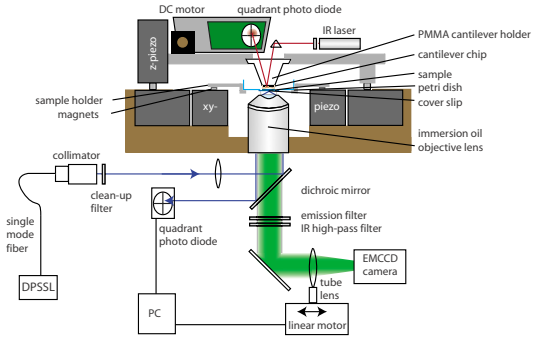

FIG. 1. (Color online) Schematic drawing of the combined AFM/TIRF microscope. TIRF excitation is performed by a diode pulsed solid-state laser coupled to a single-mode fiber. Using a collimator lens and a biconcave lens for focusing the beam on the back focal plane of the objective lens, wide-field TIRF illumination is achieved. Fluorescence emission passes through an appropriate filter set and is collected by the EMCCD camera. The tube lens is used for focusing and therefore mounted on a linear translation stage controlled by a PC that reads the position of the back-reflected beam from a quadrant photo diode. With this feedback a constantly sharp image can be ensured.

III. HYBRID TIRF/AFM

In the evolution of SPMs, compact designs, as rigid as possible, have proven to minimize both vibrations and thermal drift. This design principle should provide the best solution for the problems with the mechanical stability discussed above.[16]

We kept our AFM head as short and compact as possible (see Fig. 1). Cantilever deflection is measured with an infrared superluminescent laser diode SLD-37-HP (Superlum Diodes Ltd, Cork, Ireland), which minimizes interferences of the reflected beam and keeps the entire optical spectrum open for fluorescent measurements. Servo motors controlling the z-position of the head and the position of the deflection sensing photodiode allow for automatic compensation of lever and probe drift during long term measurements.

The major difference of the presented setup to yet existing ones is the optimization of the mechanical stability of the sample-cantilever entity. Whereas in conventional microscopes the objective lens is mounted on a revolver and/or focusing piezo, our setup contains a high NA-objective lens, which is rigidly mounted in a massive aluminum block directly connected to the AFM head, as Fig. 1 shows. This way the objective is integrated directly in the AFM head, maximizing the mechanical stability. The sample is located on the cover slip, glued over a hole drilled into the bottom of a Petri dish. The latter is clamped tightly to the xy-piezo scanner by strong magnets in order to be able to move the sample. It is adjusted with micrometer screws for coarse alignment. Modern objective lenses with high NA, such as the Nikon 100× lens (CFI Apo TIRF 100×, NA 1.49, Nikon Inc., Tokyo, Japan) we used here, allow variation in the penetration depth of the evanescent field, depending on the distance of the beam from the rim of the objective lens. This is achieved by shifting the laser orthogonally to the optical axis of the objective lens. This way the penetration depth can be varied between approximately 200–500 nm.

Focusing is facilitated by moving the tube lens via a motorized high-accuracy linear translation stage M-605, (Physik Instrumente, Karlsruhe, Germany) which focuses the fluorescence light from the sample onto the chip of the electron multiplying charge coupled device (EMCCD) camera (Andor iXon DU-897, Andor Technology, Belfast, Ireland). This motor is completely mechanically decoupled from the rest of the instrument and does not need to stand on the vibration insulation table.

In order to build a most compact instrument, for the excitation path, the light of a solid-state diode pulsed laser (532 nm DPSS Laser, CrystaLaser, Reno, NV, USA) is coupled into a single-mode optical fiber and used for fluorescence excitation via a compact slider unit consisting of a collimator lens, a clean-up filter, a lens for focusing the beam into the back focal plane of the objective lens, and an adjustable dichroic mirror that directs the light to the sample. This unit can be replaced easily with another one containing an alternative filter set, when working with a different laser. In total internal reflection the back-reflected beam hits a quadrant photo diode, which measures its position. This way a change in the lateral position of the reflected beam and hence a change in distance between the objective lens and the cover slip can be determined. Finally this information can be used for the adjustment of the focus via the tube lens.

By moving the tube lens via the linear translation stage, the relative distance from the charge coupled device chip and therefore the magnification is altered. This effect can be

Downloaded 24 Jun 2009 to 129.187.254.47. Redistribution subject to AIP license or copyright; see http://rsi.aip.org/rsi/copyright.jsp

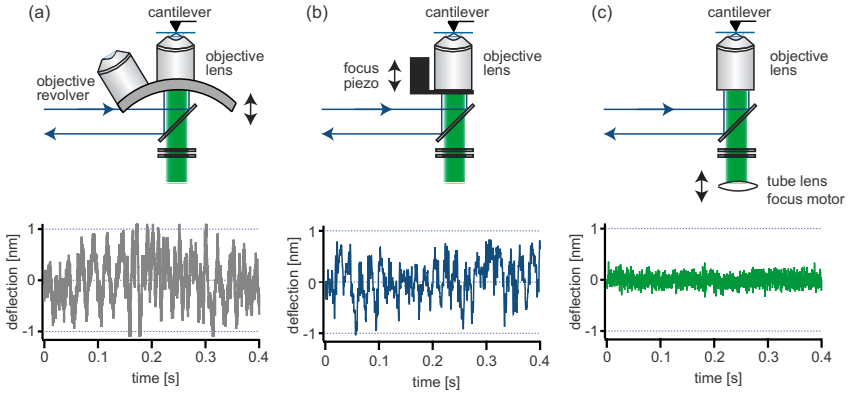

FIG. 2. (Color online) Calculated change in magnification as a function of the tube lens position, respectively, the corresponding sample position for the presented home-built microscope.

quantified by elementary optics, reducing the microscope to a one-lens system. The resulting focal length f and the position of the principal planes H_1 and H_2 are determined by the focal lengths of the objective f_1, the tube lens f_2, and their relative distance d as follows.

$$f = \frac{f_1 f_2}{f_1 + f_2 - d}, \quad H_2 = \frac{d f_2}{f_1 + f_2 - d}.$$

With the given image distance $b = f_2 + x - H_2$ the object distance $g = fb/(b-f)$ and the magnification $M = b/g$ can be calculated for each tube lens position x. Figure 2 shows the results for the described setup. Typical sample drift of 1 μm can be corrected by moving the tube lens by about 10 mm. In this range the magnification changes stay below 0.5%. Even when moving the tube lens by the maximum range of the linear motor ($\pm$25 mm) the change in magnification is below 2.0%. This effect has thus of minor influence on the imaging qualities of the microscope, also in terms of aberration correction.

IV. EXPERIMENTAL RESULTS

In order to compare the setup described above with other combined AFM-TIRF hybrids we measured the height fluctuations of the cover slip. For quantification amplitude spectra were taken with an AFM cantilever contacting the surface. All measurements were performed using a Veeco MLCT-C Cantilever at a contact force of approximately 1 nN. As first reference we used a home-built compact AFM-TIRF microscope with piezo adjustable objective lens. As a second reference a commercially available setup consisting of standard inverted microscope Zeiss Axiovert 200F, (Carl Zeiss AG, Jena, Germany) with a MFP-3D AFM, (Asylum Research, Santa Barbara, CA) and alternatively a Nanowizard II AFM (JPK Instruments, Berlin, Germany) was used. The results are plotted in Figs. 3 and 4 for direct comparison.

The combined conventional setup [Fig. 4(a)] shows the highest noise of all. Since the spectra recorded with the different AFM heads were virtually indistinguishable we conclude that the mechanics of the inverted microscope dominates the resonances. The bridge of the inverted microscope acts as a tuning fork. Vibrations are transduced via the objective revolver through the immersion oil, leading to fluctuations of the sample of approximately 1 nm and more. For high-resolution single molecule force spectroscopy such fluctuations are not tolerable!

Using a piezo driven single objective lens directly attached to the AFM such as in the home-built setup used as reference is an improvement, but as soon as the focusing piezo is operated in closed loop, simultaneous AFM measurement become very noisy [Fig. 4(b)]. Vibrations at the electrical carrier frequency of 50 Hz (and multiples) as well as other resonance frequencies of the instrument become clearly visible. As the spectra in Fig. 3 show, not only in the active focus regulation mode, but even in a passive mode with the feedback switched off, the vibrations in the microscope are coupled through the objective into the sample.

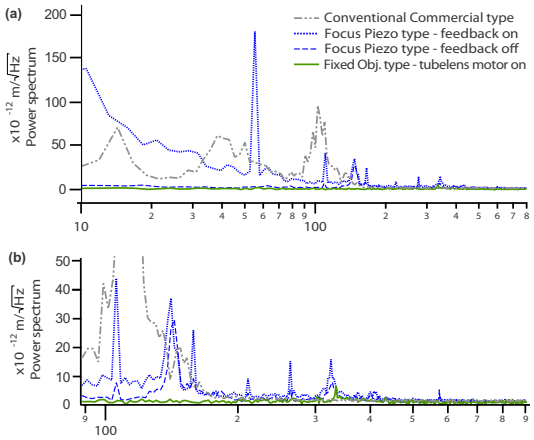

FIG. 3. (Color online) (a) Noise spectra of sample fluctuation recorded on the surface. While the conventional setup shows a broad distribution of frequencies, the home-built microscope with focus piezo exhibits mainly sharp resonance peaks, even when the closed-loop feedback of the focus piezo is switched off. The noise level is drastically reduced in the setup with fixed objective lens even with the tube lens focus motor switched on. A magnified view is given in (b).

Downloaded 24 Jun 2009 to 129.187.254.47. Redistribution subject to AIP license or copyright; see http://rsi.aip.org/rsi/copyright.jsp

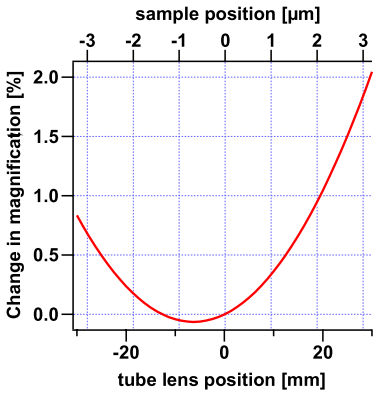

FIG. 4. (Color online) Comparison of the different setups and corresponding height fluctuations of the cover slip surface taken by contacting the surface of the cover slip with the AFM cantilever tip. (a) represents the combination of a standard inverted microscope and a commercial AFM head, (b) shows a setup with objective lens focus piezo, and (c) the new approach with moveable tube lens for focusing.

Moreover, adjusting the focus by moving the objective lens introduces drift that gets especially disturbing when performing experiments over hours.

In contrast, when operating the new setup with fixed objective but moveable tube lens cover slip vibrations are reduced to a minimum, while a sharply focused optical image is assured at all times [Fig. 4(c)]. Spectra that were taken while readjusting the focus position are virtually indistinguishable from those with fixed focus since the movable tube lens is mechanically decoupled from the AFM/sample part.

The combined AFM-TIRF instrument presented here was successfully used for simultaneous single molecule experiments such as single molecule cut-and-paste procedures as described in Ref. 17. Using molecular handles with hierarchical forces fluorescently labeled biomolecules were picked up from a depot, transported, and deposited with about 10 nm precision to a target area (Fig. 5). Figure 5(b) shows the rupture force curves measured on the depot area (left) and the target area (right), which exhibit very small noise comparable to a stand-alone AFM. The focusing mechanism described above made it possible to obtain sharp images of single fluorophores [Figs. 5(c) and 5(d)] at all times while allowing for high-resolution force spectroscopy in parallel for many hours.

V. CONCLUDING REMARKS

During day-to-day use, this combined TIRF-AFM setup proved to be a versatile instrument for many kinds of single molecule experiments.[17–19] The compact design with decoupled focusing succeeded in reaching a maximum of force resolution on the AFM side, while at the same time assuring a constantly sharp image for state-of-the-art single molecule microscopy.

Although we only show here only the combination of TIRF microscopy and AFM force spectroscopy, the principle of the setup described above can also be applied to any combinations of optical and SPMs where high sensitivity and

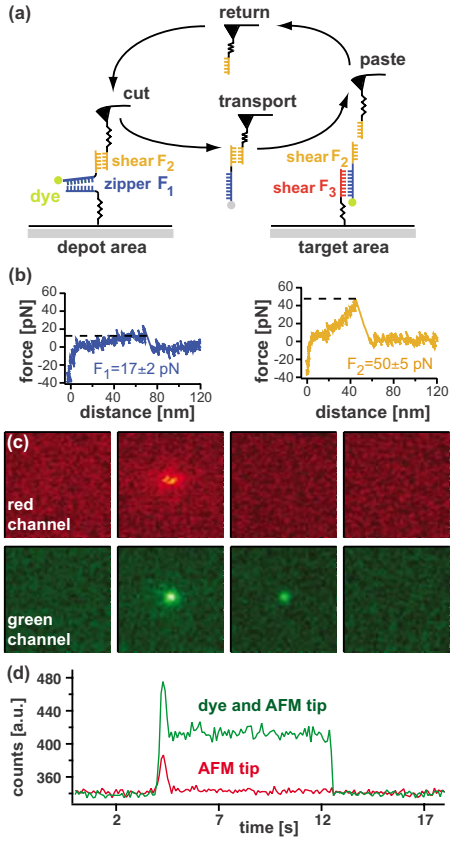

FIG. 5. (Color online) Single molecule cut-and-paste experiment performed using the combined TIRF-AFM microscope. (a) Fluorescently labeled DNA strands are transported by the AFM using a specific handle sequence on the tip and an anchor sequence on the cover slip surface. (b) High-resolution force spectra (d) and single molecule fluorescence time traces could be recorded simultaneously for many hours.

nanometer resolution is required. If no laser is used for TIRF excitation of the sample, or the laser's wavelength would interfere with the measurements, an IR laser could be used instead for determination of the cover slip distance by measuring the position of the totally reflected beam. Looking ahead, future AFM heads could already include an objective lens built in. This would not only allow for placing them directly on any (commercial) inverted microscope, but also would lower the AFM's center of mass, hence making it even more inert to interfering vibrations.

ACKNOWLEDGMENTS

We thank Ferdinand Kühner, Matthias Erdmann, and Jan Opfer for helpful discussions. This work was supported by the Nanosystems Initiative Munich (NIM) and the Stiftung Volkswagenwerk.

[1] A. Engel and H. E. Gaub, Annu. Rev. Biochem. **77**, 127 (2008).
[2] E. M. Puchner, A. Alexandrovich, A. L. Kho, U. Hensen, L. V. Schäfer, B. Brandmeier, F. Gräter, H. Grubmüller, H. E. Gaub, and M. Gautel, Proc. Natl. Acad. Sci. U.S.A. **105**, 13385 (2008).

Downloaded 24 Jun 2009 to 129.187.254.47. Redistribution subject to AIP license or copyright; see http://rsi.aip.org/rsi/copyright.jsp

[3] M. Rief, M. Gautel, and H. E. Gaub, Adv. Exp. Med. Biol. **481**, 129 (2000).
[4] P. K. Hansma, G. Schitter, G. E. Fantner, and C. Prater, Science **314**, 601 (2006).
[5] A. Hards, C. Zhou, M. Seitz, C. Bräuchle, and A. Zumbusch, ChemPhysChem **6**, 534 (2005).
[6] C. G. Morgan and A. C. Mitchell, J. Microsc. **222**, 48 (2006).
[7] L. Peng, B. J. Stephens, K. Bonin, R. Cubicciotti, and M. Guthold, Microsc. Res. Tech. **70**, 372 (2007).
[8] F. Kuhner and H. E. Gaub, Polymer **47**, 2555 (2006).
[9] D. Axelrod, N. L. Thompson, and T. P. Burghardt, J. Microsc. **129**, 19 (1983).
[10] D. Axelrod, J. Biomed. Opt. **6**, 6 (2001).
[11] M. Tokunaga, K. Kitamura, K. Saito, A. H. Iwane, and T. Yanagida, Biochem. Biophys. Res. Commun. **235**, 47 (2006).
[12] T. Funatsu, Y. Harada, H. Higuchi, M. Tokunaga, K. Saito, Y. Ishii, R. D. Vale, and T. Yanagida, Biophys. Chem. **68**, 63 (1997).
[13] A. Trache and G. A. Meininger, J. Biomed. Opt. **10**, 064023 (2005).
[14] A. Valbuena, J. Oroz, A. M. Vera, A. Gimeno, J. Gómez-Herrero, and M. Carrión-Vázquez, Rev. Sci. Instrum. **78**, 113707 (2007).
[15] T. Yamada, R. Afrin, H. Arakawa, and A. Ikai, FEBS Lett. **569**, 59 (2004).
[16] J. B. Thompson, B. Drake, J. H. Kindt, J. Hoskins, and P. K. Hansma, Nanotechnology **12**, 394 (2001).
[17] S. K. Kufer, E. M. Puchner, H. Gumpp, T. Liedl, and H. E. Gaub, Science **319**, 594 (2008).
[18] E. M. Puchner, S. K. Kufer, M. Strackharn, S. W. Stahl, and H. E. Gaub, Nano Lett. **8**, 3692 (2008).
[19] S. K. Kufer, M. Strackharn, S. W. Stahl, H. Gumpp, E. M. Puchner, and H. E. Gaub, Nat. Nanotech. **4**, 45 (2008).

Downloaded 24 Jun 2009 to 129.187.254.47. Redistribution subject to AIP license or copyright; see http://rsi.aip.org/rsi/copyright.jsp

P4 PHOTOTHERMAL CANTILEVER ACTUATION FOR FAST SINGLE-MOLECULE FORCE SPECTROSCOPY

Stahl SW, Puchner EM and Gaub HE.

REVIEW OF SCIENTIFIC INSTRUMENTS 2009 Jul;80(7):073702.

REVIEW OF SCIENTIFIC INSTRUMENTS **80**, 073702 (2009)

Photothermal cantilever actuation for fast single-molecule force spectroscopy

Stefan W. Stahl,[1,a)] Elias M. Puchner,[1,2] and Hermann E. Gaub[1]
[1]*Chair for Applied Physics and Center for NanoScience, Ludwig-Maximilians-University, Amalienstr. 54, Munich D-80799, Germany*
[2]*Center for Integrated Protein Science, Ludwig-Maximilians-University, Amalienstr. 54, Munich D-80799, Germany*

(Received 5 May 2009; accepted 2 June 2009; published online 1 July 2009)

Photothermal cantilever excitation provides a fast and easy to implement means to control the deflection of standard atomic force microscopy cantilevers. Minute heat pulses yield deflections on the order of several tens of nanometers or when the deflection is kept constant, forces of several hundreds of piconewton can be applied. In our case these pulses resulted in less than 1 K temperature changes at the sample position. Here we present and characterize the implementation of photothermal actuation for single-molecule force-spectroscopy experiments. When molecules are stretched under force-clamp conditions, fast control cycles that re-establish the pulling force after the rupture of molecular domains are essential for detecting the complete unfolding pattern with high precision. By combining the fast response of photothermal cantilever excitation with a conventional piezoactuator, a fast force-clamp with high accuracy and large working distances is reached. Simple feedback mechanisms and standard cantilever geometries lead to step response times of less than 90 μs, which is more than one order of magnitude faster than those of conventional force-clamp systems that are based only on piezo feedback. We demonstrate the fast and accurate performance of the setup by unfolding a protein construct consisting of one green fluorescent protein and eight surrounding immunoglobulin domains at constant force. © *2009 American Institute of Physics.* [DOI: 10.1063/1.3157466]

I. INTRODUCTION

Atomic force microscopy[1] (AFM) has evolved into a versatile technique for mechanical single-molecule experiments. The AFM provides high lateral precision for the one-by-one assembly of single molecules.[2–5] Also, the vertical precision and force sensitivity allows for the investigation of the energy landscape and function of biomolecules in force-spectroscopy experiments. The molecules under investigation are contacted by the tip of a cantilever, which acts as a flat spring, and are stretched, while the applied force and the extension are measured. In constant velocity experiments, the distance of the cantilever from the surface is constantly increased and force-extension traces are recorded. In this way protein domains can be unfolded and, upon approach, refolded again, allowing the examination of the potential width and the rates, which characterize the dynamic mechanical stability.[6] Changes in the unfolding profile can reveal the binding of ligands[7] and force-induced conformational transitions can alter the functional state of an enzyme as in the case of the force-sensor titin kinase.[8] Whereas force-extension experiments are ideal to measure and control the conformation related behavior of biomolecules, the force-clamp mode was developed to gain direct access to the time domain of protein unfolding,[9,10] folding,[11] or chemical reactions.[12] In these experiments the tension applied to the molecule is kept constant by adjusting the distance between cantilever and sample surface in a feedback loop. If, for example, a protein domain unfolds, the contour length of the protein increases and the force suddenly drops. The sample surface is then retracted in the feedback loop to the position at which the force is at the chosen value again.

In order to resolve details of such conformational transitions in feedback-regulated force-spectroscopy modes such as force-clamp or force-ramp, a rapid reaction of the mechanical actuator that adjusts the extension of the molecule is crucial. In most AFMs the actuation is achieved by piezoelectric elements. The response time is determined by the resonance frequency and phase shift, which depend on the stiffness and effective mass of the mechanical elements connecting either sample or cantilever base to these piezo elements. However, the upper limit of the response speed is always determined by the corner frequency of the cantilever itself. Therefore we have developed a technique that uses a cantilever as a fast actuator for force-spectroscopy by taking advantage of its photothermal bending. As depicted in Fig. 1, the conventional piezo AFM actuator design is expanded by a cantilever acting as the sample surface. The deflection of this cantilever is detected in the usual way by beam bounce. A second laser is focused on the base of the cantilever to locally heat and bend it, which is due to the different thermal expansion coefficients of its layer materials such as silicon nitride and metal coatings.

The photothermal effect has already proven to be fast

a)Electronic mail: stefan.stahl@physik.uni-muenchen.de.

 © 2009 American Institute of Physics

Downloaded 02 Jul 2009 to 129.187.254.47. Redistribution subject to AIP license or copyright; see http://rsi.aip.org/rsi/copyright.jsp

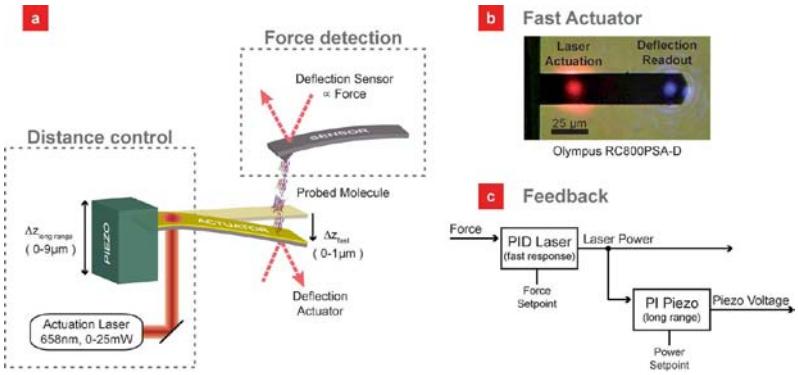

FIG. 1. (Color online) (a) Schematic drawing of the demonstrated setup. Two AFM heads are combined such that their cantilevers can get in contact. One of them serves as a force sensor like in traditional applications, the other one is used together with a piezo element as an actuator for distance control. Its deflection can be regulated by the intensity of a power-modulated laser due to the photothermal effect. The molecule of interest is probed between the two cantilevers. (b) Image of the actuator cantilever with the deflection readout and the regulating lasers focused on it. (c) Block diagram of the combined feedback loops. The actuator is regulated by the force signal from the cantilever and provides fast response to the unfolding of protein domains. The piezo adjusts the distance of the AFM head such that the feedback laser is held at an optimal operating point.

and accurate for high speed scanning AFM. It outperforms even sophisticated piezo feedbacks.[13] But its limited deflection range with standard AFM cantilevers and moderate laser power is not sufficient for force-spectroscopy applications with the goal of complete unfolding of large molecules. However, combining cantilever actuation with a slower piezo-based feedback results in both fast response and wide actuation amplitude.

Here we demonstrate and characterize for the first time a fast force-clamp AFM setup based on fast photothermal cantilever actuation combined with a long range piezo feedback. We demonstrate the performance of the setup by unfolding a fusion protein consisting of one green fluorescent protein (GFP) and eight immunoglobulin (Ig) domains[14] at a constant force.

II. EXPERIMENTS

A. Photothermal cantilever actuation

The laser illumination of the cantilever leads to a local heating of the cantilever material due to energy absorption. The resulting dynamic temperature profile depends on the material properties like thermal conductivity, density, specific heat capacity, and heat transfer coefficient to the ambient medium, as well as on the lever geometry and the illumination position. It is well described with a one-dimensional heat diffusion equation.[15] When a cantilever with layered materials is used, as is the case for the majority of standard cantilevers with a reflection enhancing metal coating, differences in the thermal expansion coefficients result in bending that releases mechanical stress. This bending principle is the same as in commonly used bimetal switches and thermometers.

For static illumination the cantilever deflection is proportional to the applied power (Fig. 2). For dynamic signals the efficiency of actuation drops with increasing frequency. Figure 3 shows the spectral amplitude response of the cantilever induced by sinusoidal laser excitation power in an aqueous solution. It is a convolution of the mechanical response of the cantilever spring (harmonic oscillator with resonant frequency f_R and quality factor Q) and the photothermal response, which decreases as the modulation frequency increases. This is because the temperature variation in the illuminated position and the thermal diffusion length decrease with higher frequency.[15] In order to obtain a precise and fast actuation response, a well-tuned controller is needed that modulates the laser power such that the deflection stays close to its set point over a wide frequency bandwidth.

B. Apparatus

The introduction of a second power-modulated laser in the AFM head adds a fast actuation element in the z direction in addition to the piezo. But the induced bending of a cantilever by photothermal actuation cancels the direct relation between the deflection and the external force applied to the stretched molecule. Therefore, one either has to calculate the photothermal effect when using a sole cantilever as sensor and actuator or introduce two distinct cantilevers that serve

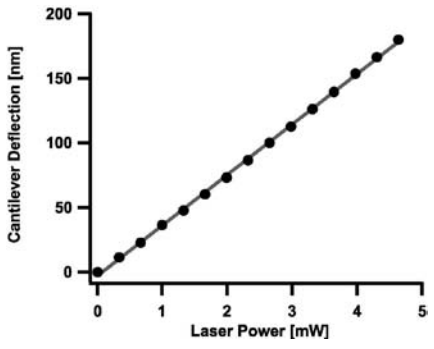

FIG. 2. Linearity of the photothermal bending of an Olympus RC800PSA-D lever. The gray line is a line fit to the measured deflection values at different laser diode powers with a slope of approximately 40 nm/mW.

Downloaded 02 Jul 2009 to 129.187.254.47. Redistribution subject to AIP license or copyright; see http://rsi.aip.org/rsi/copyright.jsp

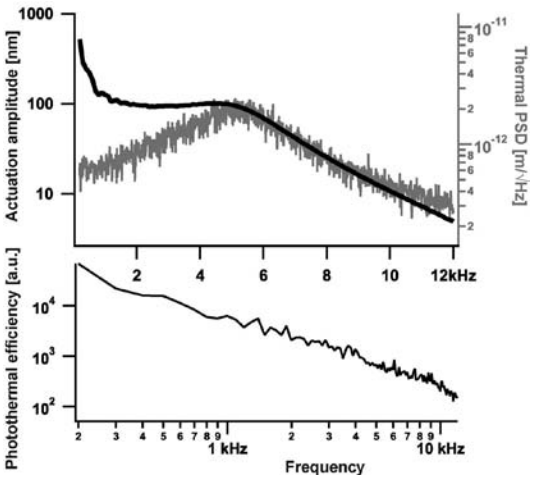

FIG. 3. Top: Frequency dependant drive efficiency of the actuator. The cantilever is driven with a sinusoidal excitation signal of about 11 mW amplitude. The resulting cantilever oscillation amplitude at the driving frequency (black) is a convolution of the photothermal excitation efficiency, decaying with increasing frequency, and the mechanical excitability of the cantilever, which is visible in the thermal noise power spectral density (thermal PSD, gray). Bottom: The photothermal excitation efficiency is the ratio of the photothermal driving amplitude and the thermal PSD.

as sensor and actuator, respectively. In the demonstrated setup we chose the latter strategy, since it allows for clearer interpretation of the data and provides a direct method for demonstrating the performance of the combined feedback system. Nevertheless, it is, in principle, possible to implement this photothermal actuation in a setup with only one cantilever if the dynamics of motion is well characterized as we will discuss later.

For the proof of principle experiments two custom-built AFM heads of the same design[16] were combined such that the two cantilevers can be brought into contact (see Fig. 1). Because they were built to work with optical microscopes, their vertical piezos are integrated in the head and such each AFM fills only one hemisphere. The two AFM controllers (MFP-3D controller, Asylum Research, Santa Barbara, CA, USA) were synchronized by a trigger channel such that the time delay for recorded data is lower than 100 μs. Cantilever positions are read out by optical beam deflection of infrared, superluminescent laser diodes. One cantilever (Olympus RC800PSA) served as actuator. Its deflection depends linearly on the power of an adjustable laser (658 nm, P_{max} =25 mW, Blue Sky Research, USA) focused on the lever near its fixed end. By mounting the lever upside down, the gold coating, which serves as a support for nonspecific protein adsorption, is oriented toward the other cantilever, which is used for force detection. Furthermore, the strength of the photothermal effect is increased roughly by a factor of 3 in this geometry since more power is absorbed by the lever when the laser hits the silicon nitride first. Infrared filters and different incident angles assure that no light from the actuation laser interferes with the deflection detection. Short bioelevers (Olympus RC150VB-A) were used as force sensors, because they combine fast response [f_R=7.9 kHz in 1x phosphate-buffered saline (PBS)] with a low spring constant (approximately 30 pN/nm) and a low photothermal response. During photothermal deflection of the actuator thermal bending of the sensor may occur due to heating of the surrounding fluid, which leads to errors in the force signal. For the given sensor/actuator combination the sensor deflection is less than 4% of the actuator deflection at constant illumination and thermal equilibrium. This corresponds to less than 1.3 pN/nm actuator deflection. During the experiment, only short laser pulses are applied and there is a time lag until equilibrium is reached, making the actual error much smaller. For typical illumination times shorter than 10 ms these values drop by one order of magnitude so that the deflection "crosstalk" amounts less than 0.4%. This effect could be completely suppressed by using uncoated cantilevers as sensors or by thoroughly adjusting the coating thickness such that the photothermal response of the sensor is minimized. Furthermore for the one-cantilever setup, which is proposed subsequently in this paper, this limiting effect is removed.

The excitation feedback used for keeping the pulling force constant consists of a combination of fast photothermal cantilever actuation with a small working range (<1 μm) and a slower piezo feedback with the full z-direction working rage of the AFM (approximately 9 μm). The deflection signal of the sensor is directly fed to a fast analog proportional-integral-derivative controller (Stanford Research Systems, SIM960, 100 kHz) that controls the current of the actuation laser. The current serves as input for the piezo PI feedback, which keeps the laser power at an optimal working point. A block diagram of the feedback system is depicted in Fig. 1(c).

The force sensing cantilever was calibrated by pushing it to a hard surface to determine the deflection sensitivity of the photodiode (nm/V) and by fitting a single harmonic oscillator response function to its thermal noise spectrum.[17] However, this method is not adequate to determine the deflection sensitivity of the actuator cantilever since the photothermally induced deflection depends on the heating spot position, and differs from the free cantilever response. Instead both cantilevers were brought into contact with the z-piezo while the photothermal force feedback was activated with a set point of about 50 pN. If the actuator is now moved further in the direction of the sensor with its piezo, the feedback compensates this movement by bending the actuator in the other direction. Since this bending equals the distance moved by the piezo, recording the actuator deflection versus the piezo position yields the actuator deflection sensitivity.

C. Combined feedback

The basic performance of the combined feedback on the actuator with input from the force sensing cantilever was tested under pushing conditions with feedback parameters keeping the cantilevers in contact at a force set point of 500 pN. The system was disturbed by applying step functions of different heights to the z-piezo of the sensor AFM head, which is not used for the position feedback and thus provides an easy means to check the regulatory behavior of the feed-

Downloaded 02 Jul 2009 to 129.187.254.47. Redistribution subject to AIP license or copyright; see http://rsi.aip.org/rsi/copyright.jsp

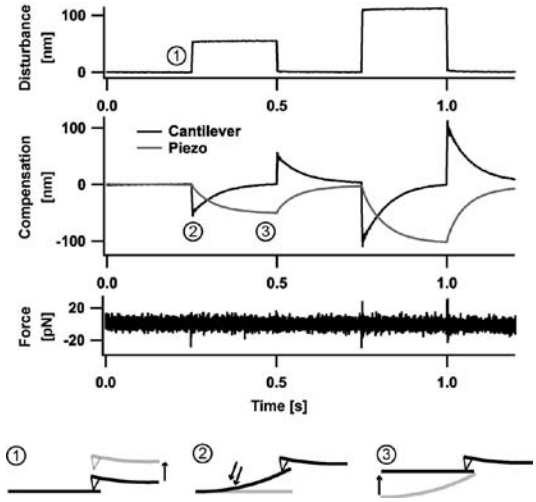

FIG. 4. Demonstration of the working principle of the combined actuator feedback. The force setpoint was chosen such that both AFM cantilevers are held together with contact force of 500 pN. If the system is disturbed with the sensor AFM piezo (top graph, step 1) the contact force is held constant (bottom graph) by the feedback loops. As a fast response the actuator is deflected photothermally (step 2). On a longer timescale the piezo feedback corrects for this deflection to assure that the actuator is held at an optimal operational point (step 3). The graph shows that the system is easily able to follow the maximum actuation speed of the disturbing piezo which nicely demonstrates that photothermal actuation is outperforming piezo actuation. The full performance of the photothermal feedback with the chosen cantilevers can be seen in Fig. 6.

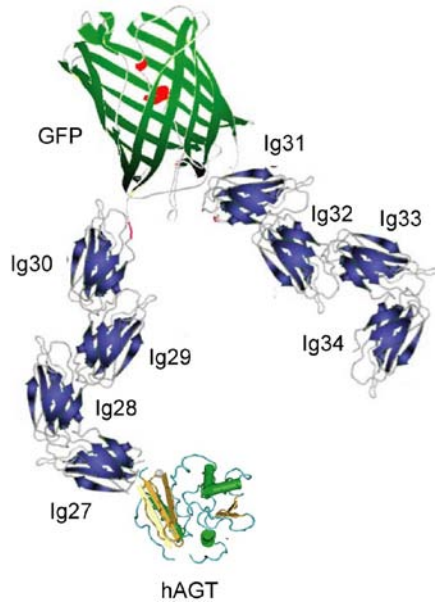

FIG. 5. (Color online) The Ig-GFP fusion protein that is used for the demonstrated force-clamp traces. It consists of eight Ig, one GFP, and one hAGT domain.

back loops. A sample trace is shown in Fig. 4. The disturbing movement is compensated with the two actuators. As a fast response, the actuation cantilever is deflected by the laser in the same direction as the disturbance. The feedback loop acting on the actuator AFM piezo recognizes the actuator deflection and moves the piezo with a slower time constant to assure that the laser power is held at a good operational point for full actuation amplitude of further steps. This proves that the combined feedback is easily able to follow the maximum response speed of the disturbing piezo (approximately 50 μm/s initial slope) and shows that photothermal actuation is outperforming a sole movement of the piezo. Under single-molecule force-clamp conditions, the response of the feedback was further increased and the cantilever and piezo response was even faster.

D. Ig-GFP fusion protein unfolding

As a model system, we used an Ig-GFP fusion protein consisting of eight titin Ig domains, one GFP-domain, and one human O^6-alkylguanine-DNA-alkyltransferase (hAGT) domain, which may be immobilized to the surface. It is depicted in Fig. 5 and described in detail in Ref. 14. The Ig domains unfold with a contour length increment of 29.0 ± 0.5 nm (Ref. 18) and the GFP in up to two substeps with a total increment of 76.6 ± 0.6 nm.[19] Proteins were allowed to adsorb to the actuator cantilever from a 300 μg/ml solution in PBS (pH 7.4, 150 mM NaCl). After 10 min of incubation, the sample was rinsed with PBS and measurements were started.

Figure 6 shows sample traces, which clearly reveal the stepwise unfolding of several protein domains with increments of 49.1, 11.2, 4.6, 26.0, 25.7, and $\pm$ 0.6 nm, respectively. The first three steps together are equal to 85% of the contour length increment in GFP and the last two correspond to 90% and 89% of the contour length increment in individual Ig domains. Due to the entropic elasticity of polymer chains, the observed step sizes in force-clamp experiments are smaller than the characteristic contour length increments and depend on the pulling force.[9] The measured values match the expectations very well[20] even though the trace plateaus are not completely stable but exhibit a drift on the order of 2 nm. This drift can be due to several effects. First, the AFM heads are not temperature stabilized and thus already small changes in the environment temperature may lead to position nonconformance of the piezo sensor in the nanometer regime. Second, there is a slight decay in the tip-sample distance that correlates with the displacement of the actuating cantilever. This might either be caused by uncertainties in the inverse cantilever sensitivity or by the thermal crosstalk with the sensing cantilever that was discussed above.

As mentioned in the introduction, the fast re-establishment of the pulling force after the rupture of a domain is crucial for the proper detection of unfolding substeps and for the interpretation of force-clamp data in terms of (un)folding. The response time for force re-establishment can be determined by fitting the force trace with a single exponential function. For the given 200 μm long actuator with a

Downloaded 02 Jul 2009 to 129.187.254.47. Redistribution subject to AIP license or copyright; see http://rsi.aip.org/rsi/copyright.jsp

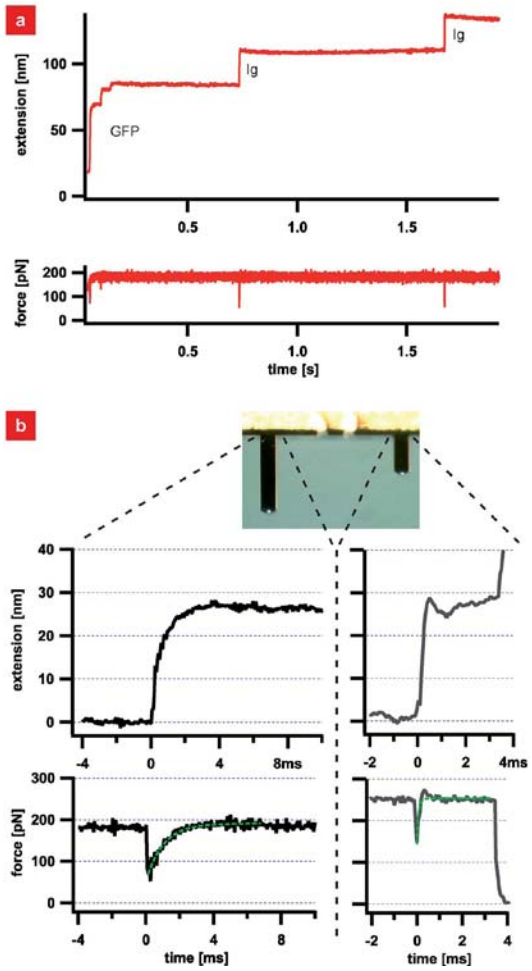

FIG. 6. (Color online) Unfolding traces of the Ig-GFP fusion protein under force-clamp conditions. (a) Unfolding of GFP and two Ig domains with an Olympus RC800PSA-D cantilever at 180 pN pulling force. Substeps of GFP unfolding are observable. (b) Black: zoom in the unfolding of the first Ig domain. The force is re-established with a time constant of 930 μs (fitted line). Gray: unfolding of an Ig domain with a faster actuator (Olympus RC800PSA-B) and higher feedback gains at 250 pN pulling force. The characteristic time constant gets reduced to 80 μs. At t=4 ms the unspecific binding to the cantilever ruptures and the force drops to zero.

resonance frequency of f_R=5.2 kHz (RC800PSA-D), the time constant of the rise was around 1 ms [Fig. 6(b), black]. Since small cantilevers provide advantages in AFM,[21] we also used a shorter actuator with a fivefold higher resonance frequency and higher feedback gains. The measured response time of only 80 μs during protein unfolding [Fig. 6(b), gray] is about one order of magnitude faster than conventional piezo based AFMs and nicely shows that the limitation is so far only given by the mechanical and photothermal response of the actuator.

One may argue that the temperature rise of the cantilever and its surroundings induced by the modulation laser modifies the ambient conditions of the protein or even denatures it. However, measuring the cantilever deflection while changing the buffer temperature gave a photothermal sensitivity of 92 ± 5 nm/K for the RC800PSA-D cantilever. This is the sensitivity for a uniform heat profile over the whole cantilever length. During photothermal bending the temperature profile has its maximum close to the rear end so the impact on the protein is even smaller. Given that typical domain lengths are shorter than 100 nm and that the piezo feedback assures that the laser power is only shortly raised during domain rupture, the temperature differences applied to the protein are below 1 K and thus negligible.

III. DISCUSSION

We have presented a novel technique that allows fast control of the cantilever position in single-molecule force-spectroscopy experiments by combining photothermal cantilever actuation with a traditional piezo actuator. As the photothermal effect acts on the cantilever itself, actuation is performed as directly as possible and response times are in principle much faster than for piezo-based feedbacks, which have to move at least the mass of the sample and its holder. The combination of the photothermal actuation with a piezo allows a wide working range. With the simple feedback mechanism and standard cantilevers, the response time for the force re-establishment after unfolding of titin Ig domains was only 80 μs, corresponding to an actuation bandwidth of 12.5 kHz. By compensating the frequency dependence of the photothermal effect electronically and by optimizing the cantilever geometries, much faster actuation could be achieved. In the AFM imaging application, for example, Yamashita *et al.*[13] reached feedback bandwidths on the order of 100 kHz for photothermal cantilever actuation. Further improvement of the feedback can be reached by electronically damping the quality factor of the first eigenmode (Q control) and by different controller types such as field programmable gate arrays.[22]

The measurement setup that we presented consists of two cantilevers, one serving as a force sensor, and the other as a displacement actuator. The separation of sensing and actuating gives a more direct insight into the dynamic variables but in principle it is possible to use the same cantilever for both. This requires a thorough characterization of the actuation dynamics and programmable sets of filters[22] in order to obtain the applied force from the deflection signal and the dynamic laser power. Such a setup would allow very fast actuation even for AFM heads that are designed to work with optical microscopes.[16] They so far have been suffering from slower dynamics since the complete head or at least a large part of it has to be moved by the piezo.

ACKNOWLEDGMENT

We thank Ann Fornof and Mathias Strackharn for discussions. This work was supported by the Nanosystems Initiative Munich (NIM), Center for Integrated Protein Science Munich (CIPSM) and the Deutsche Forschungsgemeinschaft Grant No. SFB 486.

[1] G. Binnig, C. F. Quate, and C. Gerber, Phys. Rev. Lett. **56**, 930 (1986).

Downloaded 02 Jul 2009 to 129.187.254.47. Redistribution subject to AIP license or copyright; see http://rsi.aip.org/rsi/copyright.jsp

[2] S. K. Kufer, E. M. Puchner, H. Gumpp, T. Liedl, and H. E. Gaub, Science **319**, 594 (2008).
[3] E. M. Puchner, S. K. Kufer, M. Strackharn, S. W. Stahl, and H. E. Gaub, Nano Lett. **8**, 3692 (2008).
[4] S. K. Kufer, M. Strackharn, S. W. Stahl, H. Gumpp, E. M. Puchner, and H. E. Gaub, Nat. Nanotechnol. **4**, 45 (2009).
[5] A.-S. Duwez, S. Cuenot, C. Jérôme, S. Gabriel, R. Jérôme, S. Rapino, and F. Zerbetto, Nat. Nanotechnol. **1**, 122 (2006).
[6] M. Rief, M. Gautel, F. Oesterhelt, J. M. Fernandez, and H. E. Gaub, Science **276**, 1109 (1997).
[7] J. P. Junker, F. Ziegler, and M. Rief, Science **323**, 633 (2009).
[8] E. M. Puchner, A. Alexandrovich, A. L. Kho, U. Hensen, L. V. Schäfer, B. Brandmeier, F. Gräter, H. Grubmüller, H. E. Gaub, and M. Gautel, Proc. Natl. Acad. Sci. U.S.A. **105**, 13385 (2008).
[9] A. F. Oberhauser, P. K. Hansma, M. Carrion-Vazquez, and J. M. Fernandez, Proc. Natl. Acad. Sci. U.S.A. **98**, 468 (2001).
[10] S. Garcia-Manyes, J. Brujic, C. L. Badilla, and J. M. Fernandez, Biophys. J. **93**, 2436 (2007).
[11] J. M. Fernandez and H. B. Li, Science **303**, 1674 (2004).
[12] A. P. Wiita, R. Perez-Jimenez, K. A. Walther, F. Gräter, B. J. Berne, A. Holmgren, J. M. Sanchez-Ruiz, and J. M. Fernandez, Nature (London) **450**, 124 (2007).
[13] H. Yamashita, N. Kodera, A. Miyagi, T. Uchihashi, D. Yamamoto, and T. Ando, Rev. Sci. Instrum. **78**, 083702 (2007).
[14] S. K. Kufer, H. Dietz, C. Albrecht, K. Blank, A. Kardinal, M. Rief, and H. E. Gaub, Eur. Biophys. J. **35**, 72 (2005).
[15] D. Ramos, J. Tamayo, J. Mertens, and M. Calleja, J. Appl. Phys. **99**, 124904 (2006).
[16] H. Gumpp, S. W. Stahl, M. Strackharn, E. M. Puchner, and H. E. Gaub, Rev. Sci. Instrum. **80**, 063901 (2009).
[17] H. J. Butt and M. Jaschke, Nanotechnology **6**, 1 (1995).
[18] E. M. Puchner, G. Franzen, M. Gautel, and H. E. Gaub, Biophys. J. **95**, 426 (2008).
[19] H. Dietz and M. Rief, Proc. Natl. Acad. Sci. U.S.A. **101**, 16192 (2004).
[20] The unfolding of an entropic spring that is modeled with the worm like chain model at a persistence length of 0.3 nm yields a partial stretching of 86% at 180 pN pulling force.
[21] M. B. Viani, T. E. Schäffer, A. Chand, M. Rief, H. E. Gaub, and P. K. Hansma, J. Appl. Phys. **86**, 2258 (1999).
[22] Y. Jeong, G. R. Jayanth, and C. H. Menq, Rev. Sci. Instrum. **78**, 093706 (2007).

Downloaded 02 Jul 2009 to 129.187.254.47. Redistribution subject to AIP license or copyright; see http://rsi.aip.org/rsi/copyright.jsp

P5 RESOLVING SINGLE-MOLECULE ASSEMBLED PATTERNS WITH SUPERRESOLUTION BLINK-MICROSCOPY

Cordes T, Strackharn M, Stahl SW, Summerer W, Steinhauer C, Forthmann C, Puchner EM, Vogelsang J, Gaub HE, Tinnefeld P.

NANO LETTERS 2010 Feb 10;10(2):645-51.

NANO LETTERS

pubs.acs.org/NanoLett

Resolving Single-Molecule Assembled Patterns with Superresolution Blink-Microscopy

Thorben Cordes,† Mathias Strackharn,† Stefan W. Stahl, Wolfram Summerer, Christian Steinhauer, Carsten Forthmann, Elias M. Puchner, Jan Vogelsang, Hermann E. Gaub, and Philip Tinnefeld*

Applied Physics—Biophysics and Center for NanoScience, Ludwig-Maximilians-Universität, Amalienstrasse 54, D-80799 München, Germany

ABSTRACT In this paper we experimentally combine a recently developed AFM-based molecule-by-molecule assembly (single-molecule cut-and-paste, SMCP) with subdiffraction resolution fluorescence imaging. Using "Blink-Microscopy", which exploits the fluctuating emission of single molecules for the reconstruction of superresolution images, we resolved SMCP assembled structures with features below the diffraction limit. Artificial line patterns then served as calibration structures to characterize parameters, such as the labeling density, that can influence resolution of Blink-Microscopy besides the localization precision of a single molecule. Finally, we experimentally utilized the adjustability of blink parameters to demonstrate the general connection of photophysical parameters with spatial resolution and acquisition time in superresolution microscopy.

KEYWORDS Superresolution microscopy, single-molecule cut-and-paste, superresolution calibration, single-molecule fluorescence, blink-microscopy, atomic force microscope (AFM)

Modern fluorescence microscopy techniques localize the position of individual molecules with nanometer precision,[1] and by temporally separating the fluorescence of the emitters allow subdiffraction resolution imaging of complex samples such as biological specimen.[2−7] The so-called Blink-Microscopy belongs to this class of techniques[7] that can find a broad range of novel applications in cell biology as well as material sciences. This in turn has raised fundamental questions on the interplay between fluorophore density and achievable resolution as a function of the specific parameters of the method and the fluorescent probes used.

A thorough validation of novel superresolution microscopy techniques requires well-defined samples with programmable positions of individual fluorophores. Prominent examples for bottom-up approaches to assemble such structures are DNA-origami,[8,9] dip-pen nanolithography,[10] nanopipette deposition,[11] or a "one-by-one" assembly, for example, single-molecule cut-and-paste (SMCP) surface assembly.[12−14] In this paper, we combine SMCP surface assembly with superresolution microscopy based on the subsequent localization of single fluorophores termed Blink-Microscopy. We used SMCP to create structures with subwavelength size features and used Blink-Microscopy to resolve these structures. We then assembled calibration patterns by SMCP and used them to clarify questions regarding blink parameters, achievable resolution, and maximal resolvable fluorophore density. In particular, we experimentally demonstrate the trade-off between spatial resolution and acquisition time of Blink-Microscopy and related approaches.[7,15,16]

SMCP is based on the bottom-up assembly of DNA-oligomers and offers a spatial precision down to a few nanometers for placing single molecules (see Figure 1a,b).[13] The units to be assembled, here fluorophore-labeled DNA, are picked up with an AFM tip from a depot and transferred to a target area (Figure 1, see Supporting Information, Material and Methods for details). The directionality of the process is provided by a hierarchical force system and the selectivity of DNA hybridization. The bond of the transfer DNA to the DNA immobilized at the cantilever tip is stronger than the one to the DNA in the depot area. DNA immobilized in the target area, finally, is mechanically most stable. As this process may be repeated several thousand times with the same AFM tip, SMCP allows the assembly of arbitrary structures in two dimensions. Since the small molecules are often assembled on soft surfaces, it is difficult to resolve the structures from their topology. Previous attempts to monitor the positions of molecules placed at subwavelength distances were limited to only a few single molecules.[13]

On the other hand, superresolution fluorescence microscopy has tremendously evolved over the last years starting out with stimulated emission depletion (STED) microscopy.[17,18] More recent techniques are based on the subsequent localization of single molecules and utilize the fact that the position of a single emitter, detected in a wide-field microscope, can be determined with nanometer precision. To this end the fluores-

* To whom correspondence should be addressed. E-mail: philip.tinnefeld@lmu.de. Fax: +49 89 2180 2005.

†These authors contributed equally to this work.

Received for review: 11/8/2009
Published on Web: 00/00/0000

© XXXX American Chemical Society

DOI: 10.1021/nl903730r | *Nano Lett.* **XXXX,** *xxx,* 000-000

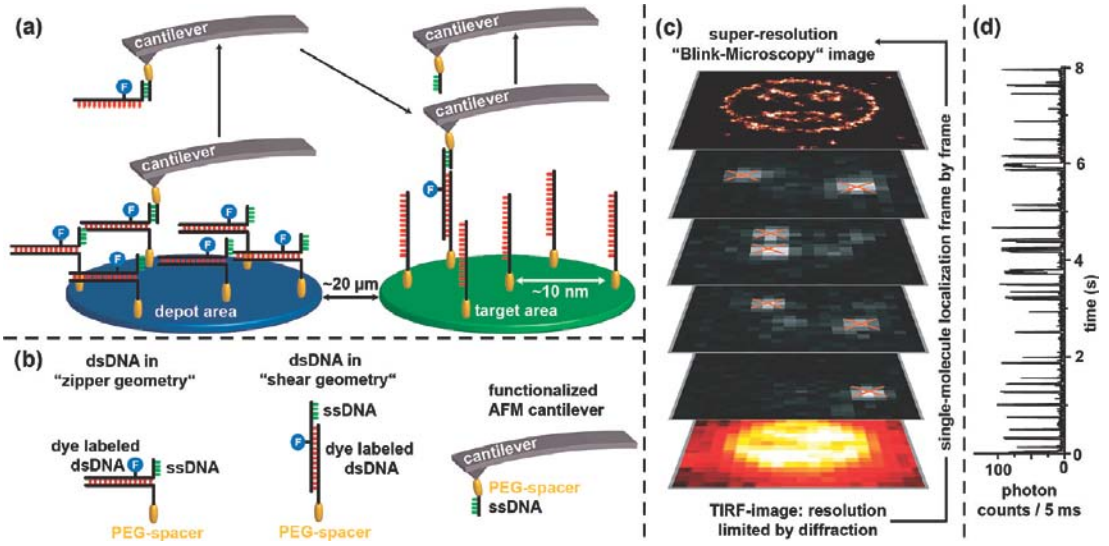

FIGURE 1. (a) Schematic illustration of single-molecule cut-and-paste and (b) corresponding caption. (c) Illustration of superresolution microscopy based on the subsequent localization of "blinking" fluorophores. (d) Fluorescent transient of a single immobilized ATTO655 molecule in aqueous PBS-buffer obtained by confocal microscopy (addition of 50 μM ascorbic acid in the presence of oxygen, excitation at 640 nm with 4 kW/cm^2).

cence of the molecules within the area of one point-spread-function is separated in time by switching all except one molecule into a nonfluorescent dark state (Figure 1c). This switching is achieved, for example, using photoswitchable fluorophores (PALM, STORM, FPALM, dSTORM)[3−6,19,20] or generic metastable dark states of the fluorophores such as radical ion states (Blink-Microscopy, GSDIM).[7,16,21−23] In Blink-Microscopy, for example, continuous ON/OFF-switching of the fluorophores is controlled by electron-transfer reactions. The environment of the fluorophore provides reductant molecules that induce the formation of radical anion states with a lifetime of nanoseconds to minutes.[7,16,24] The lifetime of these metastable OFF-states can be controlled by the oxidant concentration that restores the fluorophore in the fluorescent singlet manifold. The number of counts per cycle (ON-counts) is controlled by the reductant concentration and the ON-time is additionally adjusted by varying the excitation intensity. Blinking in single-molecule fluorescence transients reflects this redox cycle (Figure 1d).[16] Figure 1c illustrates the process of reconstructing superresolution images from movies of blinking molecules in which each single molecule is localized using a Gaussian fit.

For techniques that rely on the subsequent localization of single molecules, resolution is not clearly defined and a thorough characterization has not been performed due to the lack of calibration structures. The main factor in terms of resolution is the localization precision of single molecules, which is closely related to the number of photons detected per ON-state and the signal-to-noise ratio.[25] However, other factors that have not yet been included in a formula contribute to the achievable resolution of superresolution techniques such as the label size, the molecular and labeling density (e.g., the Nyquist criterion has to be met),[15] and the fraction of molecules that are actually (photo)activated and not photobleached. In addition, for techniques with spontaneous formation of the fluorescent form, the ratio of OFF- to ON-times (τ_{off}/τ_{on}) limits the number of fluorophores that can actually be colocalized within one diffraction limited area.[7] While this limitation obviously applies to Blink-Microscopy and related realizations of superresolution microscopy,[7,21−23] it is also important for techniques that apply photochromic molecules due to common spontaneous activation of, for example, fluorescent proteins and cyanine dyes or in case of the two wavelengths for switching and readout are used simultaneously.[26] Hitherto, the resolving power of superresolution microscopy has commonly been demonstrated with comparably undefined filamentous proteins such as actins and microtubules that were stained in vitro or in fixed cells. Test and calibration systems are required that have a defined structure with a known number of fluorophores to quantify the factors influencing resolution and to make the different techniques comparable with each other.

Recently, the use of dye-labeled DNA-origami as a nanoscopic distance ruler serving as a calibration standard for superresolution microscopy was established.[9] Here, two fluorophores with designed distance were suggested for calibrating superresolution microscopes. In contrast to this work, we now created structures by the complementary SMCP approach to demonstrate that complex structures, which are not resolvable by conventional microscopy, can be resolved utilizing Blink-Microscopy. In detail, the flexibility of SMCP was used to assemble complex structures with more than a hundred fluorophores that served for a characterization of parameters that influence resolution of

© XXXX American Chemical Society

DOI: 10.1021/nl903730r | *Nano Lett.* **XXXX,** *xxx,* 000-000

NANO LETTERS

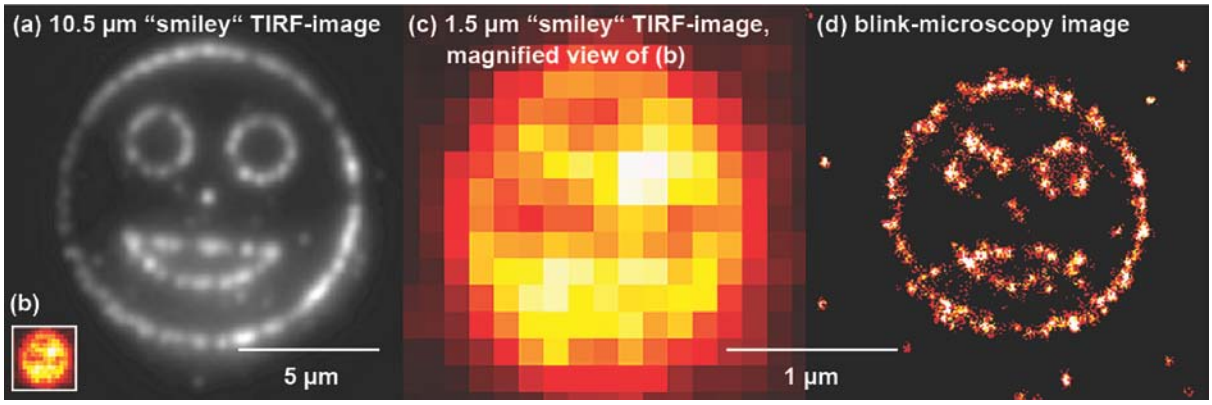

FIGURE 2. Images of patterns assembled by single-molecule cut-and-paste. (a) TIRF-image of a 10.5 μm diameter smiley (~650 transport-DNA labeled with the fluorophore Cy3; experiment conducted in PBS-buffer, 532 nm excitation with ~0.25 kW/cm^2) and (b) TIRF image of a 1.5 μm diameter smiley from another experiment as inset (~125 transported DNA labeled with the fluorophore ATTO655; experiment conducted in PBS-buffer, 50 μM AA as reductant, ambient oxygen as oxidant, 647 nm excitation with ~ 50 kW/cm^2). Scale bar for both panels (a,b) is 5 μm. (c,d) Magnified TIRF image and corresponding superresolution image of the smiley from inset panel (b) with 1.5 μm diameter; please note the smaller size of the scale bar of 1 μm corresponding to panels (c,d).

Blink-Microscopy. For example, line patterns were created to characterize the trade-off between spatial and temporal resolution of superresolution methods that separate the fluorophore emission of single emitters in time.

First, we assembled structures such as a smiley and visualized the patterns with fluorescence microscopy. Figure 2a shows an image of a smiley structure with a diameter of 10.5 μm. For this image an approximate number of 650 DNA-oligomers and attached Cy3-fluorophores were transported. All details of the structure, for example, eyes, nose, and mouth could be clearly resolved utilizing total-internal-reflection fluorescence (TIRF) microscopy.

In another experiment with the dye ATTO655 we reduced the size of the assembled smiley by a factor of ~7 down to 1.5 μm diameter, resulting in a structure with subwavelength size features. In contrast to the data in Figure 2a, no details of this smiley (Figure 2b, inset), except its circular structure, could be resolved (Figure 2b,c). Subdiffraction resolution images were subsequently recorded utilizing Blink-Microscopy. For recording these images, the oxazine dye ATTO655 was used in combination with 50 μM ascorbic acid (AA) in the presence of oxygen. Under these conditions, ATTO655 showed continuous blinking (see Figure 1d and ref 16) allowing a superresolution image to be obtained. Figure 2d clearly reveals all details of the smiley with eyes, nose, and mouth. A few gaps in the image are related to a significant fraction of inactive molecules among the transported fluorophores. In contrast to Cy3, we found that a fraction of ATTO655 fluorophores degraded during a drying step of the surface preparation procedure (see Supporting Information for details on sample preparation). The data presented in Figure 2 already demonstrates that Blink-Microscopy is a valuable tool for studying the nanomechanical assembly of SMCP on a length-scale below 200 nm.

Next, SMCP was utilized for a quantitative characterization of parameters that determine resolution for Blink-Microscopy and related approaches.[21,22] For isolated single immobilized ATTO655, that is, molecules which are not located in a distinct pattern (see points in Figures 2 and 3), OFF-times were determined to $\tau_{off} = 430$ ms, ON-times were ~2−3 ms with 800 ± 400 ON-counts under the applied buffer conditions (aerated PBS with 50 μM AA; for further details see Supporting Information). Those single molecules could be localized with a precision of 20 ± 4 nm, in accordance with theoretical expectations (a discussion of the experimentally observed versus theoretically expected resolution is found in the Supporting Information and ref 27).

When assembling line-structures with SMCP (Figure 3), we found an experimental width of a single line of 56 ± 16 nm. This value was derived from ~40 lines with 500 nm length, where each line consisted of several ATTO655 fluorophores assembled at 15 nm separation. The standard deviations were determined from Gaussian fits of a projection of the localization frequency at a single coordinate onto the *x*-axis, which results in histograms such as depicted in Figure 3c,j. This larger line width of 56 nm compared to the localization precision of single molecules of 20 nm is related to noise of the SMCP process. With a nominal tip diameter of ~20 nm and a flexible polymer handle that induces an uncertainty of ±10 nm,[13] we estimated the spatial accuracy of SMCP, which is directly related to the physical width of the assembled line to 40 nm. The SMCP-precision was caused by a denser functionalization of the cantilever compared to previous experiments.[13] Together with the optical localization precision of Blink-Microscopy of 20 nm, the expected measured line width by Blink-Microscopy was of the order of ~60 nm, a value that is in neat accordance with the experimentally determined width of a single line of 56 ± 16 nm.

© XXXX American Chemical Society

DOI: 10.1021/nl903730r | *Nano Lett.* **XXXX,** *xxx,* 000-000

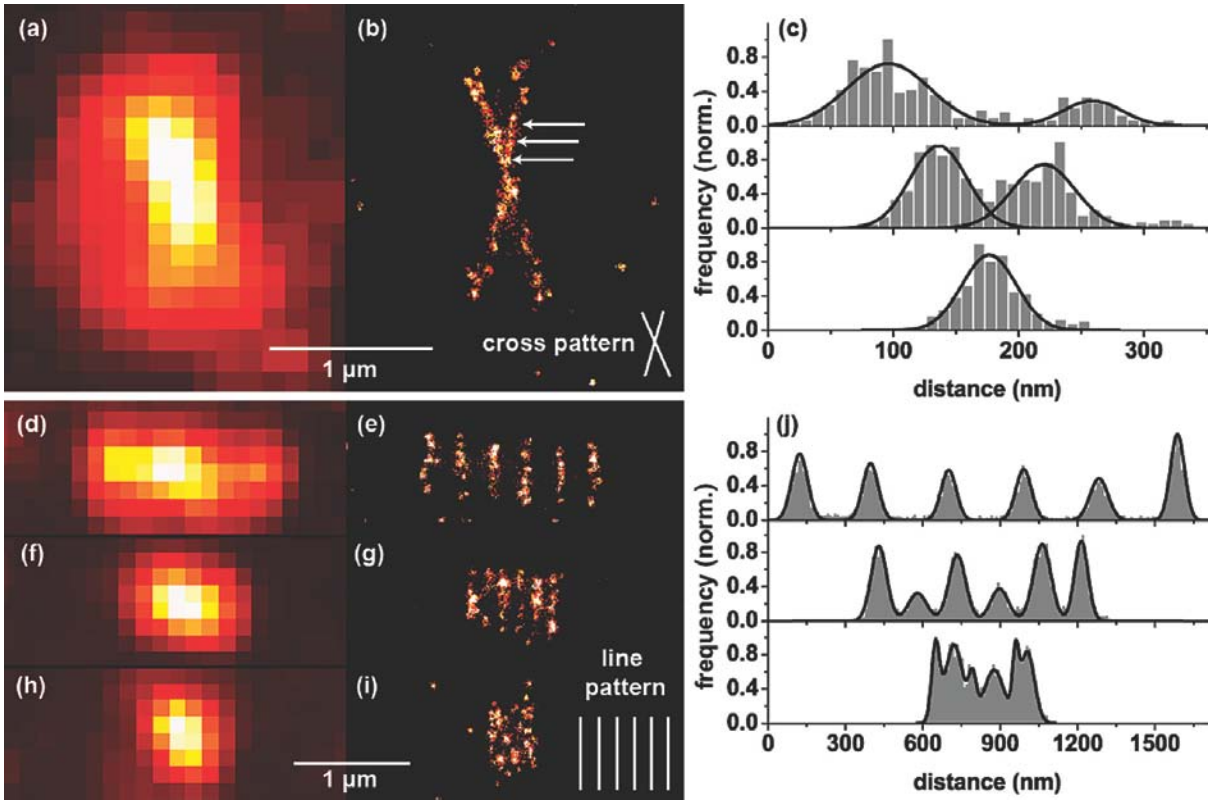

FIGURE 3. Examples of Blink-Microscopy images of subdiffraction patterns assembled by SMCP (PBS containing 50 μM AA as reductant, ambient oxygen served as oxidant). (a,b) TIRF and superresolution image of a cross pattern consisting of two lines (1.5 μm length) intersecting at an angle of 35°. The cross pattern consists of ~180 fluorophores. Panel (c) shows the corresponding histograms of single-molecule localizations at marked positions, at the positions indicated in panel (b). These histograms show that line distances of 160 nm (upper panel) and 80 nm (middle part) were clearly resolved, whereas in the range of the line-width (50 nm, lower part) the lines were no longer distinguishable. (d–i) Line grids consisting of a pattern of six parallel lines (0.5 μm length, representing ~150 active fluorophores) with decreasing spacing between the lines. Panels (d,e) show a TIRF and a superresolution image of a line grid with 300 nm spacing, (f,g) show data for 150 nm spacing, and (h,i) show data of a line grid with 75 nm spacing. Corresponding histograms of single-molecule localizations for the different superresolution images of the line grids are displayed in panel (j).

The combination of SMCP and Blink-Microscopy was then used for an actual calibration and characterization of (i) spatial resolution and (ii) resolvable fluorophore density. Therefore two different types of calibration structures were assembled with ATTO655 labeled DNA and subsequently imaged with superresolution microscopy to resolve the assembled structure. Figure 3 shows the TIRF (a) and corresponding superresolution image (b) of a "cross pattern" consisting of two lines with 1.5 μm length, intersecting at an angle of 35°. The superresolution image (Figure 3b) clearly reveals the fine-structure of the cross pattern that is not resolved in the TIRF-image (Figure 3a). The cross pattern was analyzed by taking horizontal slices of single-molecule localizations as shown in Figure 3c. Arrows in Figure 3b mark the different positions where histograms were taken. The depicted histograms were generated by a projection of the absolute number of single-molecule localizations of the respective pixel onto the horizontal axis. Histograms at the different positions reveal that a peak to peak distance of 160 nm (Figure 3c, upper panel) and 80 nm (Figure 3c, middle panel) between the lines was easily resolved. The histogram corresponding to the lowest arrow (Figure 3c, lower panel) in Figure 3b shows that in the range of the line-width of ~50–60 nm the two lines are no longer distinguishable. These data show that the achievable resolution when assembling and imaging line patterns is in the range of ~50–60 nm due to combined errors from SMCP and Blink-Microscopy.

The cross-pattern allows a qualitative estimate of the achievable spatial resolution of SMCP assembled lines. When several lines are close together the fluorophore density within one diffraction-limited area that is within 310 nm FWHM (full width at half-maximum) in our microscope increases. This leads to an increasing probability that two fluorophores emit simultaneously and deteriorate resolution. Blink-Microscopy offers an easy way to react to higher fluorophore density since the ON-counts and OFF-times are independently tunable through variation of the concentrations of reductant and oxidant, respectively.[16] At higher

© XXXX American Chemical Society

DOI: 10.1021/nl903730r | *Nano Lett.* **XXXX,** *xxx,* 000-000

NANO LETTERS

oxidant concentration, the OFF-times are shortened and the number of molecules that can be independently localized decreases. The advantage, however, is the fast recording time with fast blinking since more molecules could be localized within a shorter period of time. Vice versa, the OFF-times can be extended to react to the fluorophore density of the sample and the structural details to be resolved by decreasing the oxidant concentration. The τ_{off}/τ_{on}-ratio thereby is the central parameter that determines the resolvable fluorophore density. In order to quantify this trade-off of spatial and temporal resolution experimentally,[7,15] we assembled patterns consisting of six parallel lines with a variable spacing between them. The size of the grids was always greater than the size of the PSF, so that the grid-size is effectively infinite for an observation volume in the middle of the grid. The spacing between the lines was varied between 300 and 50 nm thereby increasing the fluorophore density. Subsequently, superresolution blink-images were recorded to check whether the respective line grid could be resolved at a given ratio of τ_{off}/τ_{on}. We defined a line grid resolved, if all the lines within the structure were clearly separated, i.e., six separate peaks with the appropriate spacing were observed in the histograms. Subsequently, we varied the OFF-times using different oxidant concentrations in order to experimentally study the trade-off between spatial and temporal resolution.

Figure 3 shows three line grids with a spacing of 300 nm (Figure 3d,e and associated histogram in the upper panel of Figure 3j), 150 nm (Figure 3f,g and associated histogram in the middle panel of Figure 3j) and 75 nm (Figure 3h,i and associated histogram in the lower panel of Figure 3j). With TIRF-microscopy, none of the grids was resolved as expected for the line-spacing and pixel-size of the TIRF-image of 137 nm. The superresolution images (Figure 3e,g,h) and the associated histograms (Figure 3j, 50 μM AA in the presence of oxygen, ratio of $\tau_{off}/\tau_{on} = 200$) reveal that the grids are resolved utilizing Blink-Microscopy; all histograms show six peaks at average distances of 292 ± 12 nm for the 300 nm line grid (Figure 3j, upper panel), 157 ± 7 nm for the 150 nm line grid (Figure 3j, middle panel), and 71 ± 15 nm for the 75 nm line grid (Figure 3j, lower panel).

Next, we quantified the fluorophore density for different line grids using the following approximation. In the case of aerated PBS with 50 μM AA and no 1,1′-dimethyl-4,4′-bipyridinium dichloride hydrate (methyl viologen, MV) present, the average number of localizations for a single-molecule over 8000 frames was 35 ± 16. A typical line grid, as shown in Figure 3, was characterized by 3000−4000 localizations over 8000 frames which translates into a maximal number of ~150 active fluorophores per grid. Note that this approximation incorporates the fact that the spot-finding algorithm discards ~25% of all localized events. This means that a single line with a length of 1 μm typically consists of ~50 active fluorophores. Using this approximation, we estimated the fluorophore density in molecules per μm^2 for different line grids; a line grid with 300 nm spacing shows a density of ~150 fluorophores/μm^2, a grid of 200 nm ~250 fluorophores/μm^2, a grid of 150 nm spacing contains ~300 fluorophores/μm^2, a grid of 100 nm spacing contains ~500 fluorophores/μm^2, a grid of 75 nm spacing contains ~650 fluorophores/μm^2, and finally a 50 nm grid contains 1000 fluorophores/μm^2.

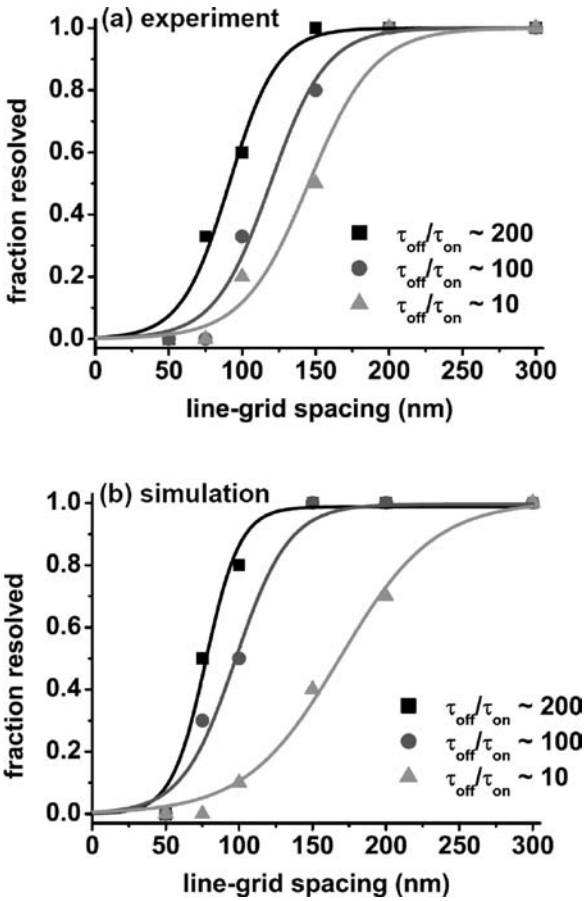

FIGURE 4. (a) Experimental values of the resolved line grid fraction for different ratios of τ_{off}/τ_{on}. The data were fitted with sigmoidal functions $y(x) = 1 - 1/(1 + e^{(x-a)/b})$ with a and b as free parameters. Further details about the statistics of the experiments and the determination of ON- and OFF-times can be found in the Supporting Information. (b) Similar results and associated fit functions of Monte Carlo-Simulations; for details, see Supporting Information.

To quantify the achievable number of resolved fluorophores per PSF-width in terms of "resolvable line grid fraction", which is the number of resolved line grids divided by the total number of measured line grids, similar experiments as depicted in Figure 3 were repeated several times. On average four line grids per spacing were analyzed (see Table S1 in Supporting Information for details). Thereby, care was taken to compare only those line grids bearing a similar number of active fluorophores. Figure 4 shows the

© XXXX American Chemical Society

DOI: 10.1021/nl903730r | *Nano Lett.* **XXXX,** *xxx,* 000-000

fraction of resolved line grids for different line-spacings together with sigmoidal fits for different values of τ_{off}/τ_{on}. The reversal point indicates the line grid spacing where 50% of the line grids were resolved for a certain τ_{off}/τ_{on}-ratio.

Starting with a ratio of τ_{off}/τ_{on} ~200 (Figure 4, black; concentration of the oxidant MV = 0 μM) shows that down to a line grid spacing of 150 nm (~300 fluorophores/μm^2) all grids were resolved while significant fractions of line grids with 100 and 75 nm spacing, corresponding to ~500−650 fluorophores/μm^2, are still resolved. Grids with 50 nm spacing and a fluorophore density of 1000 fluorophores/μm^2 cannot be resolved. A sigmoidal fit reveals that a fraction of 50% is resolved at a grid-size of 91 ± 3 nm (Figure 4, black) corresponding to an estimated fluorophore density of ~530 fluorophores/μm^2. Since this value is close to the measured line-width discussed above, this resolution and also the density of fluorophores that can be resolved are mainly influenced by other parameters than the τ_{off}/τ_{on}-ratio of ~200. The resolution in our experiments was shown to be spatially limited to ~50−60 nm, which makes it impossible for us to resolve structures with 50 nm grid-size even with infinite τ_{off}/τ_{on}-ratio.

Subsequently, the same experiments were conducted at different concentrations of the oxidant MV, that is, at different τ_{off}/τ_{on}-ratios. Reducing this ratio to τ_{off}/τ_{on} ~100 by adding 10 μM MV to the buffer significantly alters the observed behavior (Figure 4, red). While the acquisition time can be reduced by the factor the ON-OFF duty cycle is reduced, only smaller fractions of the 150, 100, and 75 nm line grids were resolved and the reversal point is found at 119 ± 5 nm corresponding to an estimate of ~400 fluorophores/μm^2. This change is directly related to the lower number of fluorophores that could be colocalized at shorter OFF-times and experimentally demonstrates the trade-off of a lower spatial resolution at increased time resolution.

At a τ_{off}/τ_{on}-ratio of ~10, that is, a concentration of MV = 250 μM, the fraction of resolved grids decreases and shifts the turning point to 145 ± 6 nm corresponding to ~300 fluorophores/μm^2 in accordance with the proposed relation.

It is not trivial to access and quantify the parameters that describe this resolution change. This is because the spot finding and localization algorithm in the analysis software uses intensity thresholds, an area size- as well as a circularity-criterion for the selected spots.[7] Accordingly, the algorithm was often able to detect and discard spots when two molecules were simultaneously fluorescent within a diffraction limited area. We carried out Monte Carlo simulations to emulate the measurements and to be able to compare our measurements with expectations. Therefore 8000 videoframes of blinking dyes, which exhibit comparable emission properties as those recorded experimentally, were generated. In these simulations, molecules were placed in analogous line patterns with the SMCP precisions determined above (for details see Supporting Information). The simulated data sets were evaluated utilizing the same analyzing software as for the experimental data and yielded graphs and fit functions depicted in Figure 4b. The theoretical values where 50% of the line grids could be resolved were derived from sigmoidal fits, 77 ± 4 nm for τ_{off}/τ_{on} ~200, 98 ± 5 nm for τ_{off}/τ_{on} ~100, and 170 ± 10 nm for τ_{off}/τ_{on} ~10. These values show a slightly larger spread than the experimental values. They, however, support the idea that the resolution is limited by the physical line widths rather than the τ_{off}/τ_{on}-ratio for the smallest grids. The simulations further demonstrate that after a thorough photophysical characterization of the probes used for superresolution microscopy the imaging speed can be adapted to the desired resolution and thus be optimized to the specific problem.

In conclusion, we presented a combination of a recently established method for the bottom-up assembly of artificial structures (SMCP) and superresolution Blink-Microscopy. Superresolution microscopy served to image subdiffraction features in smiley-, cross-, and line grid-patterns created by SMCP that are difficult to characterize by other methods. Subsequently, we used patterns created by SMCP to experimentally demonstrate the trade-off of acquisition speed and spatial resolution of superresolution techniques that rely on the subsequent localization of single molecules. The adjustability of the blinking in Blink-Microscopy allowed adapting the photophysical parameters to achieve the desired spatial resolution at optimized acquisition rate. Accordingly, SMCP one-by-one assembled patterns turn out to be valuable structures for the characterization and calibration of superresolution microscopes. Simulations of the line grid structures complement the analysis and will be helpful to optimize algorithms used for single-molecule identification and localization.

Finally, this work shows the great potential of combining the complementary techniques of single-molecule assembly and superresolution microscopy. It is envisioned to create biochemical networks and enzyme cascades via SMCP whose interactions and functioning will then be accessible using superresolution fluorescence microscopy.

Acknowledgment. The authors thank Dominik Ho for stimulating discussions. This work was supported by the DFG (Inst 86/1051-1), the Volkswagen Foundation, the Biophotonics III Program of the BMBF/VDI (grant 13N9234), the Nanosystems Initiative Munich, and the Elitenetzwerk Bayern.

Supporting Information Available. Details of material and methods, sample preparation, single-molecule cut-and-paste, TIRF-microscopy and superresolution Blink-Microscopy, confocal microscopy; additional results from confocal microscopy and statistics of the resolved line grid fraction. This material is available free of charge via the Internet at http://pubs.acs.org.

REFERENCES AND NOTES

(1) Yildiz, A.; Forkey, J. N.; McKinney, S. A.; Ha, T.; Goldman, Y. E.; Selvin, P. R. *Science* **2003**, *300* (5628), 2061–2065.
(2) Hell, S. W. *Science* **2007**, *316* (5828), 1153–1158.

© XXXX American Chemical Society

DOI: 10.1021/nl903730r | *Nano Lett.* **XXXX,** *xxx,* 000-000

NANO LETTERS

(3) Betzig, E.; Patterson, G. H.; Sougrat, R.; Lindwasser, O. W.; Olenych, S.; Bonifacino, J. S.; Davidson, M. W.; Lippincott-Schwartz, J.; Hess, H. F. *Science* **2006**, *313* (5793), 1642–1645.
(4) Rust, M. J.; Bates, M.; Zhuang, X. *Nat. Methods* **2006**, *3* (10), 793–5.
(5) Hess, S. T.; Girirajan, T. P.; Mason, M. D. *Biophys. J.* **2006**, *91* (11), 4258–72.
(6) Heilemann, M.; van de Linde, S.; Schuttpelz, M.; Kasper, R.; Seefeldt, B.; Mukherjee, A.; Tinnefeld, P.; Sauer, M. *Angew. Chem., Int. Ed.* **2008**, *47* (33), 6172–6176.
(7) Steinhauer, C.; Forthmann, C.; Vogelsang, J.; Tinnefeld, P. *J. Am. Chem. Soc.* **2008**, *130* (50), 16840–16841.
(8) Rothemund, P. W. *Nature* **2006**, *440* (7082), 297–302.
(9) Steinhauer, C.; Jungmann, R.; Sobey, T. L.; Simmel, F. C.; Tinnefeld, P. *Angew. Chem., Int. Ed.* **2009**, *48* (47), 8870–8873.
(10) Piner, R. D.; Zhu, J.; Xu, F.; Hong, S.; Mirkin, C. A. *Science* **1999**, *283* (5402), 661–3.
(11) Rodolfa, K. T.; Bruckbauer, A.; Zhou, D. J.; Korchev, Y. E.; Klenerman, D. *Angew. Chem., Int. Ed.* **2005**, *44* (42), 6854–6859.
(12) Kufer, S. K.; Puchner, E. M.; Gumpp, H.; Liedl, T.; Gaub, H. E. *Science* **2008**, *319* (5863), 594–596.
(13) Kufer, S. K.; Strackharn, M.; Stahl, S. W.; Gumpp, H.; Puchner, E. M.; Gaub, H. E. *Nat. Nanotechnol.* **2009**, *4* (1), 45–9.
(14) Puchner, E. M.; Kufer, S. K.; Strackharn, M.; Stahl, S. W.; Gaub, H. E. *Nano Lett.* **2008**, *8* (11), 3692–5.
(15) Shroff, H.; Galbraith, C. G.; Galbraith, J. A.; Betzig, E. *Nat. Methods* **2008**, *5* (5), 417–23.
(16) Vogelsang, J.; Cordes, T.; Forthmann, C.; Steinhauer, C.; Tinnefeld, P. *Proc. Natl. Acad. Sci. U.S.A.* **2009**, *106* (20), 8107–12.
(17) Hell, S. W. *Nat. Methods* **2009**, *6* (1), 24–32.
(18) Klar, T. A.; Jakobs, S.; Dyba, M.; Egner, A.; Hell, S. W. *Proc. Natl. Acad. Sci. U.S.A.* **2000**, *97* (15), 8206–8210.
(19) Sharonov, A.; Hochstrasser, R. M. *Proc. Natl. Acad. Sci. U.S.A.* **2006**, *103* (50), 18911–18916.
(20) Lemmer, P.; Gunkel, M.; Weiland, Y.; Muller, P.; Baddeley, D.; Kaufmann, R.; Urich, A.; Eipel, H.; Amberger, R.; Hausmann, M.; Cremer, C. *J. Microsc.* **2009**, *235* (2), 163–71.
(21) Folling, J.; Bossi, M.; Bock, H.; Medda, R.; Wurm, C. A.; Hein, B.; Jakobs, S.; Eggeling, C.; Hell, S. W. *Nat. Methods* **2008**, *5* (11), 943–5.
(22) van de Linde, S.; Kasper, R.; Heilemann, M.; Sauer, M. *Appl. Phys. B* **2008**, *93* (4), 725–731.
(23) Flors, C.; Ravarani, C. N.; Dryden, D. T. *ChemPhysChem* **2009**, *10* (13), 2201−2204.
(24) Vogelsang, J.; Kasper, R.; Steinhauer, C.; Person, B.; Heilemann, M.; Sauer, M.; Tinnefeld, P. *Angew. Chem. Int. Ed.* **2008**, *47*, 5465–5469.
(25) Thompson, R. E.; Larson, D. R.; Webb, W. W. *Biophys. J.* **2002**, *82* (5), 2775–2783.
(26) Egner, A.; Geisler, C.; von Middendorff, C.; Bock, H.; Wenzel, D.; Medda, R.; Andresen, M.; Stiel, A. C.; Jakobs, S.; Eggeling, C.; Schonle, A.; Hell, S. W. *Biophys. J.* **2007**, *93* (9), 3285–90.
(27) Bossi, M.; Folling, J.; Belov, V. N.; Boyarskiy, V. P.; Medda, R.; Egner, A.; Eggeling, C.; Schonle, A.; Hell, S. W. *Nano Lett.* **2008**, *8* (8), 2463−2468.

© XXXX American Chemical Society

DOI: 10.1021/nl903730r | *Nano Lett.* **XXXX,** *xxx,* 000-000

Supporting information for the manuscript

Resolving single-molecule assembled patterns with superresolution blink-microscopy

*Thorben Cordes,[1] Mathias Strackharn,[1] Stefan W. Stahl, Wolfram Summerer, Christian Steinhauer, Carsten Forthmann, Elias M. Puchner, Jan Vogelsang, Hermann E. Gaub, and Philip Tinnefeld**

Applied Physics – Biophysics & Center for NanoScience, Ludwig-Maximilians-Universität, Amalienstr. 54, D-80799 München, Germany

[1]These authors contributed equally to this work.

*Corresponding author, philip.tinnefeld@lmu.de; fax: +49 89 2180 2005

1. Material and methods

1.1. Single-molecule cut-and-paste (SMCP)

Sample-preparation: Depot and target area were prepared on circular cover slides, all details of the procedure can be found in refs. [1-3]. The slides were amino silanized and functionalized with N-hydroxy-succinimide-ester (NHS)-PEG-maleimide (M = 5000 g/mol, Rapp Polymere, Tübingen, Germany 50 mM). Subsequently, a PDMS flow chamber with two channels, connected to a peristaltic pump, was mounted on the cover slip. One channel (depot area) was rinsed for 1 h with a 10 mM solution of depot anchor oligomer while the other channel (target area) was rinsed with a 10 mM

solution of the target oligomer. Subsequently, the depot area was additionally rinsed with a 1 µM solution of transport oligomer dissolved in phosphate buffered saline (PBS) (depot oligomer: HS-5'-TTTTTTTTTAAGTAGCTATTCGAACTATAGCTTAAGGCAGTCAA-3'; transport oligomer: 5'-TTTTTGACGTCCTTAAGCTATAGTTCGAATAGCTACTTTT*TTTTTTCATCGATAAGCTTGAT ATCGAATTCCTGCAGTTTTT-3' with T* = T-ATTO655; target oligomer: 5'-AGTAGCTATTCGAACTATAGCTTAAGGACGTCTTTTTTTTTT-3'-SH). All oligomers were of HPLC grade and were synthesized by IBA (IBA, Göttingen, Germany). Thiol-modified oligomers were reduced with TCEP before coupling to PEG to generate free mercaptans. For usage in the SCMP experiment the cover slide was rinsed with PBS buffer and placed in a custom-made sample-holder.

The SMCP-setup: All SMCP experiments were performed on a custom-built AFM at room temperature in PBS buffer. Cantilevers (Veeco MSCT and Olympus BL-AC40) were covalently functionalized with NHS-PEG-maleimide (M = 5000 g/mol) and a DNA oligomer (HS-5'-TTTTTTTTTTCTGCAGGAATTCGATATCAA-3') that is able to hybridize with the transport oligomer. Spring constants of the cantilever were determined in solution by the equipartition theorem [4], with typical values of 13 pN/nm for the MSCT-C and 70 pN/nm for the BL-AC40. To transport DNA molecules, the tip and the sample were controlled in closed loop operation with a MFP-3D controller (Asylum Research, Santa Barbara, CA, USA). Software control of the SMCP process was performed in custom-made Igor Pro 5.03 (Wave Metrics).

For experiments with ATTO655 attached to the transport DNA, SMCP was performed with a cantilever with high functionalization density to transport 2-5 strands at a time. As only a fraction of 10-20% of the transported DNA-strands showed detectable emission, this was necessary to achieve a sufficient number of active fluorophores in the assembled pattern. The high number of in-active fluorophores was most likely caused by the drying process of the cover-slide within the preparation procedure and no such degradation was noticed for Cy3.

TIRF-imaging with Cy3: Imaging with transported Cy3 dyes was performed under TIRF excitation at 532 nm with at 75 mW DPSS laser (Crystalaser, Reno, USA) through an oil immersion objective (100×, NA 1.49, CFI Apochromat TIRF, Nikon, Japan). The laser was focused on the back-focal plane of the objective, the fluorescence light was filtered by a Brightline 582/75 and imaged onto a back-illuminated EMCCD camera (128x128 pixel, Andor Ixon DV-860). More details concerning all different aspects of SMCP are found in refs. [1-3].

1.2. TIRF-Imaging with ATTO655 and superresolution blink-microscopy

Fluorescence imaging was conducted on an inverted microscope (Olympus IX-71) in objective type total-internal-reflection fluorescence (TIRF) configuration. Images were collected with a back-illuminated EMCCD camera (128x128 pixel, Andor Ixon DU-860-CS0). Excitation was at 650 nm with 300 mW (single mode diode laser XTL, Toptica) and filtered by a clean-up filter (Brightline HC 650/13, AHF Analysentechnik); the beam was coupled into an oil-immersion objective (UPlanSApo 100×, NA 1.40, Olympus) using a dual-band beamsplitter (z532/658rpc, AHF, Analysentechnik). The illumination area of 600 μm^2 was approximately twice the size of the observation area of ~300 μm^2. An image magnification of ~160 fold – corresponding to a pixel size of 137 nm – was achieved by additional lenses. The fluorescent sample light was spectrally filtered by an emission filter (HQ 700/75 M, AHF Analysentechnik).

Blink-microscopy images were collected on the same setup under the following experimental conditions and without oxygen removal: 50 µM ascorbic acid (AA) were added to phosphate-buffered saline (PBS) with variable amounts, i.e. 0-250 µM, of N,N-methylviologen (MV). Under these conditions approximately N_{on} = 800 ± 400 counts were detected from a single ATTO655 molecule per on-time in the wide-field setup. According to ref. [5] the localization precision is given by ~FWHM/$(N_{on}/2)^{1/2}$ with FWHM ~310 ± 18 nm for our setup. We excluded noise arising from

background light and camera readout which suggests a theoretical localization precision of 16 nm.[6] The experimental value of 20 ± 4 nm is slightly higher – a fact that may be explained by polarization effects [7] and the internal labeling of ATTO655 to DNA. The dye molecule was separated from the PEG-linker on the surface by ~35 double-stranded base-pairs. The typical laser power for imaging was 300 mW (~50 kW/cm^2) and 4000-16000 frames were recorded at frames rates of 250-1000 Hz. The laser power was adjusted for ON-times corresponding to the integration time of the camera of ~1-4 ms.

The image reconstruction used for superresolution imaging was conducted with custom-made software as described in refs. [8]. Briefly, the first frames of the movie, typically frames 20-150, were discarded as most of the molecules were in the active state after starting laser excitation. Subsequently, the spot-finding algorithm analyses the movie frame by frame involving a lower and upper threshold. Each intensity pattern in the respective frame is then compared to its environment (commonly 7 × 7 pixels): In the case a certain contrast value (typically 2) is reached, the spot was considered for further analysis. To exclude events with two molecules being active within one diffraction limited area and to remove events when the two-dimensional Gaussian did not converge the indentified spots needed to fulfill a circularity criterion – commonly, ~25% of all events were discarded. Two-dimensional Gaussian fitting yields the position of the emitting molecule – a histogram of all molecule positions yields the superresolution image as shown in Figures 1-3 (main text).

1.3. Confocal microscopy

Fluorescent transients from single immobilized ATTO655 molecules were recorded in a home-built confocal scanning microscope. ATTO655 molecules were immobilized according to published procedures utilizing similar procedures as for SMCP-sample preparation.[1-2] Excitation at 640 nm (spectral width ~2 nm) was based on a supercontinuum laser source (SuperK Extreme, Koheras, Denmark) in combination with acousto-optical tunable filters (AOT-Fnc-VIS, AA Optoelectronic). The laser beam was coupled into an oil-immersion objective (60×, NA 1.35, UPLSAPO60X0, Olympus)

after passing a single-mode fiber, resulting in an average excitation intensity of 4 kW/cm^2. The emitted fluorescence was collected by the same objective and spatially filtered by a 50 µm pinhole. After a bandpass filter (HQ 700/75 M, AHF Analysentechnik) fluorescence was detected on an avalanche photodiode (APD, SPCM-AQR-14; Perkin Elmer).

The photophysical properties of the transport DNA from SMCP were investigated according to ref. [9]. For this purpose a constant amount of AA (50 µM) and varying amounts of MV (0-250 µM) were added to PBS-buffer. At each MV concentration ~40 single-molecule transients were recorded. Subsequently, autocorrelation analysis was employed to extract ON- and OFF-times from each single-molecule. A detailed description of the data-evaluation is found in ref. [9].

2. Results

2.1. Blinking properties of transport DNA: ATTO655

As shown in refs. [9-11] oxazine dyes show a strong dependence of their fluorescent properties on their environment (linker-structure, pH-value, oxidant- and reducer-concentration). For a determination of specific ON- and OFF-times of ATTO655 bound to the transport DNA – needed for a quantitative estimation of the resolution enhancement (see Figure 4, main text) – we recorded the blinking kinetics as shown in Figure S1. The experiments were conducted on a confocal microscope as described above. Autocorrelation analysis revealed that the addition of 50 µM AA to aerated PBS buffer leads to frequent blinking of ATTO655 with an OFF-time duration of τ_{off} = (430 ± 90) ms. As expected, the ON-counts remain constant within experimental error (data not shown) while τ_{off} reduces with increasing MV concentration (Figure S1). Further relevant OFF-times for superresolution measurements are τ_{off} = (180 ± 35) ms at 10 µM MV and τ_{off} = (14 ± 10) ms at 250 µM MV.

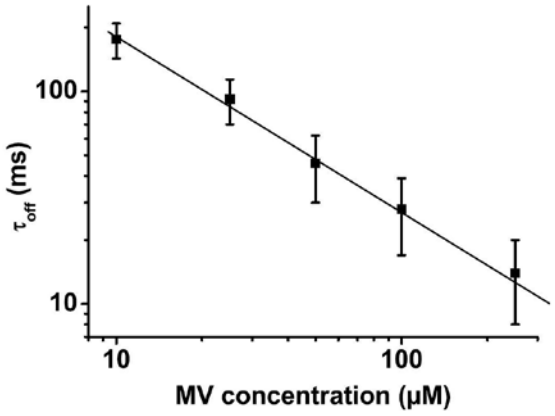

Figure S1: Double-logarithmic representation of the OFF-times of the investigated transport-DNA labeled with ATTO655 measured on a confocal microscope according to ref. [9]. For this purpose single transport DNA-strands were immobilized as described in the SCMP-section. The solid line is drawn to guide the eye.

2.2. Line grid analysis and resolved line grid fraction

In the main text an overview of the resolved line grid fraction in form of Figure 4 is given. Here, the dependence between the τ_{off}/τ_{on}-ratio and the achievable resolution, i.e., the actual number of fluorophores that can be resolved within the size of one PSF – in terms of resolved line grid fraction – is presented. Table S1 summarizes the fractions of resolved grids with respect to the numbers of measured line grids (see also Figure 4 in the main text).

Table S1: Resolved line grid fraction: actual number of resolved line grids (first number) and number of measured line grids (second number) together with the resulting resolved fraction (third number). The actual fraction is also displayed in Figure 4, main text. The values are given for a constant concentration of AA (50 µM) and varying concentrations of the oxidant MV ([MV] = 0-250 µM) for different line grid spacings (50-300 nm).

Line grid spacing	[MV] = 0 µM	[MV] = 10 µM	[MV] = 250 µM
300 nm	4 of 4; 1.0	3 of 3; 1.0	4 of 4; 1.0
200 nm	4 of 4, 1.0	3 of 3; 1.0	3 of 3; 1.0
150 nm	5 of 5; 1.0	4 of 5; 0.8	2 of 4; 0.5
100 nm	4 of 7; 0.6	3 of 6; 0.33	1 of 5; 0.2
75 nm	2 of 6; 0.33	0 of 5; 0.0	0 of 3; 0.0
50 nm	0 of 3; 0.0	0 of 3; 0.0	not determined

2.3. Monte Carlo Simulations of line grid resolved by blink-microscopy

For a detailed comparison of the experimental values from Table S1 with theory, the line grids assembled by SMCP were simulated by Monte Carlo Simulations. A description of the simulation procedure is given in ref. [8]. The simulations generated videos of 8000 frames with blinking dyes that exhibit comparable emission properties as those recorded experimentally with the EMCCD camera: ON-times were fixed to 2.5 ms with 800 ON-counts. The lines also included the experimentally determined error for the line-width and consisted of a comparable number of active fluorophores (~150). The generated videos were analyzed with the same custom-made software as described in the experimental section.

Table S2: Theoretical values of the resolved line grid fraction: actual number of resolved line grids (first number) and number of measured line grids (second number) together with the resulting resolved fraction (third number). The actual fraction is also displayed in Figure 4, main text. The values are given for a constant ON-time of 2.5 ms and varying off-time durations for different line grid spacings (50-300 nm).

Line grid spacing	τ_{off} = 400 ms	τ_{off} = 200 ms	τ_{off} = 20 ms
300 nm	5 of 5; 1.0	5 of 5; 1.0	5 of 5; 1.0
200 nm	5 of 5, 1.0	5 of 5; 1.0	7 of 10; 0.7
150 nm	5 of 5; 1.0	5 of 5; 1.0	4 of 10; 0.4
100 nm	8 of 10; 0.8	5 of 10; 0.5	1 of 10; 0.1
75 nm	5 of 10; 0.5	3 of 10; 0.3	0 of 5; 0.0
50 nm	0 of 5; 0.0	0 of 5; 0.0	0 of 5; 0.0

3. References:

1. Kufer, S.K., et al., *Single-molecule cut-and-paste surface assembly.* Science, 2008. 319(5863): p. 594-6.
2. Kufer, S.K., et al., *Optically monitoring the mechanical assembly of single molecules.* Nat Nanotechnol, 2009. 4(1): p. 45-9.
3. Puchner, E.M., et al., *Nanoparticle self-assembly on a DNA-scaffold written by single-molecule cut-and-paste.* Nano Lett, 2008. 8(11): p. 3692-5.
4. Butt, H.J. and M. Jaschke, *Calculation of thermal noise in atomic force microscopy.* Nanotechnology, 1995. 6: p. 1-7.
5. Bossi, M., et al., *Multicolor Far-Field Fluorescence Nanoscopy through Isolated Detection of Distinct Molecular Species.* Nano Letters, 2008. 8(8): p. 2463-8.
6. Thompson, R.E., D.R. Larson, and W.W. Webb, *Precise nanometer localization analysis for individual fluorescent probes.* Biophys J, 2002. 82(5): p. 2775-83.
7. Enderlein, J., E. Toprak, and P.R. Selvin, *Polarization effect on position accuracy of fluorophore localization.* Opt Express, 2006. 14(18): p. 8111-20.
8. Steinhauer, C., et al., *Superresolution microscopy on the basis of engineered dark states.* J Am

Chem Soc, 2008. 130(50): p. 16840-1.
9. Vogelsang, J., et al., *Controlling the fluorescence of ordinary oxazine dyes for single-molecule switching and superresolution microscopy.* Proc Natl Acad Sci U S A, 2009. 106(20): p. 8107-12.
10. Vogelsang, J., T. Cordes, and P. Tinnefeld, *Single-molecule photophysics of oxazines on DNA and its application in a FRET switch.* Photochem Photobiol Sci, 2009. 8(4): p. 486-96.
11. Vogelsang, J., et al., *A reducing and oxidizing system minimizes photobleaching and blinking of fluorescent dyes.* Angew Chem Int Ed Engl, 2008. 47(29): p. 5465-9.

P6 A CONDITIONAL GATING MECHANISM ASSURES THE INTEGRITY OF THE MOLECULAR FORCE-SENSOR TITIN KINASE

Stahl SW, Puchner EM, Alexandrovich A, Gautel M, Gaub HE.

BIOPHYSICAL JOURNAL 2011 Oct 19;101(8):1978-86.

1978 Biophysical Journal Volume 101 October 2011 1978–1986

A Conditional Gating Mechanism Assures the Integrity of the Molecular Force-Sensor Titin Kinase

Stefan W. Stahl,[†‡] Elias M. Puchner,[†] Alexander Alexandrovich,[§] Mathias Gautel,[§] and Hermann E. Gaub[†‡*]
[†]Chair for Applied Physics and Center for NanoScience, Ludwig-Maximilians-University Munich, Munich, Germany; [‡]Center for Integrated Protein Science Munich, Munich, Germany; and [§]Cardiovascular Division and Randall Division for Cell and Molecular Biophysics. King's College London, London, United Kingdom

ABSTRACT As more and more recent investigations point out, force plays an important role in cellular regulation mechanisms. Biological responses to mechanical stress are often based on force-induced conformational changes of single molecules. The force sensor, titin kinase, is involved in a signaling complex that regulates protein turnover and transcriptional adaptation in striated muscle. The structural architecture of such a force sensor determines its response to force and must assure both activity and mechanical integrity, which are prerequisites for its function. Here, we use single-molecule force-clamp spectroscopy to show that titin kinase is organized in such a way that the regulatory domains have to unfold before secondary structure elements that determine the overall fold and catalytic function. The stepwise unfolding over many barriers with a topologically determined sequence assures that the protein can react to force by conformational changes while maintaining its structural integrity.

INTRODUCTION

Over the recent decades, much has been learned about the networks regulating cellular behavior. Although the focus of research still lies on cellular or molecular responses to biochemical stimuli, it is increasingly recognized that other inputs such as force play an important role in regulatory signaling networks. Forces affect many physiological processes such as cell proliferation and differentiation (1), cell adhesion (2), wound-healing (3), or hearing (4). Therefore, extra- and intracellular force sensors are required that generally operate through force-induced conformational changes on the molecular level (5–7). The molecular architecture of such sensors is of special interest, because it gives further insight into their working principle, and force-dependent measurements help us to understand the fundamental effects on the relation among conformation, mechanical stability, and function (8–10).

In striated muscle, the large protein titin spans half the sarcomere, provides the muscle with passive elasticity, and serves as a molecular ruler for the sarcomere assembly (11,12). Furthermore, titin is involved in mechanical signaling pathways (13). Near the C-terminus, which is located at the M-band of the sarcomere, titin contains a kinase domain that is linked to the control of muscle gene expression and protein turnover (14). The exact molecular structure and even the constituents of the M-band are not yet completely known (15,16). However, the M-band acts as an elastic crosslinker of myosin filaments, and is exposed to shear forces between adjacent myosin filaments under active contraction that lead to buckling of the M-band on the order of at least 10 nm (15,16). Furthermore, thick filaments also undergo length changes during contraction and, to a lesser extent, stretch (17–19). The M-band and particularly M-band titin have therefore been proposed as a structure that senses muscle workload and feeds into pathways that control load-dependent remodeling (15,16).

The role of titin kinase (TK) as a force sensor was recently investigated with a combination of single-molecule force spectroscopy, molecular dynamics simulation, and enzymatic analysis (20–22). The working principle on the molecular level is shortly described as follows. In its inactive conformation, TK is autoinhibited by a dual mechanism. A C-terminal regulatory tail blocks the ATP binding site, and tyrosine-170 inhibits the catalytic base. In contrast to the situation of many other kinases, the relief of intramolecular inhibition does not occur by conformational changes induced by ligand binding, as no physiologically relevant protein activator has been identified for TK or its invertebrate analog, twitchin kinase (reviewed in Gautel (23)). Instead, forces applied between the C- and N-terminus of the protein were shown to first break a β-sheet of the C-terminal autoinhibitory tail, and then to remove the autoinhibitory α-helix R2, thus making the ATP binding pocket accessible. Single-molecule force spectroscopy measurements (24,25) performed with an atomic force microscope (AFM) (26) at physiologically relevant forces, speeds, and temperatures can therefore probe the conformational space of TK and allow predictions in the natural environment.

Previous AFM experiments at constant pulling speed revealed that the unfolding of TK occurs in a sequential and apparently predetermined manner with up to six substeps that will be called barriers in the following (Fig. 2 *a*). The barriers are labeled from 1 to 5 and barrier 2* is highlighted, because its occurrence was linked to the presence of ATP and the pulling speed and is sensitive to mutations in the

Submitted May 19, 2011, and accepted for publication September 6, 2011.

*Correspondence: gaub@lmu.de

Elias M. Puchner's current address is Department of Cellular and Molecular Pharmacology, University of California, San Francisco, CA.

Editor: Hideo Higuchi.

© 2011 by the Biophysical Society

0006-3495/11/10/1978/9 $2.00

doi: 10.1016/j.bpj.2011.09.027

ATP-binding site, indicating that it reports conformational changes in the active site. However, the cause of the mentioned regularity in unfolding could not be directly addressed. Further and deeper insight into the structural architecture of TK would therefore result in a much better understanding of the working principle of force-driven processes on the single-molecule level.

The models of mechanical hierarchy and structural topology

Looking at the arrangement of two of the structural elements that cause energy barriers in a folded protein, there are two possible scenarios that lead to an ordered sequence of unfolding events:

In the first scenario, which we call mechanical hierarchy, the structural elements are arranged in series such that the force is transmitted through both of them and such that they may unfold independently. The reason for an ordered unfolding sequence in this case would be a different strength of the two barriers, or regarding the complete unfolding pathway of TK, a continuously rising mechanical resistance from barrier 1–5.

In the second scenario, the barriers are arranged such that the unfolding is predetermined through structural topology, meaning that the elements are shielding each other and that the first barrier has to be overcome before the second one will be under load. Schematics of these scenarios are shown in Fig. 1.

Whereas the previous studies on TK in the constant velocity mode of AFM-based force spectroscopy were ideal to determine the barrier positions with nm accuracy, they were not able to discriminate between mechanical hierarchy and structural topology because force and extension were the recorded parameters. In experiments with constant retraction velocity, the mechanical stability is characterized by force and loading rate (dF/dt) (27). That complicates the interpretation of the unfolding pattern because the latter is not constant over time. Therefore a meaningful discrimination between the two scenarios may only be obtained in the time-domain, i.e., through the access to the force-induced unfolding kinetics of the barriers.

Here we employ the so-called force-clamp mode of single-molecule force spectroscopy introduced by Fernandez and Hansma (28), where a feedback loop keeps the pulling force constant by readjusting the tip or surface position after partial unfolding of the protein (29). This mode is ideally suited for a differentiation between the given scenarios because it allows access to the time-dependent unfolding probability of the different structural elements under constant pulling force. This unfolding probability should significantly differ between the cases of mechanical hierarchy and structural topology, as will be explained in the following. Exposure to force over a longer timescale but at low extension is also likely to more accurately reflect the situation of cytoskeletal elements like titin in a contracting sarcomere.

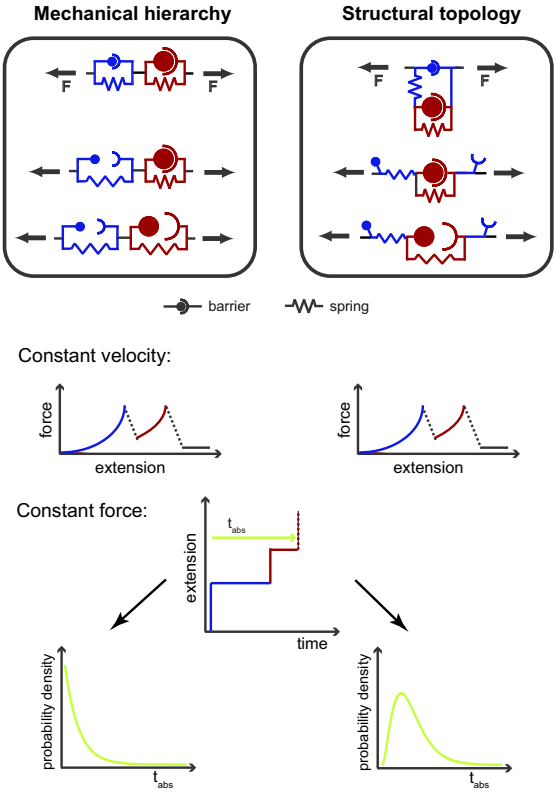

FIGURE 1 Possible mechanical architectures of proteins that consist of multiple unfolding barriers. Each structural element that causes an energy barrier in the unfolding pathway can be drawn as a combination of a bond and a nonlinear spring. In the case of mechanical hierarchy, both barriers are loaded simultaneously and the preference of opening is due to different mechanical strength. In the case of structural topology, the unfolding sequence is determined because one barrier is shielding the other. Under constant velocity single-molecule force spectroscopy conditions, the two scenarios cannot be easily distinguished because the mechanical strength is determined not only by the rupture forces but also by the loading rates of the bond that might be complex functions of the extension and speed for multibarrier proteins. Force-clamp recordings, however, can intrinsically resolve the underlying architecture because the time-dependent unfolding probabilities of the barriers are independent in the case of mechanical hierarchy and depend on each other in the case of structural topology. The distributions are expected to be single-exponential for independent two-state systems and peaked for elements that depend on the opening of another barrier.

MATERIALS AND METHODS

Single-molecule force-spectroscopy experiments

Expression and purification of the TK protein construct A168M2 (867 amino acids, from position 24422–25288 in human cardiac N2-B titin, accession No. NP 003310.3) is described in the Supporting Material of Puchner et al. (21) except that cells from the line IPLB-Sf21AE were used instead of those of

the sf9 line. Measurements were performed on mercaptosilanized glass surfaces that were functionalized with *n*-(5-(3-Maleimidopropionylamino)-1-carboxy-pentyl)iminodiacetic acid (Maleimido-C3-NTA; Dojindo, Rockville, MD) using the protocol described in Schlierf et al. (30). They specifically bind the His-Tag of the TK protein construct. After complexation of Ni^{2+} in 100 mM $NiSO_4$ solution and rinsing, diluted protein solution (400 μL; 50 μg/mL) was used for the measurement.

The buffer solution consists of 40 mM 2-[4-(2-hydroxyethyl)-1-piperazinyl]ethanesulfonic acid (HEPES)/KOH, 2 mM $MgCl_2$, 2 mM dithiothreitol, and 2 mM Adenosine-5′-triphosphate (ATP; Roche Diagnostics, Mannheim, Germany) and was adjusted to pH 7.2. Single-molecule force spectroscopy (SMFS) experiments were performed with Biolever A and B type cantilevers (Olympus, Tokyo, Japan) and a custom-built AFM (29), which can be combined with an optical microscope for single-molecule fluorescence studies (31). Spring constants of the cantilevers were determined on basis of the equipartition theorem (32) by fitting the thermal noise spectrum with the response function of a simple harmonic oscillator. A practical implementation can be found in Cook et al. (33). The obtained values are 5.2 pN/nm for the A-type and 22 pN/nm for the B-type lever.

For the force-clamp on TK, a control loop that steers a fast linear piezo (P-753; Physik Instrumente, Karlsruhe, Germany) was implemented. It adjusts the sample position in z direction in order to keep the pulling force constant. The fast stage is attached to another piezo stage (P-733; Physik Instrumente) that is used for sampling the surface in xy direction to prevent multiple picking at the same molecule and to cover a wide area. The protocol was programmed with Igor Pro 5.0 (Wavemetrics, Lake Oswego, OR) and feedbacks were operated at the MFP3D AFM controller (Asylum Research, Santa Barbara, CA). Traces were recorded at setpoints of 20, 30, 40, and 50 pN clamping force. Response times for the piezo feedback are ~5 ms. Standard deviations from the force-setpoint during force-clamp are ~3 pN for the A-type and 6 pN for the B-type lever.

Force- and extension traces were only saved if the desired force setpoint was reached and the extension at the end of the trace exceeded 30 nm to ignore traces with no tip-protein interaction and traces where unspecific tip-surface interaction prevented the lever from detaching from the surface within the acquisition time.

Force-clamp step analysis

Tip-surface extension traces were calculated by subtracting the cantilever deflection from the piezo position values. The extension traces were analyzed with an automated step finding routine written in Igor Pro 6.2 (Wavemetrics). Therefore, histograms of the position traces were generated and peaks within these histograms were detected with a modified-form of the Peak AutoFind-Package delivered with Igor Pro. Peak position and corresponding time were saved for all traces. Unfolding time was set to zero when a position 10 nm over the surface was reached to cancel out unspecific tip-surface interaction that might keep the cantilever sticking to the surface without applying a force to the measured protein. In this way, influence of unspecific tip interaction on the absolute times of unfolding is reduced.

For the calculation of the unfolding rates k_i, only those traces were considered that had a step matching the expected increment of the unfolding of TK's barrier no. 5 (i.e., 44 ± 3 nm at 30 pN pulling force) and an overall extension of at least 70 nm. For identification of the other barriers, the position before the opening of barrier no. 5 was set to zero (compare to Fig. 4). Steps were classified by selecting height and position relative to barrier 5 according to Table 1.

Rate fitting

The probability density distribution of the unfolding time for each barrier was determined as follows. Histograms over the time between two consecutive events (barriers 2–5) and the absolute time of unfolding (barrier 1) were calculated. They neglect events that are shorter than the experimentally determined average response time of the feedback (compare to Fig. S2 in the Supporting Material), because these events occur only very seldom and would distort the probability distribution. The number of bins in each histogram corresponds to the square root of the number of events. The unfolding rates k_i were determined by fitting a single-exponential function with time offset t_0 to the histogram:

$$p_{i,rel}(t) = k_i e^{-k_i(t-t_0)}.$$

The time offset t_0 again respects the finite response time of the feedback and is linear-dependent on the height of the step (see Fig. S2). Errors of the probability density histograms and the off-rates were determined by bootstrapping. Therefore, for each histogram, 100 random subpopulations were generated that consist of only 30% of the original data points. The same rate fitting was applied to the subpopulations. Error bars include the inner 90% of the bootstrapped values.

Markov-chain model

To check for consistency with the thesis that the structural elements of titin kinase (TK) are topologically ordered, the following model was developed. It describes the unfolding of TK from the natural folded conformation (F) to the completely stretched unfolded conformation (U) as a sequential Markov chain with up to five substeps (compare to Scheme 1 below) that are

TABLE 1 Identification data for the substeps of TK unfolding at 30 pN clamping force

Barrier No.	1	2→3	2→2*	2*
Contour length increment (21)	9.1 nm	28.6 nm	19.4 nm	10.1 nm
Expected increment at 30 pN*	6.8 nm	21.5 nm	14.6 nm	7.6 nm
Identification interval in force-clamp experiment	8 ± 2 nm (A_2)	22 ± 2.5 nm (C)	14 ± 3 nm (B)	8 ± 2 nm (A_2)
Identification position relative to barrier 5	−42 ± 4 nm	−20 ± 4 nm	−27 ± 5 nm	−19 ± 3 nm
Determined off-rate at 30 pN k_{off}	31 ± 8 s^{-1}	20 ± 4 s^{-1}	18 ± 6 s^{-1}	83 ± 45 s^{-1}
Barrier No.	3	4	5	Fn
Contour length increment (21)	7.3 nm (7.5 nm)	18.0 nm (16.4 nm)	57.9 nm (58.3 nm)	30.8 nm
Expected increment at 30 pN*	5.5 nm (5.6 nm)	13.5 nm (12.3 nm)	43.4 nm (43.7 nm)	23.1 nm
Identification interval in force-clamp experiment	4 ± 2 nm (A_1)	14 ± 3 nm (B)	44 ± 3 nm (D)	22 ± 2.5 nm (C)
Identification position relative to barrier 5	−15 ± 3 nm	0 ± 2 nm	44 ± 3 nm	67 ± 7 nm
Determined off-rate at 30 pN k_{off}	21 ± 4 s^{-1}	20 ± 4 s^{-1}	14 ± 2 s^{-1}	1.2 ± 0.4 s^{-1}

Barriers were identified according to Fig. 4 and rates were obtained by fitting single-exponential decays to the probability distribution histograms of relative barrier opening times (see Materials and Methods). Values in parentheses correspond to the unfolding pathway with the additional barrier 2* or denote the population identifier.
*According to a wormlike-chain fit with persistence-length $p = 0.6$ nm.

identical with the measured barriers of previous work on TK (21) and describe distinct conformational states of TK. The part of the amino-acid chain that already went into an unfolded state can be described by polymer models as the wormlike-chain model and increases with every step until the complete protein is stretched. The decay of each step under force-clamp conditions is assumed to be single-exponential with a rate constant k_i. After the decay of state 2, the additional substep 2* is reached with probability p that is dependent on the pulling velocity (21).

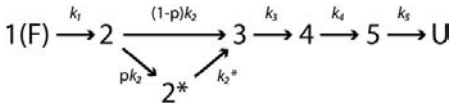

Thus, the system can be described by the following linear differential equation system,

$$\frac{d}{dt}\begin{pmatrix} p_1 \\ p_2 \\ p_{2^*} \\ p_3 \\ p_4 \\ p_5 \end{pmatrix} = \begin{pmatrix} -k_1 & & & & & \\ k_1 & -k_2 & & & & \\ & pk_2 & -k_{2^*} & & & \\ & (1-p)k_2 & k_{2^*} & -k_3 & & \\ & & & k_3 & -k_4 & \\ & & & & k_4 & -k_5 \end{pmatrix} \begin{pmatrix} p_1 \\ p_2 \\ p_{2^*} \\ p_3 \\ p_4 \\ p_5 \end{pmatrix},$$

where $p_i(t)$ describes the time-dependent probability distribution of being in state i. The differential equation system was solved under the initial condition $p_1(0) = 1$, $p_i(0) = 0$ $(i \neq 0)$ analytically with the computer algebra system MAPLE 14 (Maplesoft, Waterloo, Canada). The normalized solution of $p_5(t)$ for the experimentally determined rate constants k_i is depicted in Fig. 5. Because the probability density for going from state 5 to the unfolded conformation at time t is proportional to the probability of being in state 5 at time t, $p_5(t)$ can be directly compared with the experimentally determined unfolding times.

RESULTS

Distinction of structural barriers by step height

In one cycle of a force-clamp experiment, the tip of an AFM cantilever is brought into contact with the surface and retracted by a feedback loop that keeps the force constant. Typical unfolding traces of the tip-surface distance and the force are shown in (Fig. 2 *c*). The force is clamped over time and only shortly drops when a barrier opens, due to the finite response time of the feedback loop. For investigating the properties of the mechanically stable building blocks of TK, it is essential to discriminate the barrier-causing elements in the recorded data. Therefore, we analyzed the unfolding traces with an automated step-finding tool that detects plateaus in the extension versus time traces and records relevant parameters like step position and height or the time at which the unfolding occurred (see Materials and Methods).

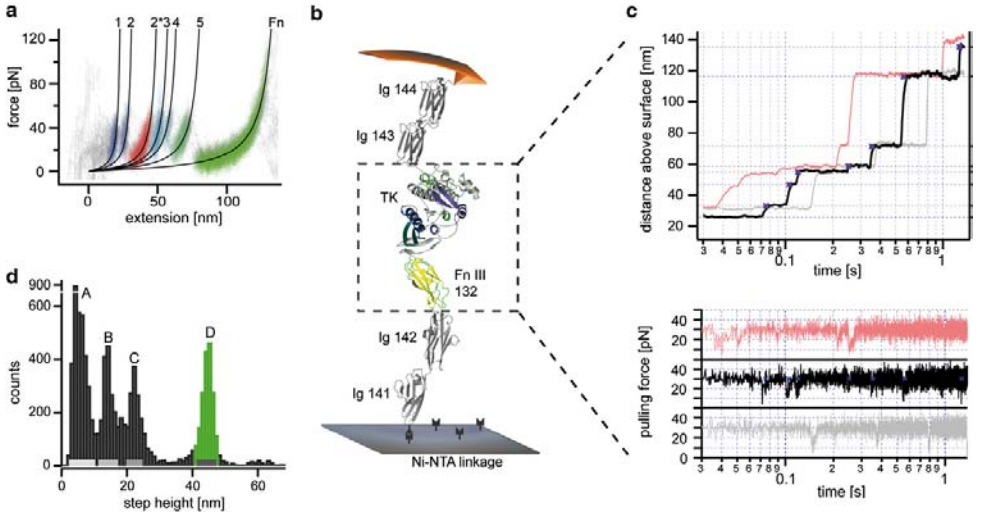

FIGURE 2 Sample data for the force-clamp experiments performed on titin kinase. (*a*) An overlay of 44 unfolding traces obtained by single-molecule force spectroscopy (SMFS) in constant retraction velocity mode points out that there is a preferred sequence of unfolding. The barriers that have to be overcome are numbered according to their position in this sequence. The probability of occurrence of barrier 2* is linked to ATP presence in solution and pulling velocity and therefore treated specially (21). Data points are displayed semitransparent. Such areas with high point density appear more intense. (*b*) For the SMFS experiments the titin construct A168-M2, which consists of the kinase domain (PDB No. 1TKI), four Ig-like domains and one fibronectin-type III domain, is immobilized on the surface by specific coupling of the His-tag to a NTA-functionalized surface and is pulled with a cantilever under constant force conditions. (*c*) Sample traces of the stepwise kinase unfolding under force-clamp conditions at a setpoint of 30 pN. Due to the difference in stability, unfolding of the Ig-domains is only very rarely observed at this force. The distance of the two thin traces is set off to match the position of the black trace. (*d*) Histogram of the heights of all steps detected in the ~10.000 unfolding traces that were recorded at 30 pN clamping force. Four populations are clearly observable (*A–D*). A comparison with the unfolding pattern obtained in constant velocity mode confirms consistency and shows that the peaks below 30 nm are formed by more than one structural element whereas the peak *D* is only due to the long increment of barrier 5 in titin kinase (compare to Table 1). Therefore, this peak is used for trace selection and first structural dependency analysis.

A histogram of the detected step heights at a pulling-force of 30 pN is given in Fig. 2 *d*. It is apparent that the heights are not evenly distributed but exhibit several populations, four of which are clearly distinguishable (*A*–*D*). A comparison with the unfolding pattern obtained by regular force-spectroscopy with constant pulling velocity allows the identification of some of the barriers by their step height. For the identification, we keep the notation of the barriers as they were introduced in Puchner et al. (21). The structural element of TK with the largest contour length (barrier 5 in Fig. 2 *a*) matches the position of population *D* around 44.5 nm (Table 1). We will initially focus on this barrier because it is of special interest: it always opened last in velocity-clamp experiments and it may be unambiguously identified by its step height only. The other populations may be due to the unfolding of at least two different structural elements of the titin construct and will be examined later.

Barrier 5 is mechanically shielded by other structural elements

In AFM experiments with constant velocity, barrier 5 of titin kinase was always observed to unfold last, but it cannot be easily distinguished whether this is due to higher mechanical stability or due to the fact that the domain is topologically shielded by other structural elements. The force-clamp recordings, however, are intrinsically able to distinguish between these two scenarios through the access to the unfolding kinetics, i.e., the probability of unfolding versus time. In the case of mechanical hierarchy, the likelihood of unfolding should not depend on other structural elements and thus yield a single exponential decay, whereas the dependence of unfolding on other structural elements in the case of structural topology would result in a peaked distribution because it takes a certain time until the observed state gets populated.

Fig. 3 *a* shows the distribution of how long it takes for barrier 5 to open after force is first applied to the protein. This absolute time distribution exhibits a well-pronounced peak with a maximum unfolding probability at ~200 ms, which is far longer than the minimal time resolution of the instrument. Note that the response time for the piezo feedback is ~5 ms (compare to the Supporting Material for experimental details). There is no doubt that the measured time distribution is not single-exponential, as would be required for independent Markovian two-state barriers (35) in a mechanical hierarchy. Deviations from two-state processes such as static (36) or dynamic (37) disorder and glassy dynamics (38) are not appropriate explanations for the measured data, because they still have monotonic decaying probability distributions. The asymmetrical shape with its pronounced peak (Fig. 3 *a*) resembles a γ-distribution very well. A simple model that yields such a distribution is that of several single-exponential decaying processes that occur one after another. For example, the time-dependent probability density for the n^{th} subsequent occurrence of a process with the rate k is given by a binomial distribution for discrete time steps (39) or, in continuous time, by an Erlang-Distribution (37,40)

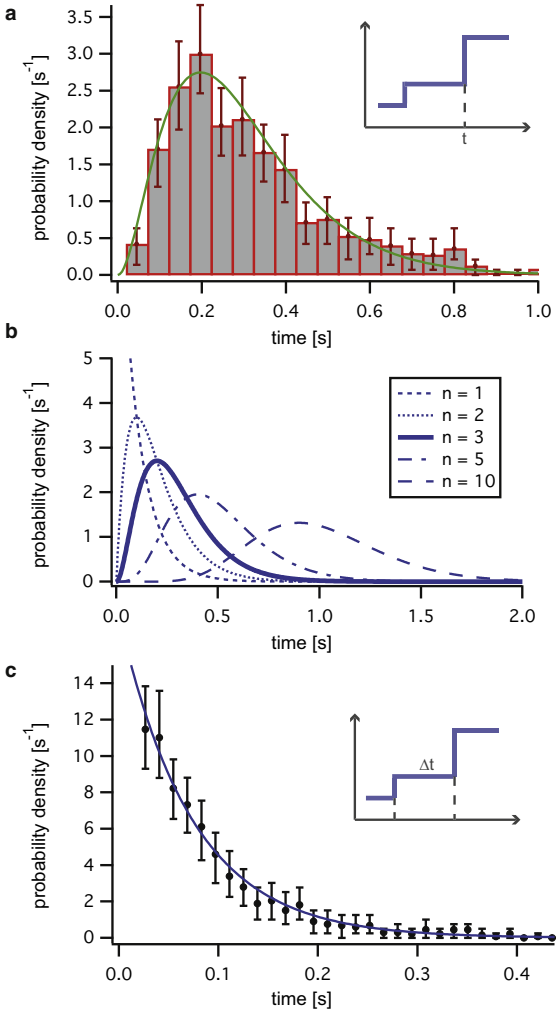

FIGURE 3 Structural dependencies of barrier no. 5 measured at a constant force of 30 pN. The timescales of the unfolding of the 44 nm increment (see Fig. 2 *d*, population *D*) were analyzed as follows. (*a*) Histogram of unfolding times after first force-appliance (t_{abs}). The distribution is clearly not single-exponential but γ-shaped, which is a premise for structural topologies. The fitted line describes a three-step Erlang-distribution with rate $k = 10.1\ s^{-1}$. (*b*) Erlang-distributions for different step numbers n from 1 to 10. For $n = 1$ the distribution reduces to a single-exponential decay. With increasing n average, unfolding times get higher and the distribution gets more symmetric until it resembles a shifted normal distribution. (*c*) Probability density histogram for the times t_{rel} between the unfolding of the preceding step and the unfolding of barrier 5. The decay probability is single-exponential and indicates that the single substeps are unfolding according to the principle of Markovian two-step behavior.

$$p(t;k,n) = \frac{k^n}{(n-1)!}t^{n-1}e^{-kt},$$

which is a special case of a γ-distribution with a discrete second parameter. The behavior is depicted in Fig. 3 *b*. For $n = 1$ the probability density reduces to a simple exponential curve. For $n > 1$, the curve has a peak and its position shifts to higher times with higher numbers of events. Furthermore, the curve gets less asymmetric with higher n. Fig. 3 *c* shows the distribution of the dwell time between the opening of barrier 5 and the previous barrier. It is again supporting a model with structural dependent barriers because it exhibits an exponential decay with a rate constant of $k_5 = 14 \pm 2\ s^{-1}$, and thus indicates that the single unfolding steps obey Markovian rules.

The absolute time distribution of the unfolding of barrier 5 is represented very well by an Erlang distribution (3 steps; $k = 10.1\ s^{-1}$) and its time constant does roughly match the measured unfolding rate of barrier 5. However, the Erlang-Model is an oversimplification by assuming all rates to be the same, and is thus not an accurate fitting model for the unfolding of TK. Nevertheless, it already illustrates that there has to be a structural dependency of the unfolding steps.

Identification of the other structural elements and Markov chain modeling

To gain further insight into the processes taking place during unfolding, the other barriers in the force-clamp traces have to be identified too. This is done by taking into account both the step height and the position at which unfolding occurs. Barrier 5 is overcome at a position 114 nm above the surface with a distribution width of 10 nm that is due to different attachment sites of cantilever and surface and partial opening of the surrounding Ig/Fn-domains (see Fig. S5). This defined position exactly matches the added unfolding lengths of all structural elements of TK at 30 pN pulling force (see Table 1) and further affirms that barrier 5 also opens last in force-clamp experiments. Fig. 4 *a* displays how the barriers 1–4 as well as the fibronectin or Ig domains can be identified by offsetting the distance trace to the position of the unfolding event before barrier 5.

For nearly all of the events, this relative position together with the step height allows the interpretation of which unfolding step belongs to which barrier. (A drawback of this method is that one only selects those traces that have the unfolding order from 1 to 5, but the histograms in Fig. 4 *a* prove that at least 88% of all detected steps in the selected traces agree with this scheme.) To reduce possible misinterpretation of the barrier number, the step height population A was split into two parts (A_1, A_2) with a cutoff at 6 nm. Therefore, there are maximally two expected barriers per histogram, and their expected positions are well separated. The histograms exhibit very pronounced peaks that match the sequential unfolding pattern, which is observed in experiments with constant retraction velocity. Now the unfolding rates of the remaining barriers can be determined (Fig. 4 *b*). They are depicted in Table 1 together with the values and population identifiers that were used to determine the barrier number.

To check the model of structural topology, we calculated the analytical solution of the coupled differential equations of a sequential Markov chain consisting of six barriers with exponentially distributed unfolding times (see Materials and Methods). There are six steps, because the additional energy barrier 2* that is observed with a velocity-dependent probability is considered as well. The resulting probability distribution of the unfolding time of the last step with the experimentally determined opening rates is depicted in Fig. 5. Maximum and minimum likelihood distributions were calculated by different combinations of rates that were chosen from the experimental error range such that they lead to most or least probable unfolding for a given time. As the graph shows, the degree of coincidence of the sequential Markov chain model with the experimentally determined distribution is high. The most probable unfolding time, for example, is 204 ms for the model and within 170–220 ms for the experimental data. However, the experimental distribution has a slightly broader tail that is shifted to longer times.

A manual revision of the unfolding traces showed that the timescale of unfolding seems to correlate for the structural elements in a single trace. All these elements tend to either open slightly faster or slower in a single trace, which causes a broadening of the probability distribution to longer times with respect to the Markov chain model. Because it cannot be distinguished whether this shift is due to an intramolecular effect like deviations from two-state behavior (38,39) or is mainly caused by faint shifts of the force setpoint due to cantilever drift, we will refrain from a further discussion of this effect and treat it as incompleteness of the model or experimental artifact. (Note that setpoints that are shifted only ~5 pN can already yield rates that differ ~50% from the desired one. Therefore, protein unfolding in traces where the setpoint is 5 pN too low would need, on average, twice the time and 0.66 of the regular time for setpoints that are too high. This effect is strong enough to explain the deviations from the modeled line. See Force Dependence of Unfolding Rates in the Supporting Material.)

Independent unfolding of the fibronectin domain

At 30 pN clamping force, in ~10% of the unfolding traces, not only is the complete titin kinase unfolding pattern observable, but another 22-nm step is present. This is due to the unfolding of one of the four surrounding Ig-domains or the fibronectin domain, which are included in the titin fragment used here and have similar step heights as barrier

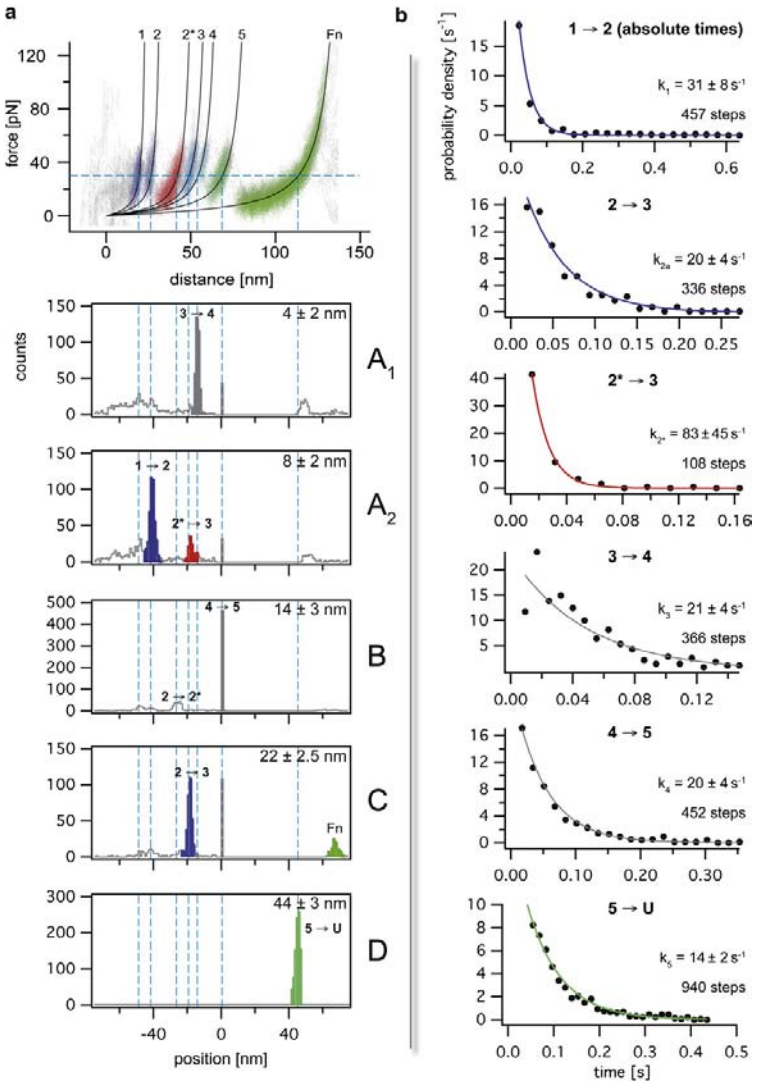

FIGURE 4 (*a*) Identification of the structural barriers by height and position relative to barrier 5. Histograms of the unfolding position relative to barrier 5 are drawn for each population introduced in Fig. 2 *d*. To reduce the possibility of misinterpretation between barriers 2* and 3, the population *A* has been split into two parts with a cutoff at 6 nm. The population identifier (*A–D*) is marked on the right of each histogram, and the contained step height is given (*top right*). The histograms exhibit well-defined peaks at the positions where they are expected for the scenario of structural topology with the constant velocity unfolding pattern as a ruler. The measurement was performed with 2 mM ATP present in solution. The probability of occurrence of peak 2* is linked to pulling velocity and ATP content (21) and was determined to be $p = 0.35$, which matches the expectations from constant velocity experiments very well. (*b*) Probability density histograms with single-exponential decay fits for the substeps of TK unfolding from the folded conformation (*F*) to the completely unfolded conformation (*U*) at 30 pN pulling force. Details of histogram generation and fitting are given in Rate Fitting (see main text).

2 (compare to Table 1). Those steps most likely describe the unfolding of the fibronectin domain, because its fold is inherently less stable than the Ig-fold (43,44). Although in the majority of the traces the additional unfolding occurs after the titin kinase barriers, a revision of the traces with two steps in the identification interval at ~22 nm pointed out that the position of this increment is random. In ~8% of the traces, the additional step is located within the unfolding of the kinase domain and does not shift the sequence of barriers 1–5. Fig. 5 *b* shows the probability distribution for the absolute unfolding times of the additional domain.

Because the Ig and Fn domains are comparatively stable (45), unfolding occurs at longer timescales. In contrast to the TK barriers, the additional domain is decaying exponentially, which demonstrates well that the unfolding of these domains is independent of the kinase unfolding according to the principle of mechanical hierarchy. The measured rate, however, does not correspond to the natural unfolding rate at this force. The natural rate is expected to be much lower; longer times are underrepresented in the histogram, because the detachment of protein from the cantilever or the surface occurs at a similar timescale (see Fig. S4 for comparison). Furthermore, the effect that the fibronectin fold may open in between the kinase domains means that some of the steps that are contained in the histograms of Fig. 4 *a* cannot be explained with the direct sequence from barrier 1 to 5.

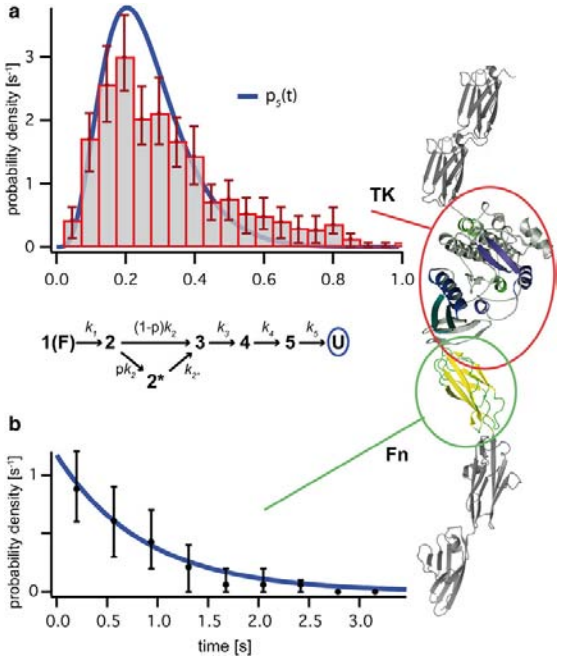

FIGURE 5 Markov-chain model and independent unfolding of the fibronectin domain. (*a*) The unfolding probability distribution from barrier 5 into the completely unfolded state (*U*) can be reasonably well fitted with the model $p_5(t)$, which consists of a sequential Markov-chain with six dependent single-exponential processes. The rates k_i are taken from Table 1. This model describes a structural topology of all barrier-causing structural elements of titin kinase. The shift to longer times in the experimental data is most likely due to slight offsets in the pulling force due to cantilever drift, which cannot be neglected at the small clamping force of only 30 pN. (*b*) Unfolding probability distribution for the fibronectin domains obtained at 30 pN pulling force. In contrast to the other barriers, the absolute unfolding times of the fibronectin domain are exponential-distributed, which demonstrates that this barrier unfolds independently from the structural elements of titin kinase.

DISCUSSION

In summary, our experiments and modeling have unraveled the mechanical architecture of titin kinase as an example of a biological mechanical force sensor. Our results confirm that forces below 30 pN, reflecting a force imbalance in the muscle sarcomere equivalent to only ~5 myosin motor domains with 6 pN each (47), can result in significant regional, but nondestructive conformational changes in TK. In fact, on a timescale of seconds, forces much lower than 30 pN are predicted to lead to opening of the TK active site, because the rate of unfolding of the TK elements strongly depends on the pulling force (see the Supporting Material). This implies that even at lower forces than those that were experimentally observable in our setup, barriers may open at longer timescales. Modeled force-responses of whole sarcomeres further suggest that the experimental forces lie in the physiological accessible range (48).

The line of evidence from our measured single-molecule force spectroscopy data proves that the underlying principle that assures enzymatic function under the constraint of applied force is the structural topology of at least some of the force-bearing elements. The measured data strongly suggest that the unfolding of the complete titin kinase construct under force occurs in a series of six exponentially distributed barriers that have to be overcome one after the other. A protein architecture like this ensures the proper function of this special enzyme, which can react to mechanical stimuli with conformational changes while maintaining its structural integrity. Before structural elements unfold that support proper conformation of the active site, barriers have to be overcome that determine the enzymatic response (21,22).

The same stabilization principle has recently been shown to be applicable also to artificially designed proteins, and may be useful for novel multifunctional designed elements in nanomechanics and nanobiotechnology (49).

Furthermore, the reliability of the experimental technique was underlined by demonstrating that the recorded data are able to prove the independent unfolding of the adjacent fibronectin fold next to the protein kinase according to the principle of mechanical hierarchy. The way in which mechanical forces control the conformational landscape of titin around its single catalytic domain suggest also that protein interactions close to the kinase domain might be subject to mechanical modulation. Integration of this molecular information into future models of the sarcomeric M-band should ultimately help us to understand how forces in this enigmatic cellular structure are both resisted and employed for signaling.

SUPPORTING MATERIAL

Additional information accompanied by five figures is available at http://www.biophysj.org/biophysj/supplemental/S0006-3495(11)01105-2.

S.W.S. thanks Mathias Strackharn for helpful discussions.

M.G. and A.A. gratefully acknowledge the generous support by the British Heart Foundation and the Medical Research Council. M.G. holds the British Heart Foundation Chair of Molecular Cardiology. E.M.P. is supported by the Deutsche Forschungsgemeinschaft. This work was supported by the Nanosystems Initiative Munich, the Volkswagenstiftung, and the Deutsche Forschungsgemeinschaft Grant SFB 863.

REFERENCES

1. Wozniak, M. A., and C. S. Chen. 2009. Mechanotransduction in development: a growing role for contractility. *Nat. Rev. Mol. Cell Biol.* 10:34–43.

2. Smith, A. S., and E. Sackmann. 2009. Progress in mimetic studies of cell adhesion and the mechanosensing. *ChemPhysChem.* 10:66–78.

3. Yagmur, C., S. Akaishi, …, E. Guneren. 2010. Mechanical receptor-related mechanisms in scar management: a review and hypothesis. *Plast. Reconstr. Surg.* 126:426–434.

4. Gillespie, P. G., and U. Müller. 2009. Mechanotransduction by hair cells: models, molecules, and mechanisms. *Cell.* 139:33–44.
5. Vogel, V. 2006. Mechanotransduction involving multimodular proteins: converting force into biochemical signals. *Annu. Rev. Biophys. Biomol. Struct.* 35:459–488.
6. Brown, A. E., and D. E. Discher. 2009. Conformational changes and signaling in cell and matrix physics. *Curr. Biol.* 19:R781–R789.
7. Zhang, X., K. Halvorsen, …, T. A. Springer. 2009. Mechanoenzymatic cleavage of the ultralarge vascular protein von Willebrand factor. *Science.* 324:1330–1334.
8. Crampton, N., and D. J. Brockwell. 2010. Unraveling the design principles for single protein mechanical strength. *Curr. Opin. Struct. Biol.* 20:508–517.
9. Puchner, E. M., and H. E. Gaub. 2009. Force and function: probing proteins with AFM-based force spectroscopy. *Curr. Opin. Struct. Biol.* 19:605–614.
10. Thomas, W. E., V. Vogel, and E. Sokurenko. 2008. Biophysics of catch bonds. *Annu. Rev. Biophys.* 37:399–416.
11. Lange, S., E. Ehler, and M. Gautel. 2006. From A to Z and back? Multicompartment proteins in the sarcomere. *Trends Cell Biol.* 16:11–18.
12. Tskhovrebova, L., and J. Trinick. 2010. Roles of titin in the structure and elasticity of the sarcomere. *J. Biomed. Biotechnol.* 2010:612482.
13. Krüger, M., and W. A. Linke. 2009. Titin-based mechanical signaling in normal and failing myocardium. *J. Mol. Cell. Cardiol.* 46:490–498.
14. Lange, S., F. Xiang, …, M. Gautel. 2005. The kinase domain of titin controls muscle gene expression and protein turnover. *Science.* 308:1599–1603.
15. Agarkova, I., and J. C. Perriard. 2005. The M-band: an elastic web that crosslinks thick filaments in the center of the sarcomere. *Trends Cell Biol.* 15:477–485.
16. Gautel, M. 2011. The sarcomeric cytoskeleton: who picks up the strain? *Curr. Opin. Cell Biol.* 23:39–46.
17. Huxley, H. E., A. Stewart, …, T. Irving. 1994. X-ray diffraction measurements of the extensibility of actin and myosin filaments in contracting muscle. *Biophys. J.* 67:2411–2421.
18. Brunello, E., P. Bianco, …, V. Lombardi. 2006. Structural changes in the myosin filament and cross-bridges during active force development in single intact frog muscle fibers: stiffness and x-ray diffraction measurements. *J. Physiol.* 577:971–984.
19. Lombardi, V., G. Piazzesi, …, M. Irving. 2004. X-ray diffraction studies of the contractile mechanism in single muscle fibers. *Philos. Trans. R. Soc. Lond. B Biol. Sci.* 359:1883–1893.
20. Gräter, F., J. Shen, …, H. Grubmüller. 2005. Mechanically induced titin kinase activation studied by force-probe molecular dynamics simulations. *Biophys. J.* 88:790–804.
21. Puchner, E. M., A. Alexandrovich, …, M. Gautel. 2008. Mechanoenzymatics of titin kinase. *Proc. Natl. Acad. Sci. USA.* 105:13385–13390.
22. Puchner, E. M., and H. E. Gaub. 2010. Exploring the conformation-regulated function of titin kinase by mechanical pump and probe experiments with single molecules. *Angew. Chem. Int. Ed. Engl.* 49: 1147–1150.
23. Gautel, M. 2011. Cytoskeletal protein kinases: titin and its relations in mechanosensing. *Pflugers Arch.* 462:119–134.
24. Oberhauser, A. F., and M. Carrión-Vázquez. 2008. Mechanical biochemistry of proteins one molecule at a time. *J. Biol. Chem.* 283:6617–6621.
25. Neuman, K. C., and A. Nagy. 2008. Single-molecule force spectroscopy: optical tweezers, magnetic tweezers and atomic force microscopy. *Nat. Methods.* 5:491–505.
26. Binnig, G., C. F. Quate, and C. Gerber. 1986. Atomic force microscope. *Phys. Rev. Lett.* 56:930–933.
27. Evans, E., and K. Ritchie. 1999. Strength of a weak bond connecting flexible polymer chains. *Biophys. J.* 76:2439–2447.
28. Oberhauser, A. F., P. K. Hansma, …, J. M. Fernandez. 2001. Stepwise unfolding of titin under force-clamp atomic force microscopy. *Proc. Natl. Acad. Sci. USA.* 98:468–472.
29. Stahl, S. W., E. M. Puchner, and H. E. Gaub. 2009. Photothermal cantilever actuation for fast single-molecule force spectroscopy. *Rev. Sci. Instrum.* 80:073702.
30. Schlierf, M., F. Berkemeier, and M. Rief. 2007. Direct observation of active protein folding using lock-in force spectroscopy. *Biophys. J.* 93:3989–3998.
31. Gumpp, H., S. W. Stahl, …, H. E. Gaub. 2009. Ultrastable combined atomic force and total internal reflection fluorescence microscope [corrected]. *Rev. Sci. Instrum.* 80:063704 (corrected).
32. Butt, H. J., and M. Jaschke. 1995. Calculation of thermal noise in atomic-force microscopy. *Nanotechnology.* 6:1–7.
33. Cook, S., T. E. Schaffer, …, K. M. Lang. 2006. Practical implementation of dynamic methods for measuring atomic force microscope cantilever spring constants. *Nanotechnology.* 17:2135–2145.
34. Reference deleted in proof.
35. Cao, Y., R. Kuske, and H. B. Li. 2008. Direct observation of Markovian behavior of the mechanical unfolding of individual proteins. *Biophys. J.* 95:782–788.
36. Kuo, T. L., S. Garcia-Manyes, …, J. M. Fernández. 2010. Probing static disorder in Arrhenius kinetics by single-molecule force spectroscopy. *Proc. Natl. Acad. Sci. USA.* 107:11336–11340.
37. Floyd, D. L., S. C. Harrison, and A. M. van Oijen. 2010. Analysis of kinetic intermediates in single-particle dwell-time distributions. *Biophys. J.* 99:360–366.
38. Brujic, J., R. I. Hermans, …, J. M. Fernandez. 2006. Single-molecule force spectroscopy reveals signatures of glassy dynamics in the energy landscape of ubiquitin. *Nat. Phys.* 2:282–286.
39. Brujic, J., R. I. Z. Hermans, …, J. M. Fernandez. 2007. Dwell-time distribution analysis of polyprotein unfolding using force-clamp spectroscopy. *Biophys. J.* 92:2896–2903.
40. Evans, M., N. Hastings, and B. Peacock. 2000. Statistical Distributions. Wiley, New York 71–73.
41. Reference deleted in proof.
42. Reference deleted in proof.
43. Rief, M., M. Gautel, …, H. E. Gaub. 1998. The mechanical stability of immunoglobulin and fibronectin III domains in the muscle protein titin measured by atomic force microscopy. *Biophys. J.* 75:3008–3014.
44. Linke, W. A., and A. Grützner. 2008. Pulling single molecules of titin by AFM—recent advances and physiological implications. *Pflugers Arch.* 456:101–115.
45. Garcia-Manyes, S., J. Brujić, …, J. M. Fernández. 2007. Force-clamp spectroscopy of single-protein monomers reveals the individual unfolding and folding pathways of I27 and ubiquitin. *Biophys. J.* 93:2436–2446.
46. Reference deleted in proof.
47. Piazzesi, G., M. Reconditi, …, V. Lombardi. 2007. Skeletal muscle performance determined by modulation of number of myosin motors rather than motor force or stroke size. *Cell.* 131:784–795.
48. Shabarchin, A. A., and A. K. Tsaturyan. 2010. Proposed role of the M-band in sarcomere mechanics and mechano-sensing: a model study. *Biomech. Model. Mechanobiol.* 9:163–175.
49. Peng, Q., and H. Li. 2009. Domain insertion effectively regulates the mechanical unfolding hierarchy of elastomeric proteins: toward engineering multifunctional elastomeric proteins. *J. Am. Chem. Soc.* 131:14050–14056.
50. Reference deleted in proof.

Supplementary Online Material

A conditional gating mechanism assures the integrity of the molecular force-sensor titin kinase

Stefan W Stahl [1], Elias M Puchner [1,4] , Alexander Alexandrovich [3] , Mathias Gautel [3] and Hermann E Gaub [1,2,]*

[1] Chair for Applied Physics and Center for NanoScience (CeNS), Ludwig-Maximilians-University Munich, Amalienstr. 54, D-80799 Germany

[2] Center for Integrated Protein Science Munich (CIPSM)

[3] Cardiovascular Division and Randall Division for Cell and Molecular Biophysics. King's College London, London SE1 1UL, United Kingdom

[4] current address: Department of Cellular and Molecular Pharmacology, University of California, San Francisco, 600 16th Street, San Francisco, CA 94158, USA

* gaub@lmu.de

Force dependence of unfolding rates:

Force clamp traces were obtained at pulling forces of 20, 30, 40 and 50 pN and the force dependence of the determined unfolding rates was examined. Results are depicted in Figure S3. Obviously the lifetime of the barriers decreases when a higher force is applied as it is expected for example in the commonly used Bell-Evans-Model (1),(2) that describes bond dissociation under force. Nevertheless due to experimental limitations it is not possible to gather reliable information on kinetic parameters such as the potential width Δx_i or the unloaded transition rate k_i. In the low force regime (20 pN) already little deviations from the desired force set point that are for example induced by cantilever drift in the time interval between force zero determination and dwell time on the surface will result in notable changes of the unfolding rates. That is observable in bigger error bars of the bootstrapping. In the high force regime (50 pN) the limitation is the speed with which the feedback can react on force decreases induced by barrier opening. Extrapolation of the values obtained at 20, 30 and 40 pN would result in force-induced transition rates between 200 and 700 s^{-1}, which is too fast for the feedback to react (5 ms typical response time). Therefore only the slower events are detected which results in too low fitted rates for the transitions 1-2, 2-2*, 2*-3, 4-5 and 5-U. In Figure S3 results of error weighted Levenberg-Marquardt fits to the Bell equation

$$\ln(k_{off})(F) = \ln(k_{off,0}) + \frac{F\Delta x}{k_B T}$$

are given. The results show that the potential widths are in the regime of other published data on protein unfolding (e.g. Titin-Ig27 (3), NuG2 (4): 0.25 nm; GFP (5): 0.12-0.45 nm) whereas for the unloaded transition rates only upper bounds may be given that exceed published data by 3 orders of magnitude.

1. Bell, G. I. 1978. Models for the specific adhesion of cells to cells. Science 200:618-627.
2. Evans, E., and K. Ritchie. 1997. Dynamic strength of molecular adhesion bonds. Biophysical Journal 72:1541-1555.
3. Dougan, L., G. Feng, H. Lu, and J. M. Fernandez. 2008. Solvent molecules bridge the mechanical unfolding transition state of a protein. P Natl Acad Sci USA 105:3185-3190.
4. Cao, Y., R. Kuske, and H. B. Li. 2008. Direct observation of Markovian behavior of the mechanical unfolding of individual proteins. Biophysical Journal 95:782-788.
5. Dietz, H., F. Berkemeier, M. Bertz, and M. Rief. 2006. Anisotropic deformation response of single protein molecules. P Natl Acad Sci USA 103:12724-12728.

Figure S 1

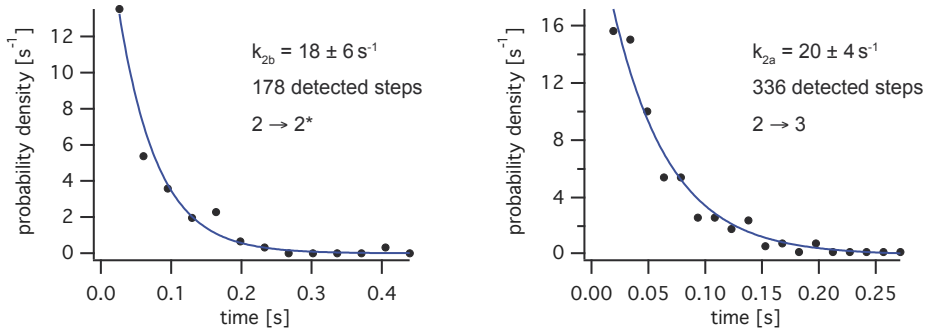

Probability density histograms with single exponential decay fits for the sub steps from barrier 2 to 2* and 2 to 3 respectively at 30 pN pulling force. Since it is not expected that the opening rate of barrier 2 depends on whether the substep 2* is taken and rates match with respect to their error range, they were treated as one rate in the model used for analysis. Details of histogram generation and fitting are given in the materials and methods paragraph “Rate Fitting”.

Figure S 2

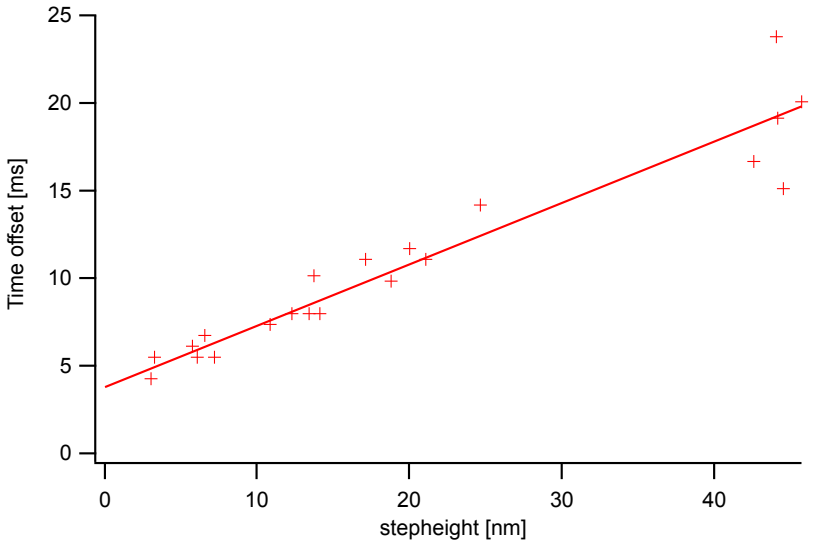

Time offset used for fitting single exponential rates.

The depicted values were picked from the steps of exemplary unfolding traces and consist of the time needed to travel the given distance plus an additional offset of 2.4 ms that accounts for the lag time of the feedback response. Values are well fitted by a linear relation with slope 0.35 ms/nm.

Figure S 3

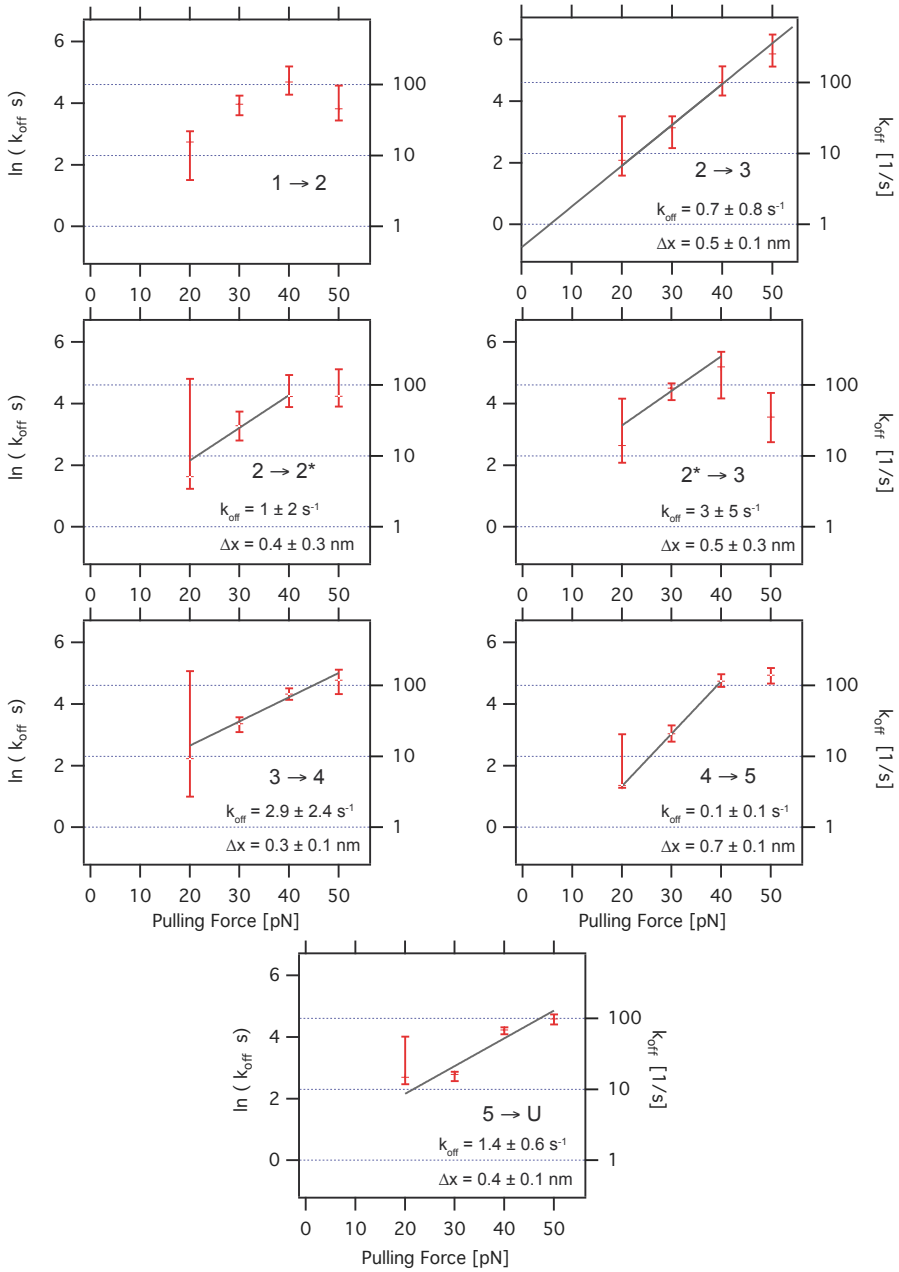

Force dependence of determined rates.
As expected, the unfolding rates rise with higher clamping fore. Due to effects of cantilever drift in the force regime below 30 pN and limited feedback bandwidth in the force regime above 40 pN fitting to the exponential dependence predicted by the Bell-Modell (1) does not yield reliable data. For details see supplementary paragraph “Force dependence of unfolding rates”.

Figure S 4

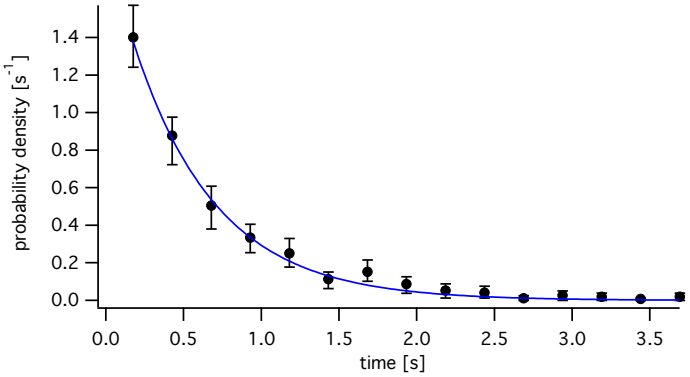

Histogram of detachment times from either the protein from the cantilever or the surface at 40 pN pulling force. The detachment process is exponential with a decay time of 0.6 s which increases to around 0.8 s at 30 pN. The detachment process influences the histogram for the opening of the Fn / Ig barriers measured in Figure 5. There longer times are underrepresented due to prior rupture of the binding between protein and cantilever or surface.

Figure S 5

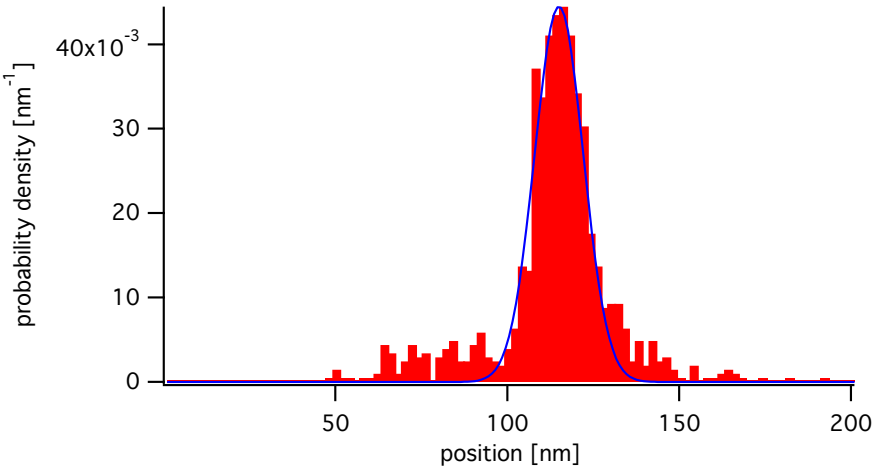

Probability density histogram for the position at which barrier 5 opens. It is approximately Gaussian distributed around 114 nm over the surface position which corresponds to the sum of all titin kinase domains and thus confirms that it also opens last in force clamp experiments.

P7 INTERLABORATORY ROUND ROBIN ON CANTILEVER CALIBRATION FOR AFM FORCE SPECTROSCOPY

te Riet J, Katan AJ, Rankl C, Stahl SW, van Buul AM, Phang IY, Gomez-Casado A, Schön P, Gerritsen JW, Cambi A, Rowan AE, Vancso GJ, Jonkheijm P, Huskens J, Oosterkamp TH, Gaub H, Hinterdorfer P, Figdor CG, Speller S.

ULTRAMICROSCOPY. 2011 Dec;111(12):1659-69.

Ultramicroscopy 111 (2011) 1659–1669

Contents lists available at SciVerse ScienceDirect

Ultramicroscopy

journal homepage: www.elsevier.com/locate/ultramic

Interlaboratory round robin on cantilever calibration for AFM force spectroscopy

Joost te Riet [a,b], Allard J. Katan [c,1], Christian Rankl [d], Stefan W. Stahl [e], Arend M. van Buul [f], In Yee Phang [g,h,2], Alberto Gomez-Casado [i], Peter Schön [g], Jan W. Gerritsen [a], Alessandra Cambi [b], Alan E. Rowan [f], G. Julius Vancso [g,h], Pascal Jonkheijm [i], Jurriaan Huskens [i], Tjerk H. Oosterkamp [c], Hermann Gaub [e], Peter Hinterdorfer [j], Carl G. Figdor [b], Sylvia Speller [a,*]

[a] Scanning Probe Microscopy, Radboud University Nijmegen, P.O. Box 9010, 6500 GL Nijmegen, The Netherlands
[b] Tumor Immunology, Radboud University Nijmegen Medical Centre, P.O. Box 9101, 6500 HB Nijmegen, The Netherlands
[c] Kamerling Onnes Laboratory, Leiden University, P.O. Box 9504, 2300 RA Leiden, The Netherlands
[d] Agilent Technologies Austria GmbH, Altenbergerstr. 52, A-4040 Linz, Austria
[e] Applied Physics, Ludwig-Maximilian-University Munich, Amalienstr. 54, 80799 München, Germany
[f] Molecular Materials, Radboud University Nijmegen, P.O. Box 9010, 6500 GL Nijmegen, The Netherlands
[g] Materials Science and Technology of Polymers, University of Twente, P.O. Box 217, 7500 AE Enschede, The Netherlands
[h] Dutch Polymer Institute, P.O. Box 902, 5600 AX Eindhoven, The Netherlands
[i] Molecular Nanofabrication, University of Twente, P.O. Box 217, 7500 AE Enschede, The Netherlands
[j] Institute for Biophysics, University of Linz, A-4040 Linz, Austria

ARTICLE INFO

Article history:
Received 13 July 2011
Received in revised form
12 September 2011
Accepted 16 September 2011
Available online 24 September 2011

Keywords:
Atomic force microscopy
AFM force spectroscopy
Spring constant
Round robin experiment
Cantilever calibration

ABSTRACT

Single-molecule force spectroscopy studies performed by Atomic Force Microscopes (AFMs) strongly rely on accurately determined cantilever spring constants. Hence, to calibrate cantilevers, a reliable calibration protocol is essential. Although the thermal noise method and the direct Sader method are frequently used for cantilever calibration, there is no consensus on the optimal calibration of soft and V-shaped cantilevers, especially those used in force spectroscopy. Therefore, in this study we aimed at establishing a commonly accepted approach to accurately calibrate compliant and V-shaped cantilevers. In a round robin experiment involving eight different laboratories we compared the thermal noise and the Sader method on ten commercial and custom-built AFMs. We found that spring constants of both rectangular and V-shaped cantilevers can accurately be determined with both methods, although the Sader method proved to be superior. Furthermore, we observed that simultaneous application of both methods on an AFM proved an accurate consistency check of the instrument and thus provides optimal and highly reproducible calibration. To illustrate the importance of optimal calibration, we show that for biological force spectroscopy studies, an erroneously calibrated cantilever can significantly affect the derived (bio)physical parameters. Taken together, our findings demonstrated that with the pre-established protocol described reliable spring constants can be obtained for different types of cantilevers.

© 2011 Published by Elsevier B.V.

1. Introduction

The Atomic Force Microscope (AFM) is a sensitive force probe [1] with a resolution in the picoNewton (pN) range, allowing characterization of inter- and intra-molecular forces. The study of single molecule bond dynamics by AFM, known as AFM force spectroscopy, is widely used to investigate biological and chemical interactions, providing insight into their intra-molecular energy landscapes [2,3]. In 1994, individual ligand–receptor interactions between avidin and biotin were measured for the first time [4,5]. Since then, force spectroscopy has been used to study, e.g., DNA structure [6,7], unfolding of native proteins [8,9], polymers [10], covalent bonds [11], rupture of supramolecular bonds [12], and cell adhesion [13,14]. All these force measurements rely on the use of well calibrated cantilevers, i.e., to know the absolute spring constant allowing one to quantify the forces. In addition, many other AFM applications such as nanostructuring [15], elasticity mapping [10,16], and static as well as resonant imaging modes [17] depend on an accurately determined spring constant in order to quantify the physical forces probed.

* Corresponding author.
E-mail address: s.speller@science.ru.nl (S. Speller).
[1] Present address: Lawrence Berkeley National Laboratory, CA, USA.
[2] Present address: Institute of Materials Research and Engineering, Singapore, Singapore.

0304-3991/$ - see front matter © 2011 Published by Elsevier B.V.
doi:10.1016/j.ultramic.2011.09.012

Over the last decades, several methods have been proposed to determine AFM cantilever spring constants that can be grouped into three categories. Dimensional modeling methods require precise knowledge of the cantilever dimensions and material properties to calculate the spring constant [18–20]. Static deflection methods use glass fibers [21,22], reference cantilevers [23,24], electrostatic forces [25], or a piezosensor [26] to determine the spring constant by loading the cantilever with a known static force. Finally, there are different dynamic deflection methods that relate the spring constant to the cantilever's resonance behavior, such as the Cleveland method [27], the thermal noise method [28], the Sader method [29,30] and laser Doppler vibrometry [31].

All these methods have previously been discussed and compared with each other [31–35]. Specifically, the thermal noise method – based on statistical mechanics – and the Sader method – based on fluid dynamics theory – have been frequently investigated and have the highest application potential, as documented by their implementation in commercial AFMs. Relatively widespread use of these approaches is mainly related to the following advantages: (i) the calibration of the cantilever is performed in situ; (ii) both methods are independent on the cantilever's material or coating; (iii) and they are (largely) nondestructive and noninvasive for the cantilevers. In addition, (iv) the AFM systems used need minimal hard- and software requirements; and finally, (v) both methods are quick and easy to learn. However, upon applying the thermal noise method, it is important to use the accurate correction factors that are described in the literature [32,36,37]. These factors mainly concern differences between rectangular versus V-shaped cantilevers, the cantilever's complex spring behavior, and the AFM's detection scheme.

In earlier studies, the implementation of the thermal noise and Sader methods were described, especially paying attention to technical and theoretical aspects [32,33], demonstrating the calibration of rectangular-shaped cantilevers within a wide spring constant range (0.1–20 N/m) [32]. However, in those studies V-shaped cantilevers were not calibrated. Other reports addressing V-shaped cantilevers did not consider the Sader method [34,38]. In view of the increasing importance of deriving quantitative forces for AFM force spectroscopy, a comparison between the methods addressing cantilevers frequently used in these studies – soft (<0.05 N/m) and V-shaped – has become necessary.

The aim of our study was to investigate potential differences of spring constants calibrated on different (commercial) instruments and in different laboratories, particularly paying attention to practical aspects of cantilever calibration. The experiments described in this article were performed sequentially, as a round robin experiment. In particular, we investigated the accuracy of the thermal noise and direct Sader method by calibrating cantilevers on different AFM systems operated by experienced users in different labs all using the same calibration protocol. Furthermore, two indirect methods by Gibson and Sader [29,39], which relate the spring constant of the rectangular to the V-shaped cantilever on one chip, were considered as alternatives. Finally, we discuss the effect of an incorrectly determined spring constant on the measured forces and micromechanical properties of a biological ligand–receptor bond. We conclude our study by proposing a practical and reliable calibration protocol to obtain reliable spring constants for different types of cantilevers.

2. Materials and methods

2.1. Round robin experiment

The round robin study was set up as a collaboration between eight laboratories from three countries. In these labs different commercial and custom-built AFMs were used to study the same 30 cantilevers on 10 different chips, which were sent around from one lab to the next to sequentially determine their spring constants. The calibrations were performed by experienced users of the AFM systems according to a protocol pre-established by all participants, see Appendix A.

2.2. Instruments

Ten different AFMs were used, of which the description, abbreviation, and location, are given in Table 1. We include a symbol (Roman numerals) to designate the AFMs throughout the study. A brief description of the instruments is given below, detailed information on the software used, the temperature, etc., can be found in Table S1 (Supplementary material).

Multimode Nanoscope IIIa (Veeco, Santa Barbara, CA, USA). Calibrations on the Nijmegen [I] and Enschede [III] AFM systems were performed on thermal noise data sampled at a rate of 62.5 kHz. In detail, false engage images (512×512) of trace and retrace at a line rate of 61 Hz were exported including time series of the successive scan lines, and a power spectral density (PSD) analysis was performed on these data, to obtain all calibration parameters by a fit for further analysis. Calibrations on the Leiden system [II] were performed by routing the deflection data from the Signal Access Module to a 16 bit DAQ card (USB 6152, National Instruments) and recording them at a sample rate of 1.25 MHz. Spectra were calculated from these data during acquisition using custom-written LabView software.

Multimode Nanoscope IV (Veeco). Calibrations on the Nijmegen system [IV] were performed by measuring the thermal noise data at a sampling rate of 62.5 kHz via the Thermal Tune box in the software. Thermal noise spectra were exported and analyzed.

Multimode Nanoscope IVa (Veeco). Calibrations on the Enschede PicoForce system [V] were performed by measuring the thermal noise data at a sampling rate of 62.5 kHz via the Thermal Tune box in the software. InvOLS (inverse optical lever sensitivity (nm/V); also known as deflection sensitivity [40]) measurements were performed

Table 1
Outline of AFM systems used.

Symbol	Abbreviation	System	Location
I	NS IIIa	Veeco Multimode Nanoscope IIIa	Nijmegen (NL)
II	NS IIIa	Veeco Multimode Nanoscope IIIa	Leiden (NL)
III	NS IIIa	Veeco Multimode Nanoscope IIIa	Enschede (NL)
IV	NS IV	Veeco Multimode Nanoscope IV	Nijmegen (NL)
V	NS IVa	Veeco Multimode Nanoscope IVa	Enschede (NL)
VI	NS V	Veeco Multimode Nanoscope V	Nijmegen (NL)
VII	JPK	JPK NanoWizard I	Nijmegen (NL)
VIII	Agilent 5500	Agilent 5500	Linz (A)
IX	CB	Custom-built based on Asylum MFP-3D	Munich (D)
X	CB	Custom-built	Leiden (NL)

cantilever is not needed. Typically the Sader method is applied in air, in which $Q > 10$. Additionally, the length to width ratio should be $L/b > 3$ [43]. By fitting the thermal spectrum of a rectangular cantilever with the SHO model (3), f_R and Q are determined. (For liquid see Ref. [38]). The spring constant can then be described by [29]

$$k = 7.5246\rho b^2 L\Gamma_i(\mathrm{Re}) f_R^2 Q \tag{6a}$$

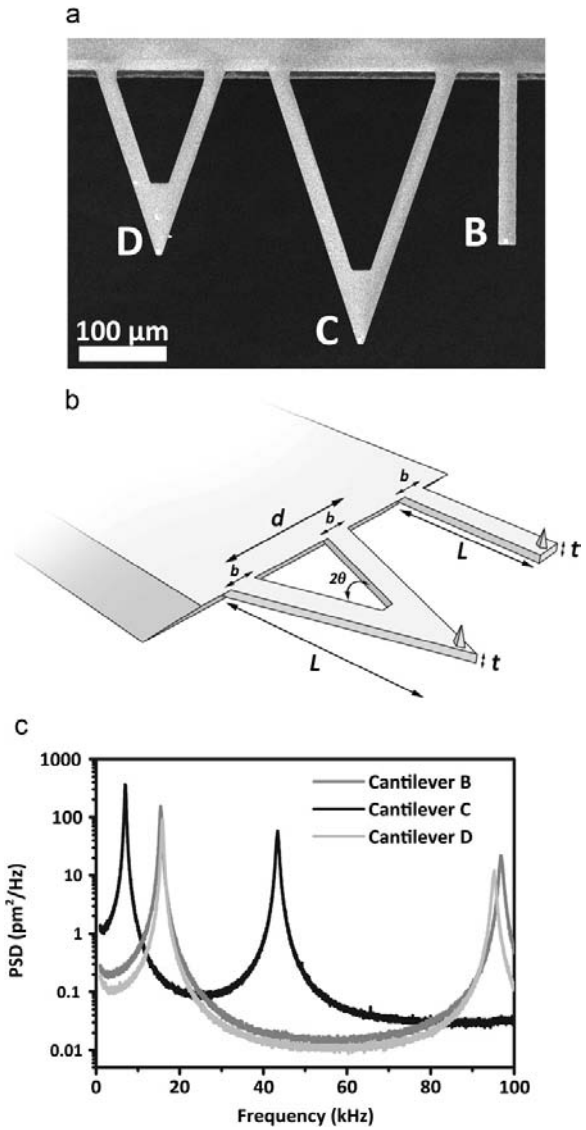

Fig. 1. Characteristics of the three types of cantilevers studied. (a) SEM image of rectangular cantilever B and V-shaped cantilevers C and D on a MSCT chip. (b) Scheme of a rectangular and V-shaped cantilever with the symbols for the dimensions as used throughout the study. (c) Thermal noise spectra of cantilevers B, C, and D on chip MLCT1 as determined with AFM system VI at a sampling rate of 200 kHz. The primary and secondary thermal noise peaks are visible for all three cantilevers. In the spectra the white noise level is low, but shows a $1/f$ noise floor. The resonance frequencies and quality factors of the primary peaks are f_R=14.5, 6.3, and 14.5 kHz and Q=23.1, 14.9, and 25.6 for cantilevers B, C, and D, respectively.

with

$$\mathrm{Re} = \frac{\pi\rho b^2 f_R}{2\eta} \tag{6b}$$

where b is the width of the cantilever, L the length of the cantilever (see Fig. 1b), and Γ_i the imaginary part of the hydrodynamic function [44].

This model is valid for any rectangular cantilever; for V-shaped cantilevers it is necessary to determine the individual dynamical response of each cantilever. This method is described by Sader et al. [30]. In short, the response of the resonance frequency and damping factor are measured according to the Reynolds number Re, which is varied by changing the air pressure. In their study formulas are derived for the V-shaped cantilevers C and D from a MSCT/MLCT chip, which are the type of cantilevers studied in this paper [30]. The formulas for cantilever type C and D are, respectively

$$k = 140.94\rho b_C^2 L_C \mathrm{Re}^{-0.728+0.00915\ln \mathrm{Re}} f_R^2 Q \tag{7a}$$

$$k = 117.25\rho b_D^2 L_D \mathrm{Re}^{-0.700+0.0215\ln \mathrm{Re}} f_R^2 Q \tag{7b}$$

with b_C or b_D the width of one of the two cantilever beams (Fig. 1b), L_C or L_D the length of the cantilever and the Reynolds numbers as in (6b).

2.6. Cantilever tilt

In an AFM cantilevers are usually mounted at a small angle with respect to the horizontal (scan) direction to prevent contact between the cantilever chip and the sample. Different AFMs have different tilt angles α varying from 6–12° (see Table S1). Therefore, it is convenient to compare intrinsic spring constants, rather than tilt-dependent effective values [45]. Intrinsic values are explicitly provided by the Sader method, while effective values are obtained by the traditional implementation of the thermal noise method. Thus, this implies that these spring constants should be corrected by a factor of $\cos^2\alpha$ as described in Ref. [45]. The relation between the effective (thermal noise) and intrinsic (Sader) spring constants is

$$k_{effective} = \frac{k_{intrinsic}}{\cos^2\alpha} \tag{8}$$

An additional correction is needed if the tip protruding from the cantilever is long compared to the cantilever's length [45]. However, this correction is small in most cases, including the present study.

3. Results and discussion

3.1. Physical characteristics of the cantilevers used for calibration

Tested cantilevers are of the MSCT/MLCT-type—one of the most applied types of cantilevers in AFM force spectroscopy studies, due to their low spring constant, uniformity, robustness, and affordability. We choose to study only the softest cantilevers of the chip, i.e., B, C, and D. The dimensions of cantilevers B, C and D, needed for the Sader method, were determined by scanning electron microscopy (SEM). In the SEM image (Fig. 1a) the arrangement of cantilevers B (rectangular), C and D (V-shaped) is shown. The dimensions of each cantilever on three MLCT- and three MSCT-cantilever chips were determined and the mean values are given in Table 2 (see Fig. 1b for labels). The differences between the manufacturer's specifications and the measured dimensions of the cantilevers were smaller than $\pm$1.9% for length and $\pm$7.9% for width. Furthermore, cantilevers from the MLCT and MSCT chips have comparable sizes,

which only vary ±3.9% in width similar to the accuracy of the SEM measurements (±3.3%). Thus, it can be concluded that the manufacturer's nominal dimensions in this specific case are in good agreement with the measured ones. However, we observed that nominal values provided by manufacturers are, in general, insufficiently accurate (±10–25%). Therefore, a check of the dimensions is always recommended.

Another important parameter for the implementation of both methods is temperature, which influences the thermal fluctuations of the cantilever. We found that the temperature, measured at the location of the cantilever in its holder in a working AFM, was usually higher (up to 6 K) than room temperature. Based on Eq. (5), neglecting this temperature difference would imply a systematic error of ~2%. Therefore, actual (measured) temperatures were used in the present study.

3.2. Calibration of the cantilever spring constant by the thermal noise method

Cantilevers are calibrated with the thermal noise method using the pre-established protocol as given in the Appendix A. After InvOLS measurements, thermal noise spectra were obtained and the fundamental resonance peak was fitted with the SHO model (Eq. (3)). Thereby, the resonance frequency f_R, the quality factor Q, the zero frequency power A_0, and the power of the white noise baseline y_0 were obtained (Fig. 1c).

The spring constant of the longest type of cantilevers (C-type) was calculated with Eq. (5) using the derived parameters f_R, Q and A_0. We decided not to calibrate the shorter B- and D-type cantilevers with the thermal noise method to prevent damage of the longer C-type cantilever. This damage might occur when the InvOLS of the shorter cantilevers is measured and the longer C-type cantilever would come into full contact with the substrate. In Fig. 2d, the result is shown of calibrating 10 C-type MLCT/MSCT-cantilevers (see Table S2d for corresponding values). In both Fig. 2d and Table S2d, the intrinsic spring constants are presented, i.e., corrected for cantilever tilt by Eq. (8). In Fig. 2d only the spring constants determined on AFMs [I–IX] are shown. On system X, which was optimized for fast sampling, it was impossible to perform calibrations with the thermal noise method; due to the small z-range of the piezo scanner, the required InvOLS could not be determined as the cantilever did not detach from the substrate, due to strong electrostatic interactions.

When comparing the results obtained on the MLCT and MSCT cantilevers, cantilevers from the same wafer, i.e., MLCT 1–5, MSCT

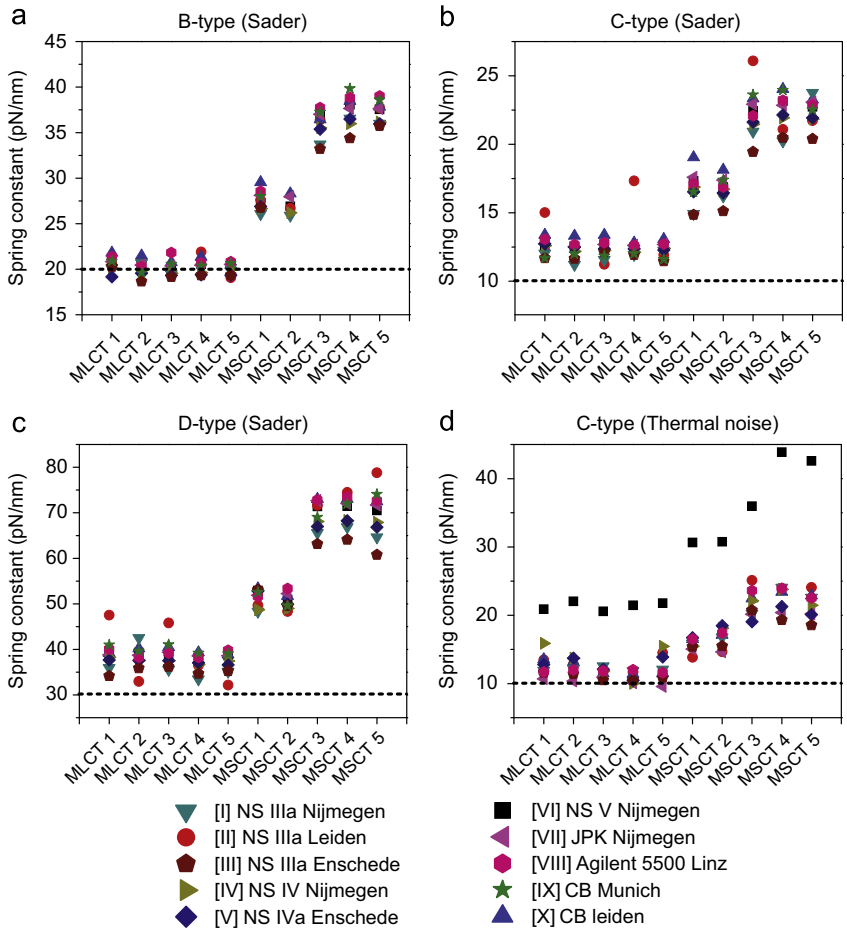

Fig. 2. Cantilever spring constants as determined on different AFMs with the thermal noise and Sader methods. The mean spring constants (N=5) determined for calibrating cantilevers of MLCT and MSCT chips on 10 AFM systems. (a) Using the Sader method to calibrate cantilevers of the B-type, (b) the C-type, (c) and the D-type. (d) Calibrating the C-type cantilevers with the thermal noise method. The different AFMs are represented by different symbols. The cantilever spring constants as given by the manufacturer are indicated by dotted lines (20, 10, and 30 pN/nm).

1–2, and MSCT 3–5, were found to nearly exhibit the same spring constants, within an error of ~4% (Fig. 2d). However, cantilevers from these different chips vary substantially in spring constants. Moreover, if compared to the nominal value given by the manufacturer (10 pN/nm) the measured values of cantilevers MSCT 3–5 are more than double. This example illustrates the importance of manual cantilever calibration instead of simply taking the provided spring constant, which could lead to errors up to ~125%.

3.3. Calibration of the cantilever spring constant by the Sader method

In order to apply the (direct) Sader method, the resonance frequency f_R and the quality factor Q of the cantilevers must be determined first. These are obtained by fitting the thermal noise spectrum of the cantilever. From the obtained parameters and the dimensions of the cantilever (Table 2), the spring constant is calculated using Eqs. (6) or (7).

For the C-type cantilevers the spring constants are instantly calculated from the earlier obtained thermal noise method data and are shown in Fig. 2b and Table S2b. The thermal noise spectra of cantilevers B and D were determined in a similar way, only the laser was re-aligned to these cantilevers, which were kept at all times well above the substrate. The corresponding spectra were analyzed to obtain f_R and Q. As A_0 is not needed for further analysis, it was not necessary to measure the InvOLS in this case. In this way, it is now possible to also calibrate the shorter cantilevers on the chip. The spring constants of cantilevers B and D were determined on all 10 AFMs and are shown in Fig. 2a and c and Table S2a and c, for the B- and D-type of the 10 MLCT/MSCT-chips, respectively. The obtained values are less scattered, and have the same mean value as those of the thermal noise method.

3.4. Comparison of the results obtained with the Sader method on different AFMs

To gain a better insight into the performance of every AFM alone and to be able to compare them with each other, each measurements was normalized to the mean value obtained for the corresponding cantilever using AFM systems [IV–X] (Table 3). We excluded the spring constants obtained on the NS IIIa systems [I–III] in calculating the mean spring constant, because of a high amount of outliers.

Table 3
Spring constants of the cantilevers (pN/nm).[a]

Chip name	*B-type*	*C-type*			*D-type*		
	k_{mean}	k_{mean}	Indirect Sader	Gibson	k_{mean}	Indirect Sader	Gibson
MLCT 1	20.7	12.9	9.9	9.9	39.1	31.0	30.8
MLCT 2	20.3	12.8	9.7	9.6	38.8	30.3	30.3
MLCT 3	20.3	12.8	9.8	10.1	39.1	30.4	31.0
MLCT 4	20.3	12.5	9.8	9.8	38.2	30.4	30.3
MLCT 5	20.3	12.6	9.7	9.8	38.4	30.4	30.0
MSCT 1	27.9	17.3	13.9	14.1	52.0	44.7	41.5
MSCT 2	27.3	16.9	13.6	13.6	51.0	43.8	40.7
MSCT 3	36.6	22.2	18.3	17.8	70.6	58.7	55.7
MSCT 4	37.9	23.0	18.9	18.3	71.2	60.8	58.2
MSCT 5	37.5	22.7	18.7	18.4	70.9	60.2	56.7

[a] Mean values are given of the spring constants obtained on AFMs [IV–X] with the Sader method in 5 subsequent measurements (see also Table S2 for the values obtained on all instruments and with both methods).

The normalized spring constants obtained with the Sader method for the rectangular B-cantilevers are relatively uniform for all AFM systems (Fig. 3a). The observed variation is only 1–3% for every single AFM, and the overall variation in normalized spring constants of all instruments is within a ±6% error in relation to the overall mean cantilever spring constant. For the V-shaped cantilevers of the C- and D-type, the results are in good agreement with the mean cantilever spring constant except for the results obtained on the three NS IIIa systems (Fig. 3b and c). Keeping the results on these three systems out of consideration for a moment, we observe a variation in mean spring constants for each individual AFM of ±2% for C-type as well as for D-type cantilevers. This is similar to the B-type cantilevers. Taking the results of all these AFMs [IV–X] together, a deviation of ±5% is found for both the C- and D-type cantilevers.

For the normalized spring constants obtained on the NS IIIa systems [I–III], however, we observe a systematic error of −4% (±7%) (Fig. 3b and c). This suggests that the obtained spring constants are underestimated and less accurate, especially on system II. An explanation could come from the different way of acquiring the thermal noise data on the NS IIIa systems [I–III] with respect to AFMs IV–IX. Thermal noise data on systems I&III, and II were acquired internally and externally, respectively, and were analyzed off line. As it is not a priori clear how many samplings are necessary to get a spectrum with an acceptable signal-to-noise ratio, the acquisition time may have been too short, resulting in a less accurate fit of the thermal noise spectra.

3.5. Comparison of the results obtained with the thermal noise method on different AFMs

The data obtained with the thermal noise method indicate that the mean spring constants determined for the C-type cantilevers are equal to those determined by the Sader method (Fig. 3d). However, for most of the AFMs, the distributions in values obtained are significant (±3 to ±11%). Having a closer look at the calibrations with the NS IIIa systems I–III, the spring constants are more accurately determined with the thermal noise method than with the Sader method. However, spring constants measured on AFMs V, VI, and VIII are systematically off from the mean. For systems V and VIII this can most likely be attributed to the calibration of the piezo-scanner. Afterwards checking the calibration with another grid, we observed that the given depth of the grid used before deviated from the actual value. An error of ±5% herein, which is reasonable from our own observations, leads to an error in the spring constant of ±10% as the calibration error scales quadratically with the depth. Another cause for the observed higher variations might be static interactions due to charging under low humidity. Actually, the soft C-cantilevers hardly got off the substrate during the InvOLS measurement, leading to non-ideal force curves in which the InvOLS is under- or overestimated. The accuracy of the thermal noise method determined in this study agrees well with the estimated error of ±8% reported by Ohler [33], which they mainly attribute to the error in the InvOLS. In addition to that error, we found that also the error in z-calibration of the AFM has to be taken into account and advise to calibrate it with great care to avoid error propagation.

Still remains the overestimation by ~74% of spring constants calibrated in system VI with the thermal noise method. In fact, on this system high quality calibrations could be performed with the Sader method (Fig. 3a–c). Moreover, this system was calibrated with the same calibration grid as systems I, IV, and VII, suggesting that something completely different is the cause of this overestimation. Most likely, a defect in the implemented hard- or software related to the InvOLS measurements gives rise to this error, for which the system is under revision. Additional information

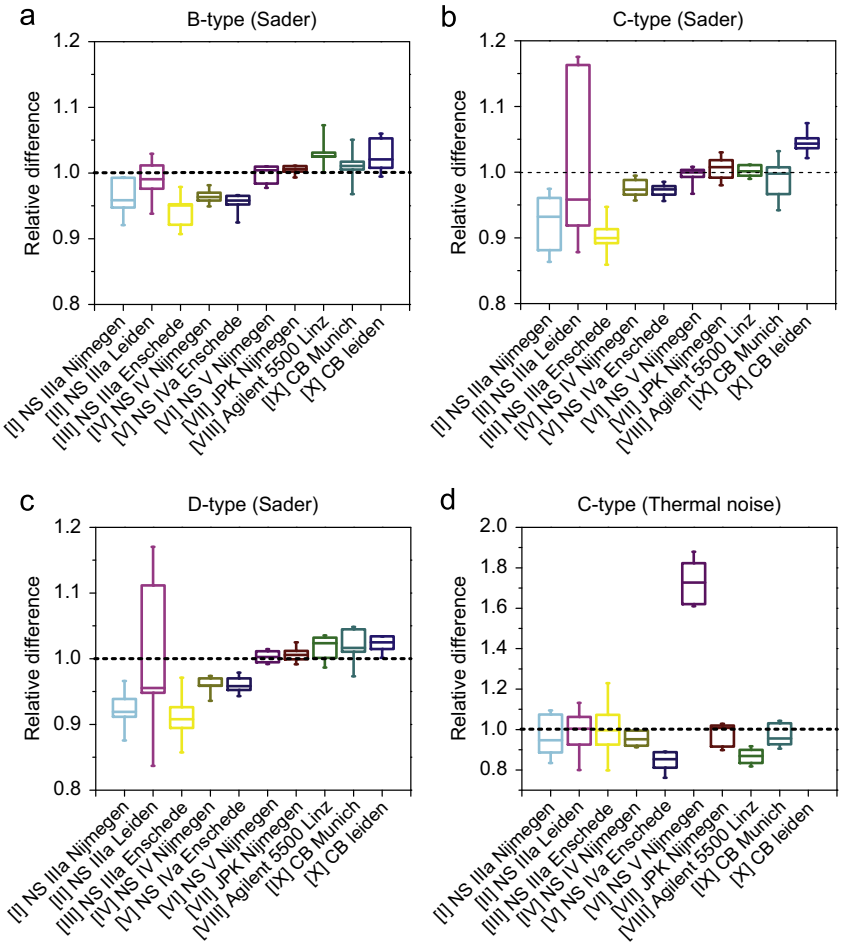

Fig. 3. Comparison of the accuracies of the AFMs. Box plot in which the accuracies of 10 AFMs are compared by normalizing each of the measured cantilever spring constants to the mean spring constant found for systems [IV–X] by the Sader method. The normalized value is set to 1 and is indicated by the dotted line in all plots. The accuracy of the systems found by applying the Sader method is plotted in, (a) in the case of the B-type, (b) C-type, and (c) D-type. (d) The accuracy of calibrating the C-type cantilever by the thermal noise method. The borders of the boxes represent the 25–75% levels, the line in the box the median and the whiskers the 10–90% levels. Note the difference in scale.

on this issue can be found on http://wiki.science.ru.nl/spm/note_calibration.

In conclusion, the above described cases of systems V, VI, and VIII nicely illustrate another interesting finding from our round robin experiment. The comparison with the other systems revealed systematic errors on these systems, which were not foreseen. Therefore, we recommend users to check consistency for the cantilever calibration on an AFM with more than one method to verify the evaluation implemented in the instrument.

3.6. The Gibson and indirect Sader method for V-shaped cantilevers

Next to direct cantilever spring constant calibration, methods also exist in which the spring constant is determined indirectly. Different theories have been described in literature, in which the spring constant of one (rectangular) cantilever can be related to the spring constant of other cantilevers located on the same chip, assuming that the material properties and thickness for each cantilever on the chip are approximately the same [29,39]. These methods are described as alternatives for the calibration of cantilevers that could not be calibrated due to technical difficulties or with differently shaped cantilevers. In our case, this implies that for the MLCT/MSCT-cantilever chips, the spring constant obtained for the rectangular cantilever B can be used to calculate the spring constant of the V-shaped cantilevers C and D on the same chip. Two different methods were selected to compare the accuracy of such indirect calibration approaches to the direct Sader method and thermal noise methods. First, we applied the indirect method described by Sader et al. [29] that combines the Euler–Bernoulli beam theory [46] for rectangular cantilevers and the parallel beam approximation (PBA) [47] for V-shaped cantilevers. This leads to the following equation for the spring constants of cantilevers C and D using that of B:

$$k_{C/D} = \frac{2k_B L_B^3 d_{C/D}}{L_{C/D}^3 b_B} \cos\theta_{C/D} \left[1 + \frac{4b_{C/D}^3}{d_{C/D}^3}(3\cos\theta_{C/D} - 2)\right]^{-1} \quad (9)$$

where $\theta_{C/D}$ is the half angle in between the two beams of the V-shaped cantilevers C or D and $d_{C/D}$ the full width at the base of the cantilevers (Fig. 1b). Secondly, the indirect method described by Gibson et al. [39] was used, in which the spring constants of two

cantilevers (k_1 and k_2) are related via

$$k_1 = \frac{n_1 A_1}{n_2 A_2}\left(\frac{f_1}{f_2}\right)^2 k_2 \quad (10)$$

where, n_1/n_2 is the ratio between the shape factors of the cantilevers, A_1/A_2 between their areas and f_1/f_2 between their resonance frequencies. The SEM images (Fig. 1a) were used to determine the areas of the cantilevers. The shape factors were derived using data from Sader et al. [48], from cantilever dimensions (Table 2) and a Poisson ratio of 0.24. For cantilever C related to B, this resulted in a factor $n_C A_c/n_B A_B = 2.486$ and for cantilever D in $n_D A_D/n_B A_B = 1.467$.

Subsequently, the spring constants for the C- and D-type cantilevers were calculated by Eqs. (9) and (10) using the spring constants of the B-type obtained earlier, and are given in Table 3. The spring constants calculated with the indirect Sader method are consequently $21 \pm 2\%$ and $18 \pm 3\%$ underestimated for cantilevers C and D, respectively. In addition, the results calculated with the Gibson method are also $21 \pm 2\%$ underestimated for both C and D. However, when the similarly shaped C- and D-cantilevers are compared, the spring constants extrapolated from one to the other are well related within a $\pm 1\%$ error (data not shown). One explanation for the discrepancy of ~20% between directly or indirectly obtained spring constants can be that in both indirect methods the V-shaped cantilever is considered as two beams connected under an angle, which does not account for their real shape [47]. Besides, both indirect methods assume a uniform material density of the cantilevers, although in reality they consist of stacked layers of SiN_4 and gold. Probably, corrections to (9), as for example suggested by Hazel and Tsukruk [49], would better describe V-shaped and bi-component cantilevers. In conclusion, indirect methods can only be used to calculate spring constants of cantilevers when the cantilevers have the same shape.

3.7. Biological implications for AFM force spectroscopy

The importance of accurate calibration of an AFM cantilever becomes evident when AFM Force Spectroscopy is used to study, e.g., biological receptor–ligand interactions at the single molecule and/or single cell level. Upon comparison of data from different studies, conclusions drawn on measured parameters might be wrong due to the use of an inaccurate spring constant calibration protocol. In general, these comparisons between rupture forces F_{rup} are done at a particular loading rate r_f (rate of increase in force). Furthermore, the rupture forces and loading rates are such related that data will appear as a straight line in a semi-logarithmical plot of the force spectrum vs. loading rate (Fig. 4), which is described by the Bell model [50]. In this model, the mean rupture force is given by

$$F_{rup} = \frac{k_B T}{x_\beta}\ln\left(\frac{x_\beta}{k^0_{off} k_B T}\right) + \frac{k_B T}{x_\beta}\ln(r_f) \quad (11)$$

where k^0_{off} is the dissociation rate in the absence of a pulling force, and x_β the mechanical bond-length [51,52]. The Bell model parameters k^0_{off} and x_β characterize the micromechanical properties of the ligand–receptor interaction under study and model their intra-molecular energy landscapes.

Now, if we assume an error of $\pm 20\%$ in cantilever spring constant – which is reasonable based on, e.g., piezo-scanner error ($\pm 10\%$), rectangular instead of V-shaped correction factor ($\pm 7\%$) and ignoring correction factors ($\pm 31\%$) – then the error in the observed rupture forces and loading rates is $\pm 20\%$. In the spectra, this error causes a linear shift up or down (Fig. 4; light and dark gray lines) of the data points. By fitting, we found that the error of

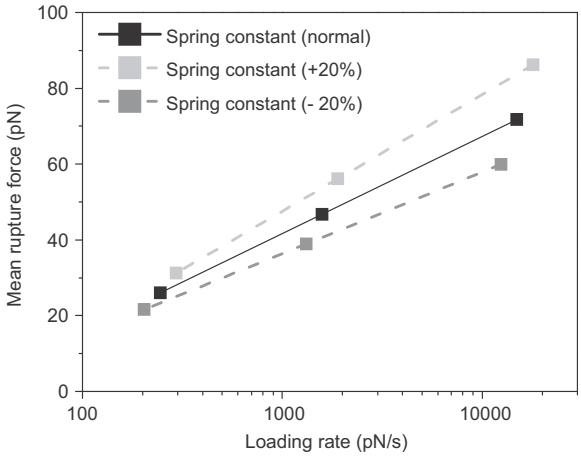

Fig. 4. Influence of under- or overestimated spring constants on the force spectrum. The relation between the mean rupture force (F_{rup}) and the loading rate (r_f) is shown in a force spectrum. Plotted is the change in obtained force spectrum by an error in spring constant of $\pm 20\%$. The data presented in this example are those acquired for the cell adhesion ligand–receptor bond ALCAM-ALCAM, as obtained in Ref. [54]. The corresponding Bell parameters are $k^0_{off} = 2.1\ s^{-1}$ and $x_\beta = 0.37$ nm. The mean rupture forces as well as the loading rates are raised or lowered according to an error of $+20\%$ (light gray) and -20% (dark gray). By fitting the newly obtained force spectra, new Bell parameters are found for these two extremes, which are $k^0_{off} = 2.1\ s^{-1}$ and $x_\beta = 0.31$ nm (for $+20\%$) and $k^0_{off} = 2.1\ s^{-1}$ and $x_\beta = 0.45$ nm (for -20%).

$\pm 20\%$ hardly influenced the Bell parameter k^0_{off}, but resulted in an error of $\pm 20\%$ for x_β. As a consequence, we conclude that when micromechanical properties of ligand–receptors in AFM force spectroscopy are compared by means of their Bell parameters [53,54], it is safe to only compare the k^0_{off}-values from different studies, rather than the x_β-values or the rupture forces at a specific loading rate [14]. However, the use of a commonly adopted protocol with a high accuracy would make the comparison of dynamical bond parameters from different studies more trustworthy.

Force spectroscopy, but also other scientific areas applying AFM in which quantitative measurements of forces are needed, would benefit from a uniform calibration protocol leading to an increase in accuracy of the obtained parameters, independent on AFM, cantilever, and operator. For force spectroscopy, we propose the improved, fast and versatile method described here to calibrate *in situ* functionalized AFM cantilevers, preferably applied in air, although also possible in liquids (see Appendix A). Upon application in liquid, damping of the cantilever becomes substantial and extra care should be taken in fitting and acquiring the data, especially due to commercial AFM limitations [38]. In view of our findings, a combination of the direct Sader method together with calculating the InvOLS – without getting into contact with a substrate, as described by Higgins et al. [55] – yields the best results.

4. Conclusions

In a round robin experiment we compared cantilever calibration methods on different AFMs. By comparing the results obtained on a single AFM versus the mean of 10 AFMs we found that the accuracies are ~6% vs. ~15% for the thermal noise method and ~3% vs. ~7% for the direct Sader method. This demonstrates that – even in the case of using a well-defined protocol – 'relative' errors between AFMs can be substantial.

The main cause for the error of the thermal noise method is that it suffers from systematic errors in determining the correct InvOLS, which can be mainly attributed to discrepancies in the *z*-calibrations of the AFM piezo scanner. On the other hand, the accuracy of the direct Sader method is predominantly defined by the quality of data acquisition of the thermal fluctuations of the cantilever. Another important factor is the accuracy of measuring the dimensions of the cantilever, especially the width, which normally can be measured with a ~3% accuracy by SEM. While this extra step of measuring the dimensions of every cantilever from a different wafer is intrinsic more time-consuming, clear advantages of the Sader method are its higher accuracy and the time saved by calculating instead of measuring the InvOLS.

In addition, the simultaneous implementation and comparison of both calibration methods represents a convenient and effective way to check the proper hardware and software operation of an AFM instrument. Furthermore, the 'sum' of both methods leads to a higher overall accuracy due to the elimination of systematic errors. In general, the systematic errors described in this study can be regarded as representative for errors encountered by any AFM user. It should be noted that, although this study focuses on soft cantilevers calibrated in air, the same two methods can be applied to stiffer cantilevers as well as to cantilevers in liquid.

Finally, we demonstrated that biophysical parameters obtained in force spectroscopy studies suffer from inaccurately derived spring constants. Therefore, an approved cantilever calibration protocol, as described in this report, will allow a better quantitative comparison of biophysical AFM results from different laboratories.

Acknowledgments

This study was supported by NanoNed, the Dutch nanotechnology program of the Ministry of Economic Affairs and in part financed by a BIO-LIGHT-TOUCH Grant (FP6-2004-NEST-C-1-028781) and Immunanomap Grant (MRTN-CT-2006-035946) of the European Union to C.G.F. I.Y.P and G.J.V. thank the Dutch Polymer Institute for financial support (DPI-695). A.C. and P.J. were supported by VENI Grants (916.66.028 and 700.57.401) of the Netherlands Organization for Scientific Research (NWO).

Appendix A

A.1. Protocol for AFM spring constant calibration

Preparation for experiments (all methods)

- Check *z*-calibration of your AFM, for instance using a calibration grid.
- Write down the temperature (°C) at the position of a mounted cantilever in a working AFM.
- Find the tilt angle off horizontal of the cantilever in its tip holder (e.g., see Table S1).
- Mount the cantilever into its holder, and align the laser-spot as close as possible to the end of the cantilever by a camera or microscope.
- Align the reflected laser beam onto the center of the photodetector and maximize the total intensity.

1. Thermal noise method

- Take force curves ($N=5$) of the cantilever in air on an ethanol cleaned silicon slide (or glass). Keep the deflection in the non-contact (flat) region at 0 V and the deflection in the contact region at a maximum of 1–2 V (<200 nm). Set the deflection set-point at 0 V.[3]
- Calculate the mean of the contact InvOLS (nm/V; sensitivity deflection) from the linear slope of the tip-sample contact region (in the approach curve). Enter this value in the software, if possible; and/or write it down.
- Raise the cantilever well above the substrate (>300 μm), without changing the laser position and re-center deflection to 0 V.[4]
- When possible, before acquiring the thermal noise data enter the measured InvOLS and temperature into the software. Also enter some correction parameters in your software to comply to Eq. (2); where $C=0.817$ for rectangular cantilevers, or $C=0.764$ for V-shaped cantilevers. (Note: The value you have to put into the software varies according the AFM system used, for NSs set the 'deflection sensitivity correction' to 1.106 or 1.144, other AFMs: check manual).
- Acquire the thermal noise power spectrum of the cantilever ($N=5$) and, if possible, save the spectrum for later analysis.

Calculating the spring constant:

- Fit the fundamental resonance peak in the spectrum with the SHO model.[5,6] Write down the fitting parameters y_0, A_0, f_R and Q of the SHO fit (Eq. (3)).
- Find the spring constant using the software, or manually calculate it with Eq. (5).

Calibration in liquid:

Alternative to calibrating in air, the thermal noise method can be applied in liquid. This implies that the InvOLS as well as the thermal noise should be acquired in this medium. Note that the InvOLS in liquid is related to that in air by the refractive index of that liquid, for further reading see [56]. Furthermore, due to higher damping, the signal-to-noise ratio is lower in the PSD. For highly damped systems, $Q\leq 10$, an adapted SHO fit should be used. For further reading on calibrating in liquid see [38].

2. Sader method
Before the calibration:

- Measure the plan-view dimensions of the cantilever by SEM or optical microscopy, and determine its length (L) and its width (b).

Calibration:

- Keep the cantilever well above the substrate (>300 μm), and set the deflection to 0 V.[3]
- Acquire the thermal noise power spectrum of the cantilever ($N=5$) and save the spectrum for later analysis.
- Fit the fundamental resonance peak with the SHO model. Write down the fitting parameters f_R and Q of the SHO fit (Eq. (3)).

[3] By calibrating at a ±0 V deflection and a 0 V setpoint in the deflection versus piezo distance curves, the photodetector and piezo scanner both stay in their linear regime.

[4] The laser has shifted due to the change in electrostatic interaction of the cantilever with the substrate.

[5] In the thermal spectra also higher order peaks can be observed. Note that these can be 'false' peaks due to aliasing, which can be avoided by an anti-aliasing filter (see [32], for more information).

[6] A SHO fit is better than a Lorentz fit, which is sometimes implemented in the software of commercial AFM systems.

Alternative 1 (rectangular cantilever):

- Use the parameters f_R and Q to calculate the spring constant of a rectangular cantilever using Eqs. (6a) and (6b). Use the length L and width b of the cantilever as determined earlier. (For cantilever B from a MLCT/MSCT chip, take the values from Table 2). Take the temperature dependent values for ρ, η from Table S3 or use the calculator on: http://www.mhtl.uwaterloo.ca/old/onlinetools/airprop/airprop.html.
- Calculate the spring constant using Eq. (5), implemented in a self-written software application (e.g., in MATLAB) or use the web tool of the Sader group on: http://www.ampc.ms.unimelb.edu.au/afm/calibration.html.
- Correct the measured intrinsic spring constant for cantilever tilt with Eq. (8).

Alternative 2 (V-shaped cantilever C or D from a MLCT/MSCT-cantilever chip):

- Use the parameters f_R and Q to calculate the spring constant of V-shaped cantilevers C and D using Eq. (7a) and (7b), respectively. Thereby, calculate Re with Eq. (6b). Take the values for ρ, η, $b_{C/D}$, and $L_{C/D}$ from Table 2 and S3.
- Correct the found intrinsic spring constant for cantilever tilt with Eq. (8).

Alternative 3 (other V-shaped or differently shaped cantilevers):

- Derive alternative formulas for Eqs. (7a) and (7b), using the method described by Sader et al. in [30].
- After deriving the formulas, continue with **Alternative 2**.

Calibration in liquid:

The Sader method can be applied in liquid too (see also thermal noise method in liquid); the viscosity and density of water can be calculated on: http://www.mhtl.uwaterloo.ca/old/onlinetools/airprop/airprop.html.

Appendix B. Supplementary materials

Supplementary data associated with this article can be found in the online version at doi:10.1016/j.ultramic.2011.09.012.

References

[1] G. Binnig, C.F. Quate, C. Gerber, Atomic force microscope, Physical Review Letters 56 (1986) 930–933.
[2] P. Hinterdorfer, Y.F. Dufrene, Detection and localization of single molecular recognition events using atomic force microscopy, Nature Methods 3 (2006) 347–355.
[3] F. Oesterhelt, D. Oesterhelt, M. Pfeiffer, A. Engel, H.E. Gaub, D.J. Muller, Unfolding pathways of individual bacteriorhodopsins, Science 288 (2000) 143–146.
[4] E.L. Florin, V.T. Moy, H.E. Gaub, Adhesion forces between individual ligand–receptor pairs, Science 264 (1994) 415–417.
[5] V.T. Moy, E.L. Florin, H.E. Gaub, Intermolecular forces and energies between ligands and receptors, Science 266 (1994) 257–259.
[6] M. Rief, H. Clausen-Schaumann, H.E. Gaub, Sequence-dependent mechanics of single DNA molecules, Nature Structural and Molecular Biology 6 (1999) 346–349.
[7] K.O. Greulich, Single-molecule studies on DNA and RNA, ChemPhysChem 6 (2005) 2458–2471.
[8] P. Frederix, P.D. Bosshart, A. Engel, Atomic force microscopy of biological membranes, Biophysical Journal 96 (2009) 329–338.
[9] M. Rief, M. Gautel, F. Oesterhelt, J.M. Fernandez, H.E. Gaub, Reversible unfolding of individual titin immunoglobulin domains by AFM, Science 276 (1997) 1109–1112.
[10] M.I. Giannotti, G.J. Vancso, Interrogation of single synthetic polymer chains and polysaccharides by AFM-based force spectroscopy, ChemPhysChem 8 (2007) 2290–2307.
[11] M. Grandbois, M. Beyer, M. Rief, H. Clausen-Schaumann, H.E. Gaub, How strong is a covalent bond? Science 283 (1999) 1727–1730.
[12] S. Zou, H. Schönherr, G.J. Vancso, Force spectroscopy of quadruple H-bonded dimers by AFM: dynamic bond rupture and molecular time-temperature superposition, Journal of the American Chemical Society 127 (2005) 11230–11231.
[13] M. Benoit, D. Gabriel, G. Gerisch, H.E. Gaub, Discrete interactions in cell adhesion measured by single-molecule force spectroscopy, Nature Cell Biology 2 (2000) 313–317.
[14] J. Helenius, C.P. Heisenberg, H.E. Gaub, D.J. Muller, Single-cell force spectroscopy, Journal of Cell Science 121 (2008) 1785–1791.
[15] S.K. Kufer, E.M. Puchner, H. Gumpp, T. Liedl, H.E. Gaub, Single-molecule cut-and-paste surface assembly, Science 319 (2008) 594–596.
[16] H.G. Hansma, K.J. Kim, D.E. Laney, R.A. Garcia, M. Argaman, M.J. Allen, S.M. Parsons, Properties of biomolecules measured from atomic force microscope images: a review, Journal of Structral Biology 119 (1997) 99–108.
[17] R. Garcia, R. Perez, Dynamic atomic force microscopy methods, Surface Science Reports 47 (2002) 197–301.
[18] C.A. Clifford, M.P. Seah, The determination of atomic force microscope cantilever spring constants via dimensional methods for nanomechanical analysis, Nanotechnology 16 (2005) 1666–1680.
[19] J.M. Neumeister, W.A. Ducker, Lateral, normal, and longitudinal spring constants of atomic-force microscopy cantilevers, Review of Scientific Instruments 65 (1994) 2527–2531.
[20] J.E. Sader, L. White, Theoretical-analysis of the static deflection of plates for atomic-force microscope applications, Journal of Applied Physics 74 (1993) 1–9.
[21] Y.Q. Li, N.J. Tao, J. Pan, A.A. Garcia, S.M. Lindsay, Direct measurement of interaction forces between colloidal particles using the scanning force microscope, Langmuir 9 (1993) 637–641.
[22] Y.I. Rabinovich, R.H. Yoon, Use of atomic-force microscope for the measurements of hydrophobic forces between silanated silica plate and glass sphere, Langmuir 10 (1994) 1903–1909.
[23] A. Torii, M. Sasaki, K. Hane, S. Okuma, A method for determining the spring constant of cantilevers for atomic force microscopy, Measurement Science and Technology 7 (1996) 179–184.
[24] S.K. Jericho, M.H. Jericho, Device for the determination of spring constants of atomic force microscope cantilevers and micromachined springs, Review of Scientific Instruments 73 (2002) 2483–2485.
[25] K.H. Chung, S. Scholz, G.A. Shaw, J.A. Kramar, J.R. Pratt, SI traceable calibration of an instrumented indentation sensor spring constant using electrostatic force, Review of Scientific Instruments 79 (2008) 095105.
[26] E.D. Langlois, G.A. Shaw, J.A. Kramar, J.R. Pratt, D.C. Hurley, Spring constant calibration of atomic force microscopy cantilevers with a piezosensor transfer standard, Review of Scientific Instruments 78 (2007) 10.
[27] J.P. Cleveland, S. Manne, D. Bocek, P.K. Hansma, A nondestructive method for determining the spring constant of cantilevers for scanning force microscopy, Review of Scientific Instruments 64 (1993) 403–405.
[28] J.L. Hutter, J. Bechhoefer, Calibration of atomic-force microscope tips, Review of Scientific Instruments 64 (1993) 1868–1873.
[29] J.E. Sader, J.W.M. Chon, P. Mulvaney, Calibration of rectangular atomic force microscope cantilevers, Review of Scientific Instruments 70 (1999) 3967–3969.
[30] J.E. Sader, J. Pacifico, C.P. Green, P. Mulvaney, General scaling law for stiffness measurement of small bodies with applications to the atomic force microscope, Journal of Applied Physics 97 (2005) 1249031–1249037.
[31] B. Ohler, Cantilever spring constant calibration using laser Doppler vibrometry, Review of Scientific Instruments 78 (2007) 0637011–0637015.
[32] S. Cook, T.E. Schaffer, K.M. Chynoweth, M. Wigton, R.W. Simmonds, K.M. Lang, Practical implementation of dynamic methods for measuring atomic force microscope cantilever spring constants, Nanotechnology 17 (2006) 2135–2145.
[33] B. Ohler, Practical advice on the determination of cantilever spring constants, Veeco Instrum. Inc. Internal Publ., 2007, pp. 1–12.
[34] N.A. Burnham, X. Chen, C.S. Hodges, G.A. Matei, E.J. Thoreson, C.J. Roberts, M.C. Davies, S.J.B. Tendler, Comparison of calibration methods for atomic-force microscopy cantilevers, Nanotechnology 14 (2003) 1–6.
[35] C.T. Gibson, D.A. Smith, C.J. Roberts, Calibration of silicon atomic force microscope cantilevers, Nanotechnology 16 (2005) 234–238.
[36] H.J. Butt, M. Jaschke, Calculation of thermal noise in atomic-force microscopy, Nanotechnology 6 (1995) 1–7.
[37] R.W. Stark, T. Drobek, W.M. Heckl, Thermomechanical noise of a free V-shaped cantilever for atomic-force microscopy, Ultramicroscopy 86 (2001) 207–215.
[38] T. Pirzer, T. Hugel, Atomic force microscopy spring constant determination in viscous liquids, Review of Scientific Instruments 80 (2009) 035110.
[39] C.T. Gibson, D.J. Johnson, C. Anderson, C. Abell, T. Rayment, Method to determine the spring constant of atomic force microscope cantilevers, Review of Scientific Instruments 75 (2004) 565–567.
[40] R. Proksch, T.E. Schaffer, J.P. Cleveland, R.C. Callahan, M.B. Viani, Finite optical spot size and position corrections in thermal spring constant calibration, Nanotechnology 15 (2004) 1344–1350.
[41] T.E. Schaffer, Calculation of thermal noise in an atomic force microscope with a finite optical spot size, Nanotechnology 16 (2005) 664–670.

[42] D.A. Walters, J.P. Cleveland, N.H. Thomson, P.K. Hansma, M.A. Wendman, G. Gurley, V. Elings, Short cantilevers for atomic force microscopy, Review of Scientific Instruments 67 (1996) 3583–3590.
[43] J.W.M. Chon, P. Mulvaney, J.E. Sader, Experimental validation of theoretical models for the frequency response of atomic force microscope cantilever beams immersed in fluids, Journal of Applied Physics 87 (2000) 3978–3988.
[44] J.E. Sader, Frequency response of cantilever beams immersed in viscous fluids with applications to the atomic force microscope, Journal of Applied Physics 84 (1998) 64–76.
[45] J.L. Hutter, Comment on tilt of atomic force microscope cantilevers: effect on spring constant and adhesion measurements, Langmuir 21 (2005) 2630–2632.
[46] W.C. Young, R.G. Budynas, R.J. Roark, Roark's Formulas for Stress and Strain , 2001.
[47] J.E. Sader, Parallel beam approximation for V-shaped atomic-force microscope cantilevers, Review of Scientific Instruments 66 (1995) 4583–4587.
[48] J.E. Sader, I. Larson, P. Mulvaney, L.R. White, Method for the calibration of atomic-force microscope cantilevers, Review of Scientific Instruments 66 (1995) 3789–3798.
[49] J.L. Hazel, V.V. Tsukruk, Spring constants of composite ceramic/gold cantilevers for scanning probe microscopy, Thin Solid Films 339 (1999) 249–257.
[50] G.I. Bell, Models for the specific adhesion of cells to cells, Science 200 (1978) 618–627.
[51] E. Evans, K. Ritchie, Dynamic strength of molecular adhesion bonds, Biophysical Journal 72 (1997) 1541–1555.
[52] D.F. Tees, R.E. Waugh, D.A. Hammer, A microcantilever device to assess the effect of force on the lifetime of selectin-carbohydrate bonds, Biophysical Journal 80 (2001) 668–682.
[53] P. Panorchan, M.S. Thompson, K.J. Davis, Y. Tseng, K. Konstantopoulos, D. Wirtz, Single-molecule analysis of cadherin-mediated cell–cell adhesion, Journal of Cell Science 119 (2006) 66–74.
[54] J. te Riet, A.W. Zimmerman, A. Cambi, B. Joosten, S. Speller, R. Torensma, F.N. van Leeuwen, C.G. Figdor, F. de Lange, Distinct kinetic and mechanical properties govern ALCAM-mediated interactions as shown by single molecule force spectroscopy, Journal of Cell Science 120 (2007) 3965–3976.
[55] M.J. Higgins, R. Proksch, J.E. Sader, M. Polcik, S. Mc Endoo, J.P. Cleveland, S.P. Jarvis, Noninvasive determination of optical lever sensitivity in atomic force microscopy, Review of Scientific Instruments 77 (2006) 013701–013705.
[56] E. Tocha, J. Song, H. Schonherr, G.J. Vancso, Calibration of friction force signals in atomic force microscopy in liquid media, Langmuir 23 (2007) 7078–7082.

P8 PEPTIDE-ANTIBODY COMPLEX AS HANDLE FOR SINGLE-MOLECULE CUT & PASTE

Strackharn M, Stahl SW, Severin PM, Nicolaus T and Gaub HE.

ChemPhysChem. 2012 Mar;13(4):914-7. doi: 10.1002/cphc.201100765.

CHEMPHYSCHEM

DOI: 10.1002/cphc.201100765

Peptide–Antibody Complex as Handle for Single-Molecule Cut & Paste

Mathias Strackharn,[a] Stefan W. Stahl,[b] Philip M. D. Severin,[a] Thomas Nicolaus,[a] and Hermann E. Gaub*[a]

Feynman is frequently quoted for having foreseen that individual atoms may be arranged one-by-one to form functional assemblies.[1] The seminal work by Don Eigler and colleagues[2,3] convincingly proved the validity of these concepts: functional assemblies of atoms forming quantum corrals showed emergent novel properties. In the life sciences, Hans Kuhn realized rather early that for many multistep biological reactions, not only the sequence but also the arrangement of the individual enzymes plays a crucial role. He envisaged that in order to investigate their interaction, novel approaches would be needed: he wished to have "…molecular pliers to pick and place individual enzymes to create functional assemblies with designed properties."[4] The application of bottom-up strategies to assemble biomolecular complexes, however, turned out to be rather challenging. A quite vivid dispute was fought in a series of papers between Smalley and Drexler on where these difficulties arise from and whether fundamental limitations prevent a molecule for molecule assembly of biomolecules in electrolyte ambient and at physiologic temperatures.[5] With the development of single-molecule cut-and-paste (SMC&P) we overcame these difficulties and provided a platform technology for the assembly of biomolecules at surfaces.[6] It combines the Å-positioning precision of atomic force microscopy (AFM)[7,8] with the selectivity of DNA hybridization to pick individual molecules from a depot chip and to arrange them on a target site by pasting the molecules one-by-one.[9] The advanced methods of single-molecule fluorescence detection[10–14] allowed us to localize the pasted molecules with nanometer accuracy and to show that the deposition accuracy is presently only limited by the length of the spacers used to couple the DNA handles and anchors to tip and construction site, respectively.[15]

In the various SMC&P implementations realized to date, the system of hierarchical binding forces was built from DNA duplexes of suitable geometry and sequence. Since one of the major goals, which spurs the development of the SMC&P technology, is the ability to arrange proteins, for example, in enzymatic networks of predefined composition and proximity, molecular anchors and handles should ultimately be of such a kind that they can be co-expressed with the proteins, for example, as tags on a protein chip. As a first step in this direction, we chose in this Communication a peptide–antibody complex to replace the DNA-based handle complex in the conventional SMC&P design. This single-chain antibody, which is part of a larger family, was selected by the Plückthun group to recognize a 12 aa long segment of a polypeptide chain with picomolar affinity.[16] In previous studies we had investigated by single-molecule force spectroscopy and molecular dynamics (MD) simulations several different peptides and antibodies and investigated the influence of the attachment site on the unbinding mechanisms.[17,18] We could confirm that the antibody (when covalently attached at the C-terminal end) stays intact when the peptide is pulled out of the binding pocket. Herein, we used this antibody immobilized at the AFM cantilever tip to pick up a fluorescently labeled transfer DNA–peptide chimera via its peptide tag and paste it on the target site of the chip.

Using a microspotter, we deposited microdroplets of a DNA solution onto a pretreated glass surface resulting in approximately 50 μm-sized spots with a distance of 70 μm (see Supporting Information, Figure 1). The ssDNA was allowed to covalently bind to the surface via PEG spacers. One drop contained ssDNA with a reactive 5′ end. The resulting spot later on forms the depot. The other drop contained DNA with a reactive 3′ end and the resulting spot forms the target. The depot area was then loaded with a complementary ssDNA strand, which was extended at the 3′ end by a 13-amino-acid-long handle peptide and labeled at the 5′ end with an atto647N fluorophore. For simplicity, this construct is called transfer strand. Single-chain antibodies were covalently attached via PEG spacers to the AFM cantilever tip (see Figure 1a for a cartoon of the SMC&P process).

To pick up an individual DNA strand, the AFM tip was lowered at the depot area, allowing the antibody at the tip to bind to the peptide at the end of the DNA strand to be transferred. Upon retract, typically the force gradually increased and finally dropped as shown in Figure 1b, where the force is plotted as a function of the distance. We chose the functionalization density of the tip and the surface such that typically only in every second attempt we found this characteristic force curve, indicating that exactly one DNA strand was picked up. In the majority of the other 50% of the attempts we found no measurable force upon retract, indicating that no molecule was picked up. In these cases, we repeated the pick-up cycle. Only in very rare cases (<2%) did we find higher values for the unbinding force, indicating that more than one molecule was picked up.

[a] M. Strackharn, P. M. D. Severin, T. Nicolaus, Prof. Dr. H. E. Gaub
Center for Nanoscience and Department of Physics
University of Munich, Amalienstrasse 54
80799 München (Germany)
Fax: (+49) 89-2180-2050
E-mail: gaub@lmu.de

[b] S. W. Stahl
Center for Integrated Protein Schience (CIPSM)
Center for Nanoscience and Department of Physics
University of Munich, Amalienstrasse 54
80799 München (Germany)

Supporting information for this article is available on the WWW under http://dx.doi.org/10.1002/cphc.201100765.

WILEY ONLINE LIBRARY © 2012 Wiley-VCH Verlag GmbH & Co. KGaA, Weinheim

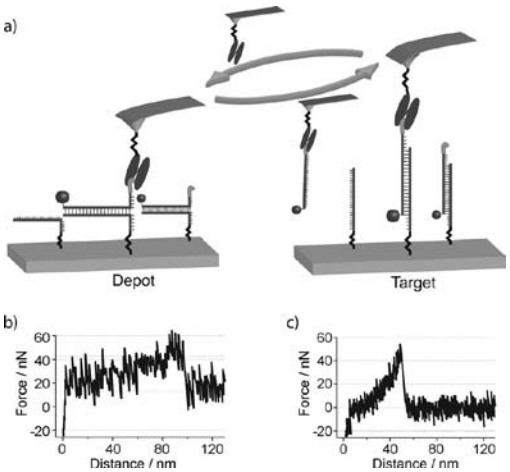

Figure 1. a) Schematic representation of a typical SMC&P cycle. A single-chain antibody fragment is covalently bound to the cantilever tip. When lowered to the depot area surface, the antibody binds to a peptide at the end of a DNA strand, which is attached to the surface via 40 bp in zipper mode. When the tip is pulled back, the basepairs open up one by one. The transfer construct remains attached to the cantilever and may be transferred to the target area. Here, the cantilever is lowered again such that the DNA part of the construct binds to the DNA target anchor. When the cantilever is retracted, this time the DNA bases are loaded in shear geometry and the antibody–peptide bond yields. The transfer construct remains in the target area and the cantilever can be used for the next transfer cycle again. b,c) Force-distance graphs of typical rupture events in the depot (b) and target (c) areas.

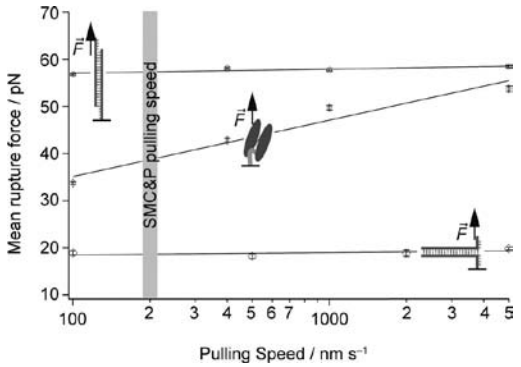

Figure 2. Dependency of the mean rupture force on the pulling speed. The mean rupture force for opening the 40 bp DNA in shear geometry is nearly 60 pN. The mean rupture force of the peptide–antibody complex is significantly lower than that of the DNA in shear geometry and shows a logarithmic dependence on the loading rate. The 40 bp DNA in unzip geometry opens at a mean rupture force of around 20 pN. Error bars depict fitting errors from fitting the force distributions. Highlighted is the pulling speed chosen for the deposition process.

The AFM tip was now moved to a chosen position in the target area and gradually lowered, allowing the transfer strand to hybridize to the target DNA. Upon retract again, the force-versus-distance curve was recorded. A typical example is given in Figure 1c. As can be seen, the force peaks at a much higher value, typically at 40 pN. Since this value is much lower than the force required to break the DNA shear bond, we conclude with a high certainty that the transfer DNA was deposited in the target area. Details of the probabilities for the rupture of bonds in series are given elsewhere.[19]

To corroborate that the force required to unzip the anchor duplex is lower than the binding force of the peptide–antibody complex and that the latter is lower than the force required to unbind the DNA duplex in shear geometry we investigated the bond strength of the three complexes in a separate series of experiments. Since unbinding forces depend in a first-order approximation given by the Bell–Evans model on the logarithm of the force loading rate,[20] we varied the latter by one and a half orders of magnitude. The result is depicted in Figure 2. For the lowest curve, the unbinding force of the depot–transfer duplex was measured under conditions where both were covalently attached to tip and sample surface via PEG spacers. Note that the depot strand was attached at its 5′ end and the transfer strand was attached at the 3′ end, mimicking the geometry during pickup. For the red curve, the peptide was attached to the sample surface, allowing the antibody, which was covalently attached to the tip, to bind the peptide in exactly the same geometry as during pick up. As can be seen, both lines differ drastically in their slopes, but more important for the issues discussed here, the force required to unzip the two DNA strands is significantly lower than that required to break the peptide–antibody bond for the entire range of pulling speeds. Since the curve of the antibody–peptide complex lies significantly below the curve recorded for the DNA duplex in shear geometry (note that the target strand was now attached with the 3′ end to the surface), it is predominantly the peptide–antibody complex that ruptures in the deposition process. From this graph we chose the optimum pulling speed window around 200 nm sec^{-1} for the SMC&P experiments described below.

In parallel to the SMC&P experiments, we followed the deposition process of the individual molecules microscopically in total internal fluorescence excitation. Details of the device are given elsewhere,[21] but it is important to note that the custom-built combined AFM–TIRF microscope was optimized for vibrational stability, which is essential to avoid the coupling of mechanical noise into the AFM via the immersion fluid required for high NA optical microscopy. Figure 3a shows a micrograph taken at the beginning of the deposition process in the target region. In Figure 3b the left image shows the scattered light from the tip and the emission of the fluorophore. The second image depicts the same spot after the tip has left the evanescent zone, leaving only the deposited fluorophore visible (a movie of this process is provided in the Supporting Information). With standard techniques, the position of this fluorophore was then determined with an accuracy of 1.4 nm.

After the deposition of the transfer strand in the target area, the tip is again in its original state and therefore ready to pick up another transfer strand from the storage area. Since the antibody–peptide bond is reversible, this pick-up and deposit

 © 2012 Wiley-VCH Verlag GmbH & Co. KGaA, Weinheim

CHEMPHYSCHEM

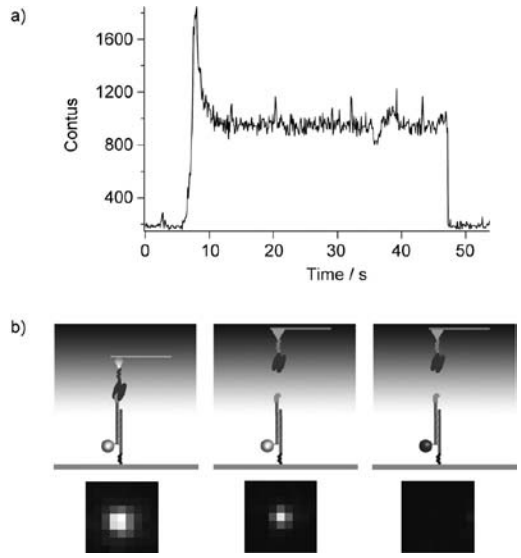

Figure 3. Deposition of a single DNA–peptide construct. The loaded cantilever is lowered towards the target area, where the DNA–peptide construct is deposited, when the lever is withdrawn. a) Fluorescence timetrace and b) cartoon of the process. When the cantilever enters the evanescent field of the TIR illumination, fluorescence from the dye-labeled construct and scattered light from the cantilever tip contribute to the signal, whereas after retraction of the cantilever, only fluorescence of the dye molecule is measured. No signal is measured after photobleaching of the dye.

or—in other words—molecular cut-and-paste process may be carried out for many cycles, allowing one molecule after the other to be transferred, unless damage to the antibody occurs during the forced unbinding of the antibody–peptide complex. To demonstrate that the antibody–peptide complex is robust and very well suited as handle complex at the AFM tip, we assembled the molecular pattern depicted in Figure 4 from approximately 600 transfer strands in a molecule-by-molecule copy-and-paste process. This convincingly demonstrates that the hierarchical force system, which is a prerequisite for SMC&P, may well be realized based on peptides or protein modules for anchor and/or handle groups. One may as well envisage covalent or organometallic coupling schemes[22,23] or even external modulation of the interaction forces by externally controlled Coulomb interactions[24] to expand the toolbox for single-molecule assembly.

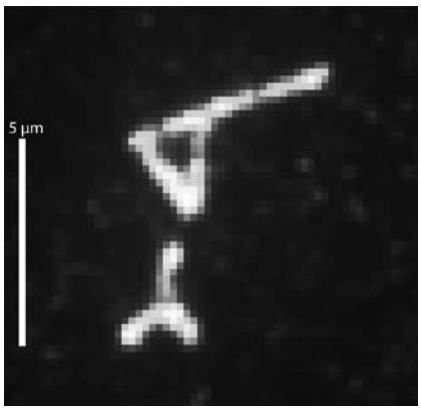

Figure 4. The robustness of the SMC&P process is demonstrated by the molecule-by-molecule assembly of a microscopic pattern showing a cantilever and an antibody. The pattern is assembled from approximately 600 molecules.

Experimental Section

All measurements described in the manuscript were carried out with a custom-designed combined AFM/TIRF microscope described in detail elsewhere.[21] We provide a detailed description of AFM measurements, TIRF microscopy, single-chain antibody fragment preparation, peptide synthesis, surface preparation, microstructuring with a microplotter, and oligomer sequences in the Supporting Information.

Acknowledgements

This work was supported by the Volkswagen foundation, the Nano Initative Munich and the German Science Foundation (SFB 863).

Keywords: biophysics · nanostructures · scanning probe microscopy · single-molecule studies · TIRF microscopy

[1] R. P. Feynman, *Eng Sci* **1960**, *23*, 22 – 36.
[2] M. F. Crommie, C. P. Lutz, D. M. Eigler, *Science* **1993**, *262*, 218 – 20.
[3] T. A. Jung, R. R. Schlittler, J. K. Gimzewski, H. Tang, C. Joachim, *Science* **1996**, *271*, 181 – 184.
[4] H. Kuhn, *Verhandlungen der Schweizerischen Naturforschenden Gesellschaft* **1965**, 245 – 266.
[5] R. Baum, *Chem. Eng. News* **2003**, *81*, 37 – 42.
[6] S. K. Kufer, E. M. Puchner, H. Gumpp, T. Liedl, H. E. Gaub, *Science* **2008**, *319*, 594 – 6.
[7] G. Binnig, C. F. Quate, C. Gerber, *Phys. Rev. Lett.* **1986**, *56*, 930 – 933.
[8] B. Drake, C. B. Prater, A. L. Weisenhorn, S. A. C. Gould, T. R. Albrecht, C. F. Quate, D. S. Cannell, H. G. Hansma, P. K. Hansma, *Science* **1989**, *243*, 1586 – 1589.
[9] E. M. Puchner, S. K. Kufer, M. Strackharn, S. W. Stahl, H. E. Gaub, *Nano Lett.* **2008**, *8*, 3692 – 5.
[10] W. E. Moerner, L. Kador, *Phys. Rev. Lett.* **1989**, *62*, 2535 – 2538.
[11] T. Schmidt, G. J. Schutz, W. Baumgartner, H. J. Gruber, H. Schindler, *Proc. Natl. Acad. Sci. USA* **1996**, *93*, 2926 – 9.
[12] R. D. Vale, T. Funatsu, D. W. Pierce, L. Romberg, Y. Harada, T. Yanagida, *Nature* **1996**, *380*, 451 – 3.
[13] A. Zurner, J. Kirstein, M. Doblinger, C. Bräuchle, T. Bein, *Nature* **2007**, *450*, 705 – 8.
[14] G. Seisenberger, M. U. Ried, T. Endress, H. Buning, M. Hallek, C. Bräuchle, *Science* **2001**, *294*, 1929 – 32.
[15] S. K. Kufer, M. Strackharn, S. W. Stahl, H. Gumpp, E. M. Puchner, H. E. Gaub, *Nat Nanotechnol* **2009**, *4*, 45 – 9.
[16] C. Zahnd, S. Spinelli, B. Luginbuhl, P. Amstutz, C. Cambillau, A. Pluckthun, *J Biol Chem.* **2004**, *279*, 18870 – 7.
[17] J. Morfill, J. Neumann, K. Blank, U. Steinbach, E. M. Puchner, K. E. Gottschalk, H. E. Gaub, *J. Mol. Biol.* **2008**, *381*, 1253 – 66.
[18] J. Morfill, K. Blank, C. Zahnd, B. Luginbuhl, F. Kuhner, K. E. Gottschalk, A. Pluckthun, H. E. Gaub, *Biophys. J.* **2007**, *93*, 3583 – 90.
[19] G. Neuert, C. H. Albrecht, H. E. Gaub, *Biophys. J.* **2007**, *93*, 1215 – 23.

 © 2012 Wiley-VCH Verlag GmbH & Co. KGaA, Weinheim

[20] F. Kühner, H. E. Gaub, *Polymer* **2006**, *47*, 2555 – 2563.
[21] H. Gumpp, S. W. Stahl, M. Strackharn, E. M. Puchner, H. E. Gaub, *Rev. Sci. Instrum.* **2009**, *80*, 063704.
[22] B. M. Gaub, C. Kaul, J. L. Zimmermann, T. Carell, H. E. Gaub, *Nanotechnology* **2009**, *20*, 434002.
[23] P. Knochel, S. Z. Zimdars, S. X. M. du Jourdin, F. Crestey, T. Carell, *Org. Lett.* **2011**, *13*, 792 – 795.
[24] M. Erdmann, R. David, A. R. Fornof, H. E. Gaub, *Nat. Chem.* **2010**, *2*, 745 – 9.

Received: September 29, 2011
Published online on December 19, 2011

 © 2012 Wiley-VCH Verlag GmbH & Co. KGaA, Weinheim

CHEMPHYSCHEM

Supporting Information

© Copyright Wiley-VCH Verlag GmbH & Co. KGaA, 69451 Weinheim, 2012

Peptide–Antibody Complex as Handle for Single-Molecule Cut & Paste

Mathias Strackharn,[a] Stefan W. Stahl,[b] Philip M. D. Severin,[a] Thomas Nicolaus,[a] and Hermann E. Gaub*[a]

cphc_201100765_sm_miscellaneous_information.pdf
cphc_201100765_sm_2.avi

Supplementary Information

Peptide:Antibody Complex as Handle for Single-Molecule Cut & Paste

Mathias Strackharn[1,*], Stefan W. Stahl[1,2], Philip M. D. Severin[1] Thomas Nicolaus[1], and Hermann E. Gaub[1]

[1] Center for Nanoscience and Department of Physics, University of Munich, Amalienstraße 54, 80799 Munich, Germany

[2] Center for Integrated Protein Science (CIPSM), Munich, Germany

[*] mathias.strackharn@physik.uni-muenchen.de

All measurements described in the manuscript were carried out with a custom designed combined AFM/TIRF microscope described in detail in [21]. Here twe provide the description of those parts and procedures, which are relevant to the experiments described in the main text:

AFM measurements

The spring constants of the DNA modified cantilevers were calibrated in solution using the equipartition theorem [25],[26]. For the single-molecule force spectroscopy BL-AC40TS-C2 levers (Olympus, Tokyo, Japan) and for SMC&P experiments MLCT-AUHW levers (Bruker, Camarillo, USA) were used. The protocol for the functional assembly as well as the data recording was programmed using Igor Pro (Wave Metrics, Lake Oswego, USA) and an Asylum Research MFP3D controller (Asylum Research, Santa Barbara, USA), which provides ACD and DAC channels as well as a DSP board for setting up feedback loops. Cantilever positioning for pick-up and delivery was controlled in closed-loop operation. The typical cycle time for one functional assembly process lies between 2 and 3 seconds depending on the sample orientation and the

traveling distance between depot and target area. The positioning feedback accuracy is ±3 nm however long term deviations may arise due to thermal drift. Extension velocities are set to 2 μm/s in the depot area and 200 nm/s in the target area. Force spectroscopy data was converted into force-extension curves and the most probable rupture force was obtained using a the program IGOR Pro 6.22 (Wave Metrics, Lake Oswego, USA) and a set of custom-made procedures. Rupture forces for each retraction speed were plottet in histograms and fitted with Gaussians to determine the most probable rupture forces.

TIRF microscopy

The fluorescence microscopy measurements were carried out with objective-type TIRF excitation on a microscope that was especially designed for a stable combination of AFM with TIRFM [21]. We excited with a fiber-coupled 637 nm diode laser (iBeam smart, TOPTICA, München, Germany) through a 100x/1.49 oil immersion objective lens (Nikon CFI Apochromat TIRF, Japan). As excitation filter, beam splitter, and emission filter a BrightLine HC 615/45, a Raman RazorEdge 633 RS, and a Chroma ET 685/70 (AHF, Tübingen, Germany) were used respectively. Images were taken with a back-illuminated EMCCD camera (DU-860D, Andor, Belfast, Ireland). Fluorescence image sequences were taken at 10 Hz frame rate, gain 150, 1 MHz readout rate in frame transfer mode. The camera was operated at -75 °C.

Preparation of the C11L34 single chain antibody fragment

The C11L34 single chain antibody fragment was prepared as described in [18]. The scFv construct harbored a C-terminal His tag followed by a Cys to allow for site-specific immobilization and was obtained by periplasmic expression in *E. coli* SB536. C11L34 was purified by Ni^{2+} and immobilized antigen affinity chromatography according to standard protocols. The concentration was adjusted to 2.5 mg/ml in storage buffer containing 50 mM sodium phosphate, pH 7.2, 50 mM NaCl and 10 mM EDTA.

Preparation of GCN4 peptides

GCN4 peptides with the sequence CYHLENEVARLKK were synthesized manually in syringe reaction chambers. 0.05 g Wang resin (Iris, Marktredwitz, Germany) were incubated with 10 eq (of the maximal loading capacity of the resin) Fmoc-L-Lys(Boc)-OH (Iris, Marktredwitz, Germany) for 4 h. The incubation was repeated for another 4 h. For the measurement of the resin loading 500 μl of DMF (Sigma, Taufkirchen, Germany) wih 20 % Piperidine (Fluka, St. Gallen, Switzerland) were added to 3 mg of the resin. The solution was shaken for 1 h, the 3 ml DMF were added. By measuring the extinction at 300 nm of a 1:10 dilution with DMF with 20% Piperidine the resin loading was determined. Remaining hydroxyl groups on the Wang resin were blocked by esterification with acetic anhydride. All other Fmoc-protected amino acids (Iris, Marktredwitz, Germany) were added by applying the following procedure: 10 eq amino acid and 100 eq HOBT (Fluka, St. Gallen, Switzerland) were dissolved in DMF, 10 eq DIC (Fluka, St. Gallen, Switzerland) was added and the solution was shaken for 1 h. Then 10 eq DIPEA (Fluka, St. Gallen, Switzerland) were added and solution was shaken for 1h again. The process was once repeated. Then then the resin was washed with 10 ml DMF, 10 ml DCM, 10 ml Ether and 6 ml DMF, again. Fmoc protection groups were removed by incubating the resin in DMF with 20 % Piperidine for 20 min twice. The resin was then flushed with 10 ml DMF, 10 ml DCM (Carl Roth, Karlsruhe, Germany), 10 ml Ether (Sigma, Taufkirchen, Germany) and 6 ml DMF. The peptide was finally separated from the resin by 3 h shaking in 50 μl p-Thiocresol (Fluka, St. Gallen, Switzerland), 50 μl Thioanisol (Fluka, St. Gallen, Switzerland) and 300 μl TFA (Sigma, Taufkirchen, Germany). The solution was transferred into a centrifuge tube, where the peptide was precipitated with 10 ml Ether at -80 °C. The solution was centrifuged at 4 °C and 4600 g and the pellet was washed in Ether six times. Finally the pellet was resolved in a 3:1 ddH_2O/tertButanol (Sigma, Taufkirchen, Germany) solution and lyophilized.

Preparation of cantilevers

Cantilevers (MLCT, Bruker, Camarillo, USA) were always oxidized in a UV-ozone Cleaner (UVOH 150 LAB, FHR Anlagenbau GmbH, Ottendorf-Okrilla, Germany). For single molecule force spectroscopy experiments and single molecule deposition they were silanized with 3-aminopropydimethylethoxysilane (ABCR, Karsruhe, Germany), baked at 80 °C, pre-incubated with sodium borate buffer (pH 8.5), PEGylated with NHS-PEG-Maleimide (MW 5000, Rapp Polymere, Tübingen, Germany), and washed with ddH2O. According to the experiment type either C11L34 antibodies at a concentration of 2.5 mg/ml or reduced thiolated transfer DNA at a concentratioin of 10 μM was bound to the pegylated cantilevers at 8 °C for 2 h. Cantilevers were then washed with PBS buffer. In case of the SMC&P experiment, where molecules were assembled to the pattern of a cantilever with antibody at the tip, the cantilever was silanized with (3-Glycidoxypropyl)trimethoxysilane (ABCR, Karlsruhe, Germany), baked at 80 °C for 30 min and incubated overnight at 8 °C with 1mg/ml aminodextrane (D1861, Invitrogen, Carlsbad, USA) in sodium borate buffer (pH 8.5). NHS-PEG-Mal was then applied to the cantilever, which was then washed in ddH_2O. Subsequently C11L34 antibodies at a concentration of 2.5 mg/ml were bound to the pegylated cantilevers at 8 °C for 2 h. The cantilever was finally washed with PBS.

Preparation of cover glass surfaces

Cover glass slips were sonicated in 50% (v/v) 2-propanol and ddH2O for 15 min and thoroughly rinsed with ddH2O. They were then oxidized in 50% (v/v) sulfuric acid and hydrogen peroxide (30%) for 45 min and were then again well rinsed with ddH2O. The oxidized cover glass slips were silanized with a mixture of 2% 3-aminopropyldimethylethoxysilane, 90% EtOH, 8% ddH2O for 1 h. Cover glasses were thoroughly rinsed with pure EtOH first and ddH2O afterwards, and were baked at 80 °C for 30 min. After 30 min soaking in 50 mM sodium borate buffer, pH 8.5 the cover glasses were treated with 50 mM NHS-PEG-maleimide (MW 5000) in the sodium borate buffer for 1 h and then rinsed with ddH2O.

In case of the SMC&P experiments depot and target oligomers were reduced, purified and dissolved again. The reduced thiolated depot and target oligomers were deposited with a microplotter (GIX, Sonoplot, Middleton, USA), nonbound DNA was washed away with ddH_2O. Transfer oligomers were deposited on top of the depot area. Nonbound transfer strands were washed away with 4xPBS buffer. (Details on the microstructuring process are given in the following section.) The sample was then covered with 50 mM sodium borate buffer, pH 8.5, 500 mM NaCl, 10 mM TCEP for 30 min for deprotonation of amines and quenching of unreacted maleimides. The sample was then rinsed with 50 mM sodium borate buffer, pH 8.5, 500 mM NaCl and incubated for 1h with 10 mM NHS-PEG-Mal dissolved in 50 mM sodium borate buffer, pH 8.5, 500 mM NaCl. It was washed with PBS, then reduced GCN4 peptides at a concentration of 100 μM in 50 mM sodium phosphate buffer, pH 7.2, 250 mM NaCl, 10 mM EDTA were added for 1 h. The sample was rinsed again with PBS.

For single molecule force spectroscopy reduced thiolated depot or target oligomers or the reduced GCN4 peptide was bound to the pegylated cover glass slips and the sample was thoroughly rinsed with water.

Structuring surfaces with a Microplotter

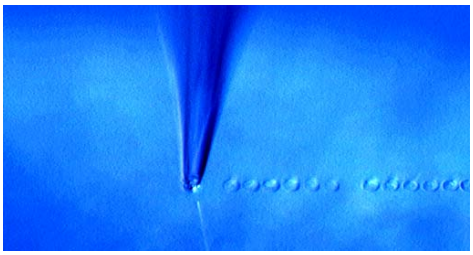

Due to the limited travel range of the AFM, the depot and target area have to be created in a distance of several micometers. For this reason these areas are produced by micro-structuring the cover glass with a microplotter (GIX, Sonoplot, Middleton, USA). A standard glass capillary (World Precision Instruments, Inc.) with an inner diameter of 30 μm was used, which results in spots of the diameter of 45 μm to 50 μm on the cover glass

(dispenser voltage 3V and 0.1 s dispensing time). The prepared DNA Oligomer solutions (see previous section) were plotted on the pegylated cover glass in two 800 μm long lines for depot and target, which were separated by a 20 μm to 30 μm broad gap.
After plotting the depot line, the cover glass was rinsed with 5 ml (4x PBS) directly in the sample holder without moving it. In a second step, the transfer strand was plotted onto the depot line. Operating experience showed that in the case of hybridizing DNA via Microplotter a contact time (capillary on the cover slide) of around 20 s per spot optimized the density of hybridized transfer strands. Afterwards the sample was rinsed as before. In a last step, the target strand was plotted in same manner as the depot.

Oligomer sequences

thiolated depot oligomer

5' SH - TTT TTT CAT GCA AGT AGC TAT TCG AAC TAT AGC TTA AGG ACG TCA A

thiolated target oligomer

5' CAT GCA AGT AGC TAT TCG AAC TAT AGC TTA AGG ACG TCA ATT TTT - SH

transfer oligomer with amine and Atto647N

5' (Atto647N) - TTG ACG TCC TTA AGC TAT AGT TCG AAT AGC TAC TTG CAT GTT TTT TTT - NH_2

thiolated transfer oligomer

5' TTG ACG TCC TTA AGC TAT AGT TCG AAT AGC TAC TTG CAT GTT TTT TTT - SH

1. H. Gumpp, S. W. Stahl, M. Strackharn, E. M. Puchner, H. E. Gaub, Ultrastable combined atomic force and total internal reflection fluorescence microscope [corrected]. *The Review of scientific instruments* **80**, 063704 (Jun, 2009).
2. E. Florin, Sensing specific molecular interactions with the atomic force microscope. *Biosensors and Bioelectronics* **10**, 895 (1995).
3. H. J. Butt, M. Jaschke, Calculation of thermal noise in atomic-force microscopy. *Nanotechnology* **6**, 1 (1995).

4. J. Morfill *et al*., Affinity-matured recombinant antibody fragments analyzed by single-molecule force spectroscopy. *Biophys J* **93**, 3583 (Nov 15, 2007).

5. A. Krebber *et al*., Reliable cloning of functional antibody variable domains from hybridomas and spleen cell repertoires employing a reengineered phage display system. *J Immunol Methods* **201**, 35 (Feb 14, 1997).

6. H. Bothmann, A. Pluckthun, Selection for a periplasmic factor improving phage display and functional periplasmic expression. *Nat Biotechnol* **16**, 376 (Apr, 1998).

7. J. Hanes, L. Jermutus, S. Weber-Bornhauser, H. R. Bosshard, A. Pluckthun, Ribosome display efficiently selects and evolves high-affinity antibodies in vitro from immune libraries. *Proc Natl Acad Sci U S A* **95**, 14130 (Nov 24, 1998).

P9 FUNCTIONAL ASSEMBLY OF APTAMER BINDING SITES BY SINGLE-MOLECULE CUT-AND-PASTE

Strackharn M, Stahl SW, Puchner EM and Gaub HE.

NANO LETTERS 2012 May 9;12(5):2425-8.

NANO LETTERS

Letter

pubs.acs.org/NanoLett

Functional Assembly of Aptamer Binding Sites by Single-Molecule Cut-and-Paste

Mathias Strackharn,[†] Stefan W. Stahl,[‡] Elias M. Puchner,[§] and Hermann E. Gaub*[,†]

[†]Center for Nanoscience and Department of Physics, University of Munich, Amalienstraße 54, 80799 Munich, Germany

[‡]Center for Integrated Protein Science (CIPSM), Munich, Germany

Supporting Information

ABSTRACT: Bottom up assembly of functional molecular ensembles with novel properties emerging from composition and arrangement of its constituents is a prime goal of nanotechnology. By single-molecule cut-and-paste we assembled binding sites for malachite green in a molecule-by-molecule assembly process from the two halves of a split aptamer. We show that only a perfectly joined binding site immobilizes the fluorophore and enhances the fluorescence quantum yield by several orders of magnitude. To corroborate the robustness of this approach we produced a micrometer-sized structure consisting of more than 500 reconstituted binding sites. To the best of our knowledge, this is the first demonstration of one by one bottom up functional biomolecular assembly.

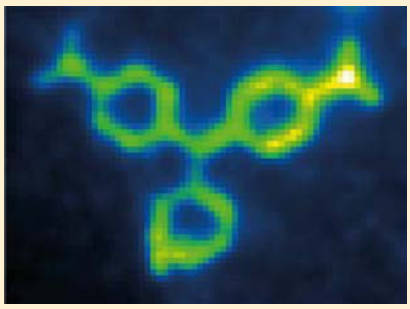

KEYWORDS: *Functional assembly, RNA aptamer, single-molecule cut-and-paste, single-molecule fluorescence, single-molecule force spectroscopy, atomic force microscope (AFM)*

Feynman is frequently quoted for having foreseen that individual atoms may be arranged one by one to form functional assemblies, moreover that covalent reactions between them may then provide a unique way to synthesize new molecules atom by atom.[1] The seminal work by Eigler and colleagues[2,3] convincingly proved the validity of these concepts: functional assemblies of atoms forming quantum corrals showed emergent novel properties. The application of these strategies to biomolecules, however, turned out to be much more challenging. A quite vivid dispute was fought in a series of papers between Smalley and Drexler on where these difficulties arise and whether fundamental limitations prevent the molecule for molecule assembly of biomolecules in electrolyte ambient at physiologic temperatures.[4] Hans Kuhn had realized early on that for many multistep biological reactions not only the sequence but also the arrangement of the individual enzymes plays a crucial role. He envisaged that in order to investigate their interaction, novel approaches would be needed; he wished to have molecular pliers to pick up and place individual enzymes to create functional assemblies with designed properties.[5]

With the development of single-molecule cut-and-paste (SMC&P), we provided a platform technology for the assembly of biomolecules at surfaces.[6] It combines the Å-positioning precision of the AFM[7,8] with the selectivity of DNA hybridization to pick up individual molecules from a depot area and arrange them at a construction site one by one.[9] We localized the pasted molecules with nanometer accuracy by single molecule fluorescence and showed that the deposition accuracy is presently limited by the length of the spacers used to couple the DNA handles and anchors to the tip and construction site, respectively.[10] We assembled structures with dimensions below the Abbé diffraction limit and imaged them by superresolution Blink-microscopy.[11] We thoroughly validated SMC&P and proved it to be a robust technology with the potential of high throughput. In this paper, we take the next important step and demonstrate the functional assembly of a biomolecular complex with a novel emergent property from individual building blocks one by one at a chosen position on a surface (see Figure 1).

Malachite green (MG) is a well-established red-emitting fluorophore whose quantum yield is known to depend strongly on the rotational degrees of freedom of its phenyl rings.[12,13] An increase in the quantum yield up to several orders of magnitude upon binding of this molecule to either BSA films,[14] specific antibody binding pockets[15] or suitable RNA structures[16,17] was reported in the literature. Particularly interesting appears the work by Kolpashchikov[18] where it was shown that a MG-aptamers may be split in two and used as DNA sensors with single mismatch resolution. Neither of the two aptamer halves was reported to improve the quantum yield of MG significantly, but both halves combined form a complete binding pocket and enhance the MG fluorescence by more than 3 orders of magnitude (cf. Supporting Information).

Received: February 1, 2012
Revised: March 28, 2012
Published: April 3, 2012

ACS Publications © 2012 American Chemical Society

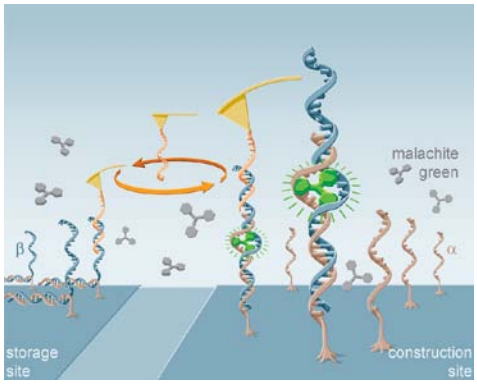

Figure 1. Schematics of the assembly of functional binding sites produced by SMC&P from individual α- and β-chains of a split malachite green aptamer. At the construction site, α-chains were covalently anchored at the 3′ end via PEG-spacers. At the storage site, β-chains were hybridized with a 40 bp overlap to an anchor oligo, which was covalently bound via its 5′ end to the surface. The other end of the β-strand had been extended by a 20 bases handle sequence, compatible to the corresponding handle oligo at the AFM cantilever tip. For transport, this handle oligo was brought into contact with a β-strand, allowing the two strands to hybridize. Upon retraction of the cantilever, the anchor oligo in unzip geometry yields and the β-strand is moved to the construction site, where it is positioned such that it hybridizes with an α-strand to form a complete MG binding site. Upon retraction of the tip, the handle sequence in shear geometry yields and the tip is free to pick up the next β-strand. When malachite green is bound in the fully assembled aptamer, its quantum yield is increased by more than 3 orders of magnitude, resulting in a bright fluorescence of the complex.

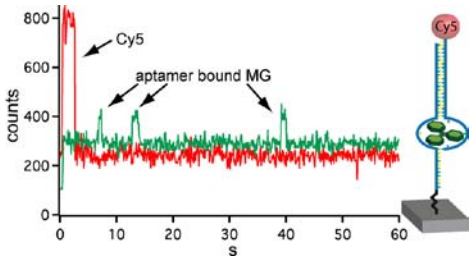

Figure 2. Typical fluorescence emission traces of individual molecules. In red, the emission of an individual Cy5 label at the 3′ end of an α-strand of the split MG-aptamer. After several seconds, the Cy5 is photobleached irreversibly and the emission drops to the background level. We then added 50 nM malachite green to the buffer solution and recorded the emission from the same aptamer under otherwise identical conditions (green trace). We measured a slightly increased background level and an intermittent fluorescence pattern with pulse durations of typically 3 ± 1 s. The typical height of the pulses was only one-fifth of the Cy5 emission. The insert depicts the molecular construct.

In order to directly compare the emission of individual MG aptamer complexes consisting of one α- and one β-strand each to that of Cy5 molecules under identical excitation and detection conditions, we covalently bound a very dilute layer (<1/5 μm^2) of β-strands with a thiol group at the 3′ end to a glass surface and then hybridized them with α-strands carrying one Cy5 label at the 3′ end. We identified individual Cy5 molecules by TIRF microscopy[19] and localized them by fitting Gauss functions to the intensity distributions. Once the Cy5 molecules were irreversibly photobleached (Figure 2 trace a) we added a 50 nM solution of MG and recorded the emission again. Now an intermittent signal was recorded. The fluorescent MG molecules were also localized to ensure that fluorescence from Cy5 and MG were collocalized (cf. Supporting Information). Trace b in Figure 2 shows a typical example of the intermittent emission pattern that we measured for extended periods of time up to several minutes. Note that the baseline of the MG emission is within an error bar of 10% indistinguishable from that of the bleached Cy5, which means that at the given concentration the free MG in solution does not significantly contribute to the measured fluorescence. It is not clear yet whether this pulsing fluorescence is caused by a change in the electronic structure of MG (e.g., population of triplet states) or by conformational changes in the molecular MG-aptamer complex (e.g., binding/unbinding of MG). It may as well reflect slow modes of the hybridization dynamics of the aptamer binding pocket. MG in the aptamer binding pocket might also become photobleached and replaced by intact MG during these traces. Detailed future studies will be required to further elucidate these interesting phenomena.

Having verified that hybridization of the aptamer leads to a marked increase in the MG fluorescence at the surface, we assembled $\alpha\beta$-aptamer arrangements by SMC&P. We modified the split aptamers such that we were able to handle and reassemble them one by one to form fully functional MG binding sites. We used different areas on a cover glass for storage and construction sites (see Figure 1) and used a functionalized AFM tip to pick up individual β-aptamer strands from the depot side and to paste them in the construction site at a given position. Since the AFM tip is then ready again to pick up a β-aptamer strand, SMC&P can be operated as a cyclic process.

All experiments were carried out with a custom built AFM/TIRF hybrid microscope[20] as follows: In the presence of 50 nM MG in solution first the background image from the still empty construction site was recorded. Then the AFM tip was traversed toward the storage area and lowered toward the surface, while a force distance trace was recorded. The functionalization densities on the tip and the storage surface were chosen such that in approximately every third approach the handle oligos on the tip and a β-strand of the aptamer hybridized, resulting in a specific molecular multisegment chain between tip and surface. Upon retraction, the force is gradually built up in this chain, and the weakest of the segments yields (see Figure 3a). Note that the attachment geometries were chosen such that the handle oligos are loaded in shear geometry, which means that the hydrogen bonds are all loaded roughly equally, whereas the anchor is loaded in unzip geometry, which means that base pair for base pair sequentially unbinds. As a result, with a 95% likelihood it is the anchor that yields while the β-strand of the aptamer remains bound to the tip via its 20 bp handle. Despite the higher hybridization energy between the β-strand of the aptamer and the anchor oligo compared to the handle oligos, the force to open the hybrid in unzip geometry is much lower than the force required to open the hybrid in shear geometry because the mechanical work to separate the two halves is performed over a much larger distance than in the first case. Typical examples of the force distance traces recorded during the cut process are shown in

dx.doi.org/10.1021/nl300422y | Nano Lett. 2012, 12, 2425−2428

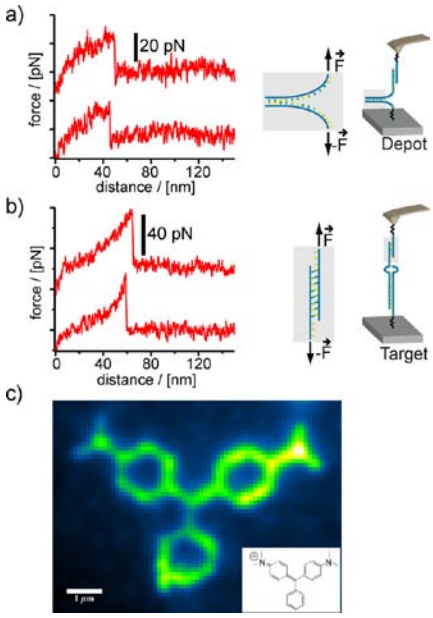

Figure 3. Typical force distance protocols of the cut (a) and paste (b) processes highlighted in Figure 1. (c) Fluorescence micrograph of a structure, consisting of more than 500 aptamers, which were assembled by SMC&P with the same tip. The insert shows the structural formula of MG that served as a blueprint of the arrangement.

Figure 3a. The rising parts of the curves reflect the entropic elasticity of the polymeric anchors, and the short plateau before the force drops to zero is caused by the unzipping of the DNA.

With the force distance curve corroborating that exactly one β-aptamer strand was picked up (see Figure 3a), the AFM tip was traversed to the construction side and lowered at a chosen position.[21] If the two halves of the split aptamer hybridize, again a chain is formed that is loaded when the tip is retracted from the surface. Since the two halves of the aptamer have a much longer sequence overlap than the handle oligos, the handle oligo complex yields (again with >90% probability) after which the tip is free to pick up a new molecule in the next cycle. Since again a force distance curve (see Figure 3b) was recorded, the deposition was either corroborated or a further attempt to paste the molecule was undertaken. Upon separation, the force distance traces depicted in Figure 3b show a continuous increase in force until the two strands loaded in shear geometry suddenly split in an all or none event and the force drops to zero.

In previous studies, we had shown that we can localize individual molecules by super resolution microscopy with an accuracy of better than 2 nm, and that the precision of the paste process is better than 10 nm. In this study here, we focused on the robustness of the process and repeated the cycle described above more than 500 times to assemble the pattern shown in Figure 3c. It depicts to the best of our knowledge the first example of a structure in which biomolecules were assembled one by one in a physiological ambient to perform a function, which emerges exclusively from their correct assembly. The bright fluorescence unambiguously corroborates that we have assembled functional binding sites from the two halves of the aptamer, and the well-pronounced contrast shows that we did so with superb selectivity.

This proof of principle opens the door toward the assembly of increasingly complex multicomponent systems at surfaces. Since we have already demonstrated that proteins or nanoparticles may be arranged by SMC&P, a large variety of systems with diverse molecular functions, which emerge from the unique arrangement of the constituents, may be envisioned. In combination with recent developments for the rapid production of protein libraries on microfluidic chips,[22] SMC&P will promote design and assembly of functional protein arrays or even entangled enzymatic networks.

■ ASSOCIATED CONTENT

Supporting Information

Details of material and methods, sample preparation, AFM measurements, TIRF-microscopy, fluorescence properties of the aptamer bound MG; additional results from nanometer precise localization and collocalization of Cy5 label and MG fluorescence. This material is available free of charge via the Internet at http://pubs.acs.org.

■ AUTHOR INFORMATION

Corresponding Author

*E-mail: gaub@lmu.de. Fax: +49 89 2180 2050.

Present Address

[§]Department of Cellular and Molecular Pharmacology, University of California, San Francisco, CA.

Notes

The authors declare no competing financial interest.

■ ACKNOWLEDGMENTS

This work was supported by the German Science Foundation and the Nanosystems Initiative Munich. Fruitful discussions with Ralf Jungman, Philip Severin, and Philip Tinnefeld are gratefully acknowledged.

■ REFERENCES

(1) Feynman, R. P. *Eng. Sci.* **1960**, *23* (5), 22–36.
(2) Crommie, M. F.; Lutz, C. P.; Eigler, D. M. *Science* **1993**, *262* (5131), 218–220.
(3) Jung, T. A.; Schlittler, R. R.; Gimzewski, J. K.; Tang, H.; Joachim, C. *Science* **1996**, *271* (5246), 181–184.
(4) Baum, R. *Chem. Eng. News* **2003**, *81* (48), 37–42.
(5) Kuhn, H. *Verh. Schweiz. Naturforsch. Ges.* **1965**, 245–266.
(6) Kufer, S. K.; Puchner, E. M.; Gumpp, H.; Liedl, T.; Gaub, H. E. *Science* **2008**, *319* (5863), 594–596.
(7) Binnig, G.; Quate, C. F.; Gerber, C. *Phys. Rev. Lett.* **1986**, *56* (9), 930–933.
(8) Drake, B.; Prater, C. B.; Weisenhorn, A. L.; Gould, S. A. C.; Albrecht, T. R.; Quate, C. F.; Cannell, D. S.; Hansma, H. G.; Hansma, P. K. *Science* **1989**, *243* (4898), 1586–1589.
(9) Puchner, E. M.; Kufer, S. K.; Strackharn, M.; Stahl, S. W.; Gaub, H. E. *Nano Lett.* **2008**, *8* (11), 3692–3695.
(10) Kufer, S. K.; Strackharn, M.; Stahl, S. W.; Gumpp, H.; Puchner, E. M.; Gaub, H. E. *Nat. Nanotechnol.* **2009**, *4* (1), 45–49.
(11) Cordes, T.; Strackharn, M.; Stahl, S. W.; Summerer, W.; Steinhauer, C.; Forthmann, C.; Puchner, E. M.; Vogelsang, J.; Gaub, H. E.; Tinnefeld, P. *Nano Lett.* **2010**, *10* (2), 645–651.
(12) Ben-Amotz, D.; Harris, C. B. *Chem. Phys. Lett.* **1985**, *119* (4), 305–311.
(13) Abedin, K. M.; Ye, J. Y.; Inouye, H.; Hattori, T.; Sumi, H.; Nakatsuka, H. *J. Chem. Phys.* **1995**, *103* (15), 6414.

(14) Bartlett, J. A.; Indig, G. L. *Dyes Pigm.* **1999**, *43* (3), 219−226.
(15) Szent-Gyorgyi, C.; Schmidt, B. F.; Creeger, Y.; Fisher, G. W.; Zakel, K. L.; Adler, S.; Fitzpatrick, J. A.; Woolford, C. A.; Yan, Q.; Vasilev, K. V.; Berget, P. B.; Bruchez, M. P.; Jarvik, J. W.; Waggoner, A. *Nat. Biotechnol.* **2008**, *26* (2), 235−240.
(16) Babendure, J. R.; Adams, S. R.; Tsien, R. Y. *J. Am. Chem. Soc.* **2003**, *125* (48), 14716−14717.
(17) Grate, D.; Wilson, C. *Proc. Natl. Acad. Sci. U.S.A.* **1999**, *96* (11), 6131−6136.
(18) Kolpashchikov, D. M. *J. Am. Chem. Soc.* **2005**, *127* (36), 12442−12443.
(19) Tokunaga, M.; Kitamura, K.; Saito, K.; Iwane, A. H.; Yanagida, T. *Biochem. Biophys. Res. Commun.* **1997**, *235* (1), 47−53.
(20) Gumpp, H.; Stahl, S. W.; Strackharn, M.; Puchner, E. M.; Gaub, H. E. *Rev. Sci. Instrum.* **2009**, *80* (6), 063704.
(21) If the force curve indicates that the pick up was not successful, the online control of the process allows for another pick-up attempt. If the force curve indicates that several molecules were picked up, they can be pasted in a "wastebasket" area rendering the tip ready again for the normal cycle.
(22) Gerber, D.; Maerkl, S. J.; Quake, S. R. *Nat. Methods* **2009**, *6* (1), 71−74.

Supporting Information

Functional Assembly of Aptamer Binding Sites by Single-Molecule Cut-and-Paste

Mathias Strackharn[1], Stefan W. Stahl[1,2], Elias M. Puchner[1,3] & Hermann E. Gaub[1,*]

[1] Center for Nanoscience and Department of Physics, University of Munich, Amalienstraße 54, 80799 Munich, Germany

[2] Center for Integrated Protein Science (CIPSM), Munich, Germany

[3] The author has moved to the Department of Cellular and Molecular Pharmacology, University of California, San Francisco, 600 16th Street, San Francisco, CA 94158, USA

[*] gaub@lmu.de

All measurements described in the manuscript were carried out with a custom designed combined AFM/TIRF microscope described in detail in [1]. Here the description of those parts and procedures, which are relevant to the experiments described above:

AFM Measurements

The spring constants of the DNA modified cantilevers were calibrated in solution using the equipartition theorem [2,3]. For the single-molecule force-extension trace recordings BL-AC40TS cantilevers (Olympus Cooporation, Tokyo, Japan) were used with a typical spring constant of about 120 pN/nm and a resonance frequency of 30 kHz. This experiment was conducted in 100 mM sodium phosphate buffer, pH 5.5, 140 mM NaCl, 5 mM $MgCl_2$. For the functional assembly of the Malachite Green structure pattern MLCT-AUHW levers (Bruker, Camarillo, USA) were used. The protocol for the functional assembly as well as the data recording was programmed using Igor Pro (Wave Metrics) and an Asylum Research MFP3D controller, which provides ACD and DAC channels as well as a DSP board for setting up feedback loops. Cantilever positioning for pick-up and delivery was controlled in closed-loop operation. The typical cycle time for one functional assembly process lies between 2 and 3 seconds depending on the sample orientation and the traveling distance between depot and target area. The positioning feedback accuracy is ±3 nm however long term deviations may arise due to thermal drift. Extension velocities are set between 1 and 2.5 µm/s.

Measurements with TIRF microscopy

The fluorescence microscopy measurements were carried out with objective-type TIRF excitation on a microscope that was especially designed for a stable combination of AFM with TIRFM [1]. We excited with a fiber-coupled 639 nm diode laser (iBeam smart, TOPTICA, München, Germany) through a 100x/1.49 oil immersion objective lens (Nikon CFI Apochromat TIRF, Japan). As excitation filter, beam splitter, and emission filter a BrightLine HC 615/45, a Raman RazorEdge 633 RS, and a Chroma ET 685/70 (AHF, Tübingen, Germany) were used respectively. Images were taken with a back-illuminated EMCCD camera (DU-860D, Andor, Belfast, Ireland). After the functional assembly of the Malachite Green structure pattern 1 µM Malachite Green (Sigma, Taufkirchen, Germany) in PBS was added. For the single-aptamer fluorescence experiment single aptamers were identified by the fluorescence of the Cy5 label and its single-step bleaching. 100 nM Malachite Green in 100 mM sodium phosphate buffer, pH 5.5, 140 mM NaCl, 5 mM $MgCl_2$, was added. Fluorescence image sequences were taken at 10 Hz frame rate, gain 200, 1 MHz readout rate in frame transfer mode. The camera was operated at -80 °C.

Preparation of cantilevers

Cantilevers (MLCT, Bruker, Camarillo, USA, and Olympus AC40TS, Japan) were oxidized in a UV-ozone Cleaner (UVOH 150 LAB, FHR Anlagenbau GmbH, Ottendorf-Okrilla, Germany) and silanized with 3-aminopropydimethylethoxysilane (ABCR, Karsruhe, Germany), baked at 80 °C, pre-incubated with sodium borate buffer (pH 8.5), PEGylated with NHS-PEG-Maleimide (MW 5000, Rapp Polymere, Tübingen, Germany), and washed with ddH_2O as described in [4].

Thiolated cantilever DNA oligomers were reduced with 5 mM TCEP (Thermo Fisher Scientific, Rockford, USA) for 1 h at room temperature, purified by ethanol precipitation and dissolved again in a 50 mM sodium phosphate buffer, pH 7.2, 50 mM NaCl, 10 mM EDTA to a final concentration of 10 µM. The PEGylated cantilevers were then incubated at room temperature with the cantilever DNA oligomers for 1 h and rinsed with ddH_2O.

Preparation of cover glass surfaces

Cover glass slips were sonicated in 50% (v/v) 2-propanol and ddH_2O for 15 min and thoroughly rinsed with ddH_2O. They were then oxidized in 50% (v/v) sulfuric acid and hydrogen peroxide (30%) for 45 min and were then again well rinsed with ddH_2O. In addition a UV-ozone treatment was applied for 15 min. For the assembly of the Malachite Green structure pattern the cover glass slips were incubated overnight with 10 mg/ml amino dextran (MW 500000, Invitrogen, Carlsbad, USA), washed afterwards with ddH_2O and dried with a nitrogen stream. NHS-PEG-maleimide (MW 5000) was dissolved to 10 mM in a 50 mM sodium borate buffer, pH 8.5 and incubated on the cover glasses for 1 h. Cover glasses were then washed with ddH_2O. A microfluidic system was fixed on the cover glass. Thiolated depot DNA oligomers and target hybrid oligomers (IBA, Göttingen, Germany) were each reduced with 5 mM TCEP (Thermo Fisher Scientific, Rockford, USA) for 1 h at room temperature, purified by ethanol precipitation and dissolved again in a 50 mM sodium phosphate buffer, pH 7.2, 50 mM NaCl, 10 mM EDTA to a final concentration of 10 µM. The depot oligomers and the target hybrid oligomers were pumped through the respective channel of the microfluidics for 1 h. Both channels were then rinsed with ddH_2O. A solution 1 µM transfer hybrid oligomers and 5 nM Atto647N labelled

transfer oligomer in PBSwere pumped through the depot channel for 30 min. We used this minor fraction of fluorescent labelled DNA to allow for an exact alignment of the sample with the AFM cantilever. The channel was then rinsed with PBS to remove non-hybridized transfer hybrids. The microfluidic system was then removed again.

For force spectroscopy of the transfer process, the oxidized cover glass slips were silanized with a mixture of 2% 3-aminopropyldimethylethoxysilane, 90% EtOH, 8% ddH_2O for 1 h. Cover glasses were thoroughly rinsed with pure EtOH first and ddH_2O afterwards, and were baked at 80 °C for 30 min. After 30 min soaking in 50 mM sodium borate buffer, pH 8.5 the cover glasses were treated with 50 mM NHS-PEG-maleimide (MW 5000) in the sodium borate buffer for 1h and then rinsed with ddH_2O. As for the Malachite Green structure writing experiment, the depot oligomers and the target hybrid oligomers were reduced, purified and dissolved again. The reduced depot and target hybrid oligomers were deposited with a 30 µm capillary of a microplotter (GIX, Sonoplot, Middleton, USA) in two 800 µm long lines separated by around 30 µm. Molecules in solution were flushed away with ddH_2O and a line with 1 µM transfer hybrid oligomers and 5 nM of Atto647N labeled transfer oligomer in 4xPBS was plotted on top of the depot line. Non-hybridized oligomers were flushed away with 4xPBS.

For fluorescence spectroscopy experiments of single aptamers, the oxidized cover glass slips were functionalized with 10 mg/ml NHS-PEG-maleimide (MW 5000) in 50 mM sodium borate buffer, pH 8.5 for 1 h and then rinsed with ddH_2O. Thiolated transfer hybrid oligomers were reduced, purified and dissolved in the same fashion as described before. The cover glass slips were incubated with the reduced thiolated transfer hybrid for 1h, the sample was then washed with ddH_2O. Cover glasses were mounted an the fluorescence microscope and Cy5 labelled target

hybrid oligomers were hybridized in a 100 mM phosphate buffer, pH 5.5, 140 mM NaCl, 5 mM $MgCl_2$ to the surface bound transfer hybrid oligomers. The density was chosen such that it allowed for single molecule fluorescence spectroscopy. Buffer was exchanged several times to avoid unbound Cy5 labelled target hybrid oligomers in solution.

Preparation of the micro-fluidics chamber

Silicon elastomer and curing agent, (Sylgard 184, Dow Corning, Wiesbaden, Germany) were well mixed in a 10:1 ratio and were degassed twice at 20 mbar. The solution was poured on a silicon wafer with a lithographically prepared positive relief structure consisting of two parallel flow channels separated by 20 µm. The channels were 20 µm high, 100 µm broad, and about 1 cm long as shown in figure S 1. The system was degassed again and then baked at 60 °C for 1 h. When taken off of the silicon wafer, the PDMS elastomer has the negative structure of the flow channels on its lower side. Cannulas (Sterican, 0,80 x 22 mm, Carl Roth, Karlsruhe, Germany) were pierced through the PDMS in order to provide connections from the upper side to all ends of the channels. The lower side of the PDMS flow channels was contacted with the cover glass slips. A pump was connected to the cannulas on the upper side, such that oligomers and rinsing solutions could be pumped through the channels.

Sequences of the oligonucleotides

DNA bases are denoted with A, C, G, T. RNA bases are denoted with rA, rC, rG, rU. (All oligomers were purchased from IBA, Göttingen, Germany.)

5’ Atto647N-

TTTGACGTCCTTAAGCTATAGTTCGAATAGCTACTTTTTGATATCGAATTCCTGCAGT

Dissociation Constant of the the split Aptamer

In order to determine the K_d, the fluorescence of a constant amount (87 nM) of assembled aptamer at variable amounts of Malachite Green was measured with a fluorescence spectrometer (Fluoromax-3, JY Horiba, New Jersey, USA). The data is shown in figure S 2. The fit was performed with the function

$$f(MG_{tot}) = F_0 + (F_{max} - F_0) \cdot \frac{A_{tot} + MG_{tot} + K_d - \sqrt{(A_{tot} + MG_{tot} + K_d)^2 - 4A_{tot}MG_{tot}}}{2A_{tot}} \quad \text{(eq. S1)}$$

with F_0 the measured offset, F_{max} the maximum fluorescence, A_{tot} the concentration of the assembled aptamer, MG_{tot} the concentration of Malachite Green. This dependency follows directly from the law of mass action and the linear dependence of the overall fluorescence on the fractions of bound and unbound malachite green dye. K_d was determined to be 107±9 nM. This value compares to the K_d of the unsplit Malachite Green Aptamer of 117 nM [5].

Fluorescence Enhancement Properties

For the determination of the enhancement of quantum efficiency the fluorescence of 400 nM malachite green was measured alone and in presence of 200 nM α-part, β-part and both parts of the split aptamer hybridized in a fluorescence spectrometer. The results are shown in figure S 3,

S 4 and S 5. The measurement was performed in a 100 mM phosphate buffer, pH 5.5, 140 mM NaCl, 5 mM $MgCl_2$.

It follows from the law of mass action, that the concentration of aptamer bound malachite green is

$$[MGA] = \frac{[MG]+[A]+K_d - \sqrt{([MG]+[A]+K_d)^2 - 4[MG][A]}}{2} \quad \text{(eq. S2)}$$

The fluorescence output of the pure malachite green measurement is

$F_{MG} = f_{spectr} A Q_1 [MG]$ (eq. S3) and $F_{Apt} = f_{spectr} A\left(Q_1([MG]-[MGA]) + Q_2[MGA]\right)$ (eq. S4) the fluorescence output for the measurement with both parts of the split aptamer and malachite green. Kd is the dissociation constant, fspectr is a spectrometer specific constant, A the absorption of malachite green is approximately independent of the bound or unbound state, [A], [MG], and [MGA] are the concentrations of assembled aptamer, malachite green and malachite green-aptamer complex, and Q1, Q2 are the quantum efficiencies of unbound and bound malachite green, respectively. From this follows immediately that the enhancement of quantum efficiency is

$$\frac{Q_2}{Q_1} = \frac{\frac{F_{Apt}}{F_{MG}} + \frac{[MGA]}{[MG]} - 1}{\frac{[MGA]}{[MG]}} \quad \text{(eq. S5)}$$

.

The enhancement factor was here determined to be 1769±74, with K_d=107±9 nM, F_{Apt}/F_{MG}=747±15, [MG]=1000±10 nM, [MGA]=500±5 nM.

The fluorescence of either 500 nM either α-part or β-part of the split aptamer with 1 µM malachite green can directly be compared to the fluorescence of 1 µM malachite green only. It turns out that fluorescence is enhanced by around a factor 3 if either α- or β-part of the split aptamer are present.

Single-Molecule Fluorescence of Assembled Aptamers

β-strands were covalently bound to the surface as described above. In a very dilute manner Cy5 labeled α-strands were then hybridized. In a 100 mM phosphate buffer, pH 5.5, 140 mM NaCl, 5mM $MgCl_2$ fluorescence of Cy5 was first recorded by TIRF microscopy until all Cy5 molecules were bleached. The buffer was then exchanged for a 100 mM phosphate buffer, pH 5.5, 140 mM NaCl, 5mM $MgCl_2$ containing 50 nM or 100 nM malachite green. Next fluorescence of malachite green was recorded by TIRF microscopy. In ImageJ Cy5 fluorescence was averaged, and a standard deviation image of the malachite green fluorescence was calculated. Cy5 fluorescence was displayed with a red color look up table and malachite green fluorescence with a green one. The two images were summed up in ImageJ, such that collocalized spots could be identified (figure S 6). A fraction of red-only and green only spots was also observed. Red-only spots can for example occur, if the surrounding of the aptamer is perturbed in such a way, that binding pockets cannot form or are not accessible. They occur also, if the contribution of the malachite green fluorescence to the overlayed standard deviation image is not exceeding the noise level. E.g. such behavior may be induced by local impurities of/on the surface. Green-only spots occur more often and may indicate, that at these locations malachite green molecules attach non-specifically in such a way, that the phenyl rings loose their rotational degrees of freedom. Here again, local impurities may play a role. Incomplete labeling of the α-strand with Cy5 may also result in a green-only detection. Displacement of the images caused by thermal drift and movements of the instrument when the buffer is exchanged, occure for all functional aptamers in the same direction. Images can after superresolution localization of malachite green and Cy5 be shifted for correction. Collocalized spots that show a displacement in a different direction were not taken into account. 4x4 pixel regions of interest were created for identified spots and z-axis

profiles were calculated with ImageJ. Data was then imported into IGOR for further evaluation. The Cy5 fluorescence timetraces were background corrected because some background bleaching was overlaying. The background average value after bleaching was then added as an offset value to the fluorescence timetraces.

Single-Molecule Localization with NanometerAccuracy

The diffraction limited single molecule fluorescence distribution was taken in TIRF microscopy as described above. Fluorescence of Cy5 and the single aptamer-bound malachite green fluorescence events were averaged in ImageJ. Average images were then imported into IGOR for further calculations. The center of the fluorescence distribution was determined in IGOR by fitting a 2D gaussian to the distribution. A result is shown in figure S 7. Thermal drift on the order of 10 nm causes, that fluorescence events do not overlay exactly. Fitting errors are below 12 nm.

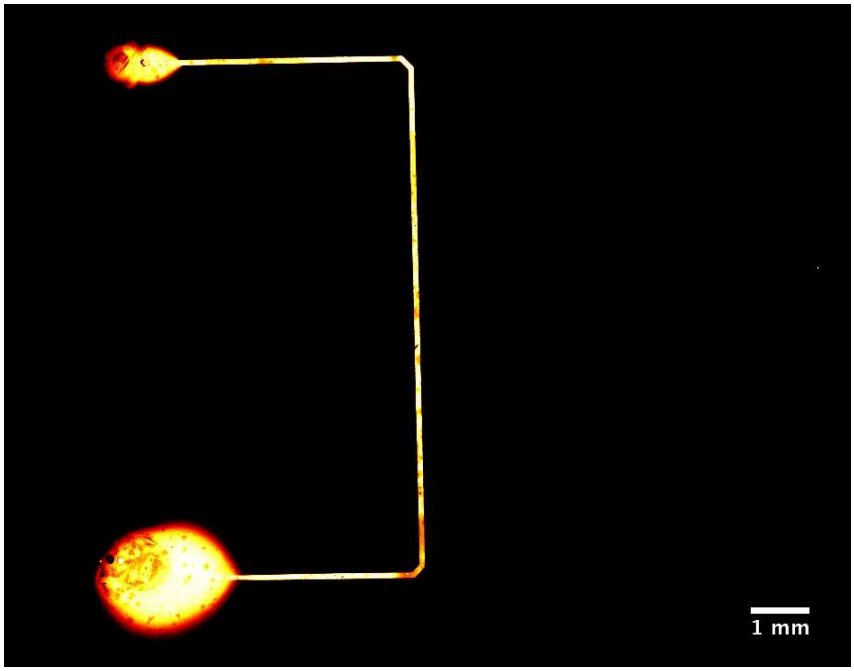

S 1. In a PDMS flow chamber a glass surface was functionalized in a depot region with thiolated depot oligomers. A dye labelled Transfer oligomer was then hybridized to the depot oligomers. The target region on the right side is functionalized with a thiolated target oligomer only. It canot be seen in fluorescence microscopy. The channel length is about 1 cm, the width 100 µm.

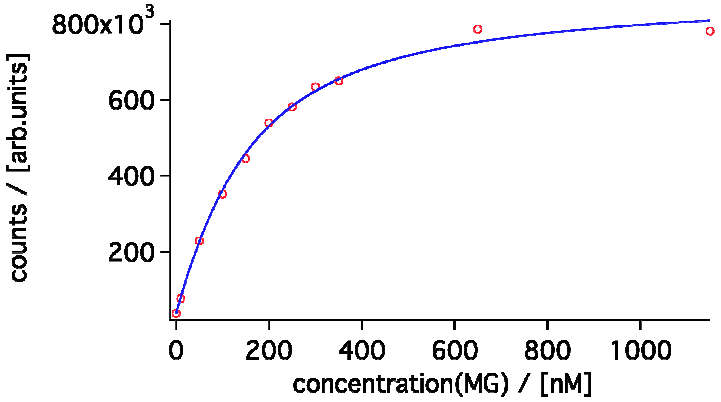

S 2. For the determination of the dissociation constant the fluorescence of aptamer bound malachite green was measured for different malachite green concentrations. The dissociation constant was determined to be 107±9 nM.

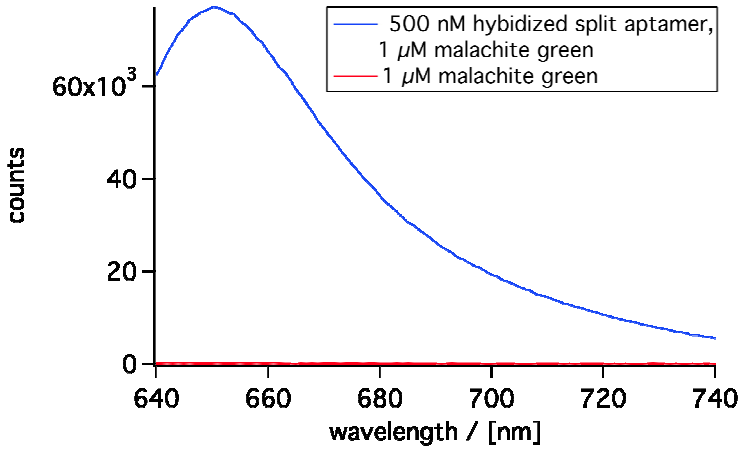

S 3. The combined split aptamer units enhance the quantum yield of malachite green by a factor of almost 1800 (blue curve). A detailed graph of the fluorescence of 1 µM malachite green only (red curve) is given in figure S 4.

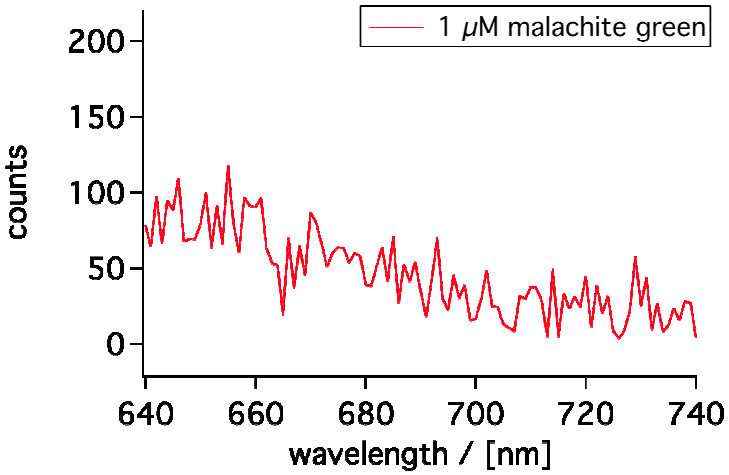

S 4. Fluorescence of 1 µM MG is depicted in this graph. It is extremely weak compared to the fluorescence of malachite green bound by the assembled aptamer.

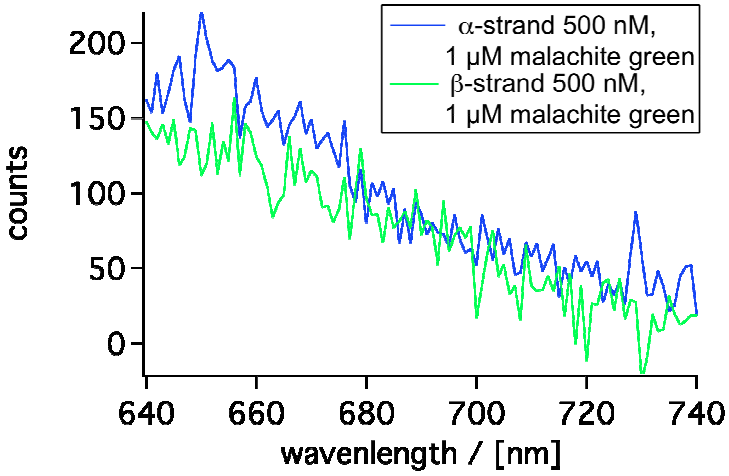

S 5. Fluorescence either of 500 nM α-strand (blue) or β-strand (green) is shown in this graph.

Fluorescence of 1 µM malachite green is enhanced by only around a factor 3.

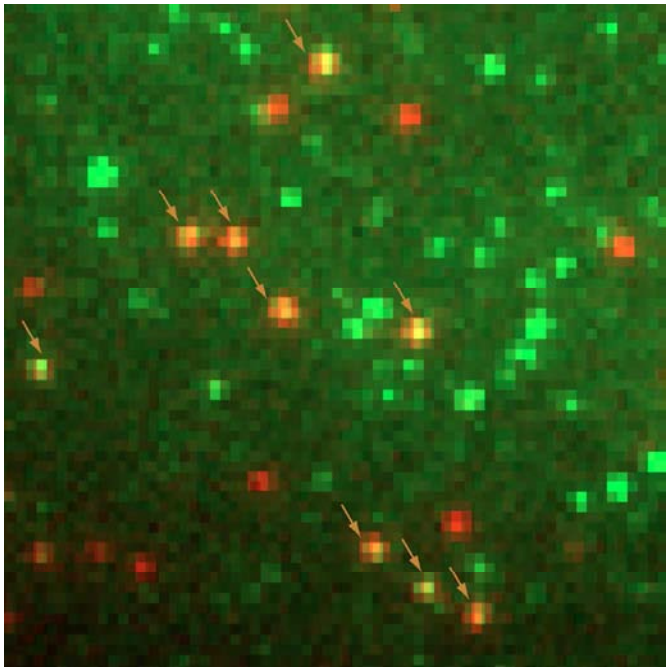

S 6. For the identification of individual functional aptamers, an averaged image of the Cy5 fluorescence (red) and an image of the malachite green fluorescence (green) were corrected for drift displacement and overlayed.

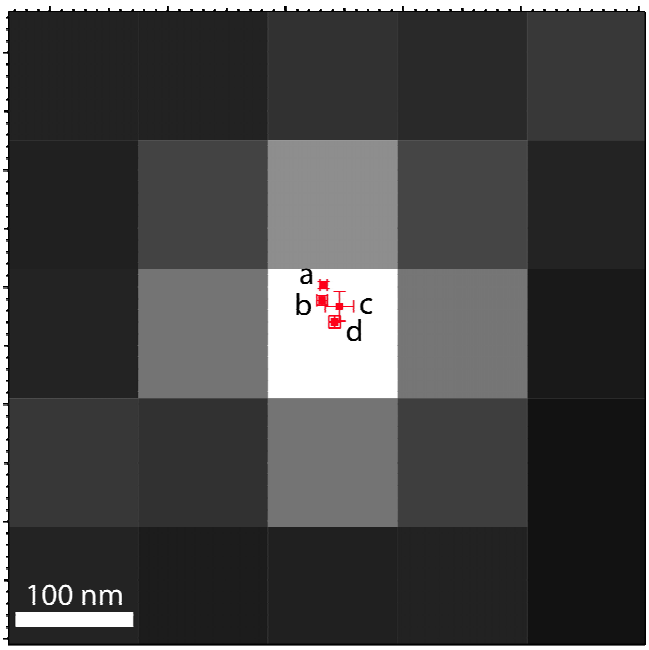

S 7. The positions of the Cy5 label (a), and the malachite green fluorescence bursts (b, c, and d in temporal order) were determined by fitting gaussians to the diffraction limited spots. The diffraction limited fluorescent pattern depicted in this graph is that of the malachite green fluorescence burst of (d). Error bars represent the fitting errors. Deviations from the original Cy5 position are on the order of 10 nm and can be assigned to thermal drift.

References:

1) Gumpp, H., Stahl, S.W., Strackharn, M., Puchner, E.M. & Gaub, H.E. Ultrastable combined atomic force and total internal reflection fluorescence microscope [corrected]. *The Review of scientific instruments* **80**, 063704 (2009).

2) Florin, E. Sensing specific molecular interactions with the atomic force microscope. *Biosensors and Bioelectronics* **10**, 895-901 (1995).

3) Butt, H.J. & Jaschke, M. *Nanotechnology* **6**, 1-7 (1995).

4) Zimmermann, J.L., Nicolaus, T., Neuert, G. & Blank, K. Thiol-based, site-specific and covalent immobilization of biomolecules for single-molecule experiments. *Nature protocols* **5**, 975-85 (2010).

5) Babendure, J.R., Adams, S.R. & Tsien, R.Y. Aptamers switch on fluorescence of triphenylmethane dyes. *Journal of the American Chemical Society* **125**, 14716-7 (2003).

8.2 Manuskripte

M1 NANOSCALE ARRANGEMENT OF PROTEINS BY SINGLE-MOLECULE CUT-AND-PASTE

Mathias Strackharn, Diana A. Pippig, Philipp Meyer, Stefan W. Stahl and Hermann E. Gaub

Nanoscale Arrangement of Proteins by Single-Molecule Cut&Paste

Mathias Strackharn[‡], Diana A. Pippig[*,‡], Philipp Meyer, Stefan W. Stahl[†], Hermann E. Gaub

Center for Nanoscience and Department of Physics, University of Munich, Amalienstraße 54, 80799 Munich, Germany

Supporting Information Placeholder

Protein-based nanostructures are key to the organization of life and it is their precise arrangement, which determines their specific functions. A single-molecule approach for the directed assembly of protein arrangements allows for a controlled composition of systems based on protein components. Applying antibodies and antigenic peptide tags we utilized the Single-Molecule Cut-and-Paste technique for the handling of single proteins. Protein-DNA complexes could be arranged to complex patterns with the functionality of the protein part remaining unimpaired.

The ability to arrange individual proteins in a controlled manner on a surface is a prerequisite for the study of complex systems e.g. of enzyme networks as a function of composition and alignment. With Single-Molecule Cut-and-Paste a technique for one-by-one arrangement of molecules under physiological conditions was implemented[1] With this technique the bottom-up assembly of biomolecular structures from biological building blocks has already been demonstrated successfully in several examples. Utilizing attachment geometries resulting in different binding forces, single DNA molecules can be repeatedly picked up from a depot region by a functionalized AFM tip and then be placed with the precision of an AFM[2] on a target surface. The accuracy of the molecular deposition process was shown to depend on the length of the crosslinker, which serves to couple the anchor DNA to the surface[3]. Until today applications of this technique were solely realized by making use of a DNA-based hierarchical force systems for pick up and deposition[4-6]. To make the SMC&P technology accessible to the field of protein science, an approach beyond mere DNA interactions is needed. We recently established an alternative implementation of a hierarchical force system, which replaces the DNA handle interaction between the transfer molecule and the AFM tip by a peptide:antibody complex[7]. Such an interaction is desirable for the transport of single proteins. A prerequisite for this is the construction of fusion proteins harboring small antigenic peptide tags, which serve as handles on the protein of interest. Thus a fully expressible system is obtained that does not require any additional modification of the protein.

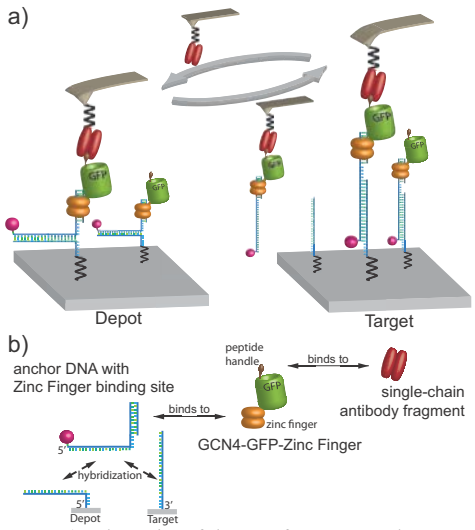

Figure 1. a) Schematics of the transfer process. The GCN4-GFP-zinc finger construct is bound with high affinity to the anchor DNA and stored via hybridization in the Depot area. A single-chain antibody fragment, which is covalently attached to the cantilever tip, can grab the GCN4, and when the cantilever is lifted, the DNA in unzip geometry opens up. Now, the GCN4-GFP-zinc finger construct with the anchor DNA can be transferred to the target site. Here the shear geometry bond to the target DNA is stronger than the bond between antibody and GCN4 peptide. The protein construct is deposited in the target area, whereas the antibody on the cantilever is free again and can be reused in the next transfer cycle. b) Toolbox for the protein transport. The GCN4-zinc finger-GFP fusion protein can specifically bind to the DNA anchor strand via the zinc finger binding site at the C-terminus. The N-terminal GCN4 peptide serves as a handle to pick up the complex.

For a first realization of a molecule-by-molecule arrangement of proteins based on this force system, an engineered fusion construct consisting of a zinc finger[8] and a GFP[9,10] moiety was used, allowing for positioning with mechanical control. A single-chain antibody fragment, that recognizes the 34 residue GCN4(7P14P) random coil peptide[11,12] was employed as handle system. For anchoring the construct to depot and target site DNA hybridization was utilized. Thus a connection between protein moiety and the DNA anchors is required. To this aim we used a six zinc finger construct that contains the three finger peptide Zif268 and its mutated variant NRE[13] separated by a flexible linker. This construct binds sequence

specifically and with a sub-picomolar affinity to a 29 bp dsDNA[14]. A GCN4-GFP-zinc finger fusion protein was expressed in E. coli and bound to a connection DNA harboring the zinc finger target sequence and a 70 nucleotide long overhang. This contains a 30 nt spacer and 40 nt stretch chosen such, that it can hybridize with the anchor sequence in the depot and in the target area. In addition the connector DNA was labeled with a Cy5 dye.

In a microfluidics system[15] mounted to a cover slip we functionalized a depot and a target site with anchor DNA on the glass surface. On the depot site these oligonucleotides were covalently attached at their 5' end, on the target site at the 3' end. Then the complex of the GCN4-GFP-zinc finger fusion protein with the connector DNA was hybridized to the depot anchors. The single-chain antibody fragments were covalently bound to the cantilever tip. For the cyclic transfer of the proteins to the target site (Fig. 1) the cantilever is first lowered towards the depot area, were the antibody is allowed to bind to the GCN4 peptide of the protein construct. In retracting the cantilever, all bonds of the system in series are loaded with the same force. Since the hybridization bond to the anchor DNA is in unzip geometry, the DNA strands separate base pair after base pair at a very low rupture force of about 25 pN, while the protein:connector-DNA complex remains attached to the cantilever, since the unbinding force of the peptide:antibody complex exceeds 40 pN at the given force loading rates. The cantilever with the zinc finger:DNA complex can then be moved by an xy-piezo system with Å precision to a predefined position in the target area. When the cantilever is lowered again, the connector DNA hybridizes to the anchor DNA. By subsequent retraction of the cantilever the hybridization bond is, in contrast to the depot process, loaded now in shear geometry. Because in this geometry all base pairs of the duplex are loaded in parallel, the rupture forces for opening up the DNA duplex bond in this configuration are in the range of 60 pN. Since the antibody:peptide complex is already broken up at forces of 40 pN[7] the protein construct is detached from the cantilever and remains bound to the designated position on the target site via its DNA anchor. The antibody at the cantilever is now free again and can be reused for the next cut & paste cycle. It should be noted here that the damage to the cantilever, e.g. by unfolding of the antibody is negligible allowing for several thousands of repeated cycles. Due to its very high affinity, the zinc finger-DNA complex was stable during the transfer[16].

Fig. 2 c) shows the time traces of a deposition process monitored in total internal reflection fluorescence from below. When the AFM tip with its zinc finger:DNA complex penetrates the evanescent field of the excitation, scattered light gives rise to the sharp increase, followed by the immediate drop when the tip is withdrawn. The remaining fluorescence of the Cy5 label of the transfer DNA can now clearly be discerned against the background. It bleaches in a single step proving at the given buffer conditions that we had indeed pasted an individual molecule. As was shown in previous studies the position of this molecule can be determined with nanometer precision given a sufficient photostability. In the trace on the right the GFP signal of a pasted complex was monitored. As it is well known the fluorophore lifetime is drastically shorter but nevertheless clearly measurable proving that the transfer process had not damaged the protein!

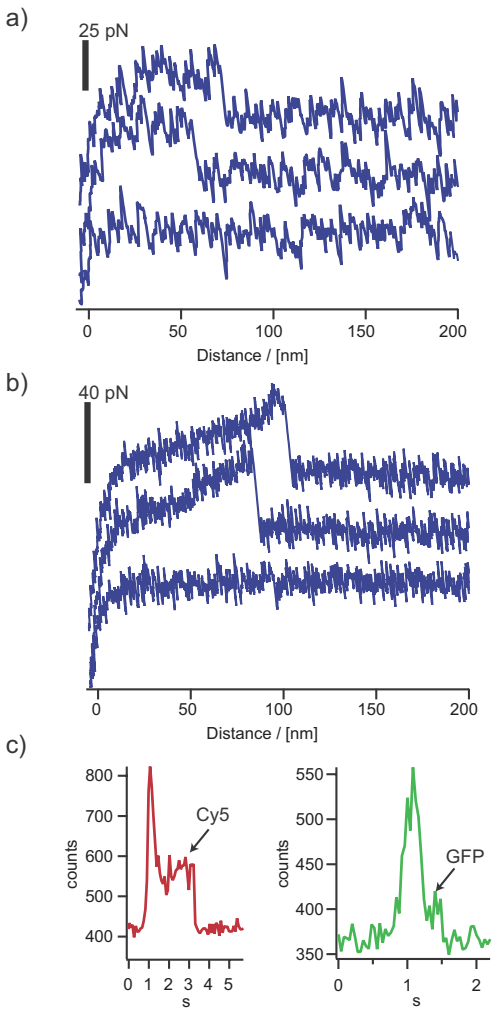

Figure 2. Typical force curves from a) the depot region and b) the target region. The cutting process in the depot region ends with a short plateau in the force-distance curve when the DNA is unzipped. When pasting the construct to the target area, the break of the antibody-antigen bond results in a sudden drop of the gradually built up force. In some cases no molecules were picked up or delivered, which is reflected in the zero-force curves. c) The deposition process can be monitored in TIRF microscopy. Photons scattered from the cantilever and those emitted by the dye contribute both to the overall signal, when the cantilever enters the evanescent field. After the cantilever is retracted, fluorescence of the Cy5 (left) or GFP (right) remains until stepwise photobleaching occurs.

During each of these cut & paste steps we independently confirmed by recording the force distance traces that individual molecules were handled. Fig. 2 shows a gallery of typical traces. In a) the force plateau prior to rupture is characteristic for the unzipping of handle and anchor DNA whereas in b) the peak is typical for the all or none rupture of the antibody-peptide bond. The blank traces show that not in all cases we were able to pick up or deliver a molecule, which required a retry.

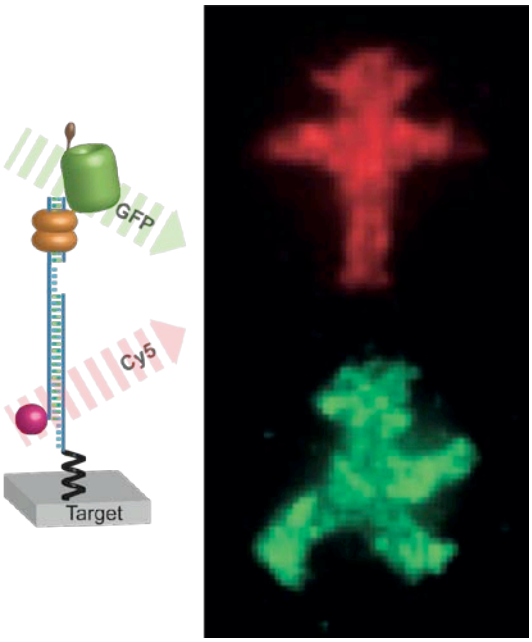

Out of hundreds of protein-DNA constructs a pattern displaying the red man of a pedestrian traffic light was assembled. The red emission of the Cy5 label at the DNA part was then measured. Next the pattern of a green man was assembled and this time the green fluorescence of the transferred GFP molecules was recorded. It proves that not only the cantilever bound antibody fragment stays intact during the transfer cycles, but also the transfer construct. The forces occurring during the transfer process are low enough, that the functionality of the transported GFP is not destroyed.

In order to demonstrate the robustness of the process, several hundred molecules were assembled to a micron-sized pattern of a red traffic light man[17]. The fluorescence of the Cy5 molecules could be imaged in objective-type TIRF microscopy[18] when excited with a red laser albeit due to the Abbe-limited optics not in single molecule resolution. The microscope was then switched to blue laser excitation and molecules were assembled to form the pattern of a green traffic light man. After the assembly the green emission of the GFP molecules was recorded. The results are shown in Fig. 3. The two strongly fluorescing patterns prove the high reliability and robustness of this transport process. They also confirm that both, the fusion protein, giving rise to the GFP fluorescence, and the Cy5 labeled DNA are transported together. It should be noted here that the imperfections in the pattern arise from the varying functionalization densities in the depot and construction area but do not affect the conclusions drawn from this figure, that SMC&P of proteins is a feasible and robust process with negligible loss in transfer efficiency

The critical component, when transferring and assembling proteins by SMC&P, are the proteins that should be arranged and observed. Twice during the transfer process forces are applied to the GFP – first during the cut and again during the paste step. Forces are required to be low enough to not alter the structure of the protein and destroy its functionality. The fluorescence of the green traffic light man unambiguously proves, that the GFP is still functional. The highest mean force that occurs during an SMC&P cycle arises as the antibody-antigen bond breaks. This force was set to be below 40 pN. Thus the hierarchical force system is gentle enough for the transfer of proteins that do not undergo serious conformational changes before this value is reached. GFP was reported to open the barrel structure only at a force of around 100 pN[19]. Destruction should therefore not be expected.

This proof of concept provides a technological approach, which will allow for the assembly of networks from arbitrary protein constituents. Systems, which develop new functionalities depending on their arrangement[20,21], can be designed and studied with respect to composition and alignment. Also the assembly of enzyme cascades will become possible and may be studied by means of single-molecule fluorescence techniques.

FIGURES (Word Style "VA_Figure_Caption"). Each figure must have a caption that includes the figure number and a brief description, preferably one or two sentences. The caption should follow the format "Figure 1. Figure caption." All figures must be mentioned in the text consecutively and numbered with Arabic numerals. The caption should be understandable without reference to the text. Whenever possible, place the key to symbols in the artwork, not in the caption. To insert the figure into the template, be sure it is already sized appropriately and paste before the figure caption. For formatting double-column figures, see the instructions at the end of the template. Do NOT modify the amount of space before and after the caption as this allows for the rules, space above and below the rules, and space above and below the figure to be inserted upon editing.

ASSOCIATED CONTENT

Supporting Information. Measurement details, preparation of proteins, surface chemistry, and oligomer sequences. This material is available free of charge via the Internet at http://pubs.acs.org.

AUTHOR INFORMATION

Corresponding Author

* diana.pippig@physik.uni-muenchen.de

Present Addresses

† Center for Integrated Protein Science (CIPSM), Munich, Germany.

Author Contributions

‡These authors contributed equally.

ACKNOWLEDGMENT

This work was supported by SFB 863 and the ERC.

REFERENCES

(1) Kufer, S. K.; Puchner, E. M.; Gumpp, H.; Liedl, T.; Gaub, H. E. Science 2008, 319, 594.
(2) Binnig, G.; Quate, C. F.; Gerber, C. Phys Rev Lett 1986, 56, 930.
(3) Kufer, S. K.; Strackharn, M.; Stahl, S. W.; Gumpp, H.; Puchner, E. M.; Gaub, H. E. Nat Nanotechnol 2009, 4, 45.
(4) Cordes, T.; Strackharn, M.; Stahl, S. W.; Summerer, W.; Steinhauer, C.; Forthmann, C.; Puchner, E. M.; Vogelsang, J.; Gaub, H. E.; Tinnefeld, P. Nano Lett 2010, 10, 645.
(5) Puchner, E. M.; Kufer, S. K.; Strackharn, M.; Stahl, S. W.; Gaub, H. E. Nano Lett 2008, 8, 3692.
(6) Strackharn, M.; Stahl, S. W.; Puchner, E. M.; Gaub, H. E. Nano Lett 2012.

(7) Strackharn, M.; Stahl, S. W.; Severin, P. M.; Nicolaus, T.; Gaub, H. E. Chemphyschem 2011.
(8) Christy, B.; Nathans, D. Proc Natl Acad Sci U S A 1989, 86, 8737.
(9) Heim, R.; Cubitt, A. B.; Tsien, R. Y. Nature 1995, 373, 663.
(10) Pedelacq, J. D.; Cabantous, S.; Tran, T.; Terwilliger, T. C.; Waldo, G. S. Nat Biotechnol 2006, 24, 79.
(11) Zahnd, C.; Spinelli, S.; Luginbuhl, B.; Amstutz, P.; Cambillau, C.; Pluckthun, A. J Biol Chem 2004, 279, 18870.
(12) Morfill, J.; Blank, K.; Zahnd, C.; Luginbuhl, B.; Kuhner, F.; Gottschalk, K. E.; Pluckthun, A.; Gaub, H. E. Biophys J 2007, 93, 3583.
(13) Greisman, H. A.; Pabo, C. O. Science 1997, 275, 657.
(14) Kim, J. S.; Pabo, C. O. Proc Natl Acad Sci U S A 1998, 95, 2812.
(15) Gerber, D.; Maerkl, S. J.; Quake, S. R. Nat Methods 2009, 6, 71.
(16) Wang, Y.; Oyokawa, S.; Han, S. W.; Huang, W.; Ikebukuro, K.; Nakamura, C.; Miyake, J. NanoBiotechnology 2006, 2, 87.
(17) The pattern we used shows a traffic light man as it was used in eastern Germany. After the reunification it mostly disappeared from the streets, but nowadays it can be found again in German cities.
.
(18) Funatsu, T.; Harada, Y.; Tokunaga, M.; Saito, K.; Yanagida, T. Nature 1995, 374, 555.
(19) Dietz, H.; Rief, M. Proc Natl Acad Sci U S A 2004, 101, 16192.
(20) Bayer, E. A.; Shimon, L. J.; Shoham, Y.; Lamed, R. J Struct Biol 1998, 124, 221.
(21) Zouni, A.; Witt, H. T.; Kern, J.; Fromme, P.; Krauss, N.; Saenger, W.; Orth, P. Nature 2001, 409, 739.

M2 COHESIN-DOCKERIN INTERACTION : THE MOLECULAR GLUE OF THE CELLULOSOME

Stefan W. Stahl, Michael A. Nash, Daniel B. Fried, Yoav Barak,
Edward A. Bayer and Hermann E. Gaub

Cohesin-Dockerin Interaction: The Molecular Glue of the Cellulosome

Stefan W. Stahl[1,2], Michael A. Nash[1,2], Daniel B. Fried[3], Yoav Barak[3], Edward A. Bayer[3], and Hermann E. Gaub[1,]*

[1]Lehrstuhl für Angewandte Physik, Center for NanoScience, and Center for Integrative Protein Science, Ludwig-Maximilians-Universität, 80799 Munich, Germany

[2]These authors contributed equally to this work

[3]Department of Biological Chemistry, The Weizmann Institute of Science, Rehovot 76100, Israel

* To whom correspondance should be addressed:
Professor Hermann E. Gaub
Lehrstuhl für Angewandte Physik and Center for NanoScience
Ludwig-Maximilians-Universität
Amalienstr. 54
80799 Munich, Germany
Tel: +49 89 2180 3172
Fax: +49 89 2180 2050
Email: gaub@physik.uni-muenchen.de

ABSTRACT
Cellulose-degrading systems have received much attention in recent years due to their potential application in second generation biofuel production. Particularly fascinating are cellulosomes, the multi-modular extracellular organelles of certain bacteria. Here, we analyze the mechanical stability of the intermolecular interfaces of this multienzyme complex. With AFM based force-spectroscopy, we studied the forced dissociation behavior of the cohesin-dockerin interaction at the single-molecule level. The observed rupture forces (>120 pN) rival those of the biotin-streptavidin system, and classify between the forces needed to destabilize the enzymatic subunits and the mechanical strength of the scaffoldin constituents. We demonstrate that high forces open the calcium binding loops in the dockerin domain, which in the presence of EDTA results in a loss of cohesin affinity. These results offer new insights into the structural and functional properties of an exquisite class of cellulose-degrading molecular machines, and provide a foundation for new interdisciplinary research on cellulosomal biophysics.

MAIN TEXT
Photosynthetic energy conversion by plants produces lignocellulosic biomass that comprises the plant cell wall. Specialized industrial enzyme formulations are being developed to break these cellulose biopolymers into their constituent high-energy glucose subunits, which can then be converted through fermentation into ethanol and other liquid fuels. Due to the significant potential economic and societal impact of such second generation biofuels, research into cellulose-degrading systems has garnered huge interest in recent years[1].

Through the course of evolution, as plants developed dense cross-linked networks of structural cell wall components to provide them with strength and support, co-evolution by aerobic and anaerobic microorganisms produced a variety of ingenious enzymatic networks for harvesting the abundant lignocellulosic carbon sources found in nature. These included secreted free cellulases, individual surface-bound cellulases, and an exquisite class of multi-modular protein assemblies, the cellulosomes. Cellulosomes are nanomachines honed through nature to self-organize on bacterial and fungal cell surfaces, adhere to plant materials, and efficiently deconstruct plant cell wall lignocellulose. Anerobic bacteria such as *Clausdridium Thermocellum* express the various cellulosome components, which are transported to the cell surface and assembled into a large (>2MDa) extracellular macromolecular complex ~100 nm in size.

Cellulosomes contain numerous different enzymatic subunits, each designed for degrading specific components of the substrate. The enzymes are organized along a single scaffold protein, the 'scaffoldin', which itself is not catalytically active, but serves to organize the catalytic enzymes at high density, and anchor the entire complex to the plant material via the cellulose binding module (CBM), as shown in Figure 1a. To anchor enzymes to the cellulosome, nature evolved the high-affinity cohesin-dockerin interaction. The dockerin comprises a highly conserved ~70 amino acid domain borne by each of the cellulosome-destined enzymes that directs assembly onto one of the diverse extracellular scaffoldin proteins. Each scaffoldin in turn bears multiple conserved cohesin domains that serve as docking sites for the dockerin-bearing enzymes, which are able to plug in like molecular breadboard components on the scaffoldin.

The cohesin-dockerin interaction belongs to those protein-protein interactions with the highest affinity known to exist, with dissociation constants $<10^{-11}$ M, making accurate measurement using conventional methods such as surface plasmon resonance biosensing problematic. Dockerins form their binding interface to the cohesin through a duplicated 22-residue calcium

binding loop-helix F-hand motif. They are belived to bind to cohesins in two different configurations, which is referred to as a dual binding mode. In each possible binding mode one F-hand alpha helix interacts together with the end part of the other F-hand calcium binding loop with the cohesin (Figure 1b & c). The two dockerin binding modes are thought to have evolved as a way to increase the conformational space of proteins bound to the extracellular scaffoldin in order to provide alternative modes of interaction between the enzymes and cellulose substrates[2]. Prior studies from our group demonstrated that a dockerin truncated at the N-terminus to eliminate one of the two possible binding modes still exhibited high affinity due to the presence of the alternative binding mode[3]. Additionally, S45A,T46A double alanine dockerin mutants were shown to exhibit a preferential binding mode, allowing for crystallization of the cohesin-dockerin complex in each of the two modes[4].

Here, we present for the first time a thorough description of cohesin-dockerin binding at the single-molecule level. Using AFM-based single-molecule force spectroscopy, we measured rupture forces among the highest receptor-ligand interaction strengths reported to date, with rupture forces rivaling the biotin-streptavidin system. Using a barrier position analysis method developed in our group, we identified characteristic unfolding fingerprints of the xylanase and CBM fusion partners and confirmed the contour lengths predicted by the amino acid sequences. In a series of calcium-dependency experiments, we characterized how application of force to the cohesin-dockerin complex in an aqueous ambient containing the divalent metal ion chelator EDTA results in dissociation of calcium from the dockerin domain, and loss of binding activity. While a site-directed cohesin mutantation that mainly destabilized the interaction between the cohesin and the bound helical part of the dockerin showed a similar activity loss, another cohesin mutation that targeted the Ca-binding loop region of the dockerin resulted in no loss of activity. This confirmed that the high interaction strength of the calcium loop towards the cohesin is required for calcium dissociation. Finally, we describe a unique double event feature found in the unfolding fingerprints, and discuss how the double event is likely a consequence of the dual binding modes of the dockerin module. This first single-molecule investigation into forced dissociation of dockerins and cohesins represents a new direction in cellulosome research, and offers significant opportunities for elucidating the structural and functional properties of these refined cellulose degrading systems.

RESULTS

Cohesin and Dockerin Fusion Constructs.

The dockerin under investigation comprised the wild type (WT) Cel48S dockerin module from *C. Thermocellum,* expressed in E. Coli as a C-terminal fusion domain with the xylanase T6 enzyme from *Geobacillus stearothermophilus*. The xylanase T6 domain was modified with a T129C mutation to introduce a cysteine residue toward the N-terminus, which was used in conjunction with maleimide chemistry to site-specifically immobilize the fusion protein on the AFM cantilever or sample surface, depending on the pulling configuration. The construct is denoted XynT6-DocS, and a version without the T129C mutation had been produced and characterized in previous works by our group [3,5].

The cohesin under investigation was an A2C site-specific cysteine mutant of the *C. Thermocellum* CipA cohesin2 module, which contained an N-terminal cellulose binding module (CBM). The CBM is located on the CipA scaffoldin between cohesins 2 and 3 (Figure 1a), and serves to adhere *C. Thermocellum* to plant materials. Expression of the cohesin domain as a

fusion protein with the CBM has the added advantage that the construct can be easily purified using a cellulose affinity column.

We used the swiss model workspace[6] in conjunction with the crystallized cohesin and dockerin structures (PDB 2CCL and 1OHZ) to model the structure of our cohesin-dockerin pair based on structural homology. The results from this modeling for dockerin binding mode 1 are shown in Figure 1c. Both dockerin binding modes visualized side-by-side for easy comparison are shown in Supporting Figure 1, with the alanine mutation sites D39 and L83 inside the cohesin domain highlighted in red.

Force spectroscopy investigations were undertaken in which the proteins were covalently immobilized onto an aminosilanized cantilever or glass surface via NHS-PEG-maleimide spacers at the engineered cysteine residues (Figure 2a). In configuration *(i)*, the more stable CBM-cohesin was attached to the cantilever and probed repeatedly. In configuration *(ii)* the positions of the two fusion proteins were exchanged.

Unfolding Fingerprints of Fusion Proteins.
Experiments were performed to determine the unfolding fingerprint of the XynT6-DocS complexed with the CBM-Coh2. We used constant velocity AFM-based single-molecule force spectroscopy, where an AFM cantilever bearing one of the binding partners was gradually lowered with Ångstrom precision and contacted with a surface displaying the second binding partner. Since the tip has a typical curvature radius of less than 10 nanometers, in general not more than one single molecular pair was formed. The base of the cantilever was then gradually withdrawn at constant speed from the surface, and the force was measured with pN sensitivity by monitoring the bend of the cantilever using the optical lever technique. The recorded force-distance traces exhibit sawtooth like peaks if a successful binding of cohesin and dockerin was established. Each peak in the force-distance trace corresponds to the unfolding of a single protein domain or folded subdomain, while the last peak always corresponded to the rupture of the cohesin-dockerin binding interface. Positions along the amino acid chain that resist the applied load represent energy barriers to unfolding. The specific positions of these energy barriers can be used as a fingerprint to identify protein domains of interest, and interrogate important amino acids involved in protein folding and stabilization. This approach has, for example, been previously used by our group and others to identify globular protein domains or key residues involved in the folding and unfolding of proteins[7-15]. After each approach-retract cycle, the x-y piezo stage was actuated, exposing a new surface location to the cantilever during the subsequent approach-retract cycle. New surface molecules were therefore presented to the same molecule on the cantilever during each approach-retract cycle.

In experimental configuration *(i)*, depicted in Figure 2a, the XynT6-DocS was conjugated to the surface, and consequently with each force-distance trace a new dockerin domain was interrogated by the same cohesin. This configuration gave rise to unfolding fingerprints such as those shown in Figure 2b. A typical force-distance trace in configuration *(i)* exhibited an initial two- to three-peaked sawtooth pattern with decreasing peak height between distances of 50 and 100 nm, followed by a high-force double peak that ruptured at ~120 pN for the given loading rate of approximately 800 pN/s (Figure 2b, 'double'). The sawtooth feature with sequentially decreasing rupture forces indicates that these events are dependent on each other. As will be explained later in more detail, the measured contour length increments match the expectations for xylanase unfolding (cf. Tables 1 and 2). Many data traces exhibited only a single peak upon

cohesin-dockerin rupture (Figure 2b, 'single'), while a small fraction exhibited an additional barrier representing CBM unfolding (Figure 2b, 'CBM'). The fractional occurrence of data traces exhibiting 'single', 'double', and 'CBM' type unfolding events are reported in Figure 2 as well. Double events were observed in ~60% of the wild type data traces, and were extremely rare in both of the destabilized cohesin mutants D39A and L83A. The double rupture event is likely a consequence of the dockerin's dual binding mode, and is discussed in further detail below.

To measure the contour lengths of the various protein domains, the force-distance data were transformed into contour length space using a worm-like chain (WLC) model[16], assuming a fixed persistence length of 0.4 nm. The chosen persistence length was previously found to be appropriate for modeling protein unfolding in a high force (>50 pN) regime[8]. After WLC transformation, a cross-correlation of all data with protein interaction was performed to correct for the polydispersity of the PEG spacers by alignment. Thus, characteristic unfolding patterns of the protein may become evident. Cross-correlation has been used in the past to align single-molecule force spectroscopy data that exhibit regular contour length increments, as is found for example in Ig-domain polyprotein unfolding[17]. Performing this type of analysis in contour length space is even more advantageous since the method there is not prone to changes of the obtained patterns on their position of appearance[16]. The transformed data traces were then combined to produce a barrier position histogram that exhibits characteristic unfolding sequences.

Shown in Figure 3 is a comparison of typical unfolding traces obtained in the two different pulling configurations *(i)* and *(ii)*. In configuration *(i),* the stable CBM-Coh2 construct was attached to the cantilever, and with each force trace a new xylanase protein was probed. In configuration *(ii),* however, the xylanase domain is located on the cantilever and consequently new cohesin molecules are probed with the same xylanase-dockerin construct with each force trace.

The barrier position histogram for configuration *(i)*, shown in Figure 3b, was assembled from 351 transformed and cross-correlated force-distance traces. The distances between the histogram peaks correspond to the end-to-end contour lengths of the various unfolded segments of the fusion proteins. By comparing the measured contour length increments in the barrier position histogram with the known lengths of the protein domains, assuming a length per amino acid of 0.365 nm[18], we were able to confirm that the first two sawtooth peaks corresponded to energy barriers in unfolding of the xylanase domain, as shown in Figure 3b 'Xyn' (cf. Table 1). In some of the traces a second substep with a not as well defined location was detected at low forces (< 30 pN) during the xylanase unfolding. A rare event was the unfolding of the cellulose binding module (CBM), which provided an extra contour length increment of 57 nm in the barrier position histogram shown in Figure 3b 'CBM'. Unfolding of the xylanase and CBM each contributed identifiable contour length increments to the force-distance traces.

Next we focus on the force-distance traces and barrier position histogram obtained in configuration *(ii)*, shown in Figures 3c & d. In configuration *(ii)*, the same xylanase-dockerin attached to the cantilever was probed with each approach-retract cycle. Within the first few approach-retract cycles, we observed the 3-peaked sawtooth pattern associated with xylanase unfolding. After the xylanase domain was unfolded, however, the three-peaked sawtooth pattern was not again observed, indicating that the xylanase domain was not able to refold during an

The cellulosomal complex is exposed to high forces in its natural environment. Both the bacterium as well as the cellulose substrate are comparatively large, and can present large loads on the cellulosomal bridges that connect them, especially when exposed to shear stress caused by flow in the ambient[30]. For proper function, the cellulosome must withstand these forces without loosing its structural integrity.

In this work we measured the extremely high mechanical strength of the cellulosomal components of *Clostridium Thermocellum*. Furthermore we observed a force-hierarchy that is well adapted to the conditions in which the cellulosome-expressing bacteria and fungi operate. The weakest component in our setup was the enzymatic subunit xylanase T6. It unfolded in multiple steps at comparatively low forces around 50 to 80 pN. For enzymes, however, this is already a comparatively high stability and the enzyme is known to be thermostable. Enzymes in nature have to be flexible during operation in order to accommodate and process their substrates. Previous work in our group found considerable reorganization of the protein fold in other mechanically loaded enzymes already at lower forces[31,32]. It should also be noted that the pulling geometry applied to the xylanase in this work is not physiologically relevant, since the attachment point was chosen arbitrarily in a surface-exposed flexible loop region of the enzyme.

The binding interface of cohesin:dockerin complex was found to be of remarkable strength in our pulling setup. The acting forces until bond rupture reach a very high level compared to other intermolecular interactions. They exceed conventional receptor-ligand interactions like those between antibodies and their target peptides[33], and even those of the strongest known biomolecular interactions like biotin-streptavidin, as we dicussed above. Solely big biomolecules with large interface areas like the titin-teletonin complex are known to withstand higher intermolecular forces[34]. Thus the characterized interaction between cohesin and dockerin represents a molecular glue for the cellulosomal components with maximum robustness.

Last, the inherent folds of the scaffoldin indicate the highest stability of the cellulosomal complex. Again this matches the requirements of the cellulosome since mainly the scaffoldin is loaded if there are shear forces acting between the cell and the substrate. In our pulling configuration, the carbohydrate binding module (CBM) only rarely unfolds before the rupture of the cohesin-dockerin interaction. The cohesin modules themselves were shown to be of superior mechanical strength compared to other stable biomolecular folds in prior studies. They unfold between 200 and 500 pN in constant velocity force-spectroscopy experiments, and it seems that this strength is dependent on their position within the scaffoldin[9].

The ‘double’ event with a distance increase of 8 nm, which appeared in 60% of the traces, is an interesting feature that might lead to new insights into the nature of the molecular interaction of cohesins and dockerins. It is a unique feature that the dockerins can bind in two configurations to their cohesin counterpart. Most likely this has been evolved to give more conformational freedom to the arrangement of the enzymes, leading to a more efficient turnover of the substrate. It would be of significant scientific interest to find out whether one of the binding modes is preferred in nature and how they are populated. Our results suggest that the unfolding event, which is causing the ‘double’ peak, is located in the dockerin domain as will be explained here shortly. If our method proves to be a means to distinguish binding modes in the future, this would give fundamental insight into the architecture of the cellulosome.

In principle there is the scenario that the 8 nm increment is located elsewhere in the structure, forming a strong bond that opens at similar forces as the force induced dissociation of the cohesin-dockerin complex. This would imply that the 'single' and the 'double 2nd' event can be caused by the same unfolding pathway. However, our investigations exclude that the event is located within the CBM or xylanase domains, since various traces showed unfolding of these domains and the detected increments matched our expectations perfectly well without the 'double' event increment. Besides the dockerin domain, there still remains the possibility that the 'double' event is caused by a partial unfolding of the cohesin domain, or that the linker region between CBM and cohesin forms a stable bond that breaks at high forces. Valbuena et al. did not observe any folding intermediates when unfolding the same cohesin2 module from *C. Thermocellum* CipA[9]. Although we cannot completely rule out that the different pulling geometry in our case exhibits intermediates, we treat this scenario as extremely unlikely. The same assumption is made for the linker hypothesis since we do not expect a part of the amino acid chain that is not part of a globular domain to withstand that high force in a folded state. The linker region is rich in threonine and proline, and is expected to be a flexible region.

We think that there is a high chance that the cohesin-dockerin interface ruptures under force in two steps, with the dockerin undergoing substantial conformational changes that are reversible if calcium is present in the ambient. As we have unambiguously proven, there is a high chance of force induced Ca^{2+}-dissociation during the unfolding process, so it is self-evident to assume a linkage between this event and the observed additional 'double' event increment. The next question is then whether the non-binding calcium loop or the cohesin-bound calcium loop is the cause of this event. Dockerin mutations that are known to have a preferential binding mode or exhibit only one binding geometry seem to be promising candidates to provide answers to these questions.

As we pointed out in our introduction, cellulosomal components are expected to have a broad range of industrial applications. Besides being a promising candidate for degradation of lignocellolitic biomass for bioethanol production on an industrial scale, there are various other applications thinkable[35]. For example, in the past they have been used for biotechnological applications, including protein purification[5]. Since they are exposed on the outside of bacterial and fungal cells, they have to withstand and operate in various ambient conditions that cover a wide pH and temperature range. We now add an extremely high intermolecular interaction force to this parameter space. From the scientific point of view, multienzyme functional systems are of high interest as well. The cooperativity of the enzymatic subunits helps to circumvent problems like diffusion limited reactions, and makes the complex more efficient than a mixture of the single parts. A deeper insight into the mechanical stability of the molecular constituents of the cellulosome is therefore desirable for multiple reasons. Future work might address the stability of the cohesin-dockerin type II interaction, which anchors the scaffoldin to the cell, as well as characterize cellulosomes from different organisms. A closer study of the nature of the observed 'double' event might draw out interesting insights into the process of molecular arrangement of the unique binding interface of cohesin and dockerin. Single-molecule force spectroscopy offers the possibility to distinguish differences in affinities for these molecular binding blocks that often are hard to distinguish with other methods due to their extremely low natural dissociation rates.

ACKNOWLEDGMENTS
ERC

AUTHOR CONTRIBUTIONS
S.W.S., M.A.N., Y.B., E.A.B and H.E.G. designed the experiments. D.B.F and Y.B. expressed and purified the protein constructs; S.W.S. and M.A.N. carried out the experiments and did the data analysis; M.A.N., S.W.S, E.A.B and H.E.G. wrote the manuscript; all authors have actively participated in revising the manuscript.

FIGURE LEGENDS

REFERENCES

ONLINE METHODS (1500 words max)
Materials. Silicon nitride cantilevers (Biolever Mini, BL-AC40TS-C2) with a nominal spring constant of 100 pN/nM and nominal resonance frequency of 25 kHz in water were purchased from Olympus. They were used for the experiments on contourlength evaluation and loading rate dependencies. For the Ca/EDTA experiments MLCT-AUHW-B levers (Bruker, Camarillo, USA) were used. Glass coverslips 22 mm in diameter were purchased from Menzel Gläser (Braunschweig, Germany). 3-Aminopropyl dimethyl ethoxysilane (APDMES) was obtained from ABCR GmbH (Karlsruhe, Germany). 5 kDa NHS-PEG-maleimide was purchased from Rapp Polymer (Tübingen, Germany). Immobilized TCEP disulfide reducing gel was obtained from Thermo Scientific (Pittsburgh, PA). The following standard chemicals were obtained from Carl Roth (Karlsruhe, Germany) and used as received: tris(hydroxymethyl)aminomethane (TRIS, >99% p.a.), $CaCl_2$ (>99% p.a.), sodium borate (>99.8% p.a.), ethylenediaminetetraacetic acid (EDTA, >99% p.a.), NaCl (>99.5% p.a.), ethanol (>99% p.a.), and toluene (>99.5% p.a.). Borate buffer was 150 mM, pH 8.5. The measurement buffer for force spectroscopy was TBS (25 mM TRIS, 75 mM NaCl, 1 mM $CaCl_2$, pH 7.2). For refolding experiments, $CaCl_2$ in the measurement buffer was replaced by 1 mM EDTA. All buffers were filtered through a sterile 0.2 μm polyethersulfone membrane filter (Nalgene, Rochester, NY, USA) prior to use.

Site-directed mutagenesis of C. thermocellum chimeric cellulosomal proteins. pET28a vectors containing previously cloned XynT6-DocS, CBM-Coh2, CBM-Coh2 D38A, and CBM-Coh2 L83A were subjected to Quick Change mutagenesis[36] to introduce the following mutations: A2C in the CBM, and T129C in the xylanase, respectively. The C129XynT6-DocS was constructed using primers 5'-cgtttcactggatcgcattcattaaccattgg-3'and 5'-ccaatggttaatgaatgcgatccagtgaaacg-3', and the C2CBM-Coh2 was constructed using the primers 5'-ttaactttaagaaggagatataccatgtgcaatacaccggtatcaggcaatttgaag-3' and 5'-cttcaaattgcctgataccggtgtattgcacatggtatatctccttcttaaagttaa-3'. The resulting mutagenesis products were confirmed by DNA sequencing analysis.

Expression and Purification of Cys-XynT6-DocS protein. The C129Xyn-Doc protein was expressed in E. coli BL21 cells in kanamycin-containing media that also contained 2 mM calcium chloride overnight at 16°C. After harvesting, cells were lysed using sonication, and the lysate was subjected to heat treatment at 60°C for 30 minutes to precipitate bacterial proteins. The lysate was then pelleted, and the supernatant was applied to a Ni-NTA column and washed

with TBS buffer containing 20mM imidazole and 2 mM calcium chloride. The bound protein was eluted using TBS buffer containing 250 mM imidazole and 2 mM calcium chloride. The solution was dialyzed to remove the imidazole, and then concentrated using an Amicon centrifugal filter device and stored in 50% glycerol at -20°C.

Expression and Purification of Cys-CBM-Coh2 proteins. The CBM-fused cohesin proteins were expressed in E. coli BL21 cells in kanamycin-containing media overnight at 16°C. After harvesting, cells were lysed using sonication, and the lysate was subjected to heat treatment at 60°C for 30 minutes to precipitate bacterial proteins. The lysate was then pelleted, and the supernatant was applied to a beaded cellulose column and incubated at 4°C for 1 hour. The column was then washed with Tris buffer (pH 7.4) containing 1.15M NaCl, and the protein was eluted using a 1% triethlyamine aqueous solution. Tris buffer was added to the eluent and the solution was neutralized with HCl. Protein was concentrated using an Amicon centrifugal filter device and stored in 50% glycerol at -20°C. The concentrations of the protein stock solutions were ~10 mg/mL for the cys-XynT6-DocS, and ~5 mg/mL for the WT and mutant cys-CBM-Coh2 proteins.

Sample Preparation. AFM cantilever and coverglass substrates were prepared according to previously published procedures[37]. Briefly, cantilevers were cleaned by UV-ozone treatment and silanized using APDMES. Coverglass substrates were cleaned with pirana solution and similarly silanized. Silanized cantilevers and coverglasses were baked for 30 minutes at 80 ºC. Coverglasses could be stored under argon at room temperature for up to 6 weeks prior to use, while cantilevers were used immediately for PEGylation and protein conjugation.

Following silanization, amine groups on the cantilever and coverglass were conjugated to a 5 kDa NHS-PEG-maleimide polymer in sodium borate buffer. Cys-CBM-Coh2 and Cys-XynT6-DocS proteins were reduced for 2.5 hours at room temperature prior to surface conjugation using a TCEP disulfide reducing gel slurry, according to manufacturer's instructions. The protein/bead mixture was centrifuged (5000xg, 5 minutes), and the supernatant was carefully collected with a micropipette. The reduced protein supernatant was diluted 1:3 with TBS, and applied to freshly PEGylated cantilevers or coverglass substrates for 1 hour. The substrates/cantilevers were then rinsed with TBS to remove non-specifically bound proteins, and stored under TBS prior to AFM measurements.

AFM Measurements. Single-molecule force spectroscopy (SMFS) experiments were performed on a custom-built AFM, which can be combined with an optical microscope for single-molecule fluorescence studies [38]. The spring constants of the cantilevers were determined on the basis of the equipartition theorem by fitting the thermal noise spectrum with the response function of a simple harmonic oscillator [39,40]. The obtained values range from 40 to 160 pN/nm for the Olympus levers and 11 to 17 pN/nm for the Bruker probes. The deviations from the nominal values matched our expectations according to the values given for each batch from the manufacturer. For the force-loading rate experiments, a second calibration was performed after the long term measurement to detect possible deviations caused by drift of the components.

All software protocols were programmed in Igor Pro 5.0 (Wavemetrics, Lake Oswego, OR). The pulling speed was controlled with a closed-loop feedback system running on an MFP-3D AFM controller (Asylum Research, Santa Barbara, CA). Speeds ranged from 50 nm/s to 5 μm/s for loading rate analysis, and were set to 700 nm/s for the Calcium dependent experiments. Before

each force trace was measured, the xy-stage was moved by 150 nm to increase the sampled area and to prevent repeated measurements of the same molecule on the surface.

Force-Extension Trace Analysis. All analysis was done using the program Igor Pro 6.2 (Wavemetrics, Lake Oswego, OR). Since low surface densities were used to avoid binding of multiple cohesin-dockerin pairs, many of the data traces exhibited no specific interaction with the surface. To remove such traces, an automated pre-selection routine was employed to throw out data traces where no interaction was observed. This routine ran by transforming the data into force-contour length space using the QM-WLC model [41] at a force threshold of 15 pN. Traces that showed interaction longer than 50 nm contour length were classified for further evaluation. All other traces with either no or only short-range interaction were discarded, which was justified since the estimator for the length of two 5 kDa PEG molecules is 80 nm. Details on contour length transformation can be found elsewhere [42]. Shortly each data point in force-distance space is assigned a contour length according to an underlying polymer elasticity model. Afterwards a histogram of the occurring contour lengths is generated that exhibits spikes at positions of unfolding intermediates.

Statistical Analysis. The probability density histograms of the occurring contour lengths (barrier position histograms) were created as follows. In a first round a template histogram was generated by aligning 60 representative curves that displayed the xylanase unfolding events together with the double event at high forces at a bin size of 1 nm. Next, the contour length histogram of each data trace that passed the above mentioned 50 nm length filter was cross-correlated with that template and aligned to the distance with the highest correlation value. Finally all aligned histograms were summed, resulting in the illustrated histograms of Figure 3. Increments reported in Table 2 were obtained by cross-correlation of contour length histograms (Peaks 1 to 3, cf. Supporting Figure 3), or alternatively for the CBM by assembling a histogram of the single increments (Peak 4, cf Supporting Figure 4).

The force-loading rate dependencies of those data traces that matched the correlation template were determined by linear fitting of the last third of the rising flank of the rupture peaks. When necessary, a non-constant lever sensitivity that may be caused by minor drift of the laser spot on the small cantilevers was compensated for by a software correction, which is based on analysis of the thermal noise over time. The rupture events at each pulling speed were combined to a point that represents the average loading rate and the most probable rupture force, which was approximated by Gaussian fitting of the rupture force probability density. Errors depict standard errors of the mean (SEM).

The bar graph representing the Calcium dependencies were generated and analyzed as follows. First the rupture forces and positions were determined using a custom-written set of procedures as described previously [33]. The number of events per trace was plotted against trace number with high pass filters for force and distance at 35 pN and 40 nm, respectively, and the average number of events for the different subcycles were evaluated. Since the interaction is assumed to strongly decrease over time in EDTA, averages were determined for the first 150 traces after the buffer exchange. And because the absolute number of events varies between different experiments, the average number of events for the first cycle in calcium buffer was used for normalization of the events in EDTA and the recovery value in calcium buffer. Error bars were determined by performing the same experiments several times (n = 4 [WT *(i)*], n = 5 [WT *(ii)*, D39A *(ii)*, L83A *(i)*, L83A *(ii)*], n = 6 [D39A *(i)*]) and represent standard errors of the

mean (SEM) that were weighted according to absolute interaction numbers in calcium buffer. To determine the configurations where values in EDTA buffer differ with statistical significance from those recovered in calcium buffer, Welch's t tests were performed between those values where significant difference was assumed for $p \leq 0.03$.

TABLES

	CBM	***Cohesin***	***Xylanase***	***Dockerin***
Amino acids (total) N_t	159	146	378 (260)	76
Folded length [nm] l_f	2	<4	6	<2
Expected increment [nm] Δl_c	*56*	<54	89	<28

Table 1. Sequence lengths and expected contour length increments for the single domains in the protein constructs. Expected increments are calculated as follows: $\Delta l_c = N_r * 0.365$ nm - l_f. For the 378 amino acid xylanase domain, only 260 amino acids located C-terminal from the mutated cysteine are relevant.

Peak	1	2	3	4
Contour length increment [nm]	19 ± 1	70 ± 1	8 ± 1	57 ± 1
Combined increments [nm]	89 ± 1			
Assigned protein domain	Xylanase		Dockerin	CBM

Table 2. Determined contour length increments for the forced unfolding of the cohesin-dockerin constructs. Assignments were made by comparing the expected increments (Table 1) with the measured increments determined from barrier position histograms.

FIGURES

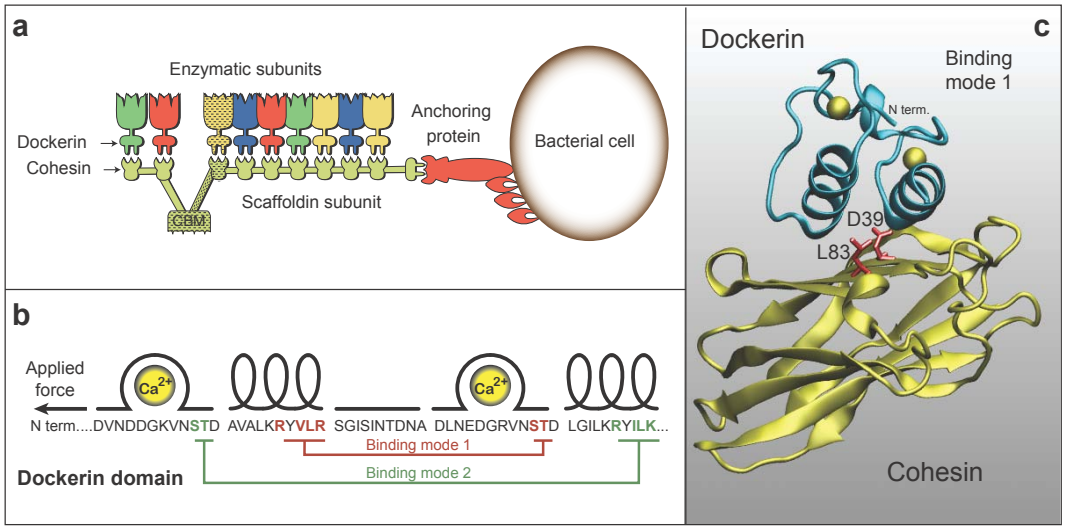

Figure 1. (a) Organization of the *C. Thermocellum* cellulosome. The enzymatic subunits are organized at high density on the scaffoldin subunit, mediated by the high affinity type I cohesin-dockerin interaction. (b) Primary sequence and secondary structural elements of the XynT6 dockerin domain. (c) Equilibrated crystal structure of the Coh2-DocS complex used in this work. The alanine mutation sites D39 and L83 on the cohesin are highlighted in red.

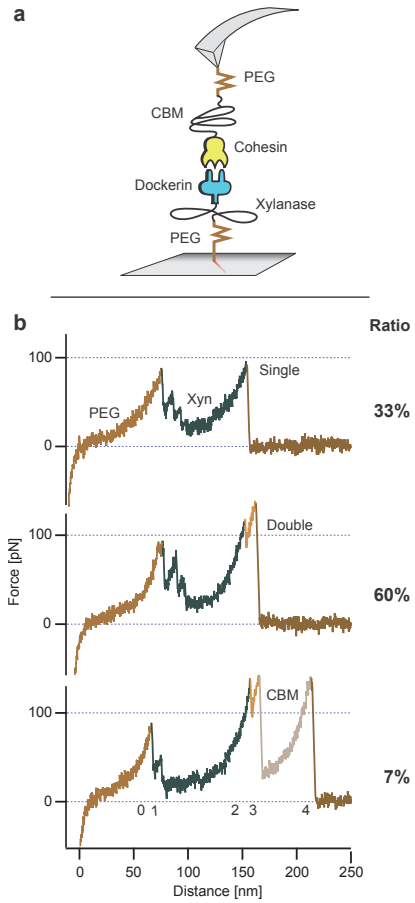

Figure 2. Force spectroscopy on the cohesin-dockerin type I interaction. (a) Schematics of the pulling geometry. The proteins were covalently attached to either the surface or cantilever via engineered cysteines and bifunctional PEG spacers. (b) Typical unfolding patterns of the WT CBM-Coh2:XynT6-DocS complex. The first nonlinear rise in force was caused by stretching of the PEG and protein linker regions. Afterwards a series of up to three rupture events with decreasing height was observed, corresponding to xylanase unfolding. Finally, the cohesin-dockerin interface ruptured in a single step (‘single’), or in a two-step process characterized by an 8 nm contour length increment (‘double’). In rare cases, an additional high-force peak was observed consistent with the unfolded length of the CBM domain (‘CBM’).

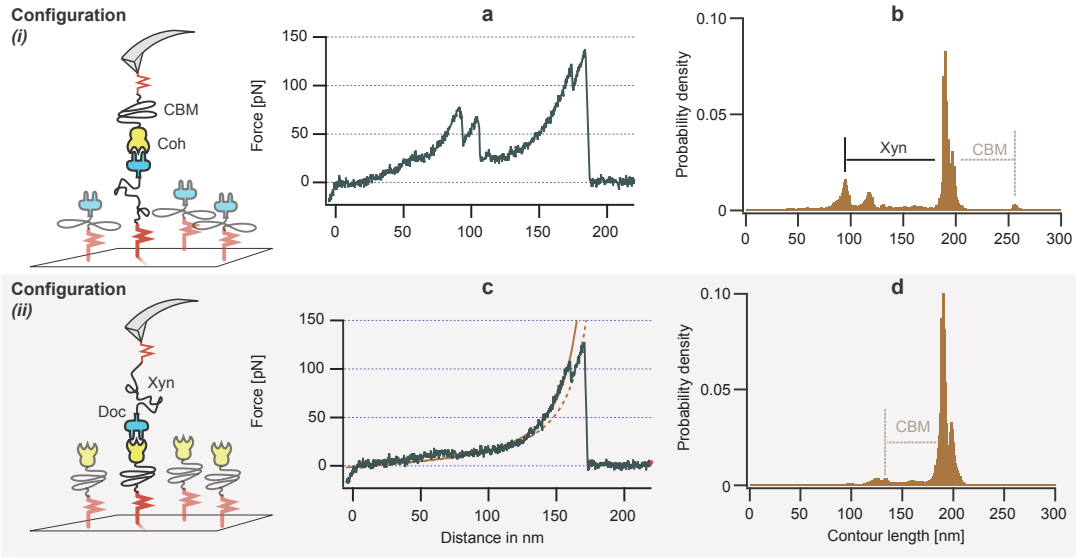

Figure 3. Single molecule unfolding fingerprints and barrier position histograms for the WT cohesin-dockerin complex in pulling configurations *(i)* and *(ii)*. In configuration *(i)*, a dockerin unfolding fingerprint was observed with each trace (a). WLC transformation and cross-correlation of the force-distance traces produced barrier position histograms that exhibited xylanase ('Xyn") and CBM contour length increments (b). In configuration *(ii)*, the xylanase domain on the cantilever was irreversibly unfolded after the first few approach-retract cycles, after which only single and double rupture events were observed. Shown here is a 'double' event with WLC fits (c). The barrier position histogram for configuration *(ii)* showed the 'double' peak increment, and the rare CBM increment (d).

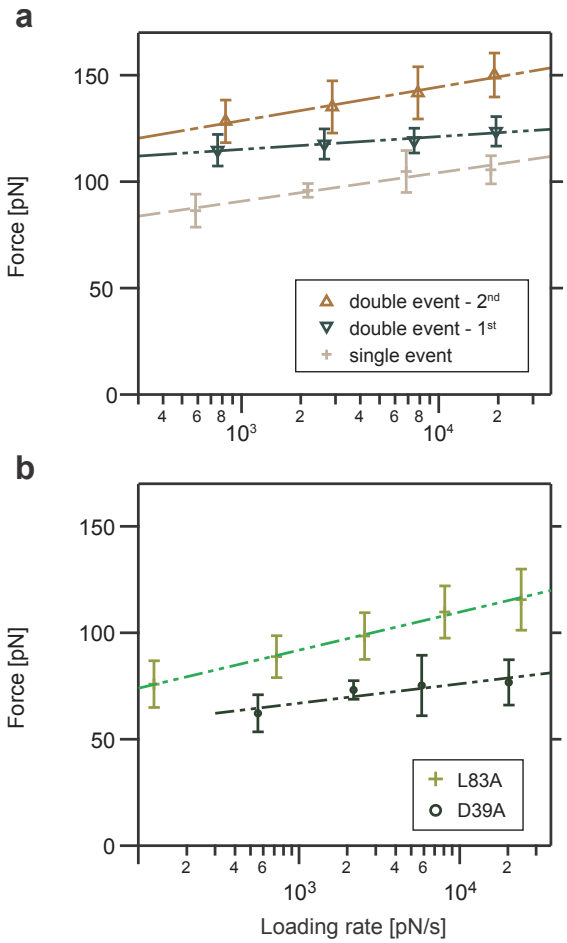

Figure 4. Loading rate dependencies of rupture events for WT cohesin-dockerin (a) and mutant cohesins (b). Error bars represent standard error of the mean.

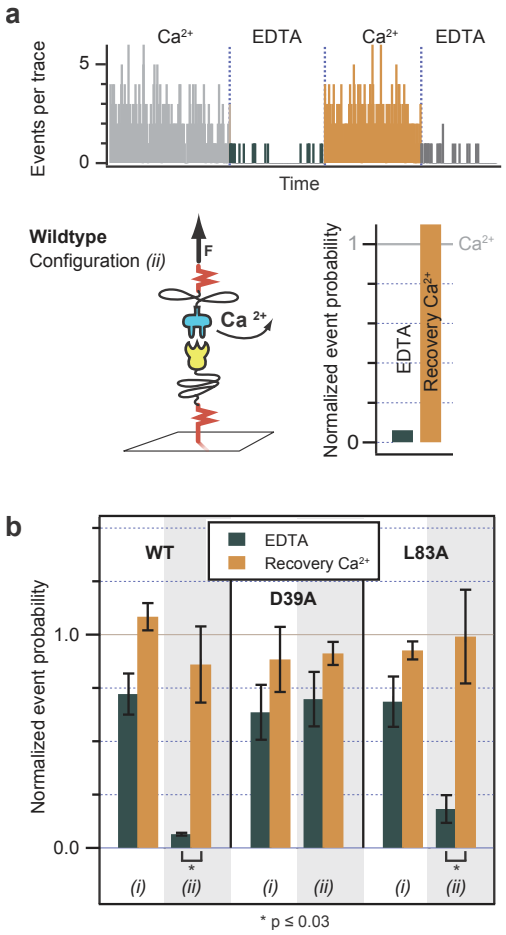

Figure 5. Force-induced dissociation of Ca^{2+} from the dockerin domain. Cantilevers with high functionalization densities that may show multiple interactions were chosen and rupture events with F > 35 pN and x > 40 nm were detected with an automated software tool.

(a) In configuration *(ii)* the event number drops drastically when Ca^{2+} is replaced with EDTA. However rupture events can be recovered by switching back to Ca-buffer. For comparability EDTA and recovered interaction numbers were normalized according to the average event number in the first Ca^{2+}-cycle.

(b) A detailed analysis of identical experiments for all configurations and constructs reveals that a statistically significant event decrease in EDTA is only observed for the wildtype and the L83A mutant in configuration 2. The minor decrease of activity for all other configurations proofs that the Ca^{2+} stays mainly bound in EDTA-buffer. However it may be dissociated when force is applied during the force-spectroscopy measurements.

REFERENCES

1. Margeot, A., Hahn-Hagerdal, B., Edlund, M., Slade, R. & Monot, F. New improvements for lignocellulosic ethanol. *Current Opinion in Biotechnology* **20**, 372-380 (2009).
2. Gilbert, H.J. Cellulosomes: microbial nanomachines that display plasticity in quaternary structure. *Molecular Microbiology* **63**, 1568-1576 (2007).
3. Karpol, A., Barak, Y., Lamed, R., Shoham, Y. & Bayer, E.A. Functional asymmetry in cohesin binding belies inherent symmetry of the dockerin module: insight into cellulosome assembly revealed by systematic mutagenesis. *Biochemical Journal* **410**, 331 (2008).
4. Carvalho, A.L. et al. Evidence for a dual binding mode of dockerin modules to cohesins. *Proceedings of the National Academy of Sciences of the United States of America* **104**, 3089-3094 (2007).
5. Demishtein, A., Karpol, A., Barak, Y., Lamed, R. & Bayer, E.A. Characterization of a dockerin-based affinity tag: application for purification of a broad variety of target proteins. *Journal of Molecular Recognition* **23**, 525-535 (2010).
6. Arnold, K., Bordoli, L., Kopp, J. & Schwede, T. The SWISS-MODEL workspace: a web-based environment for protein structure homology modelling. *Bioinformatics* **22**, 195-201 (2006).
7. Peng, Q., Fang, J., Wang, M. & Li, H. Kinetic partitioning mechanism governs the folding of the third FnIII domain of tenascin-C: evidence at the single-molecule level. *J Mol Biol* **412**, 698-709 (2011).
8. Rief, M., Gautel, M., Schemmel, A. & Gaub, H.E. The mechanical stability of immunoglobulin and fibronectin III domains in the muscle protein titin measured by atomic force microscopy. *Biophysical Journal* **75**, 3008-3014 (1998).
9. Valbuena, A. et al. On the remarkable mechanostability of scaffoldins and the mechanical clamp motif. *Proc Natl Acad Sci U S A* **106**, 13791-6 (2009).
10. Puchner, E.M. & Gaub, H.E. Force and function: probing proteins with AFM-based force spectroscopy. *Current Opinion in Structural Biology* **19**, 605-614 (2009).
11. Shank, E.A., Cecconi, C., Dill, J.W., Marqusee, S. & Bustamante, C. The folding cooperativity of a protein is controlled by its chain topology. *Nature* **465**, 637-40 (2010).
12. Kessler, M. & Gaub, H.E. Unfolding barriers in bacteriorhodopsin probed from the cytoplasmic and the extracellular side by AFM. *Structure* **14**, 521-527 (2006).
13. Ainavarapu, S.R.K. et al. Contour Length and Refolding Rate of a Small Protein Controlled by Engineered Disulfide Bonds. *Biophysical Journal* **92**, 225-233 (2007).
14. Nunes, J.M. et al. A "Force Buffer" Protecting Immunoglobulin Titin. *Angewandte Chemie-International Edition* **49**, 3528-3531 (2010).
15. Puchner, E.M. & Gaub, H.E. Exploring the conformation-regulated function of titin kinase by mechanical pump and probe experiments with single molecules. *Angew Chem Int Ed Engl* **49**, 1147-50 (2010).
16. Puchner, E.M., Franzen, G., Gautel, M. & Gaub, H.E. Comparing Proteins by Their Unfolding Pattern. *Biophysical Journal* **95**, 426-434 (2008).
17. Dietz, H. & Rief, M. Detecting Molecular Fingerprints in Single Molecule Force Spectroscopy Using Pattern Recognition. *Japanese Journal of Applied Physics* **46**, 5540-5542 (2007).
18. Dietz, H. & Rief, M. Protein structure by mechanical triangulation. *Proceedings of the National Academy of Sciences of the United States of America* **103**, 1244-1247 (2006).

19. Mechaly, A. et al. Cohesin-dockerin recognition in cellulosome assembly: Experiment versus hypothesis. *Proteins: Structure, Function, and Bioinformatics* **39**, 170-177 (2000).
20. Yuan, C., Chen, A., Kolb, P. & Moy, V.T. Energy Landscape of Streptavidin‚àíBiotin Complexes Measured by Atomic Force Microscopy ‚Ä†. *Biochemistry* **39**, 10219-10223 (2000).
21. Merkel, R., Nassoy, P., Leung, A., Ritchie, K. & Evans, E. Energy landscapes of receptor-ligand bonds explored with dynamic force spectroscopy. *Nature* **397**, 50-53 (1999).
22. Moy, V.T., Florin, E.L. & Gaub, H.E. INTERMOLECULAR FORCES AND ENERGIES BETWEEN LIGANDS AND RECEPTORS. *Science* **266**, 257-259 (1994).
23. Florin, E.L., Moy, V.T. & Gaub, H.E. ADHESION FORCES BETWEEN INDIVIDUAL LIGAND-RECEPTOR PAIRS. *Science* **264**, 415-417 (1994).
24. Dudko, O.K., Hummer, G. & Szabo, A. Theory, analysis, and interpretation of single-molecule force spectroscopy experiments. *Proceedings of the National Academy of Sciences* **105**, 15755 (2008).
25. Evans, E. & Ritchie, K. Dynamic strength of molecular adhesion bonds. *Biophysical Journal* **72**, 1541-1555 (1997).
26. Bell, G.I. Models for the specific adhesion of cells to cells. *Science* **200**, 618-27 (1978).
27. Handelsman, T. et al. Cohesin-dockerin interaction in cellulosome assembly: a single Asp-to-Asn mutation disrupts high-affinity cohesin-dockerin binding. *FEBS Lett* **572**, 195-200 (2004).
28. Junker, J.P., Ziegler, F. & Rief, M. Ligand-Dependent Equilibrium Fluctuations of Single Calmodulin Molecules. *Science* **323**, 633-637 (2009).
29. Desmeules, P., Grandbois, M., Bondarenko, V.A., Yamazaki, A. & Salesse, C. Measurement of membrane binding between recoverin, a calcium-myristoyl switch protein, and lipid bilayers by AFM-based force spectroscopy. *Biophysical Journal* **82**, 3343-3350 (2002).
30. Thomas, W.E., Trintchina, E., Forero, M., Vogel, V. & Sokurenko, E.V. Bacterial adhesion to target cells enhanced by shear force. *Cell* **109**, 913-923 (2002).
31. Puchner, E.M. et al. Mechanoenzymatics of titin kinase. *Proc Natl Acad Sci U S A* **105**, 13385-90 (2008).
32. Gumpp, H. et al. Triggering enzymatic activity with force. *Nano Lett* **9**, 3290-5 (2009).
33. Morfill, J. et al. Affinity-matured recombinant antibody fragments analyzed by single-molecule force spectroscopy. *Biophys J* **93**, 3583-90 (2007).
34. Bertz, M., Wilmanns, M. & Rief, M. The titin-telethonin complex is a directed, superstable molecular bond in the muscle Z-disk. *Proc Natl Acad Sci U S A* **106**, 13307-133310 (2009).
35. Nordon, R.E., Craig, S.J. & Foong, F.C. Molecular engineering of the cellulosome complex for affinity and bioenergy applications. *Biotechnol Lett* **31**, 465-76 (2009).
36. Wang, W.Y. & Malcolm, B.A. Two-stage PCR protocol allowing introduction of multiple mutations, deletions and insertions using QuikChange (TM) site-directed mutagenesis. *Biotechniques* **26**, 680-682 (1999).
37. Zimmermann, J.L., Nicolaus, T., Neuert, G. & Blank, K. Thiol-based, site-specific and covalent immobilization of biomolecules for single-molecule experiments. *Nature Protocols* **5**, 975-985 (2010).
38. Gumpp, H., Stahl, S.W., Strackharn, M., Puchner, E.M. & Gaub, H.E. Ultrastable combined atomic force and total internal reflection fluorescence microscope [corrected]. *Rev Sci Instrum* **80**, 063704 (2009).

39. Cook, S. et al. Practical implementation of dynamic methods for measuring atomic force microscope cantilever spring constants. *Nanotechnology* **17**, 2135-2145 (2006).
40. Butt, H.J. & Jaschke, M. Calculation of thermal noise in atomic-force microscopy. *NANOTECHNOLOGY* **6**, 1-7 (1995).
41. Hugel, T., Rief, M., Seitz, M., Gaub, H.E. & Netz, R.R. Highly stretched single polymers: atomic-force-microscope experiments versus ab-initio theory. *Phys Rev Lett* **94**, 048301 (2005).
42. Puchner, E.M., Franzen, G., Gautel, M. & Gaub, H.E. Comparing proteins by their unfolding pattern. *Biophys J* **95**, 426-34 (2008).

SUPPORTING INFORMATION
Cohesin-Dockerin Interaction: The Molecular Glue of the Cellulosome

Stefan W. Stahl[1,2], Michael A. Nash[1,2], Daniel B. Fried[3], Yoav Barak[3], Edward A. Bayer[3], and Hermann E. Gaub[1,]*

[1]Lehrstuhl für Angewandte Physik, Center for NanoScience, and Center for Integrative Protein Science, Ludwig-Maximilians-Universität, 80799 Munich, Germany

[2]These authors contributed equally to this work

[3]Department of Biological Chemistry, The Weizmann Institute of Science, Rehovot 76100, Israel

* To whom correspondance should be addressed:
Professor Hermann E. Gaub
Lehrstuhl für Angewandte Physik and Center for NanoScience
Ludwig-Maximilians-Universität
Amalienstr. 54
80799 Munich, Germany
Tel: +49 89 2180 3172
Fax: +49 89 2180 2050
Email: gaub@physik.uni-muenchen.de

PROTEIN SEQUENCES:

Dockerin fusion construct:
H6-XynT6(T129C)-DocS

MSHHHHHHKNADSYAKKPHISALNAPQLDQRYKNEFTIGAAVEPYQLQNEKDVQMLKRHFNSI
VAENVMKPISIQPEEGKFNFEQADRIVKFAKANGMDIRFHTLVWHSQVPQWFFLDKEGKPMVN
E**C**DPVKREQNKQLLLKRLETHIKTIVERYKDDIKYWDVVNEVVGDDGKLRNSPWYQIAGIDYIK
VAFQAARKYGGDNIKLYMNDYNTEVEPKRTALYNLVKQLKEEGVPIDGIGHQSHIQIGWPSEAE
IEKTINMFAALGLDNQITELDVSMYGWPPRAYPTYDAIPKQKFLDQAARYDRLFKLYEKLSDKIS
NVTFWGIADNHTWLDSRADVYYDANGNVVVDPNAPYAKVEKGKGKDAPFVFGPDYKVKPAY
WAIIDHKVVPGTPSTKLYGDVNDDGKVNSTDAVALKRYVLRSGISINTDNADLNEDGRVNSTDL
GILKRYILKEIDTLPYKN

Theoretical M_w: 53,048.09 g/mol
Theoretical pI: 6.75
Predicted extinction coefficient: 86,750 $M^{-1}cm^{-1}$ @ 280nm
Number of amino acids:
XynT6: 378 AA; After Cys: 260 AA
Doc: 76 AA

Wild type cohesin fusion construct:
CBM(A2C)-Coh2 (D39 L83 are the locations of the alanine mutations for cohesin mutants)

M**C**NTPVSGNLKVEFYNSNPSDTTNSINPQFKVTNTGSSAIDLSKLTLRYYYTVDGQKDQTFWC
DHAAIIGSNGSYNGITSNVKGTFVKMSSSTNNADTYLEISFTGGTLEPGAHVQIQGRFAKNDWS
NYTQSNDYSFKSASQFVEWDQVTAYLNGVLVWGKEPG*GSVVPSTQPVTTPPATTKPPATTIP*
*PSDDPNA*GSDGVVVEIGKVTGSVGTTVEIPVYFRGVPSKGIANC**D**FVFRYDPNVLEIIGIDPGDI
IVDPNPTKSFDTAIYPDRKIIVF**L**FAEDSGTGAYAITKDGVFAKIRATVKSSAPGYITFDEVGGFA
DNDLVEQKVSFIDGGVNVGNAT

Theoretical M_w: 36,569.58 g/mol
Theoretical pI: 4.60
Predicted extinction coefficient: 42,860 $M^{-1}cm^{-1}$ @ 280 nm
Number of amino acids:
CBM: 196 AA; Folded fraction: 159 AA
Linker: 32 AA
Coh: 146 AA

SUPPORTING FIGURES

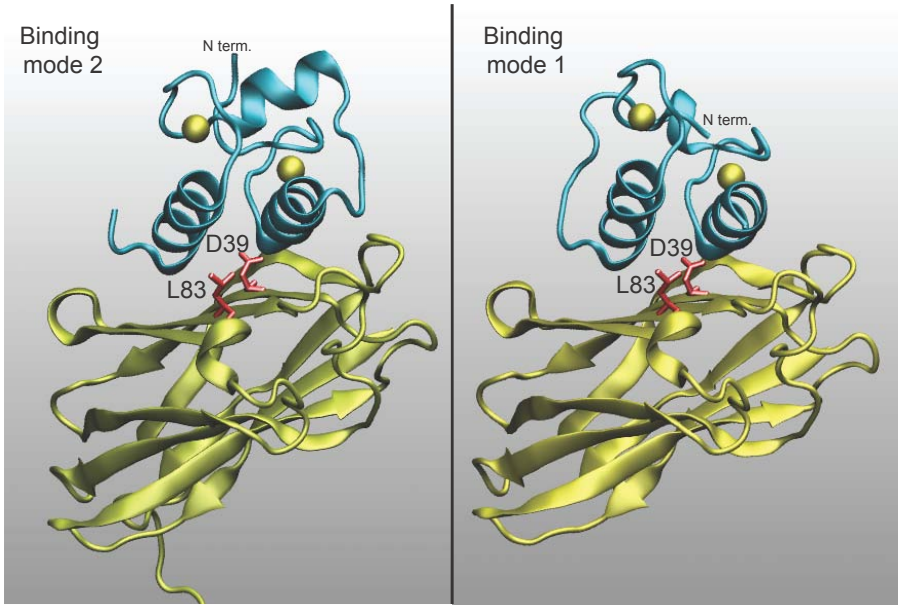

Supporting Figure 1. Crystal structures of the Coh2-DocS complex bound in binding mode 1 (left) and binding mode 2 (right). Structures were generated based on PDB 1OHZ and 2CCL with dockerin domain structure assumptions according to the Swiss model interface[1].

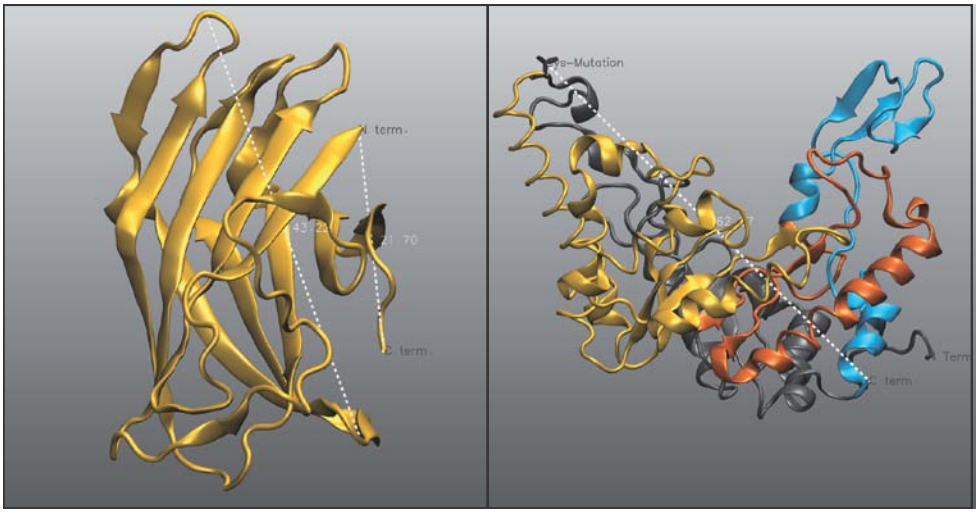

Supporting Figure 2. Crystal structures of the cellulose binding module (CBM), PDB 1NBC, (left) and the Xylanase T6, PDB 1R85 (right). For the xylanase a guess of the separate unfolding subdomains is highlighted in color. The amino acids that are N-terminal of the Cystein mutation and carry no load for the unfolded xylanase are marked in grey.

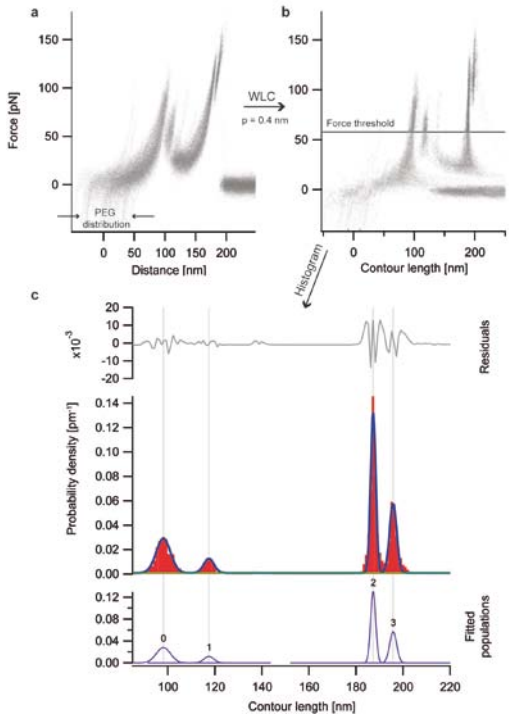

Supporting figure 3. Barrier position determination for the CBM-Coh2:XynT6-DocS construct. (a) Superposition of 94 unfolding traces in force-distance space. Due to the variety of PEG linker lengths, the overlay is not suitable for contour length fitting. (b) Superposition of traces in force-contour length space based on WLC transformation and crosscorrelation of the single traces. The distribution is much narrower because absolute distances to the surface are not relevant in contour length space. (c) Histogram of determined contour lengths above the force threshold marked in (b). Because the optimal persistence lengths are different for the PEG and the protein, not all barriers can be fitted equally well with one persistence length for the transformation. Since the first barrier is obviously tilted with regards to the others the force-threshold was set comparatively high for a more accurate determination of contour length increments. The position of the barriers was determined with Gaussian fits.

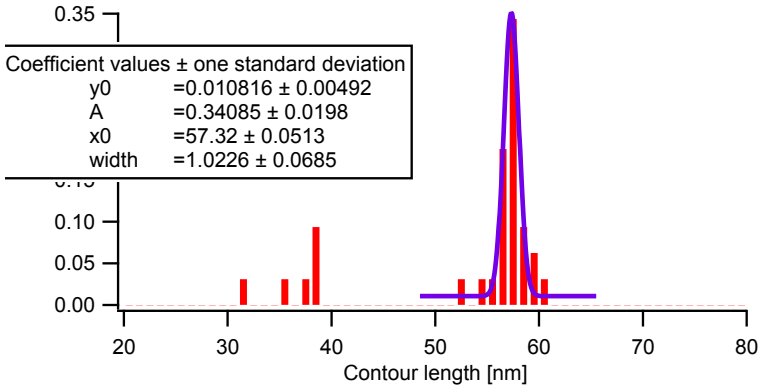

Supplemental figure 4. Contour length histogram of the additional high force increments in the unfolding pattern. Since the occurrence is rather low and the position varies, they were not generated by an automatic overlay but rather by determining the contour length histogram for each trace separately. The Gaussian fit matches the expectation for an CBM unfolding very well.

REFERENCES

1. Arnold, K., et al., *The SWISS-MODEL workspace: a web-based environment for protein structure homology modelling.* Bioinformatics, 2006. **22**(2): p. 195-201.

9 REFERENZEN

[1] J. W. Schopf, and B. M. Packer, *Early Archean (3.3-billion to 3.5-billion-year-old) microfossils from Warrawoona Group, Australia*, SCIENCE **237**, 70 (1987).

[2] M. M. Tice, and D. R. Lowe, *Photosynthetic microbial mats in the 3,416-Myr-old ocean*, NATURE **431**, 549 (2004).

[3] Alberts *et al.*, *Molekularbiologie der Zelle* (Wiley-VCH, 2011).

[4] R. Jahn, and T. C. Sudhof, *Membrane fusion and exocytosis*, ANNUAL REVIEW OF BIOCHEMISTRY **68**, 863 (1999).

[5] J. P. Abrahams, A. G. W. Leslie, R. Lutter, and J. E. Walker, *STRUCTURE AT 2.8-ANGSTROM RESOLUTION OF F1-ATPASE FROM BOVINE HEART-MITOCHONDRIA*, NATURE **370**, 621 (1994).

[6] P. D. Boyer, *The ATP synthase--a splendid molecular machine*, ANNUAL REVIEW OF BIOCHEMISTRY **66**, 717 (1997).

[7] H. Noji, R. Yasuda, M. Yoshida, and K. Kinosita, Jr., *Direct observation of the rotation of F1-ATPase*, NATURE **386**, 299 (1997).

[8] J. H. Kaplan, *Biochemistry of Na,K-ATPase*, ANNUAL REVIEW OF BIOCHEMISTRY **71**, 511 (2002).

[9] M. A. Wozniak, and C. S. Chen, *Mechanotransduction in development: a growing role for contractility*, NAT REV MOL CELL BIOL **10**, 34 (2009).

[10] A. S. Smith, and E. Sackmann, *Progress in mimetic studies of cell adhesion and the mechanosensing*, CHEMPHYSCHEM **10**, 66 (2009).

[11] C. Yagmur, S. Akaishi, R. Ogawa, and E. Guneren, *Mechanical receptor-related mechanisms in scar management: a review and hypothesis*, PLAST RECONSTR SURG **126**, 426 (2010).

[12] P. G. Gillespie, and U. Muller, *Mechanotransduction by hair cells: models, molecules, and mechanisms*, CELL **139**, 33 (2009).

[13] P. Delmas, J. Hao, and L. Rodat-Despoix, *Molecular mechanisms of mechanotransduction in mammalian sensory neurons*, NATURE REVIEWS NEUROSCIENCE **12**, 139 (2011).

[14] V. Vogel, *Mechanotransduction involving multimodular proteins: converting force into biochemical signals*, ANNU REV BIOPHYS BIOMOL STRUCT **35**, 459 (2006).

[15] A. E. Brown, and D. E. Discher, *Conformational changes and signaling in cell and matrix physics*, CURR BIOL **19**, R781 (2009).

[16] X. Zhang, K. Halvorsen, C. Z. Zhang, W. P. Wong, and T. A. Springer, *Mechanoenzymatic cleavage of the ultralarge vascular protein von Willebrand factor*, SCIENCE **324**, 1330 (2009).

[17] W. Friedrich, P. Knipping, and M. Laue, *Interference appearances in X-rays*, ANN. PHYS.-BERLIN **41**, 971 (1913).

[18] J. B. Sumner, *The isolation and crystallization of the enzyme urease. Preliminary paper*, JOURNAL OF BIOLOGICAL CHEMISTRY **69**, 435 (1926).

[19] H. Meinhardt, and A. Gierer, *Pattern formation by local self-activation and lateral inhibition*, BIOESSAYS **22**, 753 (2000).

[20] M. B. Elowitz, A. J. Levine, E. D. Siggia, and P. S. Swain, *Stochastic gene expression in a single cell*, SCIENCE **297**, 1183 (2002).

[21] B. P. English *et al.*, *Ever-fluctuating single enzyme molecules: Michaelis-Menten equation revisited*, NAT. CHEM. BIOL. **2**, 87 (2006).

[22] B. Johnsson, S. Lofas, and G. Lindquist, *IMMOBILIZATION OF PROTEINS TO A CARBOXYMETHYLDEXTRAN-MODIFIED GOLD SURFACE FOR BIOSPECIFIC INTERACTION ANALYSIS IN SURFACE-PLASMON RESONANCE SENSORS*, ANALYTICAL BIOCHEMISTRY **198**, 268 (1991).

[23] S. Krimm, and J. Bandekar, *Vibrational spectroscopy and conformation of peptides, polypeptides, and proteins*, ADVANCES IN PROTEIN CHEMISTRY **38**, 181 (1986).

[24] E. Schrödinger, BRITISH JOURNAL FOR THE PHILOSOPHY OF SCIENCE **3** (1953).
[25] T. Plakhotnik, E. A. Donley, and U. P. Wild, *Single-molecule spectroscopy*, ANNUAL REVIEW OF PHYSICAL CHEMISTRY **48**, 181 (1997).
[26] *Duden - Deutsches Universalwörterbuch* (Bibliographisches Institut, 2011), p. 2112.
[27] J. B. Listing, *Vorstudien zur Topologie* (Vandenhoeck und Ruprecht, 1848), p. 67.
[28] A. Zwar, (Brockhaus, 2005).
[29] M. J. Egenhofer, and R. D. Franzosa, *ON THE EQUIVALENCE OF TOPOLOGICAL RELATIONS*, INTERNATIONAL JOURNAL OF GEOGRAPHICAL INFORMATION SYSTEMS **9**, 133 (1995).
[30] M. W. Mislove, *Topology, domain theory and theoretical computer science*, TOPOLOGY AND ITS APPLICATIONS **89**, 3 (1998).
[31] G. Gong, Y. He, and A. C. Evans, *Brain connectivity: gender makes a difference*, THE NEUROSCIENTIST : A REVIEW JOURNAL BRINGING NEUROBIOLOGY, NEUROLOGY AND PSYCHIATRY **17**, 575 (2011).
[32] K. S. Brown *et al.*, *The statistical mechanics of complex signaling networks: nerve growth factor signaling*, PHYSICAL BIOLOGY **1**, 184 (2004).
[33] A. Krogh, B. Larsson, G. von Heijne, and E. L. Sonnhammer, *Predicting transmembrane protein topology with a hidden Markov model: application to complete genomes*, JOURNAL OF MOLECULAR BIOLOGY **305**, 567 (2001).
[34] E. A. Shank, C. Cecconi, J. W. Dill, S. Marqusee, and C. Bustamante, *The folding cooperativity of a protein is controlled by its chain topology*, NATURE **465**, 637 (2010).
[35] S. Hawking, *The Universe in a Nutshell* (Bantam, 2001), p. 224.
[36] J. D. Watson, and F. H. Crick, *Molecular structure of nucleic acids; a structure for deoxyribose nucleic acid*, NATURE **171**, 737 (1953).
[37] V. I. Danilov, and I. S. Tolokh, *Nature of the stacking of nucleic acid bases in water: a Monte Carlo simulation*, J BIOMOL STRUCT DYN **2**, 119 (1984).
[38] C. L. Peterson, and M. A. Laniel, *Histones and histone modifications*, CURR BIOL **14**, R546 (2004).
[39] P. W. Rothemund, *Folding DNA to create nanoscale shapes and patterns*, NATURE **440**, 297 (2006).
[40] S. M. Douglas *et al.*, *Self-assembly of DNA into nanoscale three-dimensional shapes*, NATURE **459**, 414 (2009).
[41] I. H. Stein, V. Schuller, P. Bohm, P. Tinnefeld, and T. Liedl, *Single-molecule FRET ruler based on rigid DNA origami blocks*, CHEMPHYSCHEM **12**, 689 (2011).
[42] H. T. Maune *et al.*, *Self-assembly of carbon nanotubes into two-dimensional geometries using DNA origami templates*, NAT NANOTECHNOL **5**, 61 (2010).
[43] G. P. Acuna *et al.*, *Distance Dependence of Single-Fluorophore Quenching by Gold Nanoparticles Studied on DNA Origami*, ACS NANO (2012).
[44] A. Kuzyk *et al.*, *DNA-based self-assembly of chiral plasmonic nanostructures with tailored optical response*, NATURE **483**, 311 (2012).
[45] M. M. Davis, and P. J. Bjorkman, *T-cell antigen receptor genes and T-cell recognition*, NATURE **334**, 395 (1988).
[46] E. M. Puchner *et al.*, *Mechanoenzymatics of titin kinase*, PROC NATL ACAD SCI U S A **105**, 13385 (2008).
[47] T. R. Kelly, H. De Silva, and R. A. Silva, *Unidirectional rotary motion in a molecular system*, NATURE **401**, 150 (1999).
[48] M. S. Dillingham, *Replicative helicases: a staircase with a twist*, CURR BIOL **16**, R844 (2006).
[49] M. Gautel, *The sarcomeric cytoskeleton: who picks up the strain?*, CURR OPIN CELL BIOL **23**, 39 (2011).
[50] S. Labeit, and B. Kolmerer, *Titins: giant proteins in charge of muscle ultrastructure and elasticity*, SCIENCE **270**, 293 (1995).
[51] H. Li *et al.*, *Multiple conformations of PEVK proteins detected by single-molecule techniques*, PROC NATL ACAD SCI U S A **98**, 10682 (2001).
[52] W. A. Linke *et al.*, *PEVK domain of titin: an entropic spring with actin-binding properties*, JOURNAL OF STRUCTURAL BIOLOGY **137**, 194 (2002).
[53] A. Sarkar, S. Caamano, and J. M. Fernandez, *The elasticity of individual titin PEVK exons measured by single molecule atomic force microscopy*, J BIOL CHEM **280**, 6261 (2005).

[54] J. F. Bazan, *Structural design and molecular evolution of a cytokine receptor superfamily*, PROC NATL ACAD SCI U S A **87**, 6934 (1990).
[55] S. Improta, A. S. Politou, and A. Pastore, *Immunoglobulin-like modules from titin I-band: extensible components of muscle elasticity*, STRUCTURE **4**, 323 (1996).
[56] M. Rief, M. Gautel, F. Oesterhelt, J. M. Fernandez, and H. E. Gaub, *Reversible unfolding of individual titin immunoglobulin domains by AFM*, SCIENCE **276**, 1109 (1997).
[57] M. Rief, M. Gautel, A. Schemmel, and H. E. Gaub, *The mechanical stability of immunoglobulin and fibronectin III domains in the muscle protein titin measured by atomic force microscopy*, BIOPHYSICAL JOURNAL **75**, 3008 (1998).
[58] M. S. Kellermayer, S. B. Smith, H. L. Granzier, and C. Bustamante, *Folding-unfolding transitions in single titin molecules characterized with laser tweezers*, SCIENCE **276**, 1112 (1997).
[59] H. Li, M. Carrion-Vazquez, A. F. Oberhauser, P. E. Marszalek, and J. M. Fernandez, *Point mutations alter the mechanical stability of immunoglobulin modules*, NATURE STRUCTURAL BIOLOGY **7**, 1117 (2000).
[60] H. Li *et al.*, *Reverse engineering of the giant muscle protein titin*, NATURE **418**, 998 (2002).
[61] H. Dietz, and M. Rief, *Exploring the energy landscape of GFP by single-molecule mechanical experiments*, PROC NATL ACAD SCI U S A **101**, 16192 (2004).
[62] I. Schwaiger, A. Kardinal, M. Schleicher, A. A. Noegel, and M. Rief, *A mechanical unfolding intermediate in an actin-crosslinking protein*, NATURE STRUCTURAL & MOLECULAR BIOLOGY **11**, 81 (2004).
[63] A. Valbuena *et al.*, *On the remarkable mechanostability of scaffoldins and the mechanical clamp motif*, PROC NATL ACAD SCI U S A **106**, 13791 (2009).
[64] E. M. Puchner, and H. E. Gaub, *Force and function: probing proteins with AFM-based force spectroscopy*, CURR OPIN STRUCT BIOL **19**, 605 (2009).
[65] M. Takeichi, *Cadherin cell adhesion receptors as a morphogenetic regulator*, SCIENCE **251**, 1451 (1991).
[66] U. Cavallaro, and G. Christofori, *Cell adhesion and signalling by cadherins and Ig-CAMs in cancer*, NATURE REVIEWS. CANCER **4**, 118 (2004).
[67] R. O. Hynes, *Integrins: versatility, modulation, and signaling in cell adhesion*, CELL **69**, 11 (1992).
[68] F. G. Giancotti, and E. Ruoslahti, *Integrin signaling*, SCIENCE **285**, 1028 (1999).
[69] A. S. French, *Mechanotransduction*, ANNUAL REVIEW OF PHYSIOLOGY **54**, 135 (1992).
[70] G. Manning, D. B. Whyte, R. Martinez, T. Hunter, and S. Sudarsanam, *The protein kinase complement of the human genome*, SCIENCE **298**, 1912 (2002).
[71] P. J. Gallagher, B. P. Herring, and J. T. Stull, *Myosin light chain kinases*, JOURNAL OF MUSCLE RESEARCH AND CELL MOTILITY **18**, 1 (1997).
[72] O. Mayans *et al.*, *Structural basis for activation of the titin kinase domain during myofibrillogenesis*, NATURE **395**, 863 (1998).
[73] F. Grater, J. Shen, H. Jiang, M. Gautel, and H. Grubmuller, *Mechanically induced titin kinase activation studied by force-probe molecular dynamics simulations*, BIOPHYS J **88**, 790 (2005).
[74] E. M. Puchner, and H. E. Gaub, *Exploring the conformation-regulated function of titin kinase by mechanical pump and probe experiments with single molecules*, ANGEW CHEM INT ED ENGL **49**, 1147 (2010).
[75] S. Lange *et al.*, *The kinase domain of titin controls muscle gene expression and protein turnover*, SCIENCE **308**, 1599 (2005).
[76] P. Nicolao *et al.*, *Autosomal dominant myopathy with proximal weakness and early respiratory muscle involvement maps to chromosome 2q*, AMERICAN JOURNAL OF HUMAN GENETICS **64**, 788 (1999).
[77] L. Edstrom, L. E. Thornell, J. Albo, S. Landin, and M. Samuelsson, *Myopathy with respiratory failure and typical myofibrillar lesions*, JOURNAL OF THE NEUROLOGICAL SCIENCES **96**, 211 (1990).
[78] J. Peng *et al.*, *Cardiac hypertrophy and reduced contractility in hearts deficient in the titin kinase region*, CIRCULATION **115**, 743 (2007).
[79] S. K. Kufer, E. M. Puchner, H. Gumpp, T. Liedl, and H. E. Gaub, *Single-molecule cut-and-paste surface assembly*, SCIENCE **319**, 594 (2008).

[80] B. Essevaz-Roulet, U. Bockelmann, and F. Heslot, *Mechanical separation of the complementary strands of DNA*, PROC NATL ACAD SCI U S A **94**, 11935 (1997).
[81] R. Krautbauer, M. Rief, and H. E. Gaub, *Unzipping DNA oligomers*, NANO LETT **3**, 493 (2003).
[82] M. Rief, H. Clausen-Schaumann, and H. E. Gaub, *Sequence-dependent mechanics of single DNA molecules*, NATURE STRUCTURAL BIOLOGY **6**, 346 (1999).
[83] C. H. Albrecht, G. Neuert, R. A. Lugmaier, and H. E. Gaub, *Molecular force balance measurements reveal that double-stranded DNA unbinds under force in rate-dependent pathways*, BIOPHYSICAL JOURNAL **94**, 4766 (2008).
[84] K. C. Neuman, and A. Nagy, *Single-molecule force spectroscopy: optical tweezers, magnetic tweezers and atomic force microscopy*, NAT METHODS **5**, 491 (2008).
[85] S. B. Smith, L. Finzi, and C. Bustamante, *Direct mechanical measurements of the elasticity of single DNA molecules by using magnetic beads*, SCIENCE **258**, 1122 (1992).
[86] T. R. Strick, V. Croquette, and D. Bensimon, *Single-molecule analysis of DNA uncoiling by a type II topoisomerase*, NATURE **404**, 901 (2000).
[87] C. Gosse, and V. Croquette, *Magnetic tweezers: micromanipulation and force measurement at the molecular level*, BIOPHYS J **82**, 3314 (2002).
[88] D. G. Grier, *A revolution in optical manipulation*, NATURE **424**, 810 (2003).
[89] A. Ashkin, *Applications of laser radiation pressure*, SCIENCE **210**, 1081 (1980).
[90] A. Ashkin, *Optical trapping and manipulation of neutral particles using lasers*, PROC NATL ACAD SCI U S A **94**, 4853 (1997).
[91] R. Merkel, P. Nassoy, A. Leung, K. Ritchie, and E. Evans, *Energy landscapes of receptor-ligand bonds explored with dynamic force spectroscopy*, NATURE **397**, 50 (1999).
[92] C. Gourier, A. Jegou, J. Husson, and F. Pincet, *A Nanospring Named Erythrocyte. The Biomembrane Force Probe*, CELLULAR AND MOLECULAR BIOENGINEERING **1**, 263 (2008).
[93] K. Halvorsen, and W. P. Wong, *Massively parallel single-molecule manipulation using centrifugal force*, BIOPHYS J **98**, L53 (2010).
[94] G. Binnig, C. F. Quate, and C. Gerber, *Atomic Force Microscope*, PHYSICAL REVIEW LETTERS **56**, 930 (1986).
[95] B. W. Hoogenboom, P. L. Frederix, D. Fotiadis, H. J. Hug, and A. Engel, *Potential of interferometric cantilever detection and its application for SFM/AFM in liquids*, NANOTECHNOLOGY **19**, 384019 (2008).
[96] S. M. Lindsay *et al.*, *STM and AFM images of nucleosome DNA under water*, J BIOMOL STRUCT DYN **7**, 279 (1989).
[97] A. L. Weisenhorn *et al.*, *Molecular-Resolution Images of Langmuir-Blodgett-Films and DNA by Atomic Force Microscopy*, LANGMUIR **7**, 8 (1991).
[98] M. Radmacher, R. W. Tillamnn, M. Fritz, and H. E. Gaub, *From molecules to cells: imaging soft samples with the atomic force microscope*, SCIENCE **257**, 1900 (1992).
[99] M. Radmacher, M. Fritz, H. G. Hansma, and P. K. Hansma, *Direct Observation of Enzyme-Activity with the Atomic-Force Microscope*, SCIENCE **265**, 1577 (1994).
[100] V. T. Moy, E. L. Florin, and H. E. Gaub, *Intermolecular forces and energies between ligands and receptors*, SCIENCE **266**, 257 (1994).
[101] H. J. Butt, and M. Jaschke, *Calculation of thermal noise in atomic-force microscopy*, NANOTECHNOLOGY **6**, 1 (1995).
[102] R. W. Stark, T. Drobek, and W. M. Heckl, *Thermomechanical noise of a free v-shaped cantilever for atomic-force microscopy*, ULTRAMICROSCOPY **86**, 207 (2001).
[103] S. Cook *et al.*, *Practical implementation of dynamic methods for measuring atomic force microscope cantilever spring constants*, NANOTECHNOLOGY **17**, 2135 (2006).
[104] M. B. Viani *et al.*, *Small cantilevers for force spectroscopy of single molecules*, JOURNAL OF APPLIED PHYSICS **86**, 2258 (1999).
[105] T. Pirzer, and T. Hugel, *Atomic force microscopy spring constant determination in viscous liquids*, REV SCI INSTRUM **80**, 035110 (2009).
[106] J. te Riet *et al.*, *Interlaboratory round robin on cantilever calibration for AFM force spectroscopy*, ULTRAMICROSCOPY **111**, 1659 (2011).
[107] C. Bustamante, J. F. Marko, E. D. Siggia, and S. Smith, *Entropic elasticity of lambda-phage DNA*, SCIENCE **265**, 1599 (1994).
[108] J. F. Marko, and E. D. Siggia, *Stretching DNA*, MACROMOLECULES **28**, 8759 (1995).

[109] T. Hugel, M. Rief, M. Seitz, H. E. Gaub, and R. R. Netz, *Highly stretched single polymers: atomic-force-microscope experiments versus ab-initio theory*, PHYS REV LETT **94**, 048301 (2005).
[110] P. H. Verdier, *RELAXATION BEHAVIOR OF FREELY JOINTED CHAIN*, JOURNAL OF CHEMICAL PHYSICS **52**, 5512 (1970).
[111] R. F. Alvarez-Estrada, *Freely jointed molecular chain: Dynamical variables, quantization, and statistical mechanics*, PHYSICAL REVIEW. A **46**, 3206 (1992).
[112] A. Perico, S. Bisio, and C. Cuniberti, *POLYMER DYNAMICS IN DILUTE-SOLUTIONS - THE FREELY ROTATING CHAIN*, MACROMOLECULES **17**, 2686 (1984).
[113] L. Livadaru, R. R. Netz, and H. J. Kreuzer, *Stretching response of discrete semiflexible polymers*, MACROMOLECULES **36**, 3732 (2003).
[114] E. M. Puchner, G. Franzen, M. Gautel, and H. E. Gaub, *Comparing proteins by their unfolding pattern*, BIOPHYS J **95**, 426 (2008).
[115] E. Evans, and K. Ritchie, *Strength of a weak bond connecting flexible polymer chains*, BIOPHYS J **76**, 2439 (1999).
[116] G. I. Bell, *Models for the specific adhesion of cells to cells*, SCIENCE **200**, 618 (1978).
[117] O. K. Dudko, G. Hummer, and A. Szabo, *Theory, analysis, and interpretation of single-molecule force spectroscopy experiments*, PROC NATL ACAD SCI U S A **105**, 15755 (2008).
[118] O. K. Dudko, *Single-molecule mechanics: new insights from the escape-over-a-barrier problem*, PROC NATL ACAD SCI U S A **106**, 8795 (2009).
[119] Y. Suzuki, and O. K. Dudko, *Single-molecule rupture dynamics on multidimensional landscapes*, PHYS REV LETT **104**, 048101 (2010).
[120] D. J. Stephens, and V. J. Allan, *Light microscopy techniques for live cell imaging*, SCIENCE **300**, 82 (2003).
[121] D. Axelrod, *Total internal reflection fluorescence microscopy in cell biology*, TRAFFIC **2**, 764 (2001).
[122] W. R. Zipfel, R. M. Williams, and W. W. Webb, *Nonlinear magic: multiphoton microscopy in the biosciences*, NATURE BIOTECHNOLOGY **21**, 1369 (2003).
[123] M. J. Levene *et al.*, *Zero-mode waveguides for single-molecule analysis at high concentrations*, SCIENCE **299**, 682 (2003).
[124] L. D. Lavis, T. Y. Chao, and R. T. Raines, *Fluorogenic label for biomolecular imaging*, ACS CHEMICAL BIOLOGY **1**, 252 (2006).
[125] S. Tyagi, and F. R. Kramer, *Molecular beacons: Probes that fluoresce upon hybridization*, NATURE BIOTECHNOLOGY **14**, 303 (1996).
[126] M. Tokunaga, K. Kitamura, K. Saito, A. H. Iwane, and T. Yanagida, *Single molecule imaging of fluorophores and enzymatic reactions achieved by objective-type total internal reflection fluorescence microscopy*, BIOCHEMICAL AND BIOPHYSICAL RESEARCH COMMUNICATIONS **235**, 47 (1997).
[127] R. E. Thompson, D. R. Larson, and W. W. Webb, *Precise nanometer localization analysis for individual fluorescent probes*, BIOPHYS J **82**, 2775 (2002).
[128] A. Yildiz, and P. R. Selvin, *Fluorescence imaging with one nanometer accuracy: application to molecular motors*, ACCOUNTS OF CHEMICAL RESEARCH **38**, 574 (2005).
[129] E. Betzig *et al.*, *Imaging intracellular fluorescent proteins at nanometer resolution*, SCIENCE **313**, 1642 (2006).
[130] S. T. Hess, T. P. K. Girirajan, and M. D. Mason, *Ultra-high resolution imaging by fluorescence photoactivation localization microscopy*, BIOPHYS J **91**, 4258 (2006).
[131] M. J. Rust, M. Bates, and X. W. Zhuang, *Sub-diffraction-limit imaging by stochastic optical reconstruction microscopy (STORM)*, NAT METHODS **3**, 793 (2006).
[132] C. Steinhauer, C. Forthmann, J. Vogelsang, and P. Tinnefeld, *Superresolution microscopy on the basis of engineered dark states*, J AM CHEM SOC **130**, 16840 (2008).
[133] T. A. Klar, and S. W. Hell, *Subdiffraction resolution in far-field fluorescence microscopy*, OPT LETT **24**, 954 (1999).
[134] D. Ramos, J. Tamayo, J. Mertens, and M. Calleja, *Photothermal excitation of microcantilevers in liquids*, JOURNAL OF APPLIED PHYSICS **99**, 124904 (2006).
[135] S. Rast, C. Wattinger, U. Gysin, and E. Meyer, *Dynamics of damped cantilevers*, REVIEW OF SCIENTIFIC INSTRUMENTS **71**, 2772 (2000).
[136] M. Vassalli, V. Pini, and B. Tiribilli, *Role of the driving laser position on atomic force microscopy cantilevers excited by photothermal and radiation pressure effects*, APPLIED PHYSICS LETTERS **97** (2010).

[137] J. W. Rogers, and L. M. Phinney, *Temperature response of silicon MEMS cantilevers during and after Nd : Yag laser irradiation*, NUMERICAL HEAT TRANSFER PART A-APPLICATIONS **45**, 737 (2004).
[138] H. Yamashita *et al.*, *Tip-sample distance control using photothermal actuation of a small cantilever for high-speed atomic force microscopy*, REVIEW OF SCIENTIFIC INSTRUMENTS **78**, 083702 (2007).
[139] A. Labuda *et al.*, *Comparison of photothermal and piezoacoustic excitation methods for frequency and phase modulation atomic force microscopy in liquid environments*, AIP ADVANCES **1** (2011).
[140] P. Paoletti, M. Basso, V. Pini, B. Tiribilli, and M. Vassalli, *Self-driven soft imaging in liquid by means of photothermal excitation*, JOURNAL OF APPLIED PHYSICS **110** (2011).
[141] T. Fukuma, K. Onishi, N. Kobayashi, A. Matsuki, and H. Asakawa, *Atomic-resolution imaging in liquid by frequency modulation atomic force microscopy using small cantilevers with megahertz-order resonance frequencies*, NANOTECHNOLOGY **23** (2012).
[142] C. Metzger *et al.*, *Self-induced oscillations in an optomechanical system driven by bolometric backaction*, PHYS REV LETT **101**, 133903 (2008).
[143] T. Ono, S. Yoshida, Y. Kawai, and M. Esashi, *Optical amplification of the resonance of a bimetal silicon cantilever*, APPLIED PHYSICS LETTERS **90** (2007).
[144] H. Fu, C. Liu, Y. Liu, J. Chu, and G. Cao, *Selective photothermal self-excitation of mechanical modes of a micro-cantilever for force microscopy*, APPLIED PHYSICS LETTERS **99** (2011).
[145] J. Park, S. Nishida, P. Lambert, H. Kawakatsu, and H. Fujita, *High-resolution cantilever biosensor resonating at air-liquid in a microchannel*, LAB ON A CHIP **11**, 4187 (2011).
[146] S. W. Stahl, E. M. Puchner, and H. E. Gaub, *Photothermal cantilever actuation for fast single-molecule force spectroscopy*, REV SCI INSTRUM **80**, 073702 (2009).
[147] Q. Peng, and H. Li, *Atomic force microscopy reveals parallel mechanical unfolding pathways of T4 lysozyme: evidence for a kinetic partitioning mechanism*, PROC NATL ACAD SCI U S A **105**, 1885 (2008).
[148] D. B. Wetlaufer, *Nucleation, rapid folding, and globular intrachain regions in proteins*, PROC NATL ACAD SCI U S A **70**, 697 (1973).
[149] J. Cellitti *et al.*, *Exploring subdomain cooperativity in T4 lysozyme I: structural and energetic studies of a circular permutant and protein fragment*, PROTEIN SCIENCE : A PUBLICATION OF THE PROTEIN SOCIETY **16**, 842 (2007).
[150] A. F. Oberhauser, P. K. Hansma, M. Carrion-Vazquez, and J. M. Fernandez, *Stepwise unfolding of titin under force-clamp atomic force microscopy*, PROC NATL ACAD SCI U S A **98**, 468 (2001).
[151] Y. Cao, and H. Li, *Single-molecule force-clamp spectroscopy: dwell time analysis and practical considerations*, LANGMUIR **27**, 1440 (2011).
[152] T. L. Kuo *et al.*, *Probing static disorder in Arrhenius kinetics by single-molecule force spectroscopy*, PROC NATL ACAD SCI U S A **107**, 11336 (2010).
[153] D. L. Floyd, S. C. Harrison, and A. M. van Oijen, *Analysis of kinetic intermediates in single-particle dwell-time distributions*, BIOPHYS J **99**, 360 (2010).
[154] B. Xu *et al.*, *RhoA/ROCK, cytoskeletal dynamics, and focal adhesion kinase are required for mechanical stretch-induced tenogenic differentiation of human mesenchymal stem cells*, JOURNAL OF CELLULAR PHYSIOLOGY **227**, 2722 (2012).
[155] N. Zebda, O. Dubrovskyi, and K. G. Birukov, *Focal adhesion kinase regulation of mechanotransduction and its impact on endothelial cell functions*, MICROVASCULAR RESEARCH **83**, 71 (2012).
[156] V. W. Wong *et al.*, *Focal adhesion kinase links mechanical force to skin fibrosis via inflammatory signaling*, NATURE MEDICINE **18**, 148 (2012).
[157] P. Leucht, J. B. Kim, J. A. Currey, J. Brunski, and J. A. Helms, *FAK-Mediated mechanotransduction in skeletal regeneration*, PLOS ONE **2**, e390 (2007).
[158] H. B. Wang, M. Dembo, S. K. Hanks, and Y. L. Wang, *Focal adhesion kinase is involved in mechanosensing during fibroblast migration*, P NATL ACAD SCI USA **98**, 11295 (2001).
[159] G. Giannone, and M. P. Sheetz, *Substrate rigidity and force define form through tyrosine phosphatase and kinase pathways*, TRENDS IN CELL BIOLOGY **16**, 213 (2006).
[160] V. Vogel, and M. Sheetz, *Local force and geometry sensing regulate cell functions*, NAT REV MOL CELL BIO **7**, 265 (2006).

[161] E. G. Arias-Salgado *et al.*, *Src kinase activation by direct interaction with the integrin beta cytoplasmic domain*, PROC NATL ACAD SCI U S A **100**, 13298 (2003).
[162] Y. Wang *et al.*, *Visualizing the mechanical activation of Src*, NATURE **434**, 1040 (2005).
[163] Y. Sawada *et al.*, *Force sensing by mechanical extension of the Src family kinase substrate p130Cas*, CELL **127**, 1015 (2006).
[164] I. Agarkova, and J. C. Perriard, *The M-band: an elastic web that crosslinks thick filaments in the center of the sarcomere*, TRENDS IN CELL BIOLOGY **15**, 477 (2005).
[165] S. W. Stahl, E. M. Puchner, A. Alexandrovich, M. Gautel, and H. E. Gaub, *A conditional gating mechanism assures the integrity of the molecular force-sensor titin kinase*, BIOPHYS J **101**, 1978 (2011).
[166] A. P. Somlyo, and A. V. Somlyo, *Ca2+ sensitivity of smooth muscle and nonmuscle myosin II: Modulated by G proteins, kinases, and myosin phosphatase*, PHYSIOLOGICAL REVIEWS **83**, 1325 (2003).
[167] V. Guerriero, D. R. Rowley, and A. R. Means, *PRODUCTION AND CHARACTERIZATION OF AN ANTIBODY TO MYOSIN LIGHT CHAIN KINASE AND INTRACELLULAR-LOCALIZATION OF THE ENZYME*, CELL **27**, 449 (1981).
[168] R. Dabrowska, S. Hinkins, M. P. Walsh, and D. J. Hartshorne, *The binding of smooth muscle myosin light chain kinase to actin*, BIOCHEMICAL AND BIOPHYSICAL RESEARCH COMMUNICATIONS **107**, 1524 (1982).
[169] S. Kanoh, M. Ito, E. Niwa, Y. Kawano, and D. J. Hartshorne, *Actin-binding peptide from smooth muscle myosin light chain kinase*, BIOCHEMISTRY **32**, 8902 (1993).
[170] P. J. Gallagher, and J. T. Stull, *Localization of an actin binding domain in smooth muscle myosin light chain kinase*, MOLECULAR AND CELLULAR BIOCHEMISTRY **173**, 51 (1997).
[171] L. Smith, X. Su, P. Lin, G. Zhi, and J. T. Stull, *Identification of a novel actin binding motif in smooth muscle myosin light chain kinase*, J BIOL CHEM **274**, 29433 (1999).
[172] J. R. Sellers, and M. D. Pato, *The binding of smooth muscle myosin light chain kinase and phosphatases to actin and myosin*, J BIOL CHEM **259**, 7740 (1984).
[173] L. H. Ye *et al.*, *The structure and function of the actin-binding domain of myosin light chain kinase of smooth muscle*, J BIOL CHEM **272**, 32182 (1997).
[174] A. Nakamura *et al.*, *Role of non-kinase activity of myosin light-chain kinase in regulating smooth muscle contraction, a review dedicated to Dr. Setsuro Ebashi*, BIOCHEMICAL AND BIOPHYSICAL RESEARCH COMMUNICATIONS **369**, 135 (2008).
[175] K. Obara, M. Uchino, M. Koide, A. Yamanaka, and K. Nakayama, *Stretch-induced triphosphorylation of myosin light chain and myogenic tone in canine basilar artery*, EUROPEAN JOURNAL OF PHARMACOLOGY **534**, 141 (2006).
[176] C. F. Lee, C. Haase, S. Deguchi, and R. Kaunas, *Cyclic stretch-induced stress fiber dynamics - dependence on strain rate, Rho-kinase and MLCK*, BIOCHEMICAL AND BIOPHYSICAL RESEARCH COMMUNICATIONS **401**, 344 (2010).
[177] S. C. Connolly *et al.*, *Chronic oscillatory strain induces MLCK associated rapid recovery from acute stretch in airway smooth muscle cells*, J APPL PHYSIOL **111**, 955 (2011).
[178] J. E. Stelzer, J. R. Patel, and R. L. Moss, *Acceleration of stretch activation in murine myocardium due to phosphorylation of myosin regulatory light chain*, THE JOURNAL OF GENERAL PHYSIOLOGY **128**, 261 (2006).
[179] M. Ikebe, *Mode of inhibition of smooth muscle myosin light chain kinase by synthetic peptide analogs of the regulatory site*, BIOCHEMICAL AND BIOPHYSICAL RESEARCH COMMUNICATIONS **168**, 714 (1990).
[180] H. Komatsu, and M. Ikebe, *Affinity labelling of smooth-muscle myosin light-chain kinase with 5'-[p-(fluorosulphonyl)benzoyl]adenosine*, THE BIOCHEMICAL JOURNAL **296 (Pt 1)**, 53 (1993).
[181] P. J. Kennelly, J. Leng, and P. Marchand, *The MgATP-binding site on chicken gizzard myosin light chain kinase remains open and functionally competent during the calmodulin-dependent activation-inactivation cycle of the enzyme*, BIOCHEMISTRY **31**, 5394 (1992).
[182] E. M. Rubin, *Genomics of cellulosic biofuels*, NATURE **454**, 841 (2008).
[183] A. Eisentraut, in *IEA Energy Papers* (OECD Publishing, 2010).
[184] D. G. Evans, (International Biofuels Strategy Project, 2007).
[185] M. E. Himmel, and E. A. Bayer, *Lignocellulose conversion to biofuels: current challenges, global perspectives*, CURRENT OPINION IN BIOTECHNOLOGY **20**, 316 (2009).

[186] A. Pollet *et al.*, *Crystallographic and activity-based evidence for thumb flexibility and its relevance in glycoside hydrolase family 11 xylanases*, PROTEINS-STRUCTURE FUNCTION AND BIOINFORMATICS **77**, 395 (2009).
[187] C. R. Santos *et al.*, *Thermal-induced conformational changes in the product release area drive the enzymatic activity of xylanases 10B: Crystal structure, conformational stability and functional characterization of the xylanase 10B from Thermotoga petrophila RKU-1*, BIOCHEMICAL AND BIOPHYSICAL RESEARCH COMMUNICATIONS **403**, 214 (2010).
[188] M. T. Murakami *et al.*, *Correlation of temperature induced conformation change with optimum catalytic activity in the recombinant G/11 xylanase A from Bacillus subtilis strain 168 (1A1)*, FEBS LETTERS **579**, 6505 (2005).
[189] C. Dash, V. Vathipadiekal, S. P. George, and M. Rao, *Slow-tight binding inhibition of xylanase by an aspartic protease inhibitor - Kinetic parameters and conformational changes that determine the affinity and selectivity of the bifunctional nature of the inhibitor's*, JOURNAL OF BIOLOGICAL CHEMISTRY **277**, 17978 (2002).
[190] A. Torronen, A. Harkki, and J. Rouvinen, *3-DIMENSIONAL STRUCTURE OF ENDO-1,4-BETA-XYLANASE-II FROM TRICHODERMA-REESEI - 2 CONFORMATIONAL STATES IN THE ACTIVE-SITE*, EMBO JOURNAL **13**, 2493 (1994).
[191] J. Muilu, A. Torronen, M. Perakyla, and J. Rouvinen, *Functional conformational changes of endo-1,4-xylanase II from Trichoderma reesei: A molecular dynamics study*, PROTEINS-STRUCTURE FUNCTION AND GENETICS **31**, 434 (1998).
[192] J. Morfill *et al.*, *Affinity-matured recombinant antibody fragments analyzed by single-molecule force spectroscopy*, BIOPHYS J **93**, 3583 (2007).
[193] J. Morfill *et al.*, *Force-based analysis of multidimensional energy landscapes: application of dynamic force spectroscopy and steered molecular dynamics simulations to an antibody fragment-peptide complex*, JOURNAL OF MOLECULAR BIOLOGY **381**, 1253 (2008).
[194] J. Schmitz, M. Benoit, and K. E. Gottschalk, *The viscoelasticity of membrane tethers and its importance for cell adhesion*, BIOPHYS J **95**, 1448 (2008).
[195] F. Kuhner *et al.*, *LexA-DNA bond strength by single molecule force spectroscopy*, BIOPHYS J **87**, 2683 (2004).
[196] G. Neuert, C. Albrecht, E. Pamir, and H. E. Gaub, *Dynamic force spectroscopy of the digoxigenin-antibody complex*, FEBS LETTERS **580**, 505 (2006).
[197] C. Yuan, A. Chen, P. Kolb, and V. T. Moy, *Energy Landscape of Streptavidin-Biotin Complexes Measured by Atomic Force Microscopy ‚Ä†*, BIOCHEMISTRY **39**, 10219 (2000).
[198] A. L. Carvalho *et al.*, *Evidence for a dual binding mode of dockerin modules to cohesins*, PROC NATL ACAD SCI U S A **104**, 3089 (2007).
[199] H. J. Gilbert, *Cellulosomes: microbial nanomachines that display plasticity in quaternary structure*, MOL MICROBIOL **63**, 1568 (2007).
[200] H. Kuhn, in Verhandlungen der Schweitzerischen Naturkundlichen Gesellschaft1965), pp. 245.
[201] W. M. Heckl *et al.*, *2-Dimensional Ordering of the DNA-Base Guanine Observed by Scanning Tunneling Microscopy*, P NATL ACAD SCI USA **88**, 8003 (1991).
[202] J. A. Stroscio, and D. M. Eigler, *Atomic and Molecular Manipulation with the Scanning Tunneling Microscope*, SCIENCE **254**, 1319 (1991).
[203] N. Kramer, J. Jorritsma, H. Birk, and C. Schonenberger, *Nanometer Lithography on Silicon and Hydrogenated Amorphous-Silicon with Low-Energy Electrons*, J VAC SCI TECHNOL B **13**, 805 (1995).
[204] M. T. Cuberes, R. R. Schlittler, and J. K. Gimzewski, *Room-temperature repositioning of individual C-60 molecules at Cu steps: Operation of a molecular counting device*, APPLIED PHYSICS LETTERS **69**, 3016 (1996).
[205] D. M. Eigler, and E. K. Schweizer, *Positioning Single Atoms with a Scanning Tunneling Microscope*, NATURE **344**, 524 (1990).
[206] M. F. Crommie, C. P. Lutz, and D. M. Eigler, *Confinement of Electrons to Quantum Corrals on a Metal-Surface*, SCIENCE **262**, 218 (1993).
[207] M. J. Holness, and M. C. Sugden, *Regulation of pyruvate dehydrogenase complex activity by reversible phosphorylation*, BIOCHEM. SOC. TRANS. **31**, 1143 (2003).
[208] K. Brettel, *Electron transfer and arrangement of the redox cofactors in photosystem I*, BIOCHIMICA ET BIOPHYSICA ACTA-BIOENERGETICS **1318**, 322 (1997).
[209] D. M. Kolpashchikov, *Split DNA enzyme for visual single nucleotide polymorphism typing*, J AM CHEM SOC **130**, 2934 (2008).

[210] K. M. Abedin *et al.*, *Diffusive Torsional Dynamics of Malachite Green Molecules in Solid Matrices Probed by Fluorescence Decay*, JOURNAL OF CHEMICAL PHYSICS **103**, 6414 (1995).
[211] L. Wang *et al.*, *Mutations in myosin light chain kinase cause familial aortic dissections*, AMERICAN JOURNAL OF HUMAN GENETICS **87**, 701 (2010).
[212] A. Karpol, Y. Barak, R. Lamed, Y. Shoham, and E. A. Bayer, *Functional asymmetry in cohesin binding belies inherent symmetry of the dockerin module: insight into cellulosome assembly revealed by systematic mutagenesis*, THE BIOCHEMICAL JOURNAL **410**, 331 (2008).
[213] H. P. Fierobe *et al.*, *Design and production of active cellulosome chimeras. Selective incorporation of dockerin-containing enzymes into defined functional complexes*, J BIOL CHEM **276**, 21257 (2001).
[214] S. Morais *et al.*, *Assembly of xylanases into designer cellulosomes promotes efficient hydrolysis of the xylan component of a natural recalcitrant cellulosic substrate*, MBIO **2** (2011).
[215] S. Morais *et al.*, *Cellulase-xylanase synergy in designer cellulosomes for enhanced degradation of a complex cellulosic substrate*, MBIO **1** (2010).
[216] N. Crampton, K. Alzahrani, G. S. Beddard, S. D. Connell, and D. J. Brockwell, *Mechanically unfolding protein L using a laser-feedback-controlled cantilever*, BIOPHYS J **100**, 1800 (2011).

10 LEBENSLAUF (ONLINEVERSION)

PERSÖNLICHE DATEN

Dipl. Physiker Stefan W. Stahl

Lehrstuhl für Angewandte Physik/Biophysik
Amalienstr. 54, 81669 München

11 DANKSAGUNG

Diese Arbeit bestand bei weitem nicht nur aus Experimenten und Auswertungen. Ohne die Unterstützung, den Ratschlag und die Gesellschaft vieler Personen wäre sie in ihrer vorliegenden Form nur schwer vorstellbar. Mein Dank gebührt unter anderem

Hermann Gaub, dafür dass er in seinem Lehrstuhl tagtäglich eine einmalige Arbeitsathmosphäre schafft, in der es einem von Ideen über Equipment, Tipps und leckerem Essen an nichts mangelt.

Mathias Strackharn, für eine überaus produktive Zusammenarbeit vom Mathevorkurs über viele Übungsblätter und Stabi-Lernmarathons bis hin zu den grenzenlosen Möglichkeiten der TIRF-AFM-Kombination. Ich drück Kathrin und Dir die Daumen für Eure zukünftigen Projekte und bin mir sicher, Du passt gut auf Deine Kleine auf!

Michael Nash, for a joyful collaboration on the cohesin-dockerin project and the nice company on our trip to Israel. May the force be with you on future cellulosomics and congratulations for your scholarship!

Stephan Heucke, als verlässlicher Kollege, für die aufmunternden Worte und die Schokolade während all der durchzechten Nächte im Cockpit der 747, für die pünktliche Wildschweinlieferung zu Weihnachten und natürlich für ’ne super Zeit während des JNN in Urbana-Champaign.

Diana Pippig, für Rat und Tat im Chemielabor und dafür, dass sie auch sonst immer ein offenes Ohr hat, aufmunternde Worte und aufmunternde Stücke Kuchen und das akribische Korrekturlesen der Arbeit.

Philip Severin, für die Geduld während der sporadischen, aber doch irgendwie regelmäßigen Stempelexperimente, interessante Diskussionen, das ein oder andere Feierabendbier und nützliche Tipps rund um das Format dieser Dissertation.

Ingo Stein, dafür, dass er auch bei scheinbar aussichtlosen Experimenten den Kopf nicht in den Sand gesteckt hast, die gute Zeit in Urbana-Champaign und viele gute Ratschläge als Kollege und Freund.

Elias Puchner, für die sagenhafte Betreuung während der Diplomarbeit, ohne die ich sicher nicht zu dieser Doktorarbeit gekommen wäre, für die vielen Ratschläge hinterher und die Unterbringung in Frisco samt Roadtrip (Vegas baby, Vegas!). Bin gespannt, wann ich dich Professor nennen muss.

Stefan Kufer, dafür dass er uns auf den richtigen Single-Molecule Cut-and-Paste Weg gebracht hat.

Thorben Cordes, für die gute Zusammenarbeit und Motivation beim Evil-Smiley-Blink Cut-and-Paste Messmarathon.

Hubert Krammer, für die konsequent pünktliche Getränkelieferung, vergangene und zukünftige Ski- und Wandertouren. Auch Maria und Dir alles Gute mit dem Nachwuchs!

Angelika Kardinal & Thomas (Tom) Nicolaus, für die Hilfe und Unterstützung bei der Proteinexpression und allen Fragen der Oberflächenfunktionalisierung.

Ed Bayer, Mathias Gautel, Daniel Fried, Birgit Brandmeier and Alex Alexandrovich for the good collaboration on interdisciplinary scientific projects.

Klaus & Zan Schulten dafür, dass sie uns mehr als herzlich in Urbana willkommen geheißen haben.

Den Leuten hinter CeNS, NIM und der LMU-Verwaltung dafür, dass sie so tolle Programme wie das JNN, das NIM Graduate Program und vieles mehr auf die Beine stellen.

Allen Korrektoren dieser Arbeit (Diana, Ingo, Mathias, Sandra, mein Vater Werner und meine Schwester Miriam) sowie *Silke „the knee“ Kirchner*, *Ilka „Chillerberg“ Kriegel* und *Manuel „Monchichi“ Wolff* für die einzigartige Überbrückung einer langen Drucknacht.

Meiner Familie, für all die Unterstützung während der letzten Jahre und dafür, dass ich weiß, dass ich mich jederzeit auf sie verlassen kann.

Und natürlich - last but not least - *meinem Schatz Clem* dafür, dass sie mich seit acht Jahren durchs Leben begleitet, mich unterstützt wenn’s mal eng wird, motiviert und meine Launen erträgt, wenn mal wieder was nicht nach Plan läuft. *Je t’aime à la folie*!